The Compositional Diversity of Small Planets Orbiting Low-Mass Stars

Thesis by
Michael C. Greklek-McKeon

In Partial Fulfillment of the Requirements for the
Degree of
Ph.D. in Planetary Science

Caltech

CALIFORNIA INSTITUTE OF TECHNOLOGY
Pasadena, California

2025
Defended May 29, 2025

ACKNOWLEDGEMENTS

Most importantly, thank you to my thesis advisor Heather Knutson. Heather is unique among advisors, and I count myself lucky to have spent these years under her mentorship. Heather helped me greatly in encouraging me to pursue the research that I found exciting, while steering me in the direction of productive ideas that played to my strengths. I am immensely thankful for all of the guidance she provided in our conversations over the years, which often converted my feelings of frustration and unease into optimism and resolve. I am also thankful that she always encouraged me when I wanted to pursue outreach and mentorship opportunities, which have made me a better scientist and teacher. The positive environment that Heather has worked to create in her group was the deciding factor in my graduate school research experience being a good one, and I am eternally grateful for that.

Thank you to Shreyas Vissapragada for being a wonderful group mate and taking me under his wing from the day I arrived at Caltech. Shreyas taught me many of the techniques that have become foundational for me as a scientist, and I am forever grateful for him as my scientific big brother and friend. Thank you to my Palomar observing crew, including Shreyas, Morgan Saidel, Jonathan Gomez Barrientos, and Garrett Levine, whose camaraderie has made the many long observing nights so much more enjoyable. And thank you for always being willing to share your time and ideas, which have led to so many exciting projects on which it is a joy to collaborate with you.

Thank you to the other members of my thesis committee, Konstantin Batygin, Gregg Hallinan, and Andrew Howard, for all the helpful scientific discussions, advice, and encouragement on various projects over the years. Thank you as well to the many staff members across the GPS Division who make my research possible, especially to Julie Lee and Ruth Loisel who made trips to the admin office something to look forward to.

To all of my teachers who came before graduate school — thank you for seeing a spark in me and going out of your way to nurture it. Special shoutout to Ms. Zefran for letting me skip class to go to that lecture at the planetarium, to Mr. Haag for letting me borrow that telescope and run wild with it, to Melissa Hayes-Gehrke for believing in me to teach astronomy for the first time, and to Drake Deming for taking a chance on me to complete a research project when I said I knew Python

but was clearly stretching the truth. I am grateful for what all of you taught me, and I will never forget how you made me feel like I could be a scientist. Thank you to my amazing mentors at Goddard — especially Yari Collado-Vega and Anna Chulaki, and to my REU mentor Dan Huber, for spending your time and energy to turn me from an enthusiastic undergraduate with no experience and few skills into a competent young researcher. Your support meant the world to me, and I would not be here without all of you.

I owe an enormous debt of gratitude to all of the Palomar observatory telescope operators, support astronomers, and staff, especially Paul Nied, Carolyn Heffner, Isaac Wilson, Jennifer Milburn, Diana Roderick, Kathleen Koviak, Rigel Rafto, John Stone, Kevin Rykoski, Tom Barlow, Kajsa Peffer, and Joel Pearman. Without you, my thesis would not be possible. I am so grateful for all of your hard work to ensure that I got as much data as possible despite battles with the weather, the instrument, and the telescope, and for your help with troubleshooting and improving WIRC observing. And I am thankful for the many clear and tranquil nights we spent together, just chatting. Thank you also to the Palomar observatory directorate, especially Andy Boden and Rick Burruss, and to all of my JPL, IPAC, and Caltech colleagues who shared Palomar time with me when last-minute situations arose, especially Gautam Vasisht, David Ciardi, Chas Beichman, and Aurora Kesseli. The data from those nights made a big difference in my thesis.

Thank you to the many collaborators around the world who have worked with me on TTV projects and shared your observational resources and expertise, especially Akihiko Fukui, Judith Korth, Fran Pozuelos, Seba Zúñiga-Fernández, Karen Collins, Cristilyn Gardner-Watkins, Avi Shporer, Norio Narita, Enric Pallé, Hannu Parviainen, Khalid Barkaoui, Daniel Jontof-Hutter, Juliana García-Mejía, and Pat Tamburo. You have greatly enriched my thesis, and shown me wonderful examples of collaboration where the sum of our collective efforts is greater than its parts.

To my fellow patients at the treatment sanctuary: Ryan, Costa, Henry, Keefe, Jordan, and Matt, and the many other friends I met along the way — I will spend the rest of my life cherishing how great it was being together in that house. Thank you for the countless fun times and memories over the years, both inside and outside of 2034 E California, may she rest in peace. All the time we spent getting up to stuff that was as far away from grad student life as possible was extremely well spent.

Thank you to my planetary science cohort — Maria Camarca, Marguerite Epstein-Martin, and Brandon Rasmussen, for your support and friendship and for helping me to get through those classes despite sometimes wanting to bang my head against a wall. Thank you to my fellow Knutson group members and other planetary science grads and postdocs whose friendship has continually brightened my time in grad school and made the planetary science department feel like home, especially Shreyas Vissapragada, Nicole Wallack, Aida Behmard, Yayaati Chachan, Jess Spake, Eva Scheller, Julie Inglis, Morgan Saidel, Kim Paragas, Zac Milby, Jonathan Gomez Barrientos, and Yu Yu Phua. Thanks to these friends who came before me for showing me the ropes and giving me advice that greatly helped me in navigating Caltech and academia, and to the ones who came after me for always being there to count on whether in times of commiseration about proposals and projects or in times of celebration about achievements and milestones.

To my amazing organizing friends who helped our union go from whispers around campus to the CGPU campaign to UAW 2478 — thank you for inspiring me, and for providing a community that I never thought I would find at Caltech. Building our union with you all is the best thing I did in grad school. I am so proud to have worked alongside so many incredible organizers, especially my bargaining team family Sam, Nadia, Korbi, James, Varun, Sim, Emma, David, Pat, Jessica, Ruolin, Matthew, Quinn, and Tessa, and my fellow organizers Ryan, Jack, Abdullah, Rohan, Jakob, Dee, Natasha, Sophie, Kyle, Harshda, Jasmine, Aditi, Tom, and many others. I learned so much from you all and will always be in awe of what we accomplished — a bunch of grads and postdocs, volunteering their time to stand together for what's right against a multi-billion dollar institution that hired the nation's top "labor lawyers," and we won. Caltech is a better place because of all your hard work and sacrifices, and I can't wait to see what comes next.

Thank you mom and dad, for buying me that telescope, and for not freaking out too much when I stomped around in the middle of the night on the roof with it. Thank you for for supporting me while I chased my childhood dream. Thank you to my siblings, Brian and Kelly, for paving the way for me. Thanks to Kelly for giving me the impression as a kid that doing science is cool, and for being my first role model.

Many of my findings during graduate school have brought me great happiness, including fulfilling a lifelong dream of discovering new planets. It is a rare and special thing, to explore a brand new world for the first time. I could never have predicted that what would bring me the most happiness, by far, was finding Molly. Having you by my side in these past five years has brought me the greatest joy in my life. Thank you Molly, for everything.

ABSTRACT

The Kepler and TESS missions have discovered thousands of exoplanets on close-in orbits. The most common planets discovered by these missions are between the size of Earth and Neptune, yet we have no examples of these planets in our solar system. Kepler revealed that these planets exhibit a bimodal radius distribution with peaks above and below approximately 1.8 Earth radii, suggesting distinct formation pathways or evolutionary histories that are not yet completely understood. Planets above and below this "radius valley" are commonly interpreted as planets with and without primordial hydrogen-rich atmospheres. The favorable planet-to-star size ratios of M dwarf stars offer exceptional opportunities to characterize these small planets. However, small planets around M dwarfs may have fundamentally different properties than those around Sun-like stars, including more water-rich compositions and higher atmospheric mass loss rates. We can shed light on the nature of these small M dwarf planets by measuring their masses, radii, and bulk compositions.

This thesis presents results from the first systematic transit timing variation (TTV) survey of TESS-discovered M dwarf planets. Systems with multiple planets on near-resonant orbits experience gravitational perturbations that produce TTVs. For faint or active M dwarf stars, TTVs are sometimes the only method capable of measuring masses for sub-Neptune-sized planets. However, the precision of the TTVs measured by TESS is often not sufficient for this purpose, and high-precision follow-up is required in order to obtain dynamical mass measurements. To enable the studies described below, I conducted an international ground-based observing campaign to collect more more than 80 transits of near-resonant M dwarf planets from the Hale telescope at Palomar Observatory, which served as the backbone of this survey, and regularly achieved transit timing precisions an order of magnitude better than TESS. I also collected over 20 transits from the Las Cumbres Observatory Global Telescope Network (LCOGT), and dozens of additional TTV observations from collaborators at other observatories. In this thesis, I present the results from 4 key systems observed by this survey. For each of these systems, I leveraged precise ground-based transit observations to provide improved measurements of the masses, densities, and corresponding bulk compositions of the near-resonant planet pairs.

In the first study, I analyzed the Kepler-289 system, which contains two inner sub-Neptune sized planets and an outer gas giant near the 1:2:4 resonance chain. I combined Kepler photometry with new Palomar observations to extend the TTV

baseline by 7.5 years and improve the mass constraints by more than a factor of two for all planets. I found that the inner planets have low densities requiring hydrogen-rich envelopes, while the outer gas giant contains approximately 30 Earth masses of heavy elements. By comparing the planets' current locations to the mass budget available in the inner protoplanetary disk, I placed a lower limit on the formation location of the outer gas giant beyond 3 au, well beyond its present-day location.

In the second study, I analyzed the TOI-1266 system, which contains two sub-Neptune-sized planets with a rare inverted architecture where the interior planet is larger than its exterior companion. I combined TESS photometry, ground-based transit observations, and radial velocity (RV) measurements in a joint TTV+RV dynamical model. My combined fit revealed that the inner planet likely has a non-zero eccentricity, suggesting that it may have an inflated hydrogen-rich envelope powered by tidal heating. Interior structure modeling indicates that the outer planet could host a water-rich envelope, and both planets are excellent candidates for atmospheric characterization with JWST.

In the third study, I characterized the LP 791-18 system, which contains three planets with radii equal to 1.2, 1.0, and 2.5 times that of the Earth. I used new high-precision transit observations to improve the mass and eccentricity measurements for the Earth-sized planet LP 791-18 d. I confirmed with dynamical modeling that LP 791-18 d may have a non-zero eccentricity forced by gravitational interactions with its larger neighbor, potentially resulting in significant tidal heating and volcanic activity. Contrary to a previous analysis, I showed that if LP 791-18 d has an Earth-like tidal dissipation efficiency, then the TTV observations are not sensitive to this forced eccentricity. I made predictions for the timing of upcoming JWST secondary eclipse observations that could reveal the planet's unknown tidal dissipation efficiency and potentially detect a volcanically outgassed atmosphere.

In the fourth study, I confirmed a new Earth-sized planet in the binary M dwarf system TOI-2267, which has a projected separation of just 8 au. If this planet orbits the secondary star it may be large enough to host a volatile-rich envelope, making it a valuable target for studying atmospheric mass loss around active M dwarfs. The new planet's orbital period is extremely close to the other two confirmed planets in this system. I used dynamical modeling to show that either this new planet orbits a different star than the other two, or it must be located in an extremely high 8:9 first-order resonance with planet b. This can be tested with TTV observations, and if confirmed would make this the most compact exoplanet system discovered to date.

These studies expand our understanding of the properties of small planets orbiting low-mass stars, and enable new investigations of planet composition and evolution within the same system. Future observations of additional systems will further expand our understanding of the compositional diversity among sub-Neptune-sized planets, identify additional candidate water worlds, and quantify the importance of eccentricity-driven tidal heating for the interiors and atmospheres of rocky worlds in compact multi-planet systems.

PUBLISHED CONTENT AND CONTRIBUTIONS

Greklek-McKeon, Michael, Shreyas Vissapragada, and Heather A. Knutson, et al. (2025). "Tidally Heated Sub-Neptunes, Refined Planetary Compositions, and Confirmation of a Third Planet in the TOI-1266 System". In: *The Astronomical Journal* 169.6, p. 292. DOI: `10.3847/1538-3881/adc0fe`.
M.G.M. conceived the project with input from coauthors, wrote observing proposals to collect the data, led the observational program, reduced the data, analyzed the results, and wrote the manuscript.

Greklek-McKeon, Michael, Heather A. Knutson, and W. Garrett Levine, et al. (2025). "Updated Mass, Eccentricity, and Tidal Heating Constraints for the Earth-sized Planet LP 791-18 d". In: *arXiv e-prints* arXiv:2501.18700. DOI: `10.48550/arXiv.2501.18700`.
M.G.M. conceived the project with input from coauthors, wrote observing proposals to collect the data, led the observational program, reduced the data, analyzed the results, and wrote the manuscript.

Greklek-McKeon, Michael, Heather A. Knutson, and Shreyas Vissapragada, et al. (2023). "Constraining the Densities of the Three Kepler-289 Planets with Transit Timing Variations". In: *The Astronomical Journal* 165.2, p. 48. DOI: `10.3847/1538-3881/ac8553`.
M.G.M. wrote an observing proposal to obstain a portion of the data, collected the observations, reduced the data, analyzed the results, and wrote the manuscript.

TABLE OF CONTENTS

LIST OF ILLUSTRATIONS

LIST OF TABLES

Chapter 1

INTRODUCTION

1.1 The Galactic Census of Rocky Planets

"In space there are countless constellations, suns and planets; we see only the suns because they give light; the planets remain invisible, for they are small and dark. There are also numberless earths circling around their suns, no worse and no less than this globe of ours."

– Giordano Bruno (1548 - 1600), *On the Infinity of the Universe and the Worlds, Third Dialog (Paraphrase)*, 1584

"Imagine how much the ancient laborious enquirers would envy us ... that a time would come, when mankind should be able to stretch out their eyes ... by which means, they should be able to discover ... every nebulous star appearing as if it were the firmament of some other world, at an incomprehensible distance, bury'd in the vast abyss of intermundious vacuum."

– Christopher Wren, *Gresham College Inaugural Lecture,* 1657

In the three decades since the discovery of the first planet orbiting a main sequence star, ongoing surveys have discovered more than 5,800 additional extrasolar planets, with thousands more candidates awaiting confirmation. The Kepler mission (Borucki et al., 2010) is responsible for discovering nearly half of all currently known exoplanets (NASA Exoplanet Archive, 2025). Kepler was a space telescope designed to search for planets in a small region of our galactic neighborhood by continuously monitoring the brightness of around 150,000 main sequence stars over a period of four years. One of the main science goals of the mission was to detect periodic dimming caused by exoplanets as they cross in front of their host star, and to identify small Earth-sized planets on long-period orbits by obtaining a long observational baseline. These long-period Earth-sized planets might orbit in the habitable zone of their host stars, where temperatures are just right for liquid water.

Kepler was successful in identifying several temperate Earth-sized planets, but one of the biggest discoveries of the mission was completely unexpected. Kepler

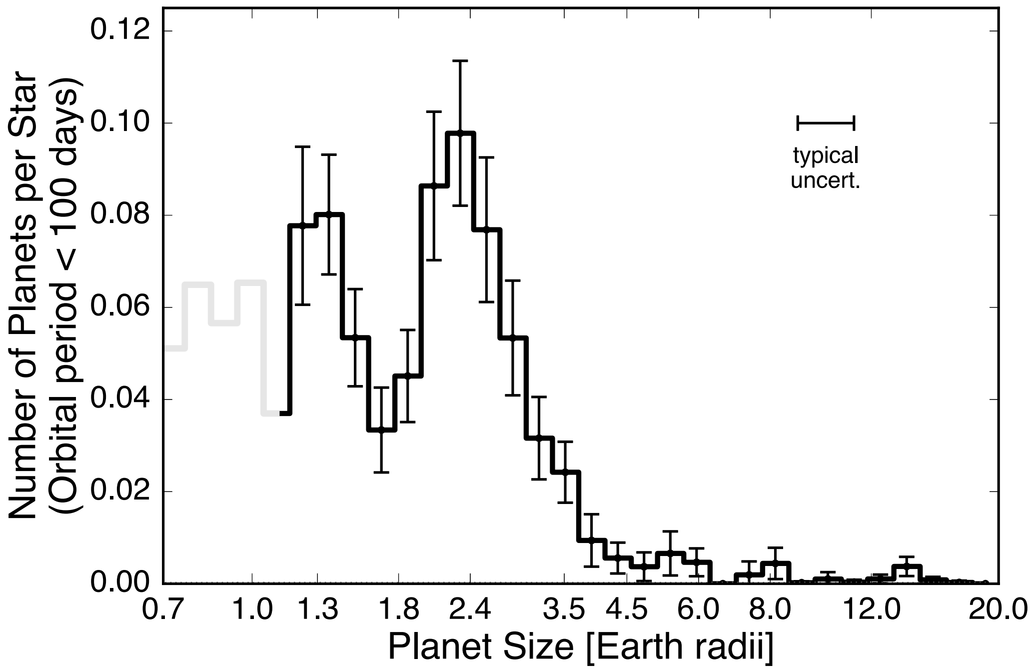

Figure 1.1 Figure 7 of Fulton et al., 2017. Completeness-corrected histogram of planet radii for planets with orbital periods shorter than 100 days. Uncertainties in the bin amplitudes are calculated using the suite of simulated surveys described in Appendix C of Fulton et al., 2017. The light gray region of the histogram for radii smaller than 1.14 $R_\oplus$ suffers from low completeness. The median radius uncertainty is plotted in the upper right portion of the plot. Planets in the lower peak near 1.5 $R_\oplus$ are known as "super-Earths," while planets in the upper peak near 2.4 $R_\oplus$ are known as "sub-Neptunes," and the gap between them is the "radius valley."

revealed that around half of all Sun-like stars host planets with sizes intermediate between that of Earth and Neptune on close-in orbits (Fulton et al., 2017; Hsu et al., 2019; Berger et al., 2020; J.-Y. Yang et al., 2020; Petigura et al., 2022). Subsequent studies have shown that this kind of planet is even more common around low-mass M dwarf stars (Hardegree-Ullman et al., 2019; Hsu et al., 2020; Ment et al., 2023; Parc et al., 2024). Yet, we have no example of this type of planet in our own solar system. Questions immediately arose about these ubiquitous but mysterious worlds — what are the typical compositions of these planets? How do they form, and how do they change over their lifetimes? Do they have atmospheres, and if so, what are they made of? Are they habitable? We are still attempting to answer these questions.

Kepler also revealed that planets in this size range, from 1 to 4 Earth radii, are split into two distinct sub-populations. There is a group of "super-Earths" peaked around 1.5 $R_\oplus$ and a group of "sub-Neptunes" peaked around 2.4 $R_\oplus$, with a distinct "radius valley", or dearth of planets, between them (Figure 1.1). This discovery sparked a flurry of new theoretical and observational work to explain our most common galactic neighbors and determine what separates these two populations of small planets. Follow-up studies to measure the masses of transiting super-Earths and sub-Neptunes have revealed typical bulk densities consistent with mass budgets dominated by rocky or water-rich cores, (Luque et al., 2022; Parc et al., 2024), although there are many plausible explanations for the radius valley.

One main class of models to explain the radius valley assumes that sub-Neptunes have hydrogen-rich envelopes, and it is the presence or absence of these envelopes that leads to the radius valley. Within this framework, one model type asserts that planet formation during the gas-poor phase of disk evolution can explain the radius valley through primordial differences in atmospheric mass (e.g., E. J. Lee et al., 2016; E. J. Lee et al., 2021; E. J. Lee et al., 2022). Another model type asserts that irradiation from the host star strips away the primoridal hydrogen-rich atmospheres of the close-in sub-Neptunes, turning them into super-Earths that are bare rocky cores (e.g., Owen et al., 2013; Lopez et al., 2014; Chen et al., 2016; Lopez et al., 2016). Another model type also asserts that sub-Neptunes are the planets that kept their primordial atmospheres while super-Earths lost them, but that core-powered internal heat from formation is sufficient to drive this atmospheric mass loss from within and carve the radius valley (Gupta et al., 2019; Gupta et al., 2020). The other major class class of models to explain the radius valley assumes that sub-Neptunes have water-rich envelopes, and that the radius valley can be explained by primordial differences in the composition of planetary cores (Luque et al., 2022).

To determine which of these factors are responsible for creating the observed small planet population, we must obtain planetary mass measurements. Mass measurements for individual transiting planets constrain the bulk compositions and envelope masses. This allows us to test these theories of planet formation and evolution that are based on the distribution of planets in radius-period space, and serve as cornerstones upon which the population-level models can be calibrated. By obtaining masses and other detailed properties for an ever-growing sample of planets, we can refine current planet formation and evolution theories and reveal trends that guide the development of new models.

1.2 The Opportunities and Challenges of Low-Mass Stars

We can measure the masses and radii of small planets by observing the decrease in light caused by a planet passing in front of its star (transit) or the Doppler shift of the star as it is gravitationally perturbed by the orbiting planet (radial velocity; see Section 1.4). M dwarfs are the lowest mass main-sequence stars, and they have smaller sizes and cooler temperatures than Sun-like stars. A small planet orbiting an M dwarf will exhibit much larger transit and radial velocity signals than an equivalent planet orbiting a Sun-like star, due to its larger planet-to-star radius and mass ratios. This means that M dwarfs are some of the most favorable targets for studies of small planets. M dwarfs are also the most abundant stars in our galaxy (Winters et al., 2015), and the occurrence rate of small close-in planets around M dwarfs is higher than it is for Sun-like stars (Dressing et al., 2015; Mulders et al., 2015; Ribas et al., 2023; Mignon et al., 2025). M dwarfs are therefore the logical place to start in our quest to understand the formation and evolution of sub-Neptune-sized planets.

Despite their favorable transit and radial velocity signal sizes, studies of small planets around M dwarfs also come with additional challenges. Because M dwarfs are smaller and cooler than Sun-like stars, they are also fainter. This means that ground-based observations of M dwarfs often require larger telescopes or longer observation times to achieve the required precision, even though small M dwarf planets typically have larger signal-to-noise ratios. The light emitted by M dwarfs also peaks at longer wavelengths than that of Sun-like stars, and near-infrared detectors are often more suitable than optical detectors for characterizing M dwarf planets. M dwarfs are also much more active than Sun-like Stars, which can make detecting transiting planets and obtaining follow-up mass measurements more difficult. Extracting the small signal of a planet from an optically faint, potentially rapidly varying active star can be challenging, but in most systems the large signal size more than compensates for these difficulties.

Kepler discovered thousands of small ($< 4\ R_\oplus$) transiting planets, but only $\sim$100 of them were around M dwarfs. Since the original Kepler survey was limited to a single 100 square degree patch of sky, the M dwarf planets discovered by Kepler typically orbit relatively faint stars, and are therefore challenging targets for radial velocity mass measurements. Thankfully, the all-sky Transiting Exoplanet Survey Satellite (TESS, Ricker et al., 2014) has recently expanded this sample to include an additional $\sim$125 small planets orbiting nearby M dwarfs.

There are several reasons to think that small, rocky planets around M dwarf stars might have fundamentally different properties than their counterparts around Sun-like stars. The lower effective temperatures of M dwarfs means that the disks from which planets form are colder, and the water ice line is located closer in. M dwarfs also host fewer giant planets than Sun-like stars (e.g., Bonfils et al., 2013; Montet et al., 2014; Bryant et al., 2023; Gan et al., 2023; Pass et al., 2023; Mignon et al., 2025), which can reduce the flow of solid material to the inner disk. This means that more of this ice-rich material may be available to small M dwarf planets on close-in orbits. Therefore, M dwarf planets may form with more water than small planets around other stars, and if they migrate in from these water-rich regions to the inner disk where we typically detect them (e.g., Chapter 2), then the known small M dwarf planets may be abundant in water (e.g., Bitsch et al., 2021). Whether that water is in the form of high-pressure ice in the planetary mantle, or potentially habitable liquid water at the surface, or as gas in a global steam atmosphere, depends on the specific conditions of each planet (e.g., Baumeister et al., 2020; Huang et al., 2022; Baumeister et al., 2023). M dwarfs also have higher fractional XUV fluxes, more frequent flares than their Sun-like counterparts, and a longer activity lifetime, which could result in enhanced atmospheric mass loss rates (Johnstone, 2020; Atri et al., 2021; Harbach et al., 2021). If this activity strips away the primordial hydrogen-rich atmospheres of sub-Neptunes around M dwarfs more efficiently than for Sun-like stars, then their low bulk densities might instead by explained by water-rich envelopes.

1.3 From Masses and Radii to Planet Compositions

Measurements of planetary masses, radii, and bulk densities can be used to constrain their bulk compositions and internal structures. The measured bulk densities of super-Earths appear to be largely consistent with an Earth-like rock-iron fraction, and definitively rule out the presence of extended volatile-rich envelopes (e.g., Luque et al., 2022; Rogers et al., 2023). In contrast to this result, sub-Neptunes have lower bulk densities (<3 g/cm^3), indicating the presence of a higher density core surrounded by a volatile-rich envelope comprising several percent or more of the total planetary mass (e.g., E. J. Lee, 2019). However, the fraction of hydrogen and helium relative to water in these envelopes is not well constrained by these observations (e.g., Parc et al., 2024)

For highly irradiated planets on close-in orbits, models of atmospheric mass loss can be used to provide additional constraints on the presence or absence of a significant atmosphere (e.g., Diamond-Lowe et al., 2022; Piaulet et al., 2023). For super-Earths, this allows us to minimize degeneracies between the retrieved rock-iron fraction and the possible presence of a water-rich layer in the case where a hydrogen-rich atmosphere can be ruled out (e.g., Baumeister et al., 2023). Sub-Neptunes that are able to retain their volatile-rich envelopes despite high predicted mass loss rates might have higher water mass fractions and/or higher overall atmospheric metallicities, which act to reduce the predicted mass loss rate (e.g., Zhang et al., 2025). Multi-planet systems provide an especially useful test case for models of atmospheric mass loss, as all of the planets experienced the same stellar irradiation history scaled by their orbital distances (e.g., Owen et al., 2020; Van Eylen et al., 2021).

A recent study by Luque et al., 2022 argued that the measured masses and radii of sub-Neptunes orbiting M dwarfs is best explained by the presence of a population of water worlds, although a subsequent study argued that these measurements can be equally well matched by a population of sub-Neptunes with hydrogen-rich envelopes sculpted by atmospheric mass loss (Rogers et al., 2023). Atmospheric characterization studies with JWST can provide a definitive answer to this question by directly measuring the water content of sub-Neptune envelopes. These studies have identified one planet with compelling evidence for a steam-dominated atmosphere to date (Piaulet-Ghorayeb et al., 2024a), while several others appear to have hydrogen-rich atmospheres with enhanced metallicities (Kempton et al., 2023; Benneke et al., 2024). However, these studies are limited by the relatively small pool of sub-Neptune targets with well-measured masses and radii that are amenable to atmospheric characterization with JWST.

1.4 Methods to Measure Planet Masses and Other Orbital Properties

The vast majority of known exoplanets have been discovered via the transit technique (NASA Exoplanet Archive, 2025). This technique was the focus of the Kepler and TESS missions, and in many cases is easily accessible to ground-based observatories. When the orbit of an exoplanet happens to be aligned with our line of sight to the star, we can measure the decrease in light when the planet passes in front of the star during the transit. The depth of this transit signal is related to the ratio of sky-projected planet-to-star surface areas ($\delta = (R_p/R_\star)^2$). If we know the radius of the host star, either from the Gaia mission (Gaia Collaboration et al., 2016) or ground-based follow-up, then these transit detections can be converted to measurements of the planetary radii.

For an isolated planet, these transits occur at regular intervals governed by the orbital period. However, changes to the planet's orbit can result in shifts in the timing of these transit events. These changes in expected transit time relative to a static orbit are referred to as transit timing variations (TTVs). When a star hosts multiple transiting planets on compact orbits, gravitational interactions between planets can produce transit timing variations. These variations are strongest in systems that have orbital period ratios close to mean-motion resonances (MMR; e.g. period ratios close to 2:1, 3:2, 5:3, etc., Lithwick et al., 2012). These MMRs are observed to occur in our own solar system, most notably among the Galilean moons of Jupiter Ganymede, Europa, and Io, which have orbital periods in the 1:2:4 ratio. TTVs occur in exoplanet systems where the planets reside within a stable MMR; these systems are characterized by a critical resonance angle that depends on the mean longitudes of the planets and the longitude of periastron and librates around a fixed value (e.g., Goldberg et al., 2022). TTVs can also occur in systems where the planets are simply near but not in a resonance (e.g., Deck et al., 2016). Observationally, most planetary systems that exhibit TTVs are not actually in an orbital resonance (e.g., Fabrycky et al., 2014). The amplitude and frequency of these TTVs depends sensitively on the proximity of the planets to resonance, as well as the planetary masses and eccentricities (Lithwick et al., 2012).

Observations of TTVs can be combined with dynamical modeling of the planetary orbits to constrain the masses and orbital properties in near-resonant exoplanet systems. By testing various combinations of planetary masses and orbital properties for a given star and calculating the corresponding equations of motion, we can predict when transits should occur and compare these predicted TTVs to an observed set of TTVs to determine which planetary masses and eccentricities are consistent with the data. Several public software tools exist to do this n-body TTV model fitting (**ttvfast**), and these techniques have been extensively used to characterize near-resonant small planets (e.g., Holczer et al., 2016; Jontof-Hutter et al., 2016; Jontof-Hutter et al., 2021).

For small planets orbiting M dwarfs, measuring planetary masses and eccentricities with TTVs has some distinct advantages. The other commonly used method to measure planetary masses is the radial velocity (RV) technique (e.g., Latham et al., 1989). This method uses observations of the stellar spectral lines at various points during the planetary orbit. Any given star and planet orbit their mutual center of gravity (also known as barycenter) between the two objects, and stars therefore move back and forth slightly over the duration of a planetary orbital period. Due to the Doppler effect, the star's light is redshifted when moving away from Earth and blueshifted when moving towards the Earth. By observing the amplitude of the Doppler shift in the star's spectral lines and correcting for Earth's motion, we can measure the mass of transiting planets. But this technique performs best for massive and close-in planets around bright stars, where the stellar wobbles around the barycenter are larger and the spectral lines can be measured at high signal to noise.

For small planets orbiting faint M dwarfs, the amplitude of stellar Doppler shift is often smaller than 1 m/s, a challenging measurement for the most advanced current RV instruments. The activity of M dwarfs also poses a challenge to the RV technique, since stellar rotation and flares can make it difficult to precisely measure the center wavelength of spectral lines, which decreases the precision of RV mass measurements, and makes it difficult to measure masses for planets whose orbital periods are close to the stellar rotation period. For rocky planets around M dwarfs, TTVs are often a preferable method to determine planetary masses, and for the smallest planets sometimes the only feasible way to measure a mass. Of the 67 currently known small ($< 3R_\oplus$) planets around M dwarfs that have measured masses with a fractional mass uncertainty better han 33%, 24 are near-resonant and exhibit TTVs (NASA Exoplanet Archive, 2025).

TTVs are also generally more sensitive to planetary eccentricities than RVs. This is of critical importance for close-in eccentric rocky planets, which can be tidally heated due to internal distortion from gravitational forces on a non-circular orbits. The planetary eccentricity can be related to the tidal heating rate through a tidal dissipation efficiency factor (e.g. Equation 4, Jackson et al., 2008). This factor is related to the planetary composition and structure and is typically highly uncertain for exoplanets. Close-in compact orbits in multi-planet systems produce dynamically excited eccentricities, which then damp down to non-zero equilibria that can be stable long-term (e.g., Peterson et al., 2023). These damped-state forced eccentricities can be identified through long-term n-body integrations that account for tidal forces (e.g., Lu et al., 2023). Even eccentricities $\lesssim 0.01$ can produce enormous tidal heat fluxes for close-in M dwarf planets, sometimes comparable to the insolation flux of the planet even when accounting for the uncertain tidal efficiency parameters (e.g., Seligman et al., 2024). Understanding these forced eccentricities is therefore vital to understanding the total planetary energy budget. Comparing the observed

TTV-based eccentricities to the lower limit damped state eccentricities and system age can also constrain the tidal efficiency factor, which tells us about the planetary internal structure and temperature (e.g., Welbanks et al., 2024).

In cases where RV observations are possible, they can be combined with TTV observations to obtain improved constraints on the planet's mass and orbital properties. For a given near-resonant planet pair, TTVs are sensitive to the planetary masses and combined eccentricity of both planets (Lithwick et al., 2012), with a known degeneracy between planet mass and orbital eccentricity. Detections of second-order TTV oscillations can be used to break this degeneracy and obtain an independent measurement of planetary mass (Deck et al., 2015), but RV-based measurements provide a complementary constraint on both planetary mass and eccentricity. This means that TTV and RV data can be combined to significantly improve the precision on planetary radii, masses, and orbital properties, which enables insights into planetary composition and tidal heating (e.g., Chapter 2).

Prior to my thesis, relatively little work had been done to follow-up the many new near-resonant small planet systems orbiting M dwarfs detected by TESS. The precision of TTV-based mass estimates depends sensitively on the orbital architecture of the system, the sampling of the TTV curve, and on our ability to obtain precise transit midtimes. Because of this, planets that are observed at low SNR with TESS require further high SNR transit observations at epochs that are well-separated from the TESS photometry, and this is the case for the majority of M dwarf planets from the TESS sample (Ballard 2019).

To address this gap, I conducted an observational survey to characterize TTVs in small planet M dwarf systems, which forms the core of my thesis. At the beginning of the survey, there were only 22 small M dwarf planets with well-measured masses and radii. During the course of my thesis work, I have observed TTVs in 11 M dwarf systems that host 32 total small planets. Although most of my transit timing observations were collected using the 200-inch Hale telescope at Palomar Observatory, I have also incorporated complementary observations from approximately a dozen other ground-based observatories located around the world thanks to a network of international collaborators. With these ground-based transit observations, I regularly achieved transit timing precisions of $\sim$1 minute per transit, while typical TESS timing precisions were $>$ 10 minutes per transit for these systems. This improved measurement precision is critical for TTV studies, as the predicted TTV amplitudes in these systems range from a few minutes to a few tens of minutes.

At the same time that I was collecting these TTV observations, ongoing radial velocity surveys were also making significant progress in measuring additional planet masses for this population. Over the past 5 years, the number of small planets orbiting M dwarfs with well-measured masses and radii has more than tripled, standing at 68 as of May 2025 (NASA Exoplanet Archive, 2025). By expanding our knowledge of these small M dwarf planets, we can reveal the secrets of this mysterious population. With new and improved mass and radius measurements, we can better understand how common each sub-type of small planet is, and determine which processes are responsible for shaping the formation, evolution, and habitability of these rocky worlds. In Chapters 2-5, I present TTV observations and analyses that address these topics in four different planetary systems. In Chapter 6, I summarize these results in the context of the broader M dwarf planet population, identify remaining gaps in our knowledge of small planets that can be addressed with further TTV-based studies, and describe the broader landscape of TTV measurements from ongoing and upcoming space missions.

Chapter 2

CONSTRAINING THE DENSITIES OF THE THREE KEPLER-289 PLANETS WITH TRANSIT TIMING VARIATIONS

Greklek-McKeon, Michael et al. (Feb. 2023). “Constraining the Densities of the Three Kepler-289 Planets with Transit Timing Variations”. In: *AJ* 165.2, 48, p. 48. DOI: `10.3847/1538-3881/ac8553`. arXiv: `2208.00022 [astro-ph.EP]`.

2.1 Abstract

Kepler-289 is a three-planet system containing two sub-Neptunes and one cool giant planet orbiting a young, Sun-like star. All three planets exhibit transit timing variations (TTVs), with both adjacent planet pairs having orbital periods close to the 2:1 orbital resonance. We observe two transits of Kepler-289c with the Wide-field InfraRed Camera (WIRC) on the 200” Hale Telescope at Palomar Observatory, using diffuser-assisted photometry to achieve space-like photometric precision from the ground. These new transit observations extend the original four-year Kepler TTV baseline by an additional 7.5 years. We re-reduce the archival *Kepler* data with an improved stellar activity correction and carry out a joint fit with the Palomar data to constrain the transit shapes and derive updated transit times. We then model the TTVs to determine the masses of the three planets and constrain their densities and bulk compositions. Our new analysis improves on previous mass and density constraints by a factor of two or more for all three planets, with the innermost planet showing the largest improvement. Our updated atmospheric mass fractions for the inner two planets indicate that they likely have hydrogen-rich envelopes, consistent with their location on the upper side of the radius valley. We also constrain the heavy element composition of the outer saturn-mass planet, Kepler-289c, for the first time, finding that it contains 30.5 ± 6.9 $M_\oplus$ of metals. We use dust evolution models to show that Kepler-289c must have formed beyond 1 au, and likely beyond 3 au, and then migrated inward.

2.2 Introduction

The *Kepler* space telescope (Borucki et al., 2010) discovered thousands of new transiting exoplanet systems, including hundreds of multi-planet systems. *Kepler* was decommissioned in 2018, but the science value of the data it provided has yet to be exhausted. Part of this legacy science includes follow-up observations of the most interesting dynamically interacting multi-planet systems. *Kepler* transit photometry provides us with information about the planetary radius, orbital period, inclination, and semi-major axis of transiting planets. For the subset of dynamically interacting systems, observations of transit timing variations (TTVs; Agol et al., 2005; Holman et al., 2005) also provide complementary constraints on planetary masses, eccentricities, and bulk densities. We can use this information to characterize the bulk compositions and atmospheric mass fractions of these planets, as well as their dynamical architectures, which in turn provide key constraints on planet formation and evolution models.

For an isolated transiting planet on a stable circular orbit, transits occur at uniform intervals. In multi-planet systems, however, gravitational interactions between planets can cause the transit mid-times to deviate from a linear ephemeris by amounts ranging from minutes to hours. The amplitude of these TTVs depends on the masses of the planets and their orbital elements (Agol et al., 2018). Planets near first-order mean-motion resonances (MMRs) typically have the largest TTV amplitudes (e.g., Deck et al., 2016) and are therefore the most favorable for dynamical mass measurements.

Kepler discovered hundreds of multi-planet systems exhibiting detectable TTVs (Holczer et al., 2016; Hadden et al., 2017). For many of these systems, the data from the four-year *Kepler* prime mission was sufficient to obtain a large sample of transits for each planet spanning the TTV “super-period", the timescale on which the TTVs oscillate (Lithwick et al., 2012). However, the *Kepler* data are unable to provide strong constraints on the dynamical states of some planets with orbital periods longer than ~100 days, where relatively few transits were observed and/or the baseline is shorter than the predicted super-period. In cases where the *Kepler* baseline is longer than the TTV super-period and we can obtain good dynamical mass constraints, TTVs provide us with a unique opportunity to measure the bulk densities of long-period planets, without requiring an extensive multi-year radial velocity (RV) follow-up campaign (e.g. Chachan et al., 2022). There are currently only 18 transiting planets with a fractional mass uncertainty less than 1/3 (e.g., $> 3\sigma$ mass measurement) that have orbital periods greater than 100 days listed in the Exoplanet Archive (Akeson et al., 2013). Of these 18, 11 were characterized using TTVs.

In this study we focus on Kepler-289, a young (~1 Gyr) Sun-like ($T_{\rm eff}$ = 5990 ± 38

K) star that hosts three planets with orbital periods of 34.5, 66.1, and 125.9 days, corresponding to period ratios of 1.9:1 for each adjacent planet pair (Schmitt et al., 2014). These period ratios are reminiscent of those of the Galilean moons of Jupiter, which are in a Laplace resonance. We calculate a normalized distance to resonance Δ of 0.04 for both planet pairs (Lithwick et al., 2012), indicating that they are likely to exhibit TTVs. This is consistent with the population of near-resonant Kepler systems identified in previous studies, which typically have $\Delta < 0.05$ (Holczer et al., 2016; Jontof-Hutter et al., 2016; Jontof-Hutter et al., 2021). Unlike most of these sytems, the Kepler-289 planets have period ratios interior to resonance, rather than the more common exterior configuration (Fabrycky et al., 2014).

Although sub-Neptune planets frequently have outer Jovian companions (Bryan et al., 2019; Zhu et al., 2018), these companions are typically located at much larger orbital separations ($\gtrsim$ 1 au). The relatively close spacing between the outer gas giant and the inner sub-Neptunes in the Kepler-289 system, along with their near-resonant orbital configuration, suggests that this system may have started with a much wider orbital spacing before undergoing migration (Charalambous et al., 2022). The planets are not currently in resonance, however, and by obtaining improved mass measurements and bulk composition constraints for all three planets we can further examine the unique history of this unusual system.

All three planets in the Kepler-289 system exhibit detectable TTVs in the *Kepler* data, with amplitudes ranging from ~ 0.5 – 5 hours (Schmitt et al., 2014). Previous TTV studies of this system were complicated by the fact that the light curve of Kepler-289 is significantly variable (~3% amplitude in the *Kepler* bandpass) due to rotational modulation from starspots. This makes it difficult to obtain reliable transit mid-time measurements for the inner and middle planets, which both have relatively shallow transit depths of ~400 ppm (Schmitt et al., 2014). In addition, the outermost planet, Kepler-289c, only transited ten times during the *Kepler* observations, which cover only slightly more than one full TTV super-period (Jontof-Hutter et al., 2021). This makes this planet an ideal target for ground-based follow-up observations, which allow us to extend the TTV baseline by many years and to obtain improved dynamical mass constraints for all three planets.

In this study we re-analyze existing *Kepler* photometry of this system and combine it with two new observations of Kepler-289c obtained using the Wide Field InfraRed Camera (WIRC) on the 200" Hale Telescope at Palomar Observatory. We achieve space-quality infrared photometry of this system by using a beam-shaping diffuser

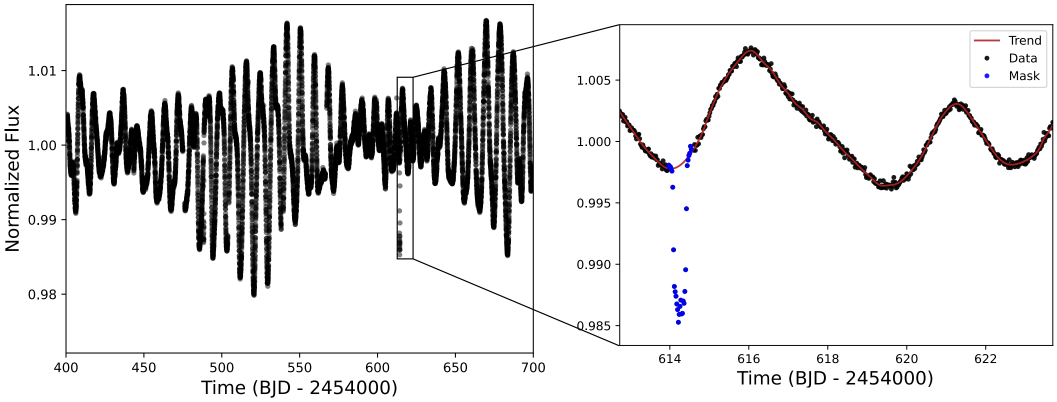

Figure 2.1 Representative photometry of Kepler-289 from *Kepler* quarter 5, exhibiting significant rotational modulation. A deep transit of planet c, the outermost planet, is easily visible around 614 (BJD-2454000). The right panel shows a zoomed-in view of this transit with the masked region around the transit indicated in blue and the baseline trend we use to remove the stellar variability overplotted in red.

whose properties are described in more detail in Stefansson et al., 2017 and Vissapragada et al., 2020. By observing in the infrared, we mitigate the effects of stellar activity on the transit light curve. In Section 2.3, we describe each observational data set. In Section 2.4, we describe our stellar activity correction for the *Kepler* photometry, our reduction of the Palomar transit light curves, and the TTV analysis. In Section 2.5 we discuss the results of our analysis, and in Section 2.6 we conclude and discuss the implications for these new set of constraints on the Kepler-289 system.

2.3 Observations

Space-Based Photometry

The Kepler-289 system was observed continuously during *Kepler* Quarters 1–16, with only long-cadence (30 minute integrations) data available for the first eleven quarters, and short-cadence (1 minute integrations) data in the remaining five. We obtained the Pre-search Data Conditioning Simple Aperture Photometry (PDCSAP) flux from the Kepler-289 postage stamp in Quarters 1–16 from the Mikulski Archive for Space Telescopes (MAST), and we perform our own reduction of the Kepler photometry, described further in the following section. The PDCSAP photometry already has long-term instrumental trends removed from the data using co-trending basis vectors.

There are also *TESS* (Ricker et al., 2014) data available in sectors 14, 15, and 41 for Kepler-289, which we downloaded using the lightkurve package (Lightkurve Collaboration et al., 2018) and checked for transits of the outer planet, Kepler-289c. We find that *TESS* observed the same two transits that we observed with WIRC, but the *TESS* photometric precision is significantly worse. We therefore exclude the *TESS* data from our subsequent analysis.

Ground-based WIRC Photometry

Kepler-289c's 126-day orbital period makes it a challenging target to observe from the ground, as the transit has a total duration of ~8 hours and there are typically no opportunities to observe full transits of this planet at Palomar. We obtained two partial transits of Kepler-289c in J band using the Wide-field InfraRed Camera (WIRC) instrument at the prime focus of the 200" Hale Telescope at Palomar Observatory. Our first observation was taken on on UT 24 August 2019 with a baseline spanning slightly more than half of the total transit duration, beginning approximately an hour before the transit center and ending approximately an hour after the end of egress. We observed a second partial transit on UT 17 September 2021, beginning ~2.5 hours pre-ingress and observing until just past the mid-transit time.

WIRC has an 8.7×8.7 field of view, ensuring that there are at least 10 comparison stars with magnitudes comparable to that of Kepler-289 visible in the same field. We utilized a custom near-infrared beam-shaping diffuser for these observations, which creates a top-hat PSF with a full width at half maximum of 3. This diffuser improved our observing efficiency and mitigated time-correlated noise from PSF variations, increasing our observing precision to levels comparable with space-based infrared photometry for a star of this magnitude (J = 12.9; Stefansson et al., 2017; Vissapragada et al., 2020). We minimized the time-correlated noise contribution from flat-fielding errors by utilizing custom guiding software, which limits the pointing drift over the night to a few pixels (Zhao et al., 2014). This software guides on science images by fitting 2D Gaussian profiles to comparison stars and determining guiding offsets on each image. We observed on both nights with an exposure time of 25 seconds, which we co-added to a total exposure time of 50 seconds. On both nights we achieved a guiding stability of less than two pixels ($0\farcs5$) throughout the night. On the first night, our observations began at airmass 2.5, reached a minimum airmass of 1.02, and continued until airmass 2.5. On the second night, our observations began near airmass 1.0 and continued until airmass 2.5 when the target set.

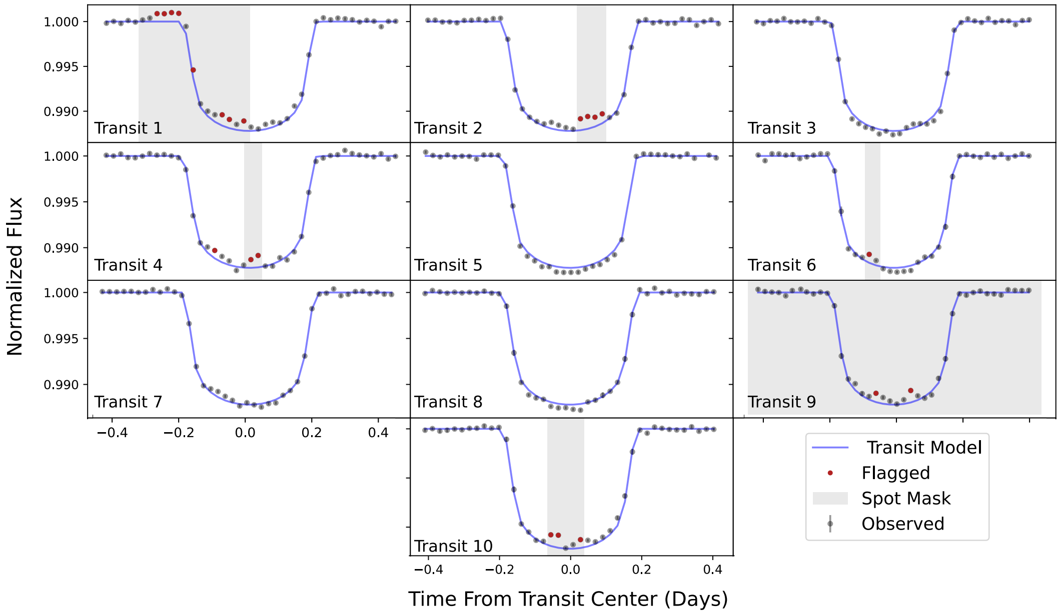

Figure 2.2 *Kepler* transit photometry of Kepler-289c. Our initial masks from visual inspection of the transits are shown as grey shading, the final best-fit transit model from the stacked transit profile is overplotted as a blue curve, and our final 3σ outlier masks are shown as red points. We binned the short-cadence data to match the long cadence data (30 minute bins) for this figure.

2.4 Data Analysis

Kepler Transit Fits and Stellar Activity Correction

The Kepler simple aperture photometry already has instrumental variations removed, but there is significant astrophysical variability in the light curve of Kepler-289 due to rotational modulation from starspots. This variability is on the scale of ∼3%, while the transits of the inner two planets have depths of approximately 0.4%, and the outer planet ∼1%. To obtain the highest possible precision on the individual *Kepler* transit times, we first need to remove the astrophysical variability.

We began by using the transit mid-times reported in Holczer et al., 2016, or Rowe et al., 2014 where mid-times are not available in Holczer et al., 2016, to mask all of the data within ±1.5 transit durations (for the relevant planet) of each transit mid-time. We then broke up the light curve into segments, using any gap in the data longer than a day as a break point. For each segment, we fit the long-term trends in flux using a cubic B-spline with knots defined by a smoothing factor of $m + \sqrt{2m}$, with m being the total number of data points (Dierckx, 1993), and interpolated the trend over the masked transit points. We then divided out this trend to flatten the light curve. We show a representative section of the original *Kepler* light curve from quarter 5, displaying significant astrophysical variability, along with a close-up of the trend and mask we used, in 2.1.

After removing the stellar variability, our next step was to fit the phased transit profiles for each planet. We used the transit mid-times from Schmitt et al., 2014 to phase up the individual transits for each planet. For the inner and middle planets, which have more shallow transits, no additional steps were required to correct for stellar activity in the light curve for fitting. For the outer planet, which has a relatively deep transit, we noted that there appear to be “bump"-like features consistent with starspot crossings (e.g., Wolter et al., 2009; Davenport et al., 2014) in many of the individual transit light curves. These features were most readily evident in the second, fourth, sixth, and tenth *Kepler* transits, and we masked them in our initial transit fits. The ninth transit was of generally poor quality due to instrumental effects present in the *Kepler* photometry and did not have a well-constrained transit mid-time in the Holczer catalog, so we excluded it from the stacked transit profile. The first half of the first transit also appeared to be affected by uncorrected instrumental effects, so we masked it as well. After defining this initial set of masks, we fit the phased transit profile. We then removed our initial masks for the likely spot crossings and instead flagged all points that were more than 3σ away from the best-fit stacked transit model. We found that the majority of the outliers flagged were indeed in the same regions of the light curves as our original spot masks. We use this updated 3σ outlier mask in the final joint-fit between the phased *Kepler* data and Palomar data. Masking these spot crossings and instrumental outliers allowed us to obtain an improved constraint on the transit depth and ensured that the transit mid-time measurements were not biased. In 2.2 we plot all of the individual *Kepler* transit observations of Kepler-289c, with our initial and final spot masks over-plotted for reference.

We modeled the transit light curves for the inner two planets using the exoplanet light curve modeling package `BATMAN` (Kreidberg, 2015). We fit for the planet to star radius ratio, orbital inclination, semi-major axis to stellar radius ratio, and quadratic stellar limb-darkening parameters. We used the results reported in Schmitt et al., 2014 as initial guesses for the planet parameters, and sampled their posterior distributions using the affine-invariant ensemble Markov chain Monte Carlo fitting package `emcee` (Foreman-Mackey et al., 2013). We run the sampler with 50 walkers for 5.5×10^5 iterations and discard the initial 5×10^4 steps as burn-in. We checked for convergence by verifying that the number of iterations for each parameter in our

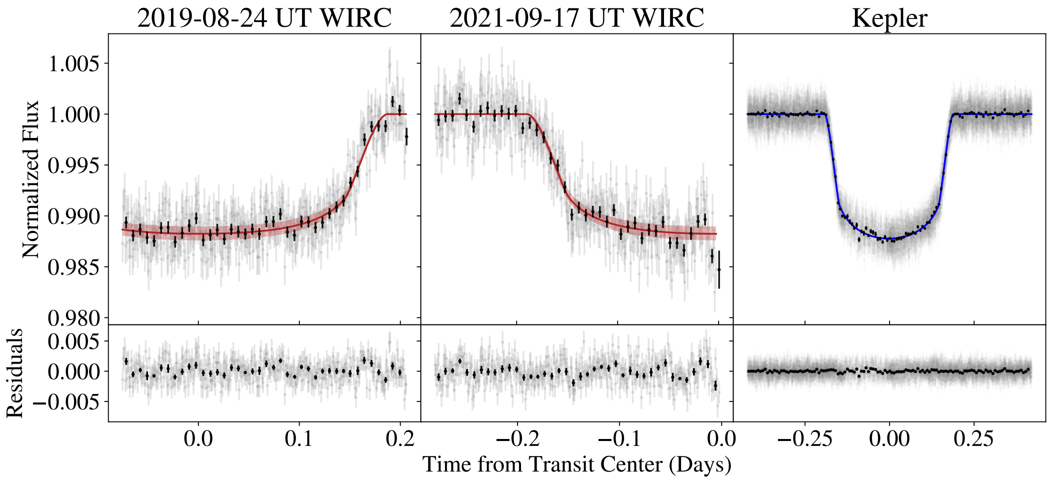

Figure 2.3 The left panel shows the first partial transit observation in J band from Palomar/WIRC in 2019, middle panel shows the second partial transit observation from WIRC in 2021, and right panel shows the phased *Kepler* transit. The red lines in the left and center panels are the best-fit transit models for the WIRC light curves, and the red shaded region is the 1σ confidence interval on that model. The blue line in the right panel shows the best-fit transit model for the *Kepler* data, along with blue shading for the 1σ confidence interval. All three of these transit data sets are fit jointly with `exoplanet`, where the *Kepler* transit profile has separate depth and limb-darkening parameters, and all other parameters are shared aside from transit mid-times.

MCMC chain exceeded 50 autocorrelation lengths as calculated by `emcee`. After fitting the transit shape parameters, we retrieved the “best-fit" values from a χ^2 minimization on the 50^{th} percentile parameter set in our posterior chain, and then used the 16^{th} and 84^{th} percentile parameter values from the posterior distribution as our 68% $\pm1\sigma$ confidence interval. We then fit each transit of the inner and middle planets in the *Kepler* photometry with each parameter from the best-fit transit profile fixed except for the transit time, to re-derive transit times for both planets. These times are listed in 2.1, and the stacked transit profiles for Kepler-289b and d are shown in 2.8. The radii we retrieve for Kepler-289b and Kepler-289d are slightly different than the radii reported in Schmitt et al., 2014 (within 2σ for the inner planet, and 1σ for the middle planet), which we attribute to our different stellar activity removal process.

Palomar Photometry and Transit Fits for Kepler-289c

We dark-subtracted, flat-fielded, and corrected our WIRC images for bad pixels and hot pixels using the methods described in Vissapragada et al., 2020. We then

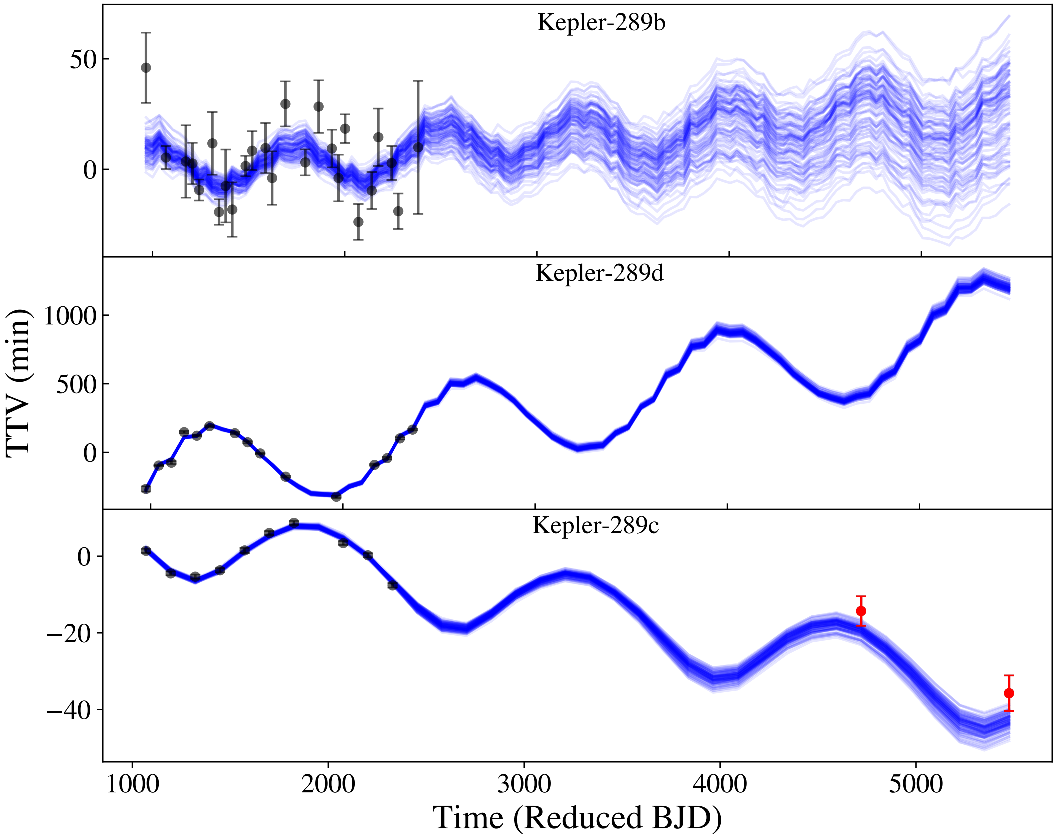

Figure 2.4 Observed TTVs from *Kepler* (black points) and Palomar/WIRC (red points) for each of the Kepler-289 planets, along with 100 random posterior draws from our TTV model (blue curves). The inner, middle, and outer planets of Kepler-289b, Kepler-289d, and Kepler-289c, respectively, have mean orbital periods of 34.55, 66.06, and 125.85 days. The planets are labeled in alphabetical order of their discovery in the *Kepler* data. The Palomar transit observations extend the *Kepler* TTV baseline by more than 7.5 years and help refine the TTV super-period originally inferred from the *Kepler* data to ~1344 days. The reduced BJD time is BJD-2454000.

used aperture photometry with the `photutils` package (Bradley et al., 2020) to determine the relative fluxes of Kepler-289 and a set of comparison stars in each image. We tested every aperture size from 5-25 pixels and compared the root-mean-square deviation of the final light curves for each aperture radius. We found that the optimal aperture radius was 9 pixels ($2\overset{\prime\prime}{.}25$) for the first night, and 11 pixels ($2\overset{\prime\prime}{.}75$) for the second night. We calculated light curves for every star in the image whose cumulative PSF had a signal-to-noise ratio of 100 or more relative to the sky background, and selected the ten stars with the lowest median absolute deviation relative to Kepler-289's flux as our final set of comparison stars. The full set of comparison stars are not identical across our two WIRC observation nights, due to slightly different detector positioning on the sky. We estimated and subtracted the sky background from each star using an uncontaminated sky annulus with inner and outer radii of 25 and 50 pixels, respectively.

We then constructed a systematic noise model that accounts for changes in Kepler-289's flux due to changing airmass, atmospheric seeing, telescope pointing, and other instrumental effects. This systematics model is a linear function of the ten comparison star light curves, the airmass, the PSF width, the distance moved on the detector relative to the initial centroid position, the local sky background, and the mean-subtracted times. For more details on the WIRC data reduction pipeline and instrumental noise model, see Vissapragada et al., 2020. The WIRC data reduction and light curve modeling software are publicly available online at https://exowirc.readthedocs.io/en/latest/?readthedocs.

We jointly fit the *Kepler* and Palomar transit light curves using `exoplanet`. The `exoplanet` package (Foreman-Mackey et al., 2021) uses `starry` (Luger et al., 2019) to quickly calculate accurate limb-darkened light curves and `PyMC3` (Salvatier et al., 2016) to explore the posterior distribution of modeled parameters with No-U-Turn Sampling (Hoffman et al., 2011), an extension of the Hamiltonian Monte Carlo algorithm that utilizes first order gradient information to step through posterior distributions quickly and efficiently. We allowed the mid-time of each transit to vary individually in this fit using the `TTVOrbit` model, with the stacked *Kepler* transit profile shifted to a reference time one orbital period before the first WIRC transit observation. In our joint *Kepler*/WIRC transit fit, we use global parameters for the planetary orbital period, impact parameter, and semi-major axis to stellar radius ratio. We fit for separate planet to star radius ratios and quadratic limb darkening parameters in each bandpass. We also fit for a jitter parameter describing the excess

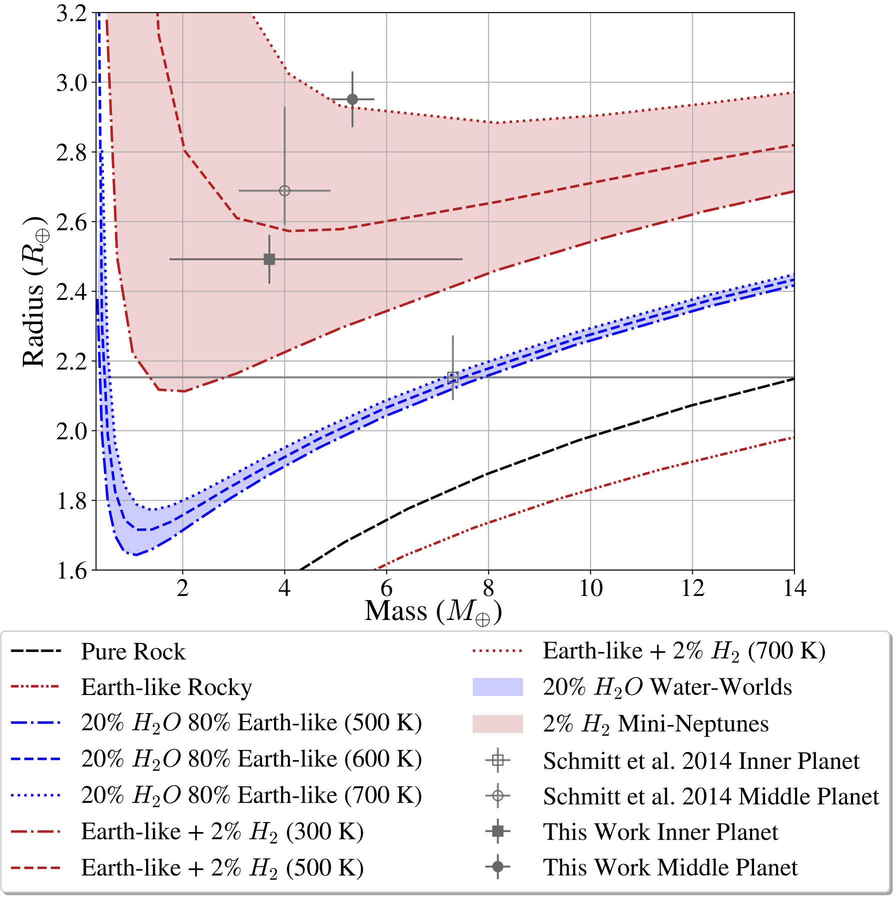

Figure 2.5 Updated mass and radius measurements for the two inner sub-Neptunes (Kepler-289b and d) compared to the original values from Schmitt et al., 2014. We overplot constant composition curves for 100% iron, an earth-like rock-iron mix, irradiated hydrogen-rich atmospheres on top of an Earth-like rocky core, and irradiated water worlds from Zeng et al., 2016.

noise added in quadrature to the photon noise in each bandpass. In the left and middle panels of 2.3, we show the final WIRC transit light curves and their residuals. In the right panel, we show the stacked *Kepler* light curve. Our WIRC light curves result in a transit mid-time precision of ~4 minutes, compared to a median mid-time precision of 0.55 minutes from the space-based *Kepler* photometry. This is because the long duration of the transit limits us to partial transit baselines when observing with WIRC, which also has a slightly lower photometric precision than *Kepler*. In 2.9, we plot the posterior probability distributions for the physically meaningful transit shape parameters from the joint fit (all parameters are global other than $\frac{R_p}{R_*}$ in the *Kepler* and WIRC bandpasses, and the t_0 parameter on each WIRC night).

TTV Analysis

We fit our updated set of transit mid-time measurements using the `TTVfast` package (**ttvfast**). `TTVfast` is a computationally efficient n-body code that computes transit times as a function of the planetary masses and orbital elements at a reference epoch, which we chose to be $T_0 = 2455865$ (BJD). We fixed the orbital inclinations to 90° and the longitudes of the ascending nodes to 0° because our transit profile fits indicate that the inclination dispersion is small, and the TTV solution is second order in mutual inclination (Nesvorný et al., 2014; Hadden et al., 2016). We used `emcee` to map the posterior probability distributions for the masses and orbital elements for this three-planet system. We ran the sampler with 50 walkers for 3.5×10^6 iterations and discard the initial 5×10^5 steps as burn-in. We checked for convergence by verifying that the number of iterations for each parameter in our MCMC chain exceeded 50 autocorrelation lengths as calculated by `emcee`. Our observed TTVs, as well as 100 random draws of the TTV posterior distribution from our TTVfast fit, are shown in 2.4, while the corner plot showing the posterior probability distributions for the planet masses and eccentricity vectors is shown in 2.10. We use our improved dynamical solution to predict the transit mid-times for all three planets until 2032, which are listed along with our observed transit times in 2.1.

Table 2.1 All observed transit epochs, mid-times, and uncertainties for the three Kepler-289 planets, as well as the predicted mid-times and associated 1σ uncertainties from our best-fit TTV model, extending until January 1^{st}, 2032. The table is abbreviated here, but available in full in the arXiv source documents.

Planet	**Transit Number**	**Observed Mid-time (JD-2454000)**	**Error (days)**	**Predicted Mid-time (JD-2454000)**	**Error (days)**
Kepler-289b	0	965.7135	0.0110	965.6898	0.0031
Kepler-289b	1	-	-	1000.2328	0.0036
Kepler-289b	2	-	-	1034.7792	0.0041
Kepler-289b	3	1069.3174	0.0036	1069.3195	0.0054
Kepler-289b	4	-	-	1103.8616	0.0056

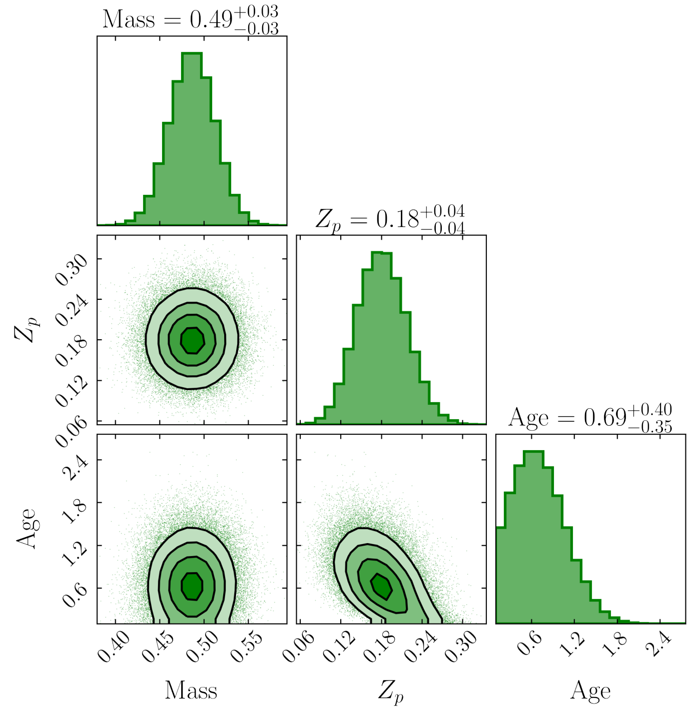

Figure 2.6 Posterior probability distributions for the bulk metallicity, planetary mass, and age of the outermost planet (Kepler-289c). We use a planetary evolution model as described in D. P. Thorngren et al., 2016 to compute the planet's bulk metal content as a function of its observed radius, mass, and age, which are taken from published values in the literature.

2.5 Results

Our new analysis decreases the mass uncertainties for all three planets by more than a factor of 2, with the innermost planet seeing the greatest improvement relative to the original constraints found in Schmitt et al., 2014. We summarize the final planetary masses, radii, densities, and orbital properties from our photometric and TTV analyses in 2.2. In this section, we use these values to constrain the bulk densities and possible compositions of the three planets.

We find that Kepler-289b is a 4.1 $M_{\oplus}$ low-density sub-Neptune, as illustrated in 2.5. Both the inner and middle planets are significantly larger than a pure-water planet of the same mass. This implies that both planets likely possess a primordial hydrogen- and helium-rich atmosphere, which increases their apparent radii. We use the models in Lopez et al., 2014 to calculate the core-to-atmosphere mass fraction for a scenario in which we assume that the planets consist of Earth-like rocky cores surrounded by a solar metallicity gas envelope. We find that the measured densities of the inner and middle planets can be matched by hydrogen-rich envelopes that constitute 3% and 0.9% of their total planet masses, respectively. Both of these values are consistent with the estimated atmospheric mass fractions of the broader sub-Neptune population (e.g., Owen et al., 2013; Lopez et al., 2014; Lee, 2019a).

Table 2.2 Orbital and planetary parameters for Kepler-289b, d, and c. Each of these parameters is retrieved from our transit and TTV fits, other than the derived parameters of M_p, R_p, and ρ, which incorporate errors on the stellar mass and radius of $M_\star = 1.08 \pm 0.02\ M_\odot$ and $R_\star = 1.00 \pm 0.02\ R_\odot$ from Schmitt et al., 2014.

Kepler-289b

	Schmitt et al. 2014	Kepler Reanalysis	Kepler Reanalysis + Palomar
P (days)	34.5450 ± 0.0005	$34.5383^{+0.0006}_{-0.0006}$	$34.5383^{+0.0006}_{-0.0006}$
T_0 (JD-2454000)	965.6404 ± 0.0040	$965.6880^{+0.0030}_{-0.0032}$	$965.6879^{+0.0006}_{-0.0006}$
M_p ($M_\oplus$)	7.3 ± 6.8	$4.39^{+4.32}_{-2.30}$	$3.70^{+3.79}_{-1.96}$
R_p ($R_\oplus$)	2.15 ± 0.10	2.49 ± 0.07	2.49 ± 0.07
ρ (g cm^{-3})	4.1 ± 3.9	$1.56^{+1.54}_{-0.82}$	$1.45^{+1.5}_{-0.77}$
R_p/R_*	$0.0197^{+0.0011}_{-0.0006}$	$0.0228^{+0.0004}_{-0.0004}$	$0.0228^{+0.0004}_{-0.0004}$
$M_p/M_*(\times10^{-5})$	2.0 ± 1.9	$1.22^{+1.2}_{-0.64}$	$1.13^{+1.17}_{-0.6}$
a/R_*	71.1^{+10}_{-20}	$46.38^{+2.1}_{-2.0}$	$46.38^{+2.1}_{-2.0}$
$i(^\circ)$	$89.59^{+0.30}_{-0.48}$	$88.98^{+0.06}_{-0.07}$	$88.98^{+0.06}_{-0.07}$
$e\cos(\omega)$	-0.0215±0.0255	-	-
$e\sin(\omega)$	-0.0113±0.0239	-	-
$\sqrt{e}\cos(\omega)$	-	$-0.0364^{+0.0802}_{-0.0756}$	$-0.0333^{+0.0757}_{-0.0873}$
$\sqrt{e}\sin(\omega)$	-	$-0.1776^{+0.0816}_{-0.0564}$	$-0.1858^{+0.0820}_{-0.0564}$

Kepler-289d

	Schmitt et al. 2014	Kepler Reanalysis	Kepler Reanalysis + Palomar
P (days)	66.0634 ± 0.0114	$66.0281^{+0.0048}_{-0.0042}$	$66.0282^{+0.0044}_{-0.0039}$
T_0 (JD-2454000)	975.6436 ± 0.0068	$975.6436^{+0.0053}_{-0.0053}$	$975.6240^{+0.0051}_{-0.0052}$
M_p ($M_\oplus$)	4.00 ± 0.90	$5.97^{+0.50}_{-0.50}$	$5.33^{+0.43}_{-0.42}$
R_p ($R_\oplus$)	2.68 ± 0.17	3.03 ± 0.08	3.03 ± 0.08
ρ (g cm^{-3})	1.2 ± 0.3	$1.18^{+0.1}_{-0.1}$	$1.14^{+0.09}_{-0.09}$
$R_p/R_\star$	$0.0246^{+0.0022}_{-0.0009}$	$0.0270^{+0.0005}_{-0.0005}$	$0.0270^{+0.0005}_{-0.0005}$
$M_p/M_\star(\times10^{-5})$	1.1 ± 0.2	$1.66^{+0.14}_{-0.14}$	$1.6^{+0.13}_{-0.13}$
$a/R_\star$	117.8^{+21}_{-42}	$70.52^{+2.95}_{-2.85}$	$70.52^{+2.95}_{-2.85}$
$i(^\circ)$	$89.73^{+0.20}_{-0.38}$	$89.31^{+0.04}_{-0.04}$	$89.31^{+0.04}_{-0.04}$
$e\cos(\omega)$	-0.0035±0.0022	-	-
$e\sin(\omega)$	-0.0108±0.0122	-	-
$\sqrt{e}\cos(\omega)$	-	$0.0340^{+0.0164}_{-0.0208}$	$0.0293^{+0.0174}_{-0.0225}$
$\sqrt{e}\sin(\omega)$	-	$-0.0164^{+0.0537}_{-0.0498}$	$-0.0096^{+0.0501}_{-0.0500}$

Kepler-289c

	Schmitt et al. 2014	Kepler Reanalysis	Kepler Reanalysis + Palomar
P (days)	125.8518 ± 0.0076	$125.8727^{+0.0036}_{-0.0022}$	$125.8723^{+0.0035}_{-0.0021}$
T_0 (JD-2454000)	1069.6528 ± 0.0077	$1069.6744^{+0.0035}_{-0.0023}$	$1069.6734^{+0.0035}_{-0.0021}$
$M_p(M_\oplus)$	132 ± 17	$170.35^{+7.95}_{-8.67}$	$157.18^{+7.041}_{-7.31}$
$R_p(R_\oplus)$	11.59 ± 0.19	11.31 ± 0.23	11.23 ± 0.21
ρ (g cm^{-3})	0.47 ± 0.06	$0.65^{+0.03}_{-0.03}$	$0.66^{+0.03}_{-0.03}$
$R_p/R_\star$	$0.10620^{+0.00049}_{-0.00050}$	$0.10373^{+0.00040}_{-0.00038}$	$0.10297^{+0.00027}_{-0.00026}$
$M_p/M_\star(\times10^{-5})$	36.43 ± 4.66	$47.36^{+2.21}_{-2.41}$	$47.19^{+2.11}_{-2.23}$
$a/R_\star$	109.5 ± 1.2	$104.7^{+5.9}_{-5.1}$	$108.95^{+0.75}_{-0.75}$
i ($^\circ$)	$89.794^{+0.017}_{-0.016}$	$89.74^{+0.07}_{-0.05}$	$89.78^{+0.04}_{-0.04}$
$e\cos(\omega)$	0.0032±0.0066	-	-
$e\sin(\omega)$	0.0033±0.0086	-	-
$\sqrt{e}\cos(\omega)$	-	$0.1160^{+0.0152}_{-0.0187}$	$0.1114^{+0.0164}_{-0.0194}$
$\sqrt{e}\sin(\omega)$	-	$0.0277^{+0.0386}_{-0.0382}$	$0.0399^{+0.0278}_{-0.0350}$

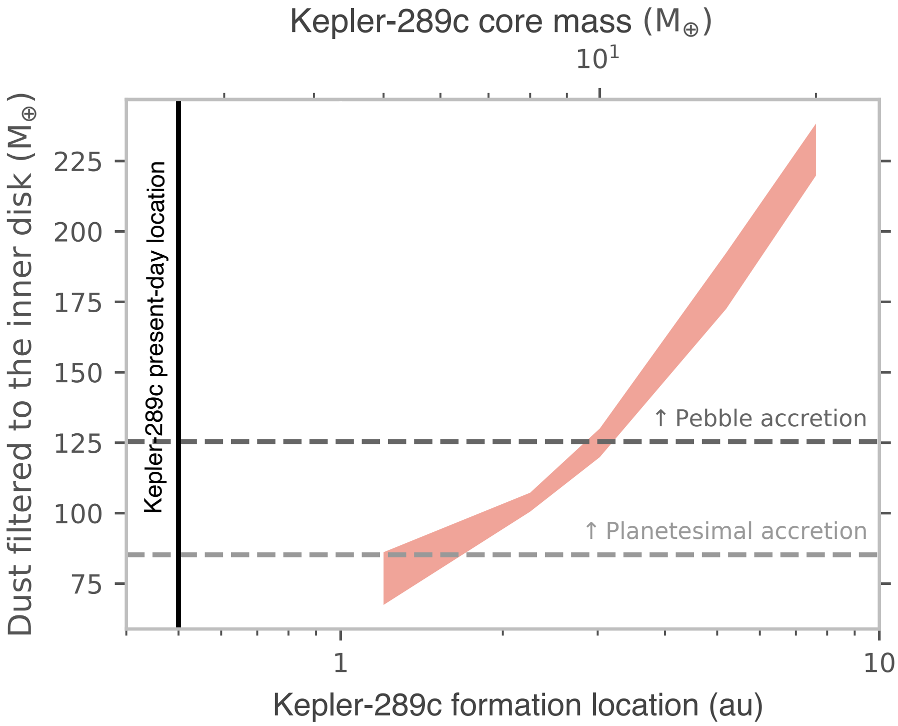

Figure 2.7 Total dust mass that reaches the inner disk as a function of the assumed giant planet pebble isolation (core) mass (top x axis), and its corresponding formation location (bottom x axis, this is set by the assumed isolation mass). The dust mass is calculated using the disk models from Chachan et al., 2022, where the red shading denotes the spread in predictions caused by varying the assumed disk radii, masses, and dust-to-gas ratios. The minimum estimated dust masses required to form the two inner planets in the planetesimal (grey dashed line) and pebble accretion (black dashed line) are overplotted. Kepler-289c's current orbital semi-major axis is shown as a solid black line.

For the outermost planet, Kepler-289c, we find an updated mass of 0.49 ±0.02 M_{Jup}. We use a giant planet interior structure and evolution model (D. P. Thorngren et al., 2016; D. Thorngren et al., 2019) to calculate the corresponding bulk metallicity as a function of the planet's mass, age, and radius. We allow these three parameters to vary freely in the fit with priors based on their measured values from this study and Schmitt et al., 2014, and show the resulting posterior probability distributions in 2.6. For more details on the giant planet structure model, see D. Thorngren et al., 2019. We find that this planet has a bulk metallicity of 0.18 ± 0.04, significantly higher than its approximately solar metallicity host star. This corresponds to a bulk metal content of 30.5 ± 6.9 $M_{\oplus}$. We compare Kepler-289c to the broader population of giant planets characterized in D. P. Thorngren et al., 2016 and find that its bulk metallicity is slightly lower than average based on the best-fit mass-metallicity trend model, but still consistent with the overall population distribution.

Core accretion models for gas giant formation indicate that it is relatively difficult to form planets like Kepler-289c in-situ on close-in orbits (Dawson et al., 2018; Poon et al., 2021). It is therefore possible that Kepler-289c formed farther out and then migrated inward. Observational studies suggest that the gas giant planet population peaks at separations between 1 – 10 au (Fulton et al., 2021), much farther out that Kepler-289c's present-day orbital separation of ~0.5 au. Although the sample of outer gas giants with inner super-Earths is much smaller, observational studies find that the gas giants in these systems are also typically located on relatively wide orbits (Zhu et al., 2018; Bryan et al., 2019). Kepler 289c's lower-than-average bulk metallicity also suggests a more distant formation location, as dust evolution models indicate that the dust opacity should be lower (and the corresponding gas accretion rates for a fixed core mass should be higher) beyond the ice line (Chachan et al., 2021).

The fact that both planet pairs in this system have a normalized distance to resonance $\Delta < 0.05$ is also consistent with the hypothesis that they might have migrated inward through the 2:1 resonance at some point in the past (e.g., Weiss et al., 2022), although the current observational constraints strongly disfavor a resonant configuration. Schmitt et al., 2014 calculated the 3-body Laplace resonance width for this system, and found that both pairs of planets are many tens of widths away from resonance. We empirically estimate the three-body Laplace resonance angle using the method from Mills et al., 2016 and find that it circulates from 0°–360° over the course of the *Kepler* observations, with no indication of libration. We therefore conclude that the Kepler-289 planets are not currently in an orbital resonance, in agreement with Schmitt et al., 2014. This might be explained by post-nebular dynamical instabilities, which can nudge resonant systems into configurations that are either interior to or exterior to the original resonance (Goldberg et al., 2022).

Constraining the formation location of Kepler-289c

We next explore whether or not we can place more quantitative constraints on the likely formation location of Kepler-289c using a pebble accretion model as described in Chachan et al., 2022. This model assumes that the material available in the inner disk alone is not sufficient to form a system of super-Earths, but must instead be enhanced by a flow of small solids migrating in from the outer disk. When the outer giant planet core reaches the pebble isolation mass, it cuts off this flow of solids.

Chachan et al., 2022 used disk evolution models to show that the integrated dust mass that reaches the inner disk in this scenario is primarily a function of the giant planet's formation location and corresponding isolation mass, with more distant formation locations (higher isolation masses) allowing more material to reach the inner disk.

As discussed in the previous section, the masses of the two inner planets in the Kepler-289 system are dominated by solids. This means that they must have accreted a combined total of approximately $\sim 10\ M_\oplus$ of solids. If we compare this to the solid mass budget for the inner disk, using the minimum mass extrasolar nebula (Chiang et al., 2013) to estimate the solid content within the orbit of Kepler-289c yields a total solid mass of $\sim 8\ M_\oplus$. Clearly, some material must have been transported to the inner disk to form Kepler-289b and d. If this material predominately came from beyond the ice line, approximately 50% of the original solid mass would have been lost to evaporation when the pebbles crossed the water ice line. The remaining solids must accrete into larger bodies to avoid migrating all the way onto the star. Drążkowska et al., 2016 combined dust evolution models with planet formation models to show that dust is converted into planetesimals with an efficiency of ~23% in the inner disk. This implies that 85 $M_\oplus$ of solids must have been delivered to the inner disk in order to form the two inner planets in the Kepler-289 system. If the inner super-Earths formed via pebble accretion, the efficiency with which solids are accreted is somewhat lower due to Kepler-289's large stellar mass (see discussion in § 5.3 and Appendix A of Chachan et al., 2022), resulting in a higher mass threshold of approximately 125 $M_\oplus$.

Since the total dust mass delivered to the inner disk is a function of the giant planet's formation location, we can use the corresponding pebble isolation mass for a given formation location to place a lower limit on the initial orbital distance of Kepler-289c. We run a new grid of disk models that account for Kepler-289's mass and its expected protostellar luminosity but is otherwise identical to models presented in Chachan et al., 2022. This grid spans a range of assumed disk radii, solid masses, and dust-to-gas ratios, and we only consider the subset of disks where the giant planet core reaches the isolation mass in less than 1 Myr. We show the resulting solid fluxes as a function of the giant planet's formation location and corresponding pebble isolation mass in 2.7. In these models, a giant planet core located just outside 1 au, which has a corresponding pebble isolation mass of $\sim 5\ M_\oplus$, allows $\sim 85\ M_\oplus$ to be delivered to the inner disk. This is enough material to form the inner super-Earths via planetesimal accretion, but such a small core is unlikely to accrete enough gas to become a gas giant (e.g., Rafikov, 2006; Lee, 2019b). A core located just outside 3 au would have an isolation mass of 10 $M_{\oplus}$, making it easier to accrete a massive gas envelope and also providing enough solids to the inner disk to exceed the higher pebble accretion threshold of 125 $M_{\oplus}$. A formation location beyond 3 au would also be consistent with the semi-major axis distribution of the broader population of giant planets measured in Fulton et al., 2021, which peaks at $3.6^{+2.0}_{-1.8}$ au.

Kepler-289c has a total metal content of $\sim$30 $M_{\oplus}$ from our bulk metallicity constraints, but if it has a structure similar to that of Jupiter and Saturn it is likely that a significant fraction of these solids are distributed throughout its interior (Wahl et al., 2017; Mankovich et al., 2021). Such a distribution might plausibly be attributed to the continued accretion of large solids (planetesimals) after the giant planet core reaches the isolation mass (see Helled et al., 2022, for a review), allowing for a core mass that is less than the planet's total estimated solid mass. If a larger fraction of Kepler-289c's solids originated from its core, it would imply a more distant formation location and a correspondingly larger flux of solids to the inner disk. We therefore conclude that 3 au is a reasonable lower limit for the likely formation location of Kepler-289c.

2.6 Conclusions

In this study, we used transit timing variations to obtain improved mass measurements for the three planets in the Kepler-289 system, which have orbital period ratios of 1.9:1 for each adjacent pair of planets. We re-analyzed the *Kepler* photometry for this system and observed two new transits of the outermost planet, Kepler-289c, with WIRC on the 200" Hale Telescope at Palomar Observatory. Our re-analysis of the *Kepler* photometry allowed us to better correct for the star's high photometric variability, resulting in modestly improved radius constraints and transit times. Our Palomar transit observations extended the original four-year *Kepler* TTV baseline by an additional 7.5 years, allowing for an improved dynamical solution. Our updated mass uncertainties for all three planets are more than a factor of two smaller than the original values reported by Schmitt et al., 2014.

We use our improved mass and radii constraints to establish that the sub-Neptune sized inner and middle planets, Kepler-289b and d, are both low-density (1.45 and 1.14 g cm^{-3}) planets. If we assume that these planets both have Earth-like cores with solar metallicity envelopes, we calculate that they should have atmospheric mass fractions of 3.0% and 0.9%, respectively. This is consistent with their location on the upper side of the radius valley. Since Kepler-289 is relatively young, it is possible that these two planets may host present-day atmospheric outflows. Although this system is too faint to measure helium outflow signatures with current ground-based telescopes, it might be accessible to upcoming thirty-meter class telescopes.

We calculate the three-body Laplace resonance angles for the system and find that Kepler-289 is not in the 1:2:4 Laplace orbital resonance, in agreement with Schmitt et al., 2014. We argue that this system might have migrated into a resonant chain, which was later disrupted by dynamical instabilities. This is consistent with both observations and models of giant planet formation, which suggest that planets like Kepler-289c (0.5 M_{Jup}, 0.5 au present-day location) form more readily outside 1 au. We combine our updated planet masses with disk evolution models to constrain the formation location of Kepler-289c, and conclude that it likely originated at or beyond 3 au.

Transiting, dynamically interacting multi-planet systems provide us with a wealth of information about planet formation and migration processes. Kepler-289's unique architecture makes it a particularly valuable test case for exploring the connections between close-in sup-Neptune planets and outer gas giant companions. Although its relative faintness also makes it a challenging target for the *James Webb Space Telescope*, atmospheric composition studies of Kepler-289c with next-generation space telescopes could provide additional constraints on its formation location (Madhusudhan, 2019).

2.7 Appendix

Transit and TTV Model Plots and Posterior Distributions

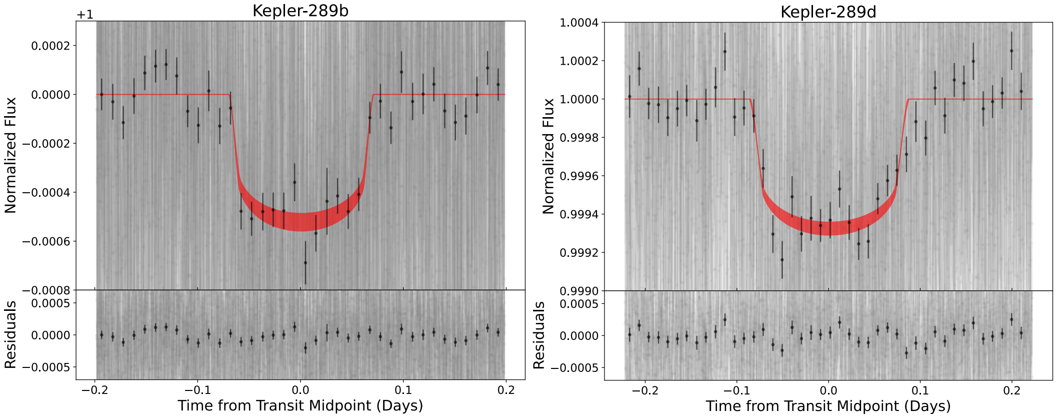

Figure 2.8 Gray points show the phased *Kepler* data. The left and right panels are the inner and middle planets, respectively. Black points are binned to 15 minutes. The red shading indicates the middle 68% range from our posterior distribution.

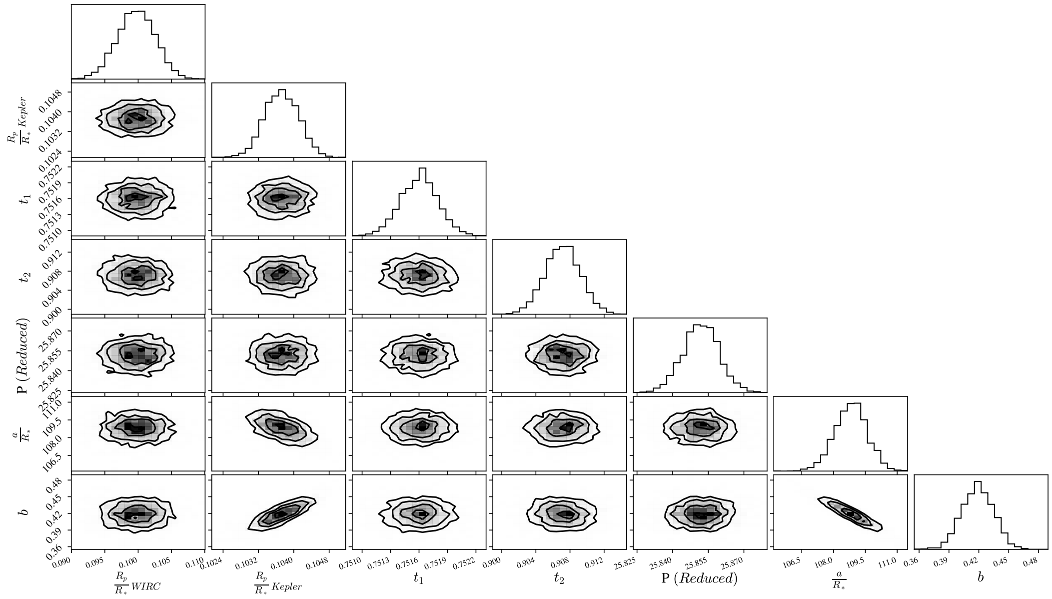

Figure 2.9 Posterior probability distributions for the transit shape parameters from the MCMC joint fit to the *Kepler* and WIRC data. For ease of viewing in the plot, we label the period minus 100 days as the reduced period. t_1 is the BJD transit center time of the first WIRC night — 2458719 days, and t_2 is the BJD transit center time of the second WIRC night - 2459474 days.

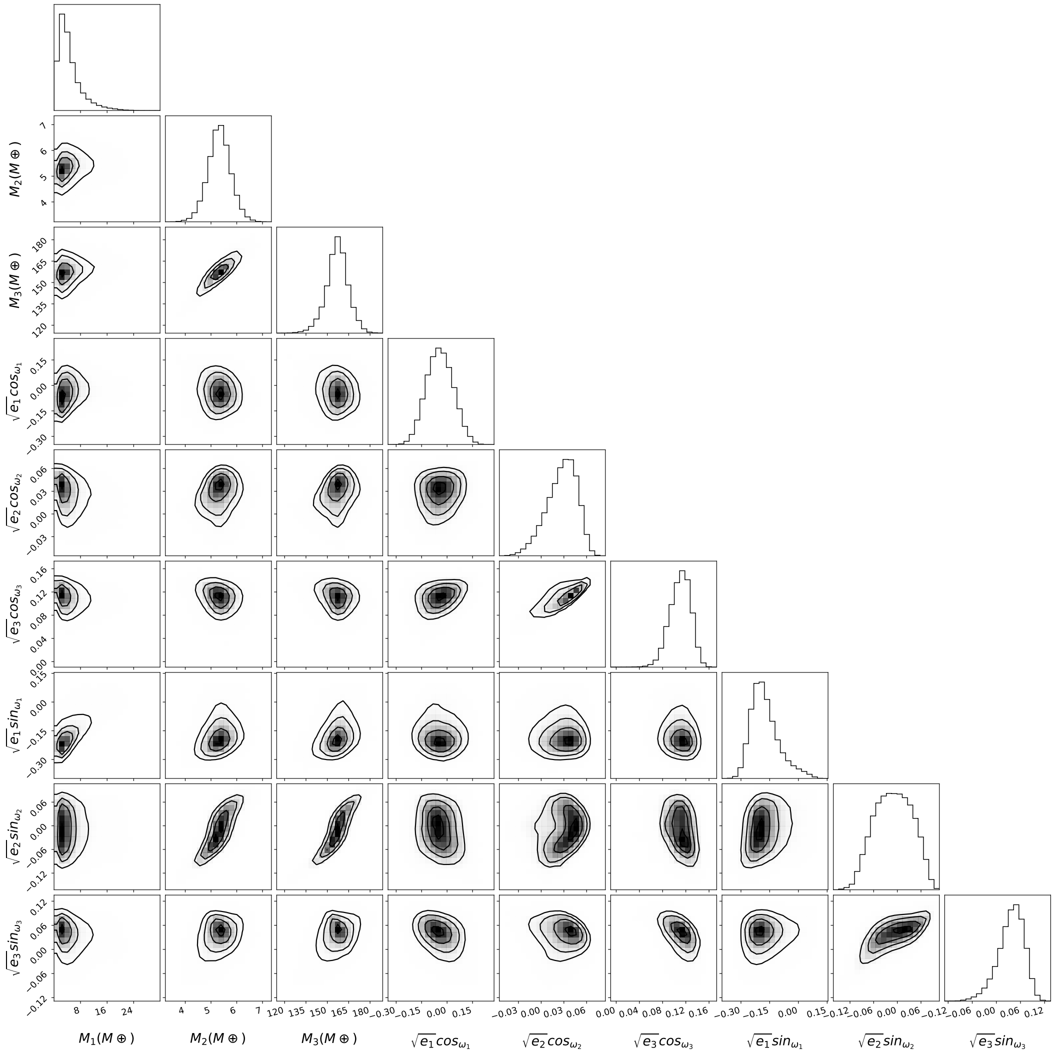

Figure 2.10 Posterior probability distributions for the planet masses and eccentricity vectors from the TTV fit. We also allowed the orbital periods and initial transit times for each planet to vary as free parameters in this fit, but we omit them from this plot for ease of viewing.

References

Agol, Eric et al. (May 2005). “On detecting terrestrial planets with timing of giant planet transits”. In: *MNRAS* 359.2, pp. 567–579. DOI: `10.1111/j.1365-2966.2005.08922.x`.

Agol, Eric et al. (2018). “Transit-Timing and Duration Variations for the Discovery and Characterization of Exoplanets”. In: *Handbook of Exoplanets*, pp. 797–816. DOI: `10.1007/978-3-319-55333-7_7`. URL: `http://dx.doi.org/10.1007/978-3-319-55333-7_7`.

Akeson, R. L. et al. (Aug. 2013). “The NASA Exoplanet Archive: Data and Tools for Exoplanet Research”. In: *Publications of the Astronomical Society of the Pacific* 125.930, pp. 989–999. ISSN: 1538-3873. DOI: `10.1086/672273`. URL: `http://dx.doi.org/10.1086/672273`.

Borucki, W. J. et al. (Feb. 2010). “Kepler Planet-Detection Mission: Introduction and First Results”. In: *Science* 327, p. 977. DOI: `10.1126/science.1185402`.

Bradley, Larry et al. (Sept. 2020). *astropy/photutils: 1.0.0.* Version 1.0.0. DOI: `10.5281/zenodo.4044744`. URL: `https://doi.org/10.5281/zenodo.4044744`.

Bryan, Marta L. et al. (Jan. 2019). “An Excess of Jupiter Analogs in Super-Earth Systems”. In: *The Astronomical Journal* 157.2, p. 52. ISSN: 1538-3881. DOI: `10.3847/1538-3881/aaf57f`. URL: `http://dx.doi.org/10.3847/1538-3881/aaf57f`.

Chachan, Yayaati et al. (Sept. 2021). “Radial Gradients in Dust-to-gas Ratio Lead to Preferred Region for Giant Planet Formation”. In: *ApJ* 919.1, 63, p. 63. DOI: `10.3847/1538-4357/ac0bb6`. arXiv: `2101.10333 [astro-ph.EP]`.

Chachan, Yayaati et al. (Feb. 2022). “Kepler-167e as a Probe of the Formation Histories of Cold Giants with Inner Super-Earths”. In: *ApJ* 926.1, 62, p. 62. DOI: `10.3847/1538-4357/ac3ed6`. arXiv: `2112.00747 [astro-ph.EP]`.

Charalambous, C et al. (June 2022). “Proximity of exoplanets to first-order mean-motion resonances”. In: *Monthly Notices of the Royal Astronomical Society* 514.3, pp. 3844–3856. DOI: `10.1093/mnras/stac1554`. URL: `https://doi.org/10.1093%2Fmnras%2Fstac1554`.

Chiang, Eugene et al. (Apr. 2013). “The minimum-mass extrasolar nebula: in situ formation of close-in super-Earths”. In: *Monthly Notices of the Royal Astronomical Society* 431.4, pp. 3444–3455. DOI: `10.1093/mnras/stt424`. URL: `https://doi.org/10.1093%2Fmnras%2Fstt424`.

Davenport, James R. A. et al. (2014). *Using Transiting Planets to Model Starspot Evolution*. arXiv: `1408.5201 [astro-ph.SR]`.

Dawson, Rebekah I. et al. (Sept. 2018). “Origins of Hot Jupiters”. In: *ARA&A* 56, pp. 175–221. DOI: `10.1146/annurev-astro-081817-051853`. arXiv: `1801.06117 [astro-ph.EP]`.

Deck, Katherine M. et al. (Apr. 2016). “Transit Timing Variations for Planets near Eccentricity-type Mean Motion Resonances”. In: *ApJ* 821.2, 96, p. 96. DOI: `10.3847/0004-637X/821/2/96`. arXiv: `1509.08460 [astro-ph.EP]`.

Dierckx, P. (1993). *Curve and surface fitting with splines*. Oxford University Press.

Drążkowska, J. et al. (Oct. 2016). “Close-in planetesimal formation by pile-up of drifting pebbles”. In: *A&A* 594, A105, A105. DOI: `10.1051/0004-6361/201628983`. arXiv: `1607.05734 [astro-ph.EP]`.

Fabrycky, Daniel C. et al. (Aug. 2014). “Architecture of Kepler’s Multi-transiting Systems. II. New Investigations with Twice as Many Candidates”. In: *ApJ* 790.2, 146, p. 146. DOI: `10.1088/0004-637X/790/2/146`. arXiv: `1202.6328 [astro-ph.EP]`.

Foreman-Mackey, Daniel et al. (Mar. 2013). “emcee: The MCMC Hammer”. In: *Publications of the Astronomical Society of the Pacific* 125.925, pp. 306–312. ISSN: 1538-3873. DOI: `10.1086/670067`. URL: `http://dx.doi.org/10.1086/670067`.

Foreman-Mackey, Daniel et al. (May 2021). “exoplanet: Gradient-based probabilistic inference for exoplanet data & other astronomical time series”. In: *arXiv e-prints*, arXiv:2105.01994, arXiv:2105.01994. arXiv: `2105.01994 [astro-ph.IM]`.

Fulton, Benjamin J. et al. (July 2021). “California Legacy Survey. II. Occurrence of Giant Planets beyond the Ice Line”. In: *ApJS* 255.1, 14, p. 14. DOI: `10.3847/1538-4365/abfcc1`. arXiv: `2105.11584 [astro-ph.EP]`.

Goldberg, Max et al. (Mar. 2022). “Architectures of Compact Super-Earth Systems Shaped by Instabilities”. In: *arXiv e-prints*, arXiv:2203.00801, arXiv:2203.00801. arXiv: `2203.00801 [astro-ph.EP]`.

Hadden, Sam et al. (Sept. 2016). “Numerical and Analytical Modeling of Transit Timing Variations”. In: *ApJ* 828.1, 44, p. 44. DOI: `10.3847/0004-637X/828/1/44`. arXiv: `1510.02476 [astro-ph.EP]`.

– (June 2017). “Kepler Planet Masses and Eccentricities from TTV Analysis”. In: *The Astronomical Journal* 154.1, p. 5. ISSN: 1538-3881. DOI: `10.3847/1538-3881/aa71ef`. URL: `http://dx.doi.org/10.3847/1538-3881/aa71ef`.

Helled, Ravit et al. (May 2022). “Revelations on Jupiter’s formation, evolution and interior: Challenges from Juno results”. In: *Icarus* 378, 114937, p. 114937. DOI: `10.1016/j.icarus.2022.114937`. arXiv: `2202.10041 [astro-ph.EP]`.

Hoffman, Matthew D. et al. (2011). *The No-U-Turn Sampler: Adaptively Setting Path Lengths in Hamiltonian Monte Carlo*. arXiv: `1111.4246 [stat.CO]`.

Holczer, Tomer et al. (July 2016). “Transit Timing Observations from Kepler. IX. Catalog of the Full Long-cadence Data Set”. In: *ApJS* 225.1, 9, p. 9. DOI: `10.3847/0067-0049/225/1/9`. arXiv: `1606.01744 [astro-ph.EP]`.

Holman, Matthew J. et al. (Feb. 2005). “The Use of Transit Timing to Detect Terrestrial-Mass Extrasolar Planets”. In: *Science* 307.5713, pp. 1288–1291. DOI: `10.1126/science.1107822`. arXiv: `astro-ph/0412028 [astro-ph]`.

Jontof-Hutter, Daniel et al. (Mar. 2016). “Secure Mass Measurements from Transit Timing: 10 Kepler Exoplanets between 3 and 8 $M_\oplus$ with Diverse Densities and Incident Fluxes”. In: *ApJ* 820.1, 39, p. 39. DOI: `10.3847/0004-637X/820/1/39`. arXiv: `1512.02003 [astro-ph.EP]`.

Jontof-Hutter, Daniel et al. (May 2021). “Following Up the Kepler Field: Masses of Targets for Transit Timing and Atmospheric Characterization”. In: *AJ* 161.5, 246, p. 246. DOI: `10.3847/1538-3881/abd93f`. arXiv: `2101.01202 [astro-ph.EP]`.

Kreidberg, Laura (2015). “batman: BAsic Transit Model cAlculatioN in Python”. In: *Publications of the Astronomical Society of the Pacific* 127.957, p. 1161.

Lee, Eve J. (June 2019a). “The Boundary between Gas-rich and Gas-poor Planets”. In: *The Astrophysical Journal* 878.1, p. 36. ISSN: 1538-4357. DOI: `10.3847/1538-4357/ab1b40`. URL: `http://dx.doi.org/10.3847/1538-4357/ab1b40`.

– (June 2019b). “The Boundary between Gas-rich and Gas-poor Planets”. In: *ApJ* 878.1, 36, p. 36. DOI: `10.3847/1538-4357/ab1b40`. arXiv: `1904.10470 [astro-ph.EP]`.

Lightkurve Collaboration et al. (Dec. 2018). *Lightkurve: Kepler and TESS time series analysis in Python*. Astrophysics Source Code Library. ascl: `1812.013`.

Lithwick, Yoram et al. (Dec. 2012). “Extracting Planet Mass and Eccentricity from TTV Data”. In: *ApJ* 761.2, 122, p. 122. DOI: `10.1088/0004-637X/761/2/122`. arXiv: `1207.4192 [astro-ph.EP]`.

Lopez, Eric D. et al. (Sept. 2014). “Understanding the Mass-Radius Relation for Sub-neptunes: Radius as a Proxy for Composition”. In: *ApJ* 792.1, 1, p. 1. DOI: `10.1088/0004-637X/792/1/1`. arXiv: `1311.0329 [astro-ph.EP]`.

Luger, Rodrigo et al. (Jan. 2019). “`starry`: Analytic Occultation Light Curves”. In: *The Astronomical Journal* 157.2, p. 64. ISSN: 1538-3881. DOI: `10.3847/1538-3881/aae8e5`. URL: `http://dx.doi.org/10.3847/1538-3881/aae8e5`.

Madhusudhan, Nikku (Aug. 2019). “Exoplanetary Atmospheres: Key Insights, Challenges, and Prospects”. In: *ARA&A* 57, pp. 617–663. DOI: `10.1146/annurev-astro-081817-051846`. arXiv: `1904.03190 [astro-ph.EP]`.

Mankovich, Christopher R. et al. (Aug. 2021). “A diffuse core in Saturn revealed by ring seismology”. In: *Nature Astronomy* 5, pp. 1103–1109. DOI: `10.1038/s41550-021-01448-3`. arXiv: `2104.13385 [astro-ph.EP]`.

Mills, Sean M. et al. (May 2016). “A resonant chain of four transiting, sub-Neptune planets”. In: *Nature* 533.7604, pp. 509–512. ISSN: 1476-4687. DOI: `10.1038/nature17445`. URL: `http://dx.doi.org/10.1038/nature17445`.

Nesvorný, David et al. (July 2014). “The Effect of Conjunctions on the Transit Timing Variations of Exoplanets”. In: *ApJ* 790.1, 58, p. 58. DOI: `10.1088/0004-637X/790/1/58`. arXiv: `1405.7433 [astro-ph.EP]`.

Owen, James E. et al. (Oct. 2013). “Kepler Planets: A Tale of Evaporation”. In: *ApJ* 775.2, 105, p. 105. DOI: `10.1088/0004-637X/775/2/105`. arXiv: `1303.3899 [astro-ph.EP]`.

Poon, Sanson T S et al. (May 2021). “iIn situ/i formation of hot Jupiters with companion super-Earths”. In: *Monthly Notices of the Royal Astronomical Society* 505.2, pp. 2500–2516. DOI: `10.1093/mnras/stab1466`. URL: `https://doi.org/10.1093%2Fmnras%2Fstab1466`.

Rafikov, Roman R. (Sept. 2006). “Atmospheres of Protoplanetary Cores: Critical Mass for Nucleated Instability”. In: *ApJ* 648.1, pp. 666–682. DOI: `10.1086/505695`. arXiv: `astro-ph/0405507 [astro-ph]`.

Ricker, George R. et al. (Oct. 2014). “Transiting Exoplanet Survey Satellite”. In: *Journal of Astronomical Telescopes, Instruments, and Systems* 1.1, p. 014003. ISSN: 2329-4124. DOI: `10.1117/1.jatis.1.1.014003`. URL: `http://dx.doi.org/10.1117/1.JATIS.1.1.014003`.

Rowe, Jason F. et al. (Mar. 2014). “Validation of Kepler’s Multiple Planet Candidates. III. Light Curve Analysis and Announcement of Hundreds of New Multi-planet Systems”. In: *ApJ* 784.1, 45, p. 45. DOI: `10.1088/0004-637X/784/1/45`. arXiv: `1402.6534 [astro-ph.EP]`.

Salvatier, John et al. (2016). “Probabilistic programming in Python using PyMC3”. In: *PeerJ Computer Science* 2, e55.

Schmitt, Joseph R. et al. (Nov. 2014). “Planet Hunters. VII. Discovery of a New Low-mass, Low-density Planet (PH3 C) Orbiting Kepler-289 with Mass Measurements of Two Additional Planets (PH3 B and D)”. In: *ApJ* 795.2, 167, p. 167. DOI: `10.1088/0004-637X/795/2/167`. arXiv: `1410.8114 [astro-ph.EP]`.

Stefansson, Gudmundur et al. (Oct. 2017). “Toward Space-like Photometric Precision from the Ground with Beam-shaping Diffusers”. In: *ApJ* 848.1, 9, p. 9. DOI: `10.3847/1538-4357/aa88aa`. arXiv: `1710.01790 [astro-ph.IM]`.

Thorngren, Daniel et al. (Apr. 2019). “Connecting Giant Planet Atmosphere and Interior Modeling: Constraints on Atmospheric Metal Enrichment”. In: *The Astrophysical Journal* 874.2, p. L31. ISSN: 2041-8213. DOI: `10.3847/2041-8213/ab1137`. URL: `http://dx.doi.org/10.3847/2041-8213/ab1137`.

Thorngren, Daniel P. et al. (Nov. 2016). “The Mass-Metallicity Relation for Giant Planets”. In: *ApJ* 831.1, 64, p. 64. DOI: `10.3847/0004-637X/831/1/64`. arXiv: `1511.07854 [astro-ph.EP]`.

Vissapragada, Shreyas et al. (Feb. 2020). “Diffuser-assisted Infrared Transit Photometry for Four Dynamically Interacting Kepler Systems”. In: *The Astronomical Journal* 159.3, p. 108. issn: 1538-3881. doi: `10.3847/1538-3881/ab65c8`. url: `http://dx.doi.org/10.3847/1538-3881/ab65c8`.

Wahl, S. M. et al. (May 2017). “Comparing Jupiter interior structure models to Juno gravity measurements and the role of a dilute core”. In: *Geophys. Res. Lett.* 44.10, pp. 4649–4659. doi: `10.1002/2017GL073160`. arXiv: `1707.01997 [astro-ph.EP]`.

Weiss, Lauren M. et al. (Mar. 2022). “Architectures of Compact Multi-planet Systems: Diversity and Uniformity”. In: *arXiv e-prints*, arXiv:2203.10076, arXiv:2203.10076. arXiv: `2203.10076 [astro-ph.EP]`.

Wolter, U. et al. (July 2009). “Transit mapping of a starspot on CoRoT-2”. In: *Astronomy & Astrophysics* 504.2, pp. 561–564. issn: 1432-0746. doi: `10.1051/0004-6361/200912329`. url: `http://dx.doi.org/10.1051/0004-6361/200912329`.

Zeng, Li et al. (Mar. 2016). “Mass-Radius Relation for Rocky Planets Based on PREM”. In: *ApJ* 819.2, 127, p. 127. doi: `10.3847/0004-637X/819/2/127`. arXiv: `1512.08827 [astro-ph.EP]`.

Zhao, Ming et al. (Dec. 2014). “Characterization of the Atmosphere of the Hot Jupiter HAT-P-32Ab and the M-dwarf Companion HAT-P-32B”. In: *ApJ* 796.2, 115, p. 115. doi: `10.1088/0004-637X/796/2/115`. arXiv: `1410.0968 [astro-ph.EP]`.

Zhu, Wei et al. (Aug. 2018). “The Super Earth–Cold Jupiter Relations”. In: *The Astronomical Journal* 156.3, p. 92. issn: 1538-3881. doi: `10.3847/1538-3881/aad22a`. url: `http://dx.doi.org/10.3847/1538-3881/aad22a`.

Chapter 3

TIDALLY HEATED SUB-NEPTUNES, REFINED PLANETARY COMPOSITIONS, AND CONFIRMATION OF A THIRD PLANET IN THE TOI-1266 SYSTEM

Greklek-McKeon, Michael, Shreyas Vissapragada, and Heather A. Knutson, et al. (2025). “Tidally Heated Sub-Neptunes, Refined Planetary Compositions, and Confirmation of a Third Planet in the TOI-1266 System”. In: *The Astronomical Journal* 169.6, p. 292. doi: `10.3847/1538-3881/adc0fe`.

Abstract

TOI-1266 is a benchmark system of two temperate (< 450 K) sub-Neptune-sized planets orbiting a nearby M dwarf exhibiting a rare inverted architecture with a larger interior planet. In this study, we characterize transit timing variations (TTVs) in the TOI-1266 system using high-precision ground-based follow-up and new TESS data. We confirm the presence of a third exterior non-transiting planet, TOI-1266 d (P = 32.5 d, $M_d = 3.68^{+1.05}_{-1.11} M_\oplus$), and combine the TTVs with archival radial velocity (RV) measurements to improve our knowledge of the planetary masses and radii. We find that, consistent with previous studies, TOI-1266 b ($R_b = 2.52 \pm 0.08\ R_\oplus$, $M_b = 4.46 \pm 0.69\ M_\oplus$) has a low bulk density requiring the presence of a hydrogen-rich envelope, while TOI-1266 c ($R_c = 1.98 \pm 0.10\ R_\oplus$, $M_c = 3.17 \pm 0.76\ M_\oplus$) has a higher bulk density that can be matched by either a hydrogen-rich or water-rich envelope. Our new dynamical model reveals that this system is arranged in a rare configuration with the inner and outer planets located near the 3:1 period ratio with a non-resonant planet in between them. Our dynamical fits indicate that the inner and outer planet have significantly nonzero eccentricities ($e_b + e_d = 0.076^{+0.029}_{-0.019}$), suggesting that TOI-1266 b may have an inflated envelope due to tidal heating. Finally, we explore the corresponding implications for the formation and long-term evolution of the system, which contains two of the most favorable cool (< 500 K) sub-Neptunes for atmospheric characterization with JWST.

3.1 Introduction

Planets transiting nearby M dwarf stars are the best laboratory we have to characterize the properties of sub-Neptune-sized exoplanets. Their relatively large planet-star radius and mass ratios make M dwarf planets amenable to high precision bulk density measurements, and these systems are among the most favorable targets for atmospheric studies. However, the atmospheric compositions of sub-Neptune-sized planets orbiting M dwarfs on close-in orbits may be systematically enriched in water and depleted in hydrogen relative to their counterparts orbiting Sun-like stars.

Since the ice lines for M dwarfs are much closer in than for Sun-like stars, close-in sub-Neptune-sized planets orbiting these stars might accrete more water than their counterparts orbiting hotter stars (e.g., Alibert et al., 2017; Ormel et al., 2017; Bitsch et al., 2020; Kimura et al., 2022). Even if small planets orbiting M dwarfs initially form with H-rich atmospheres, they may be less likely to retain them even at relatively low equilibrium temperatures (e.g., Hori et al., 2020). M dwarfs have much higher flare rates and higher fractional XUV fluxes than Sun-like stars, and this can drive increased atmospheric mass loss (Roettenbacher et al., 2017; Fleming et al., 2020).

We can obtain initial constraints on the envelope compositions of sub-Neptune-sized planets by measuring their masses, radii, and corresponding bulk densities. Population-level studies of small planets orbiting M dwarfs (e.g., Luque et al., 2022) indicate that some planets have high bulk densities consistent with rocky Earth-like compositions, while the densities of others are so low that they can only be matched with a hydrogen-rich envelope, and some planets with intermediate densities are consistent with a wide range of possible envelope compositions (Parc et al., 2024), including water-rich steam atmospheres (Aguichine et al., 2021; Luque et al., 2022; Pierrehumbert, 2023) or more tenuous hydrogen-rich envelopes (Rogers et al., 2023). Some studies have used mass loss models to rule out solar metallicity gas envelopes and provide evidence in favor of water-rich compositions for individual sub-Neptunes (e.g., Diamond-Lowe et al., 2022; Piaulet et al., 2023; Castro-González et al., 2023). But if sub-Neptunes have moderately enriched atmospheric metallicities ($\geq 50 - 200\times$ solar; Zhang et al., 2022) making atmospheric mass loss much less efficient (Linssen et al., 2024), it is more difficult to rule out the presence of H/He envelopes and break degeneracies in planet composition type.

We can directly characterize the atmospheric compositions of sub-Neptune-sized planets using transmission spectroscopy, but most warm ($T_{eq} \in 500 - 1000$ K) sub-Neptunes observed to date appear to host thick photochemical hazes that obscure the expected molecular absorption features (Wallack et al., 2024; Gao et al., 2023). The recent JWST detections of strong atmospheric absorption from TOI-270d and

K2-18b (Madhusudhan et al., 2023; Benneke et al., 2024), both of which have equilibrium temperatures lower than 400 K, suggests that these obscuring hazes may disappear in cooler atmospheres, e.g., Brande et al., 2024. Both TOI-270d and K2-18b have hydrogen-rich atmospheres that contain significant quantities of CH_4, CO_2 and H_2O (correspnding to atmospheric metallicities of $\sim 100 - 200\times$ solar; Madhusudhan et al., 2023; Wogan et al., 2024; Benneke et al., 2024), or the atmosphere of K2-18 b could also be explained with C and N abundances $\sim 10\times$ solar and a high H_2O/H_2 ratio (Yang et al., 2024). Recent JWST observations of the temperate super-Earth LHS 1140 b (T_{eq} = 226 K, R_p = 1.73 $R_\oplus$, Cadieux et al., 2024) ruled out the presence of an H_2-rich envelope, indicating that the planet is likely water rich (Damiano et al., 2024).

It is unclear whether or not these few planets are representative of the true diversity in the M dwarf sub-Neptune population. Unfortunately, there are currently only a handful of temperate sub-Neptune-sized planets orbiting M dwarfs with well-measured masses and radii that are also favorable targets for atmospheric characterization with JWST. As a result, there are only seven planets with radii between $2 - 3$ $R_\oplus$ and $T_{eq} < 500$ K with scheduled JWST observations (TOI-270 d, LP 791-18 c, LTT 3780 c, K2-18 b, TOI-776 c, TOI-1468 c, and TOI-4336 b). The predicted amplitude of the atmospheric absorption signal during transit is inversely proportional to the planet's surface gravity, and well-constrained mass and radius measurements are therefore an essential requirement for JWST observation planning (e.g., Batalha et al., 2017; Batalha et al., 2019; Di Maio et al., 2023). For sub-Neptunes, bulk density measurements can also be used in conjunction with transmission spectroscopy to constrain the composition of the planet's envelope (e.g., Benneke et al., 2024; Piaulet-Ghorayeb et al., 2024).

Measuring masses of temperate sub-Neptunes with radial velocities (RVs) can be challenging because the host stars are faint and/or active, and low-mass planets with long orbital periods have correspondingly small RV semi-amplitudes. For planets in dynamically interacting multi-planet systems, the masses can be measured with transit timing variations (TTVs, e.g. Greklek-McKeon et al., 2023). The size of the TTV signal is maximized in systems where the planets have orbital period ratios close to mean-motion resonance (MMR; Lithwick et al., 2012), and in systems with larger planet-star mass ratios (e.g., M dwarfs; Agol et al., 2021). The Transiting Exoplanet Survey Satellite (TESS, Ricker et al., 2014) has detected many such systems orbiting M dwarfs and obtained an initial set of transit timing measurements. However, the precision of TTV-based mass estimates depends on the orbital architecture of the system, the sampling of the TTV oscillations, and on our ability to obtain precise transit mid-times. Because of this, planets that are observed at low SNR with TESS require additional high SNR transit observations at later epochs in order to obtain useful mass constraints (Ballard, 2019).

In this study we focus on TOI-1266, a nearby (d = 36 pc) M3 star ($T_* = 3563 \pm 77$ K, Stefánsson et al., 2020) that hosts two sub-Neptune-sized transiting planets with equilibrium temperatures of 415 K and 346 K, respectively (Demory et al., 2020; Stefánsson et al., 2020, hereafter D20 and S20). Systems with multiple planets of different sizes and bulk densities such as TOI-1266 are uniquely advantageous for testing theories of planet formation and evolution (e.g., Diamond-Lowe et al., 2022; Piaulet et al., 2023) because the planets formed from the same protoplanetary disk and experienced the same irradiation history scaled to their orbital separations. We can use these multi-planet systems to explore how small differences in initial conditions and irradiation environment can lead to different final planetary composition types.

The TOI-1266 system has been previously studied in the literature, with two discovery papers characterizing the properties of the inner two transiting planets (D20 and S20), followed by a paper presenting detailed atmospheric modeling for TOI-1266 c (Harman et al., 2022). This system was also the subject of a separate RV analysis that measured the masses of both transiting planets and reported tentative evidence for a third non-transiting planet candidate (Cloutier et al., 2024, hereafter C24). These three studies find that the inner two TOI-1266 planets ($R_b = 2.59 \pm 0.10\ R_\oplus$, $R_c = 2.04 \pm 0.11\ R_\oplus$, $M_b = 4.40^{+0.68}_{-0.70}\ M_\oplus$, $M_c = 3.12 \pm 0.76\ M_\oplus$, C24) display an 'inverted' architecture with a larger interior planet. Most multi-planet systems that span the radius valley have the smaller super-Earth on an interior orbit to the larger sub-Neptune (e.g., Weiss et al., 2018). The TOI-1266 system therefore runs counter to the canonical narrative that it should be easier for more distant planets to retain larger primordial hydrogen-rich envelopes, even when accounting for the lower mass of TOI-1266 c (C24). Notably, TOI-1266 b has a higher Transmission Spectroscopy Metric (TSM; this indicates the planet's relative favorability for atmospheric characterization with transmission spectroscopy, see Kempton et al., 2018, C24, and Table 3.3) than all currently selected JWST sub-Neptune ($2-3\ R_\oplus$) targets cooler than 500 K aside from L98-59 d.

The two transiting planets in the TOI-1266 system have period ratios that are 3.5%

away from the 5:3 orbital resonance and 1.3% away from the 7:4 orbital resonance, making this system a favorable target for TTV mass measurements. Demory et al., 2020 reported a preliminary detection of a TTV signal from a combination of TESS and ground-based transit observations, suggesting that additional transit timing variations might provide useful constraints on the planet masses. Recent work has revealed that there is a systematic, population-level discrepancy between the densities of sub-Neptune planets whose masses come from TTV measurements versus RV measurements, which is consistent with near-resonant planets being puffier and can be reproduced in the RV sample alone (Adrien Leleu et al., 2024). Rare systems such as TOI-1266 which contain both near-resonant and non-resonant planets, and separate RV and TTV mass measurements, enable detailed investigation of this trend.

In this paper, we extend the TTV baseline by 730 days with new space- and ground-based observations, and carry out a joint TTV and RV analysis of TESS photometry including new data from the second extended mission, new ground-based photometric follow-up from the Wide-field InfraRed Camera (WIRC) at Palomar Observatory, the Multicolor Simultaneous Camera for studying Atmospheres of Transiting exoplanets (MuSCAT) instrument series at the National Astronomical Observatory of Japan (NAOJ) and the Las Cumbres Observatory Global Telescope network (LCOGT), a Sinistro imager at LCOGT, and archival RV measurements from the High Accuracy Radial velocity Planet Searcher for the Northern hemisphere (HARPS-N).

In §3.2, we describe our observations. In §3.3, we summarize information on the host star, including new abundance analysis. In §3.4, we present our transit analysis. In §3.5, we present our TTV analysis, and in §3.6 we present our RV and joint RV+TTV analysis. In §3.7 we present our analysis on the dynamics of the system. In §3.8 we present results on the planetary compositions. In §3.8 we discuss our results. In §3.9 we discuss the prospects of future observations before concluding with a summary of our key findings in §3.10.

3.2 Observations

TESS

TOI-1266 has been observed by TESS during the prime mission (PM), extended mission (EM), and second extended mission (SEM). D20 and S20 reported on the discovery of TOI-1266 b and c using PM data from TESS sectors 14, 15, 21, and

22, from UT 2019 July 18 to 2020 March 17. Follow-up work in C24 improved the characterization of the planetary radii with TESS EM data from sectors 41, 48, and 49 between from UT 2021 July 23 to 2022 March 06. In this study, we extend the analysis to SEM data in TESS sectors 75 and 76 between UT 2024 Jan 30 and 2024 March 26.

The TOI-1266 b and c discovery papers (D20 and S20) use the TESS 2-min Presearch Data Conditioning Simple Aperture Photometry (PDCSAP) light curves. C24 performs a more in-depth analysis of the TESS PM and EM data, including PDCSAP light curves and custom light curve extractions from the 2-min cadence TESS Target Pixel Files (TPFs) and the 30- and 10-min cadence Full Frame Images (FFIs). This comprehensive multi-pipeline analysis of the TESS data by C24 was motivated by significant differences in the transit depths of TOI-1266 b and c between the TESS PM and EM data. C24 finds these transit depth discrepancies to be consistent across different photometry sources. We use the 2-min cadence PDCSAP light curves across all TESS sectors.

Table 3.1 Summary of ground-based observations of TOI-1266 b and c.

Instrument	Planet	UT Date	Start	Finish	Transit %	Baseline %	z_{st}	z_{min}	z_{end}	$t_{\mathrm{exp}}(s)$
WIRC	TOI-1266 b	2022 Feb 28	04:37:11	11:05:29	100%	100%	1.94	1.18	1.19	15
WIRC	TOI-1266 b	2022 June 6	06:04:42	10:41:17	100%	120%	1.26	1.22	2.26	12.5
MuSCAT	TOI-1266 b	2021 April 7	10:32:47	14:08:56	100%	80%	1.60	1.19	1.19	25, 12, 12
MuSCAT3	TOI-1266 b	2021 April 18	07:47:49	11:12:35	100%	70%	1.54	1.41	1.46	8, 12, 20, 12
MuSCAT3	TOI-1266 b	2022 Jan 26	13:35:60	15:31:47	20%	70%	1.49	1.41	1.41	8, 12, 20, 12
MuSCAT3	TOI-1266 b	2022 Feb 28	08:12:24	11:08:16	70%	80%	2.34	1.53	1.53	8, 12, 20, 12
MuSCAT3	TOI-1266 c	2021 May 13	09:32:09	12:57:38	80%	80%	1.46	1.46	2.23	8, 12, 20, 12
MuSCAT	TOI-1266 c	2022 Jan 31	14:07:23	20:05:53	100%	>200%	1.79	1.17	1.17	25, 18, 17
Sinistro	TOI-1266 c	2022 March 10	06:36:24	10:02:06	100%	90%	1.33	1.22	1.24	40
WIRC	TOI-1266 c	2022 March 10	04:58:26	10:51:59	100%	>200%	1.65	1.20	1.18	12.5

Start and Finish columns represent the time of first and last science images in UT time, the transit and baseline fractions are relative to the total transit duration for each planet, z_{min} is the minimum airmass of the science sequence while z_{st} and z_{end} are the starting and ending airmasses, and t_{exp} is the exposure time used, which is varied on the night of observation based on the sky conditions (Moon fraction and proximity, cloud cover, etc.). The t_{exp} values for MuSCAT represent the values for the g, r, and z_s bands, and those for MuSCAT3 represent the values for the g, r, i, and z_s bands, respectively.

Palomar/WIRC

We observed three transits each of TOI-1226 b and c in the *J*-band with the Wide-field Infared Camera (WIRC) on the Hale Telescope at Palomar Observatory, California, USA. The Hale Telescope is a 5.08-m telescope equipped with a 2048 x 2048 Rockwell Hawaii-II NIR detector, providing a field of view of 8′.7 × 8′.7 with a plate scale of 0.”25 per pixel (WIRC, Wilson et al., 2003). Our data were taken with a beam-shaping diffuser that increased our observing efficiency and improved the photometric precision and guiding stability (Stefansson et al., 2017; Vissapragada et al., 2020).

We observed transits of TOI-1266 b on UT February 28, 2022, June 6, 2022, and April 7, 2023. Transits of TOI-1266 c were observed on UT March 10, 2022, June 12, 2022, and December 9, 2023. The full details of our WIRC observations, including observation dates, exposure times, airmass values, and transit and baseline coverage fractions are included in Table 3.1. For each night, we obtained calibration images to dark-subtract, flat-field, remove dead and hot pixels, and remove detector structure with a 9-point dithered sky background frame following the methodology of Vissapragada et al., 2020. We extracted photometry and detrended the light curves with the procedure described in Greklek-McKeon et al., 2023.

Our diffuser reshapes the stellar PSFs into a top-hat shape with a 3″.0 full width at half maximum (FWHM), but for our UT April 7, 2023 observations of TOI-1266 b, conditions were cloudy and the seeing was intermittently worse than 3″.0, allowing the PSF to spill out beyond the diffuser bounds and introduce a more complicated scintillation noise structure. Since most comparison stars in the field of view on this night also had PSFs interior or exterior to the diffuser bounds at various points, our photometric precision in the final light curve was significantly lower than other nights, and we choose not to include this night of observation in our analysis. We also chose not to include the UT June 12, 2022, and December 9, 2023 observations in our analysis of TOI-1266 c. Dome closures due to clouds and humidity on these nights meant our coverage was insufficient to provide baseline on both sides of transit, and therefore the precision on our extracted midtimes suffered.

NAOJ 188cm/MuSCAT

We observed one full transit each of TOI-1266 b and TOI-1266 c on UT 2021 April 7 and 2022 January 31, respectively, with the Multiband Simultaneous Camera for studying Atmospheres of Transiting exoplanets (MuSCAT; Narita et al., 2015) mounted on the NAOJ 188 cm telescope located in Okayama, Japan. MuSCAT has three optical channels for the g, r, and z_s bands, each having a 1024×1024 pixel CCD camera with a pixel scale of $0\farcs36$ and an FoV of $6\farcm1 \times 6\farcm1$. Both observations were conducted with the telescope slightly defocused so that the FWHM of the stellar PSF was 8–12 pixels. The exposure times were set at 12–25 s depending on the band and the night.

The raw images were calibrated for dark and flat-field in a standard manner. After that, aperture photometry was performed for the target and several comparison stars to produce relative light curves using a custom pipeline described in Fukui et al. (2011).

LCOGT/MuSCAT3

We observed four (one full and three partial) transits of TOI-1266 b and two (both partial) transits of TOI-1266 c with MuSCAT3 (Narita et al., 2020), which is mounted on the 2 m Faulkes Telescope North (FTN) operated by Las Cumbres Observatory Global Telescope (LCOGT, Brown et al., 2013). MuSCAT3 is similar to MuSCAT but has four optical channels for the g, r, i, and z_s bands, each with a 2048×2048 pixel CCD camera with a pixel scale of $0\farcs27$ and an FoV of $9\farcm1 \times 9\farcm1$. The observations of TOI-1266 b were conducted on the night of UT 2021 April 18, 2022 January 26, 2022 February 28, and 2022 May 26, while the observations of TOI-1266 c were conducted on 2021 May 13 and 2022 May 24. During the observations the telescope was defocused, which results in FWHM of stellar PSF of 10–20 pixels depending on the night. The exposure times were set at 8, 12, 20, and 12 s for the g, r, i, and z_s bands, respectively, for all nights.

The raw images were calibrated using the `BANZAI` pipeline (McCully et al., 2018), and aperture photometry was performed in the same way as for the MuSCAT data. Due to poor photometric quality or insufficient baseline coverage, we decided to omit data from 2022 May 24 and 2022 May 26 from the subsequent analysis.

LCOGT/Sinistro

We observed one full transit of TOI-1266 c on UT 2022 March 10 with the Sinistro imager on one of the 1 m telescopes of LCOGT at the McDonald observatory in TX, US. Sinistro is equipped with a 4K × 4K pixel CCD with a pixel scale of $0\farcs39$ and an FoV of $26\farcm5 \times 26\farcm5$. The observation was conducted through the i band filter with an exposure time of 40 s and moderate defocusing. The obtained data were reduced in the same way as the MuSCAT3 data.

3.3 Stellar Characterization

TOI-1266 is a single star located at a distance of 36 pc (C24) that has been characterized extensively with several different spectroscopic instruments and techniques. D20 used multiple methods to independently derive stellar parameters, including the pseudo equivalent-width method described in Maldonado et al., 2015 for TRES spectra, the SpecMatch-Empirical method of Yee et al., 2017 for HIRES spectra, and the broadband spectral energy distribution (SED) together with the Gaia DR2 parallax (Stassun et al., 2016; Stassun et al., 2017; Stassun et al., 2018). D20 found consistent stellar parameters across all three methods, and conclude based on a HIRES RV measurement and the proper motion and parallax from Gaia DR2 that TOI-1266 has a ~96% probability of belonging to the galactic thin disc population. D20 also concluded based on TESS prime mission data, both from the PDC pipeline and their own custom reduction from the TESS Target Pixel Files, that TOI-1266 does not exhibit any rotational modulation or flares, consistent with an old, slightly metal-poor early M dwarf with an unspotted photosphere and negligible chromospheric activity.

Table 3.2. Summary of stellar parameters.

Parameter	Description	Value	Reference
Main identifiers:			
TIC	-	467179528	TIC
TOI	-	1266	TIC
2MASS	-	J13115955+6550017	TIC
Gaia DR3	-	1678074272650459008	Gaia
Equatorial Coordinates, Proper Motion and Spectral Type:			
$\alpha_{\rm J2000}$	Right Ascension (RA)	13:11:59.18	Gaia
$\delta_{\rm J2000}$	Declination (Dec)	+65:50:01.31	Gaia
μ_α	Proper motion (RA, mas yr^{-1})	-150.652 ± 0.041	Gaia
μ_δ	Proper motion (Dec, mas yr^{-1})	-25.368 ± 0.039	Gaia
Spectral Type	-	M2	S20
Magnitudes:			
B	APASS Johnson B mag	14.578 ± 0.048	APASS
V	APASS Johnson V mag	12.941 ± 0.049	APASS
g'	APASS Sloan g' mag	13.811 ± 0.050	APASS
r'	APASS Sloan r' mag	12.297 ± 0.070	APASS
i'	APASS Sloan i' mag	11.246 ± 0.150	APASS
T	TESS magnitude	11.040 ± 0.007	TIC
J	2MASS J mag	9.706 ± 0.023	2MASS
H	2MASS H mag	9.065 ± 0.030	2MASS
K_s	2MASS K_s mag	8.840 ± 0.020	2MASS
$W1$	WISE1 mag	8.715 ± 0.022	WISE
$W2$	WISE2 mag	8.612 ± 0.019	WISE
$W3$	WISE3 mag	8.504 ± 0.024	WISE
$W4$	WISE4 mag	8.233 ± 0.207	WISE
Stellar Parameters^a:			
$T_{\rm eff}$	Effective temperature in K	3563 ± 77	S20
$\log(g)$	Surface gravity in cgs units	$4.826^{+0.020}_{-0.021}$	S20
M_*	Mass in $M_\odot$	0.437 ± 0.021	S20
R_*	Radius in $R_\odot$	$0.4232^{+0.0077}_{-0.0079}$	S20
ρ_*	Density in g cm^{-3}	$8.13^{+0.47}_{-0.46}$	S20
Age	Age in Gyrs	$4.6^{+1.6}_{-1.2}$	This work
L_*	Luminosity in $L_\odot$	$0.02629^{+0.00071}_{-0.00075}$	S20
A_v	Visual extinction in mag	$0.015^{+0.011}_{-0.010}$	S20
d	Distance in pc	$36.011^{+0.029}_{-0.030}$	Gaia, Bailer-Jones
π	Parallax in mas	$27.769^{+0.023}_{-0.022}$	Gaia
Other Stellar Parameters:			
$v \sin i_*$	Stellar rotational velocity in km s^{-1}	< 1.3	C24
P_{rot}	Stellar rotational period in days	$44.6^{+0.5}_{-0.8}$	C24
$logR'_{HK}$	Chromospheric Ca II H and K flux ratio	$-5.5^{+0.35}_{-0.44}$	C24
RV	Absolute radial velocity in km s^{-1} (γ)	-41.58 ± 0.26	C24
U	Galactic U Velocity (km/s)	-5.8 ± 0.2	S20
V	Galactic V Velocity (km/s)	-40.3 ± 0.4	S20
W	Galactic W Velocity (km/s)	-27.9 ± 0.6	S20
Stellar Abundances^b:			
[C/H]	Carbon metallicity in dex	-0.132 ± 0.130	This work
[N/H]	Nitrogen metallicity in dex	-0.085 ± 0.166	This work
[O/H]	Oxygen metallicity in dex	-0.114 ± 0.102	This work
[Mg/H]	Magnesium metallicity in dex	-0.052 ± 0.105	This work
[Al/H]	Aluminum metallicity in dex	-0.048 ± 0.134	This work
[Si/H]	Silicon metallicity in dex	-0.104 ± 0.101	This work
[Ca/H]	Calcium metallicity in dex	-0.091 ± 0.094	This work
[Ti/H]	Titanium metallicity in dex	-0.019 ± 0.167	This work
[Cr/H]	Chromium metallicity in dex	-0.077 ± 0.132	This work
[Fe/H]	Iron metallicity in dex	-0.109 ± 0.092	This work
[Ni/H]	Nickel metallicity in dex	-0.105 ± 0.096	This work

S20 used the empirical spectral matching algorithm described in Stefansson et al., 2020 on HPF spectra to obtain stellar parameters, along with an independent analysis of the SED. Stellar parameters from the two methods of S20 are consistent with D20, with a similar 97.2% probability that TOI-1266 is a galactic thin disk member. S20 also reported a limit on the projected stellar rotational velocity of $v \sin i_* < 2$ km/s along with a lack of rotational modulation based on Lomb-Scargle periodograms of the TESS PM photometry, ground-based photometry from the All-Sky Automated Survey for SuperNovae (ASAS-SN; Kochanek et al., 2017), and the Zwicky Transient Facility (ZTF; Masci et al., 2019). S20 also do not detect any variability in the Ca II infrared triplet or differential line widths from their HPF spectra, as expected for an inactive star with a moderately long rotation period.

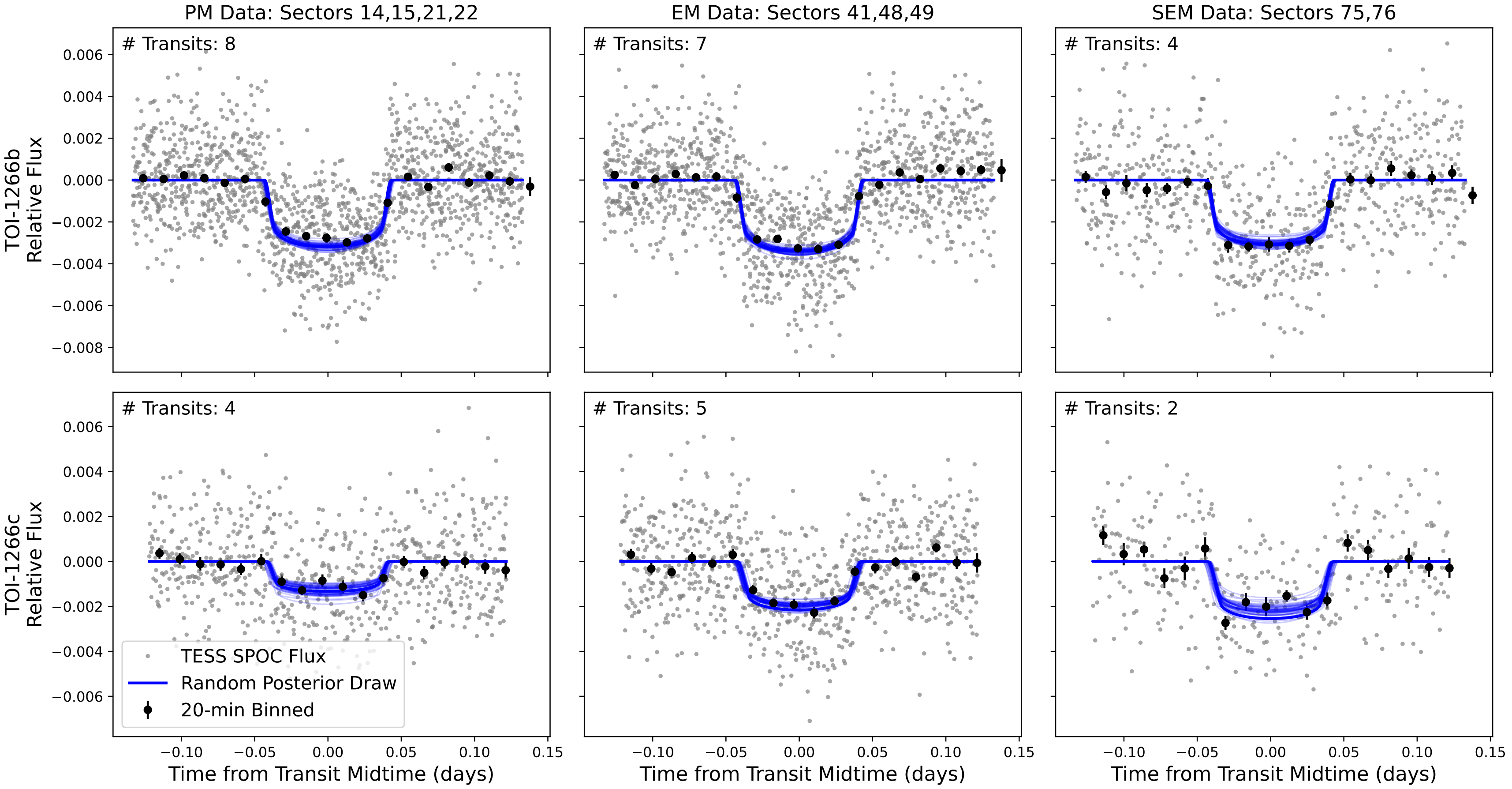

Figure 3.1 Stacked TESS light curves for TOI-1266 b (top row) and c (bottom row) for the prime mission (left column), extended mission (middle column), and second extended mission (right column). Individual transits are stacked by their best fit midtimes, with the total number of transits per mission noted, and 100 random draws from the transit model posteriors shown in blue.

C24 is likewise unable to recover the stellar rotation period in the TESS PM or EM data. We extend the Lomb-Scargle periodogram search to the TESS PM, EM, and SEM data but find no significant peaks indicative of rotational modulation. However, C24 did find evidence for a stellar rotation period of ~45 days in the spectroscopic HARPS-N time series, and carried out detailed activity modeling to show that this is consistent with bright plages and inconsistent with dark starspots. C24 also reported a $\log R'_{HK}$ = $-5.5^{+0.35}_{-0.44}$, in good agreement with D20 and S20's previous conclusion that TOI-1266 is inactive.

S20 reports the age of TOI-1266 as $7.9^{+4.2}_{-5.2}$ Gyr based on a fit to the stellar spectral energy distribution. We update this age constraint using the stellar rotation period and $\log R'_{HK}$ values from C24 with the M dwarf age-rotation and age-activity relations detailed in Engle et al., 2023 and Engle, 2024 assuming an M2 spectral type (S20). We find that the age estimates from the stellar rotation relation and $\log R'_{HK}$ relation are consistent with each other within 1σ, but the rotation relation provides a more precise estimate of $4.6^{+1.6}_{-1.2}$ Gyr, which we adopt in this work. Future measurement of the stellar X-ray luminosity would provide another independent constraint on the stellar age (Engle, 2024) and might further improve the measurement (see §3.9).

We adopt stellar parameters for our analysis from S20, which are consistent with previously reported values in D20 and C24, and are based on spectroscopic analysis. D20 also reports stellar parameters from spectroscopic analysis but at lower precision than S20, while C24 adopts stellar parameters from the TESS Input Catalog v8.2 (TIC; Stassun et al., 2019), which are based on empirical scaling relations from color magnitudes. We comment on the effect of stellar parameter choice on planet properties in §3.8.

Literature values for the metallicity of TOI-1266 include -0.5±0.5 dex from D20 and $-0.08^{+0.13}_{-0.10}$ from S20, indicating that TOI-1266 may be moderately metal poor. We report the previously published stellar parameters in Table 3.2, including the parameters we adopt from S20 and newly derived parameters from our work. Table 3.2 is adapted from Stefánsson et al., 2020, using information from the TIC (Stassun et al., 2018; Stassun et al., 2019), Gaia (Gaia Collaboration, 2018), APASS (Henden et al., 2015), 2MASS/WISE (Cutri et al., 2021), Bailer-Jones (Bailer-Jones et al., 2018), S20 (Stefánsson et al., 2020), C24 (Cloutier et al., 2024), stellar parameters[a] derived using stellar SED and isochrone fits with gaussian priors on stellar T_{eff}, logg, and [Fe/H] from HPF spectroscopic analysis in Stefánsson et al., 2020, and stellar abundances[b] derived from SDSS-V/APOGEE spectrum using The Cannon

(Behmard et al., 2025).

We perform an updated analysis to improve the iron abundance constraint, and measure several other refractory element stellar abundances including [Mg/H] and [Si/H] for the first time. The detailed abundance analysis was carried out with an implementation of *The Cannon* (Behmard et al., 2025), a data-driven method capable of inferring stellar abundances that does not rely on stellar evolution models. This makes *The Cannon* an excellent choice for characterizing M dwarfs, which have notoriously complex spectra due to the presence of molecular features. This *Cannon* implementation was trained on M dwarfs with FGK companions from the Sloan Digital Sky Survey-V/Apache Point Observatory Galactic Evolution Experiment (SDSS-V/APOGEE). SDSS-V/APOGEE is a high resolution ($R \sim$ 22,500), H-band (1.51$-$1.7 μm) spectroscopic survey. Its wavelength coverage is ideal for M dwarfs, which have peak brightness in the near-infrared.

3.4 Transit Modeling

TESS

We constructed our TESS photometric model using the `exoplanet` package (Daniel Foreman-Mackey et al., 2021) for the transit light curve component. Our transit model includes the following free parameters: the stellar radius R_*, impact parameter b, scaled semimajor axis a/R_*, and individual transit mid-center times. We used separate planet-to-star radius ratios R_p/R_* for each segment of TESS data (separated by PM, EM, and SEM) to account for possible changes in transit depth (see §3.4). In §3.4, §3.4, and §3.4, we refer to b, a/R_*, and R_p/R_* as "transit shape parameters". We allowed the mid-time of each transit to vary individually in our fit using the `TTVOrbit` module of `exoplanet`, rather than fitting for a constant orbital period and t_0 corresponding to a linear ephemeris.

We simultaneously modeled systematics in the TESS data from instrumental and stellar variability with a Matern-3/2 kernel GP from `celerite2` (D. Foreman-Mackey et al., 2017; D. Foreman-Mackey, 2018). This kernel is commonly utilized for its ability to model quasi-periodic stellar variability signals (e.g., Demory et al., 2020; Stefánsson et al., 2020; Gan et al., 2022; Cointepas et al., 2024). For this part of the model, we included a mean offset parameter μ and GP hyperparameters σ and ρ corresponding to the amplitude and timescale of quasi-periodic oscillations, along with an error scaling term added in quadrature to the flux errors.

We fixed the planetary eccentricities to zero in the transit fit, as our TTV modeling indicates that both planets must have orbital eccentricities less than 0.1 (see §3.6) and the corresponding effect on the transit light curve shape is therefore negligible. We also fixed the quadratic limb darkening parameters $u_1 = 0.3442$ and $u_2 = 0.2006$. These are the values predicted by the `ldtk` (Parviainen et al., 2015) package using the stellar temperature, [Fe/H], and $\log g$ reported in Table 3.2. `ldtk` uses the library of high-resolution synthetic spectra from Husser et al., 2013, which are based on the PHOENIX stellar atmosphere code and includes synthetic spectra for stellar temperatures as low as 2300 K. We list the priors for our transit model and GP hyperparameters in Table 3.3. Although we used uniform priors for most parameters, we placed a Gaussian prior on R_* and a/R_* based on the stellar mass, radius, and planetary orbital period from S20. We used the `PyMC3` package (Salvatier et al., 2016) to sample the posterior distribution of our model with No U-Turn Sampling (NUTS), with four parallel chains run with 5000 burn-in steps and 3000 posterior sample draws. We confirmed that the chains evolved until the Gelman-Rubin statistic values are < 1.01 for all parameters. The posterior distributions of each parameter are summarized in Table 3.3. The detrended transit light curves and their best fit models are shown in Figure 3.1.

TTV model fits to transit midtimes that have multi-modal or asymmetric posteriors can introduce biases into the retrieved dynamical parameters (Judkovsky et al., 2023). We therefore examined the posterior distributions of the individual TESS midtime parameters to determine whether or not all of the individual transits were detected at high enough significance to yield a unimodal and approximately normally distributed transit midtime constraint. We found that all of the observed TESS transits for both planets satisfied these criteria.

WIRC

We fit the WIRC light curves using `exoplanet` with a combined systematics and transit model. Our systematics model for each night includes a linear combination of comparison star light curve weights, an error inflation term added in quadrature to the flux errors, and a linear slope. We also tested systematics models with linear combinations of weights for the target centroid offset, PSF width, airmass, and local sky background as a function of time. We compared the Bayesian Information Criterion (BIC, Schwarz, 1978) for all possible combinations of these systematic noise parameters using the same framework as Pérez-González et al., 2024. We found that the model that produced the lowest BIC value included weights for the target PSF width and airmass for TOI-1266 b and c on UT 2022-02-28 and UT 2022-

03-10, respectively, while our UT 2022-06-06 observation of TOI-1266 c preferred only the PSF width as an additional detrending parameter. The transit midtime posteriors for the UT 2023-04-07 observation of TOI-1266 b and UT 2022-06-12 and UT 2023-12-09 observations of TOI-1266 c were not well constrained by the data due to poor weather and lack of baseline coverage, so we excluded them from our analysis. During our UT 2022-02-28 observation we experienced variable cloud cover and multiple flux drops $> 50\%$ of their peak value, and we excluded images with relative flux decrease $> 20\%$ for this night.

We fit the WIRC transits jointly with the phased TESS transit profile from stacking all transits using their best fit individual midtimes and removing the best fit GP model of out-of-transit variability. We used the same model framework as in Greklek-McKeon et al., 2023, with a wide uniform prior of ±5 hours on the transit times. We used the same transit shape parameter priors as in §3.4, summarized in Table 3.3. As before, we used `ldtk` to calculate the J band quadratic WIRC limb darkening parameters $u_1 = 0.167$ and $u_2 = 0.164$, and held them fixed in our fits. We explored the parameter space with the NUTS sampler in `PyMC3` for 2000 tune and 2000 draw steps, and confirmed that the chains have evolved until the Gelman-Rubin statistic values are < 1.01 for all parameters. Our measured transit times are listed in Table 3.4 in the Appendix, and the final transit light curves are shown in Figure 3.2.

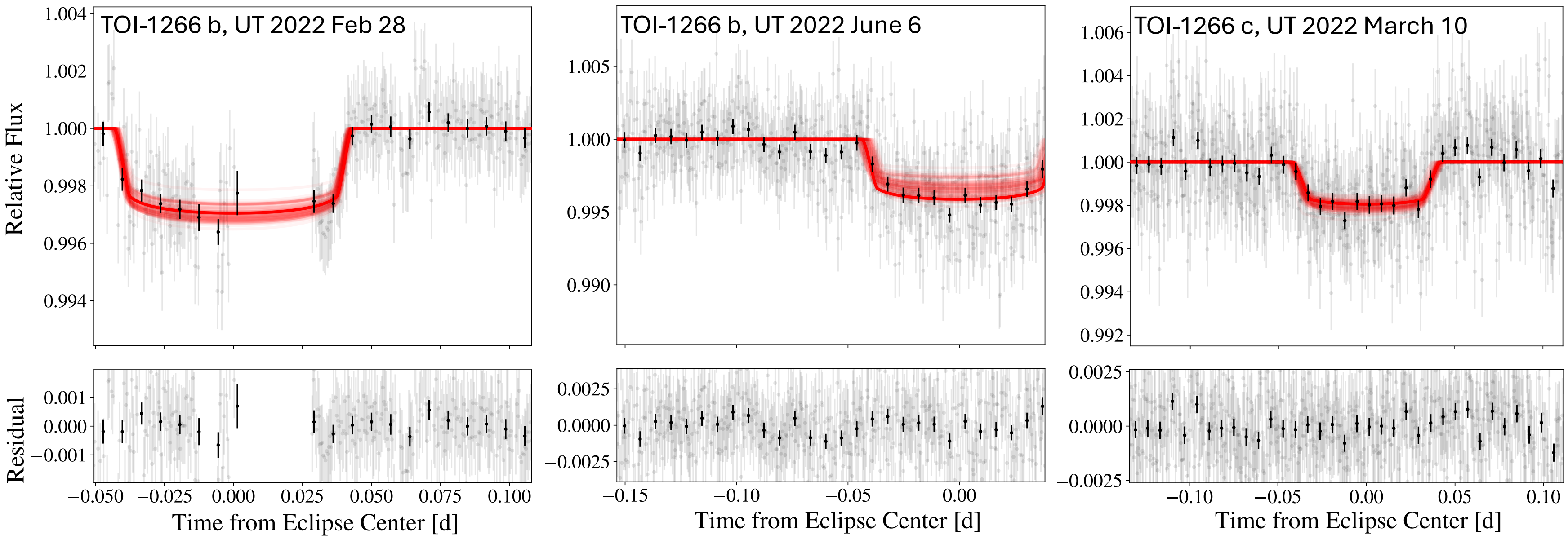

Figure 3.2 Detrended WIRC light curves for TOI-1266 b night 1 (left) and 2 (middle) and TOI-1266 c (right). The best fit transit models are overplotted as red lines, with red shading to indicate the 1σ uncertainties.

MuSCAT imagers and Sinistro

We fit the MuSCAT series (MuSCAT + MuSCAT3) and Sinistro observations with a similar procedure as described in §3.4. Since the MuSCATs + Sinistro ground-based observations are not obtained with a beam-shaping diffuser, the noise properties of the light curves are different from the WIRC observations. Consistent with previous MuSCAT and Sinistro transit light curve analysis (e.g., Kuzuhara et al., 2024; Cointepas et al., 2024) and our TESS analysis, we used a Matern-3/2 GP kernel from `celerite2` to model residual flux variability, with σ and ρ parameters corresponding to the amplitude and timescale of variability. We let σ vary for each band within each night, while sharing ρ across bands under the assumption that the timescale of the time-correlated noise is common among all bands for a given night. We tested MuSCATs + Sinistro systematics models for each night that also included linear combinations of weights for the target x and y detector positions, total centroid offset, PSF width, and airmass, but found that a pure transit+GP model performed better for all nights.

The MuSCAT and MuSCAT3 observations include simultaneous photometry in three or four bands, respectively, and each night has a different transit coverage fraction. We initially allowed R_p/R_* to vary for each band and each night, fitting for individual t_0 values shared across all bands for a given night, with all other transit shape parameters shared across bands and nights. We fit the MuSCATs + Sinistro transits jointly with the phased TESS transit profile, used the same priors on the transit parameters as in our WIRC modeling, and fixed the quadratic limb darkening parameters to the predicted values from `ldtk` for each bandpass. For g, we use $u_1 = 0.5976$ and $u_2 = 0.1739$, for r we use $u_1 = 0.5674$ and $u_2 = 0.1542$, for i we use $u_1 = 0.3900$ and $u_2 = 0.1957$, and for z_s we use $u_1 = 0.3064$ and $u_2 = 0.1924$. We explored the parameter space with the NUTS sampler in PyMC3 for 2000 tune and 2000 draw steps and verified that the Gelman-Rubin statistic values are < 1.01 for all parameters. We then determined the detection significance of the R_p/R_* constraint in each band on each night, and excluded any light curves where R_p/R_* is consistent with 0 within 3σ. This ensures that we only include strongly detected transits in our subsequent analysis. This eliminated most partial transit observations and some light curves in g' or r' band with higher noise levels. We then repeated the same fitting procedure with a single R_p/R_* parameter shared across bands for a given night in order to account for possible changes in transit depth (see §3.4) and to obtain a final set of transit mid-times. As before, we confirmed that all transit mid-times had normally distributed posterior distributions. Our measured transit times are provided in Table 3.4 in the Appendix, and the final transit light curves for TOI-1266 b and c are shown in Figures 3.3 and 3.4, respectively.

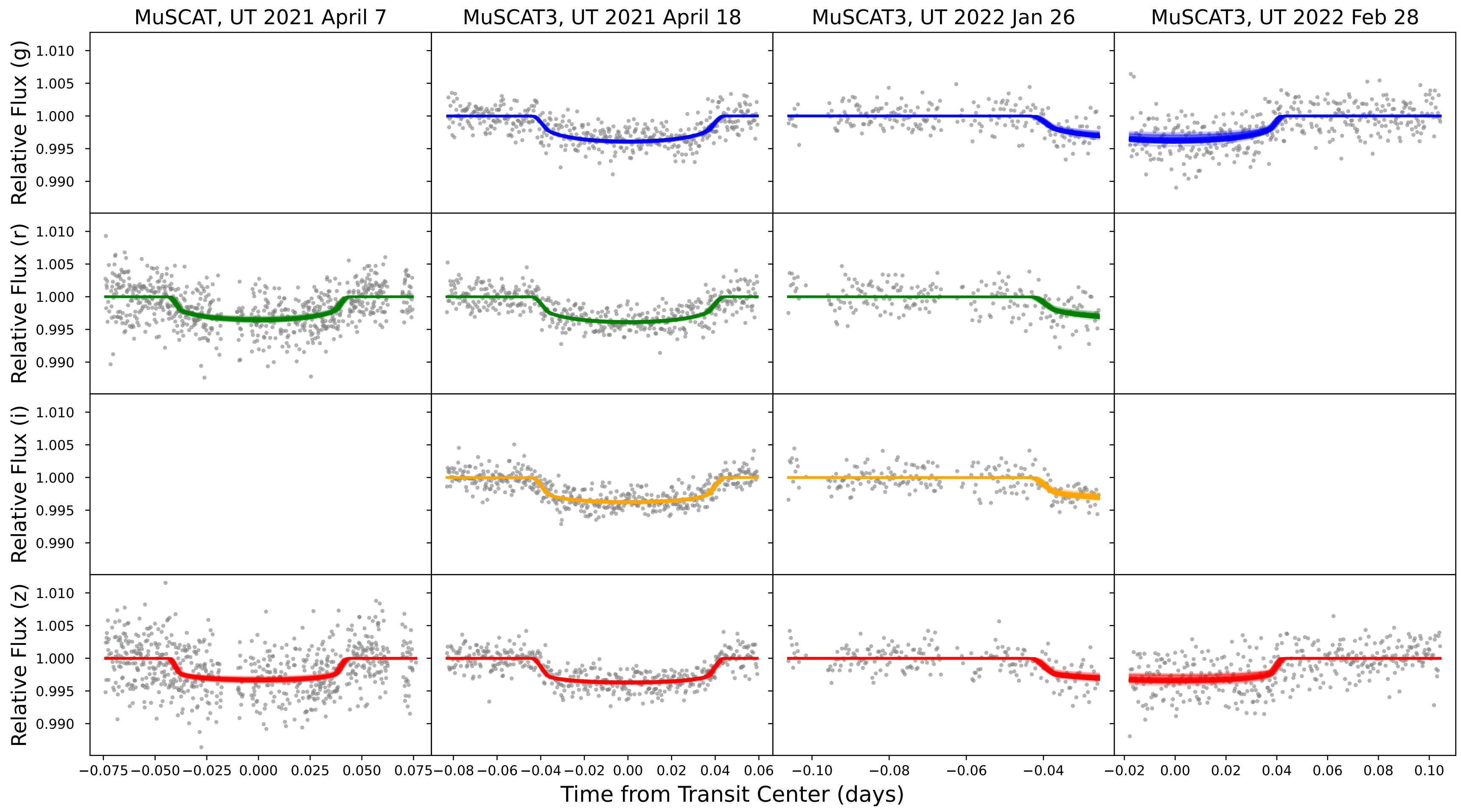

Figure 3.3 Detrended MuSCAT and MuSCAT3 light curves for TOI-1266 b. Colored lines are transit light curve models generated using 100 random draws from the posterior distribution for each bandpass.

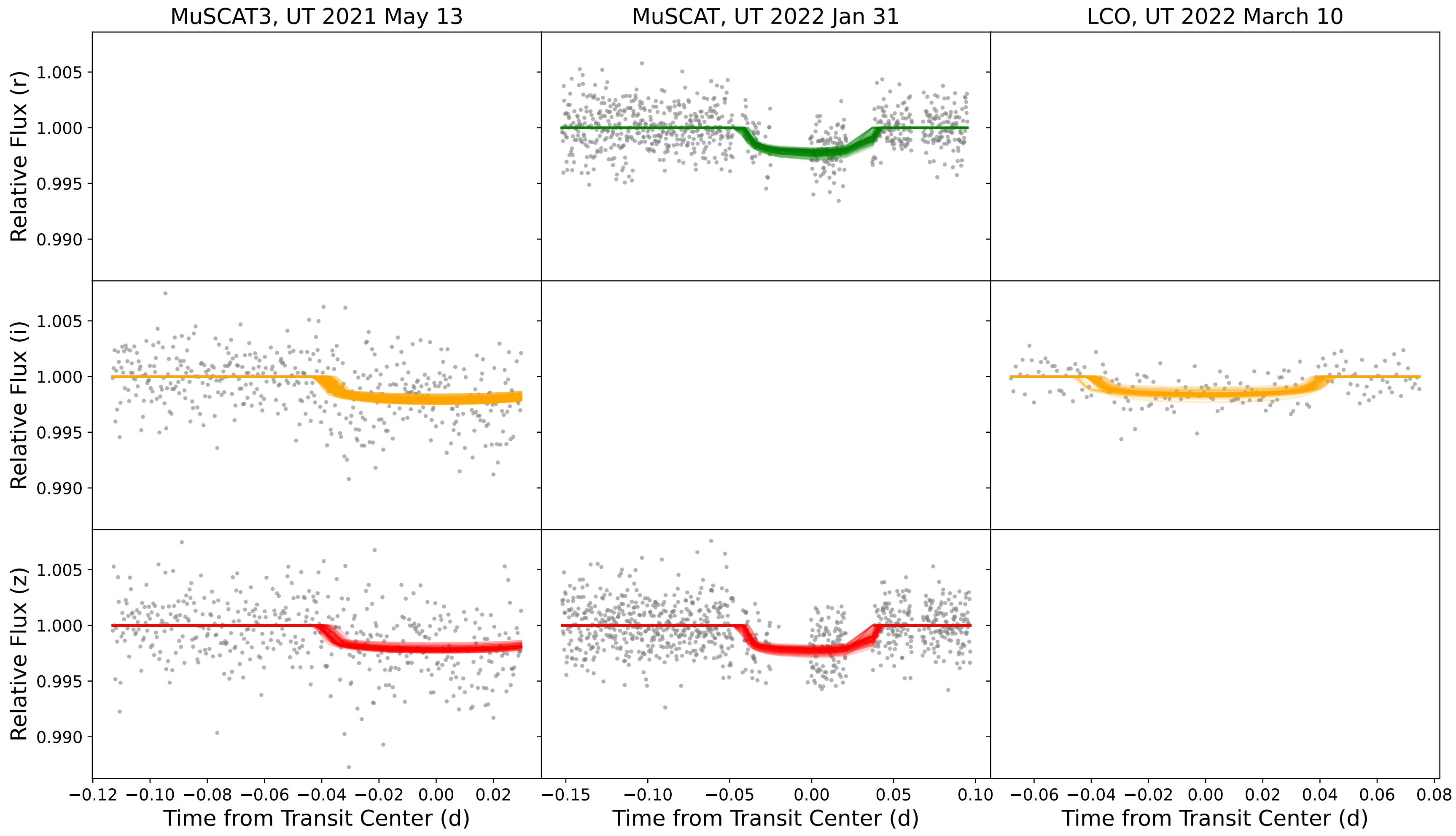

Figure 3.4 Detrended MuSCAT, MuSCAT3 and Sinistro light curves for TOI-1266 c. Colored lines are transit light curve models generated using 100 random draws from the posterior distribution for each bandpass.

Planetary Radius Analysis

C24 reported significant variation (3.5σ) in the transit depth of TOI-1266 c, and smaller variation in the transit depth of TOI-1266 b (1.9σ) between the TESS PM and EM observations. These apparent transit depth changes were confirmed by four additional ground-based transits near the TESS PM and EM observations, and were not accompanied by changes in the transit duration, which could have been indicative of orbital variability on short timescales.

C24 investigated many possible explanations for the transit depth discrepancies, including variable flux dilution, orbital precession, residual artifacts from different TESS extraction methods, changes in stellar activity, and stochastic effects in the TESS data. C24 performed an exhaustive analysis on these possible causes of the transit depth discrepancies, and we refer the reader to Cloutier et al., 2024 for further details. They concluded that the depth discrepancy is likely caused in part by a small increase in stellar activity and the presence of bright plages from the TESS PM to EM epochs, and by stochastic effects affecting the measurement accuracy of TOI-1266 c's transit depth in the PM data.

Motivated by this unexpected change in transit depth from TESS PM to EM data, we perform modeling of the TESS, WIRC, MuSCAT imagers, and Sinistro photometry assuming different transit depths for each epoch to further investigate this behavior. We model the TESS data with the procedure described in §3.4, including separate transit depths for the PM, EM, and SEM data. We model the WIRC and MuSCATs + Sinistro data with the procedures described in §3.4, and use a separate transit depth parameter for each night of observation per planet. The resulting transit depths from this analysis are shown in Figure 3.5. We reproduce the observed discrepancies between TESS PM and EM data and the WIRC observations that originally confirmed the discrepancy as reported in C24. However, we find that the inclusion of additional WIRC transits, the MuSCATs + Sinistro transits, and the new TESS SEM data weaken the statistical significance of the original discrepancy between TESS PM and EM. The depth of TOI-1266 c in the TESS PM data is now only 2.7σ from the average measured depth, mostly driven by the addition of two ground-based transits with observed depths close to the PM value. Likewise, the discrepancy for TOI-1266 b from the average observed depth decreases to 0.9σ – mostly driven by the lower observed TESS SEM depth, which is consistent with the PM data.

We conclude that there is no statistically significant discrepancy in the TESS PM

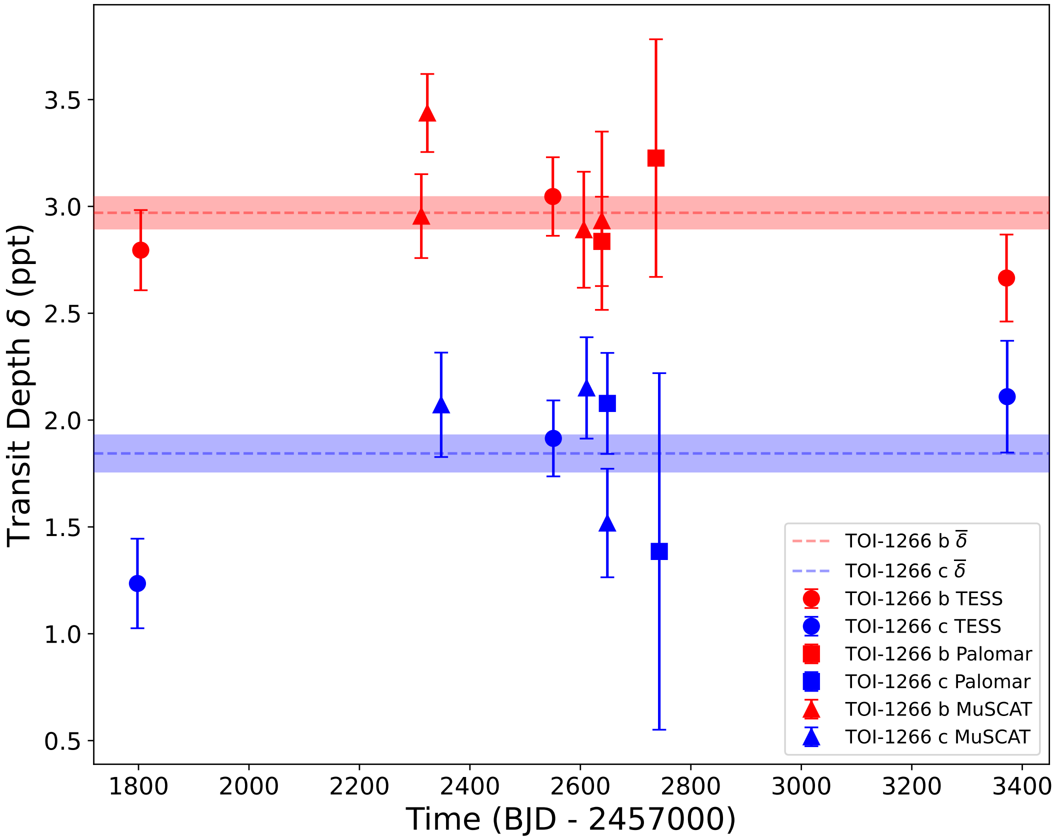

Figure 3.5 Observed transit depths of TOI-1266 b (blue) and c (red), including TESS PM, EM, and SEM data (circles), WIRC data (squares), and MuSCATs + Sinistro data (triangles). The error-weighted average transit depths are shown with dashed lines along with their associated 1σ uncertainties (shaded region).

transit depths relative to the remaining TESS and ground-based data, and that the dispersion in measured transit depths is consistent with stochastic variations — though we cannot rule out the transit depth variability due to evolution of stellar plage coverage described in C24. We therefore assume that the transit depths for each planet are drawn from one underlying distribution, but report planetary radii and uncertainties based on the error-weighted average transit depths.

3.5 TTV Modeling

Three previous studies of the TOI-1266 system (S20, D20, C24) have searched for evidence of TTVs. One of the discovery papers, S20, fit individual transit times from the TESS PM data and two ground-based transits using the `TTVOrbit` module within `exoplanet` and found no evidence for statistically significant TTVs. D20 reported marginal evidence for TTVs using the same TESS PM data examined by

S20. C24 extended this analysis to the TESS PM and EM data along with several additional ground-based transits and also concluded that there was no compelling evidence for TTVs. C24 then used the lack of TESS TTVs in TOI-1266 b to place upper limits on the combined eccentricities of TOI-1266 b and c (e.g., Hadden, 2019).

The addition of the TESS SEM data nearly doubles our observational baseline and allows us to detect TTVs for planet b at high significance. The main oscillation period of this TTV signal is approximately twice the baseline of the data examined in previous studies and still only a fraction of the predicted TTV super-period for TOI-1266 b and d ($P_{TTV} \simeq 2000$ d, see §3.5 and Equation 5 of Lithwick et al., 2012). This explains the previous non-detections: with data covering less than half of the TTV super-period, this signal can be effectively removed by changes to the linear ephemeris of planet b in the TTV retrieval.

In the following sections we outline our analysis of these TTVs, which exhibit a long-term trend for TOI-1266 b that is driven by near-resonant commensurability with a third external planet, and short-term chopping signatures for both TOI-1266 b and c. The low-significance TTV detection reported in D20 is likely the same second-order short-term chopping signature we detect here. D20 ascribed this signal to near-resonant 2-planet interactions between TOI-1266 b and c, but we now understand it to be part of a more complex 3-planet system in which the inner and outer planets are near the 3:1 mean-motion commensurability.

The 2-Planet Case

We initially attempted to fit the set of transit times summarized in Table 3.4 with a 2-planet model, since there are only two transiting planets identified in the system and the RV signal at ~32.3 days reported by C24 is characterized as a tentative detection. We used the `TTVFast` package to model the observed transit times in Table 3.4 in the Appendix. `TTVFast` (Deck et al., 2014) is a computationally efficient *n*-body code that uses a symplectic integrator with a Keplerian interpolator to calculate transit times in multi-planet systems. The modeled transit times are a function of the planetary masses and orbital elements relative to a reference epoch, which we chose to be $T_0 = 1689.0$ (BJD - 2457000) – shortly before the first transit of TOI-1266 observed by TESS.

In our TTV modeling, we fixed the planetary orbital inclinations (i) to 90° because our transit fits show a low mutual inclination between planets b and c and are very close to edge-on (i_b = 89.12 ± 0.08, i_c = 89.17 ± 0.04). The difference between M_p and $M_p\sin(i)$ is $< 0.01\%$ for both transiting planets. The TTV solution is second-order in mutual inclination, with the strength of the planet-planet gravitational interaction and corresponding TTV amplitudes diminishing rapidly as the planetary mutual inclination increases (Nesvorný et al., 2014a; Hadden et al., 2016). For a purely edge-on orbital inclination the longitude of the ascending node (Ω) becomes undefined, so we arbitrarily set it to 90° for both planets.

Our 2-planet TTV model has ten free parameters in total. These include: the planet-to-star mass ratios, Keplerian orbital periods, mean anomalies reparamaterized with the time of first transit (t_0), and the planetary eccentricities and longitudes of periastron. We reparameterized the latter two quantities as $\sqrt{e}\cos(\omega)$ and $\sqrt{e}\sin(\omega)$ in order to mitigate the degeneracy between e and ω in our fits while retaining an effective uniform prior on e (Eastman et al., 2013). The orbital periods, mean anomalies, eccentricities, and longitudes of periastron are osculating orbital elements defined at the TTV model start time T_0. We fit this model to the data using the affine invariant Markov chain Monte Carlo (MCMC) ensemble sampler `emcee` (Daniel Foreman-Mackey et al., 2013), and chose wide uniform priors for all parameters: U(-1, 1) for $\sqrt{e}\cos(\omega)$ and $\sqrt{e}\sin(\omega)$, $U(0, 15M_\oplus)$ for the planetary masses sampled in M_p/M_* space, $U(P_b$-0.1, P_b+0.1) and $U(P_c$-0.2, P_c+0.2), and $U(t_{0_b}$-1.0, t_{0_b}-1.0) and $U(t_{0_c}$-2.0, t_{0_c}-2.0) from the planetary orbital period and t_0 values reported in C24.

We initialized the MCMC fit with 2000 walkers (200 per free parameter) randomly distributed across the full prior volume in order to ensure that our MCMC analysis located all of the high likelihood regions of parameter space. Although nested sampling algorithms utilize a similar approach, they can be very computationally expensive for TTV fits due to the large number of live points required to fully map the large prior volume (Higson, Handley, Mike Hobson, et al., 2019; Higson, Handley, Michael Hobson, et al., 2019). Our MCMC walkers achieve a comparable result with fewer function calls. When proposing new steps for the walkers we randomly selected the DEMove (Nelson et al., 2014) or DESnookerMove[1] (Braak et al., 2008) at a rate of 80% to 20%, as recommended by Daniel Foreman-Mackey et al., 2019 for potentially multi-modal posterior distributions. This approach is advantageous for TTV fits because TTV model parameters are often degenerate and strongly correlated (e.g., in mass and eccentricity, Lithwick et al., 2012), their

---

[1] https://emcee.readthedocs.io/en/stable/user/moves/emcee.readthedocs.io

posterior distributions can be non-Gaussian or multi-modal, and the range of parameter combinations that produce a good fit to the observed data are often a very narrow subset of the total prior volume even for well-motivated but non-restrictive priors (e.g., Dai et al., 2023). This makes it difficult for conventional MCMC walker evolution methods to identify and map the region of posterior space near the true maximum of the log-likelihood distribution when starting from a static initial guess or the output of a least-squares minimization, as is commonly done in exoplanet modeling.

We initially ran the sampler for 10000 steps in order to allow the 2000 walkers randomly distributed across the prior volume to identify the highest likelihood regions of posterior space. We then sorted the walkers by increasing likelihood and retained the walkers with median likelihoods in the top 20% from the last 100 steps. Finally, we ran the remaining walkers for 10^6 steps. We confirmed that the length of the MCMC chain was at least 10 autocorrelation lengths for all parameters. We plot 100 random draws from the resulting TTV posterior distribution and compare them to the observed TTVs in Panels 1 and 2 of Figure 3.6.

The 2-planet TTV retrieval identifies two distinct families of solutions – neither of which are a satisfactory fit to the data. One family of solutions prefers very low mass values for both planets, with 95% upper limits of $M_b < 0.05M_\oplus$ and $M_c < 0.45M_\oplus$, and high eccentricity values, $e_b \simeq 0.15$ and $e_c \simeq 0.4$. This set of models (shown in light blue in Figure 3.6) is better at reproducing the long-term TTV variability revealed in the TESS SEM data, but does not accurately model the TESS PM data and struggles to reproduce the short-timescale chopping TTV signature. Unlike the dominant long-term TTV trend with a super-period defined by the proximity of the planetary orbital periods to resonance (Lithwick et al., 2012), the short-timescale chopping signature super-imposed on this trend is defined by the planetary mass and eccentricity vectors (Deck et al., 2015). The other family of solutions (shown in light gray in Figure 3.6) prefers lower planetary eccentricities $e_b \simeq 0.12$ and $e_c \simeq 0.21$ and a very large mass for TOI-1266 c ($M_c = 13.2 \pm 4.1M_\oplus$) that is inconsistent with the RV mass constraint reported in C24, and cannot reproduce the long-term TTV trend revealed by the TESS SEM data.

In general, any isolated TTV model suffers from inherent degeneracies because it constrains a pair of canonical action/angle coordinates (e and ϖ) and not the individual planetary eccentricities. Recent work has shown that orbital solutions with different planetary ϖ values and therefore TTV phases can produce high

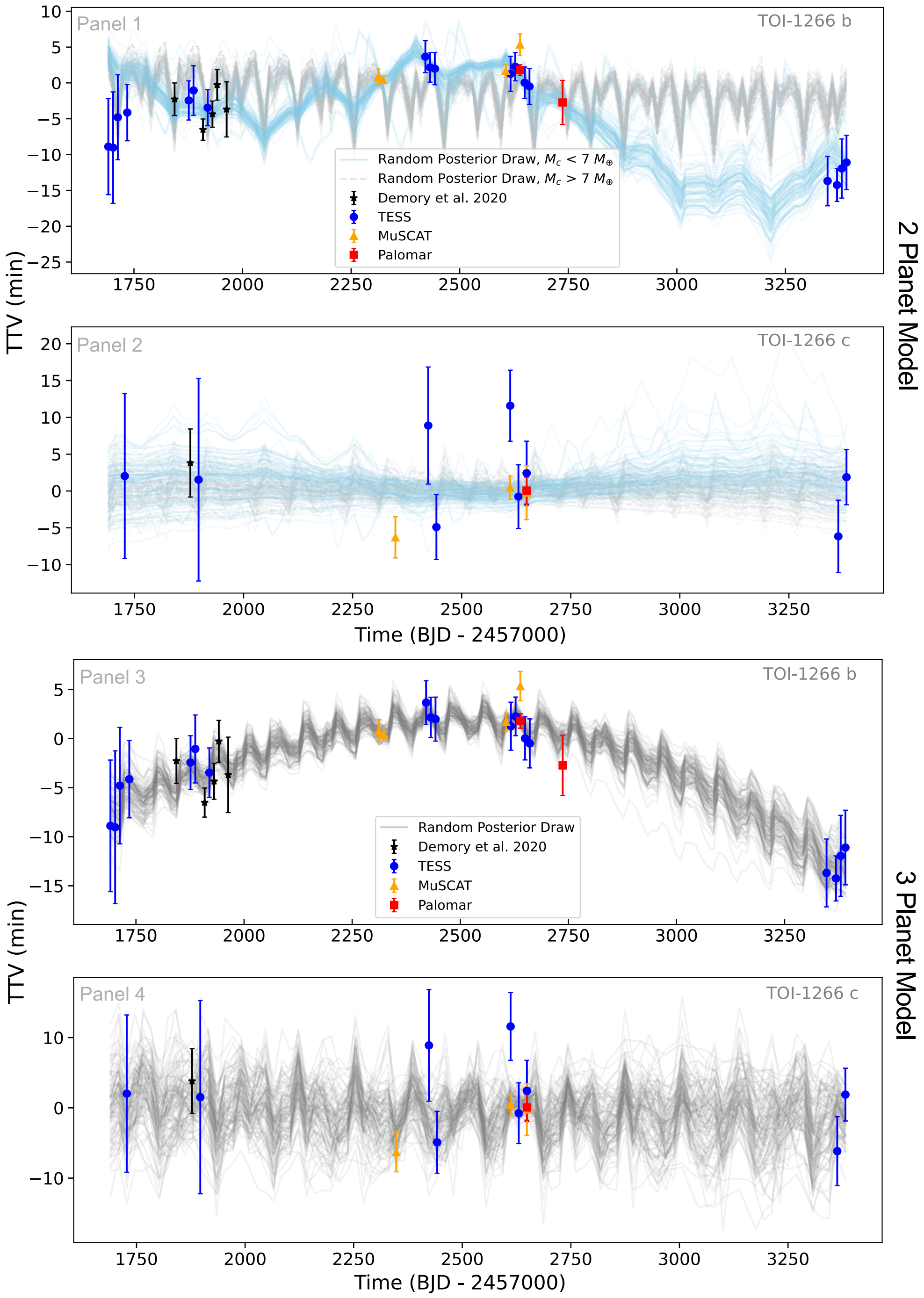

Figure 3.6 TTVs from TESS (blue circles), WIRC (red squares), and MuSCATs + Sinistro (yellow triangles) for TOI-1266 b (Panels 1 and 2) and TOI-1266 c (Panels 3 and 4) with 100 random posterior draws from our TTV model. Panels 1 and 2 show our 2-planet models with posterior draws from the samples with low M_c and higher eccentricities shown in light blue, while those with higher M_c and lower eccentricities are shown in light gray. Panels 3 and 4 show 100 random posterior draws from our 3-planet TTV model in dark gray. One TESS and one WIRC transit time each for TOI-1266 c are included in TTV fitting but omitted from these plots for clarity as they have timing uncertainties > 15 min.

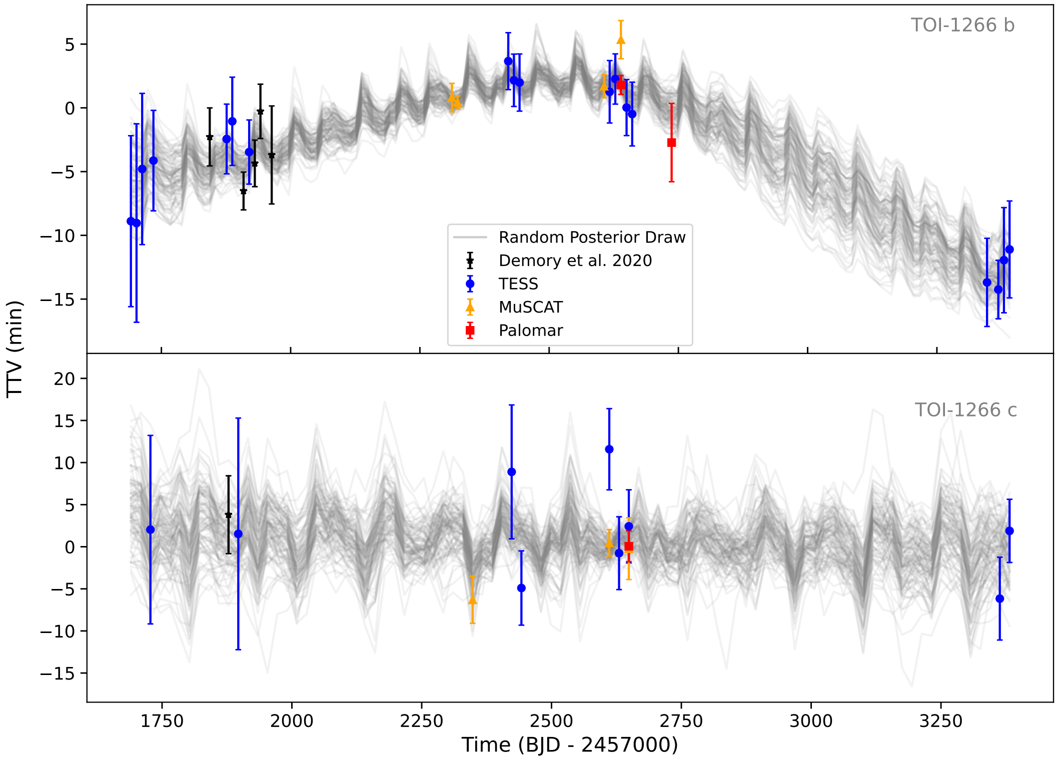

Figure 3.7 The same as Figure 3.6, with 100 random posterior draws from our 3-planet joint TTV+RV model (gray curves).

eccentricity variants of the same TTV signal for a given system (Goldberg et al., 2023; Choksi et al., 2023). But in this case the different families of eccentricity solutions do not produce consistent TTV predictions for different combinations of M, e, and ϖ. Each of these solutions can reproduce some of the observed TTV data, but neither provide a good fit to the entirety of the observations, and both are in tension with the planetary masses and eccentricities reported in C24 from RV observations.

The 3-Planet Case

Motivated by the candidate RV planet reported in C24, we used the same framework described in §3.5 to fit the TTV data with a 3-planet model. This increased the total number of free parameters in the fit from 10 to 15. Consistent with the 2-planet fits, we fix $i_d = \Omega_d = 90$ for simplicity. Since the properties of the exterior planet candidate are unconstrained by transit photometry, we performed a brute force search with the same priors as described in §3.5 for TOI-1266 b and c. We used wider priors for the orbital period of the third planet, with an orbital period range of 19 to

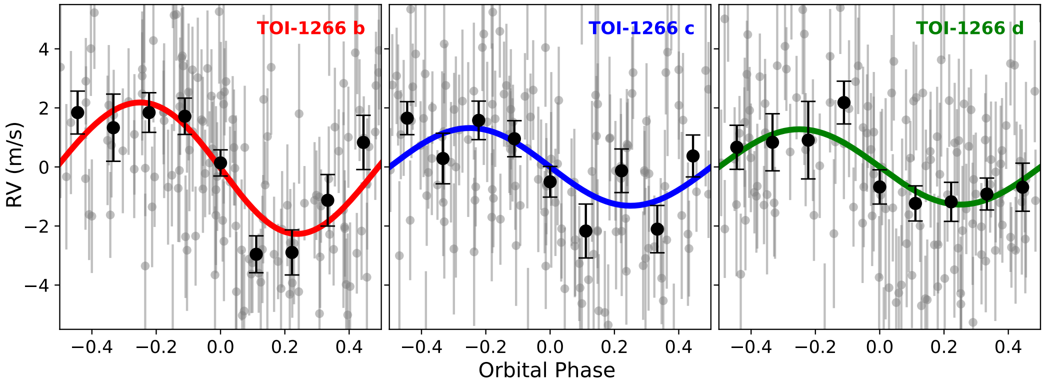

Figure 3.8 Phase-folded RV data with best fit model results from our joint TTV+RV fit for TOI-1266 b (left), TOI-1266 c (middle), and TOI-1266 d (right).

58 days and a corresponding t_{0_d} range from the simulation start time T_0 to T_0 + 58 days. This allows the third planet's orbit to be anywhere from immediately exterior to TOI-1266 c to just beyond the 3:1 commensurability with TOI-1266 c, including the ~32-day period reported for the tentative planet candidate in C24.

We ran the MCMC retrieval utilizing the same general approach as in §3.5. For this fit, we found that fewer walkers were required to reach more than 10 autocorrelation lengths for all parameters. We therefore used 600 walkers and ran them for a total of 2×10^5 steps. We then selected the most likely 50% of walkers and ran them for 10^6 additional steps. We verified that the number of steps in the resulting chain was at least 10 times the shortest parameter autocorrelation length. The posterior from this blind search strongly favors a planet near the 3:1 commensurability with the inner planet TOI-1266 b, corresponding to an orbital period of $32.509^{+0.061}_{-0.059}$. The ΔBIC value for the 3-planet TTV model compared to a 2-planet model is <-10, indicating very strong preference for the 3-planet case (Raftery, 1995).

Results from our 3-planet TTV retrieval are shown in Panels 3 and 4 of Figure 3.6. The new 3-planet model is capable of simultaneously describing both the long-term TTV oscillation that samples part of the super-period of TOI-1266 b, and the short-term chopping signal for planets b and c. The fitted orbital period for TOI-1266 d from our TTV modeling is larger than the reported value from C24 by 3.2σ (see §3.6 for a discussion on the source of this discrepancy), although our TTV model is consistent with the RV modeling of C24 for the planetary masses and eccentricities. We summarize the prior and posterior distributions for all planets from our 3-planet TTV modeling, the RV modeling described in §3.6, and the TTV+RV joint modeling described in §3.6 and in Table 3.3.

For completeness, we also consider a scenario in which the third planet has an orbital period intermediate between that of TOI-1266 b and TOI-1266 c. We fit this model to the data using the same brute-force TTV retrieval as above, but find that there are no combinations of parameters that can adequately describe the complete set of observations – similar to the results of the 2-planet model fit in §3.5. Lastly, we consider a case in which the third planet is located interior to TOI-1266 b instead of exterior to TOI-1266 c. We find that the posterior distribution for this fit also prefers a third planet near the 3:1 commensurability with TOI-1266 b, corresponding to an orbital period near 3.6 days. The overall quality of this fit is similar to that of the external 3:1 scenario shown in Panels 3 and 4 of Figure 3.6.

We used several factors to rule out the interior 3:1 scenario as the true solution. First, we phased the TESS photometry up using the predicted individual transit times from the TTV model in order to search for transits from planet d, but we did not find any transit signal. The short orbital period of planet d in this model means that if it is not transiting, it must have a mutual inclination of $> 2.6^\circ$ relative to TOI-1266 b – much higher than the mutual inclination between TOI-1266 b and c (0.04°). Population-level studies of mutual inclinations in other compact multi-planet systems (e.g., Lissauer et al., 2011) suggest that this degree of misalignment is unlikely. Additionally, C24 used RV observations to rule out the presence of any planets $\gtrsim 1 M_\oplus$ with orbital periods at 3.6 days. The preferred TTV mass for a planet at this location is $2.3 \pm 1.3 M_\oplus$, which would have a ~84% recovery rate in the RV data. This leaves the exterior 3:1 solution as the more plausible explanation for the observed TTV signal. This conclusion is additionally supported by C24's RV analysis, which independently reported the detection of a candidate planet with an orbital period very close to 32 days, though slightly below our TTV-based constraints ($P_{d_{RV}} = 32.340 \pm 0.099$ d, $P_{d_{TTV}} = 32.706^{+0.057}_{-0.049}$ d).

In the section below, we jointly model the TTV and RV data in order to obtain improved constraints on the orbital parameters of all three planets and to reconcile the slight tension between orbital periods for the planet candidate in TTV versus RV data.

3.6 TTV and RV Joint Modeling

RV-Only Modeling

Before performing a joint fit on the available TTV and RV data, we first sought to independently reproduce the RV results reported in C24 using our `TTVFast` retrieval framework, which utilizes an n-body integrator rather than Keplerian orbital models to predict the stellar RV at a specified time. We constructed our RV-only `TTVFast` model using the same 15 free parameters described in §3.5 to model the planet signals, along with an additional seven free parameters to describe non-planetary structure in the RV data. These include a scalar jitter term σ_{RV} added in quadrature to the RV observation uncertainties, the systematic RV γ_{RV}, and the same Gaussian Process (GP) regression model used in C24 to fit the stellar activity signal. The power spectral density of this GP kernel is the superposition of two damped simple harmonic oscillators, and it is therefore well-suited to modeling stellar activity signals. The GP model consists of five free parameters: Σ, P_{rot} Q_0, dQ, and f, corresponding to the standard deviation of the process, the primary variability period, the quality factor of the secondary oscillation, the difference in quality factor for the two oscillation modes, and the fractional amplitudes of primary and secondary modes, respectively. C24 trained the GP on the Hα time series of TOI-1266, which exhibits a periodic signal at ~44.6 d attributed to stellar rotation. We adopted Gaussian priors for the four GP hyperparameters that were trained on the Hα timeseries (P_{rot}, Q_0, dQ, f) from Table 4 of C24, with the same wide uniform priors on the other RV model parameters as in C24.

We use `emcee` to fit our `TTVFast` model to the RV data from Table 2 of C24, with the same fitting procedure, number of walkers, and step numbers as in §3.5, though we impose Gaussian priors on the orbital period and t_0 values from our TTV analysis because these are poorly constrained by the RV data and typically assigned Gaussian priors from transit fits where available. We ensure that the total number of steps is more than 10 times the autocorrelation length of all parameters. We find that our TTVFast model agrees with the planetary masses, orbital parameters, and RV noise model parameters reported in C24 at better than 1σ for all parameters and has similar uncertainties ($< 10\%$ difference).

Joint TTV + RV Modeling

Next, we performed a joint fit of the TTV observations from Table 3.4 and the RV observations from C24 using `TTVFast` and `emcee`, with the same 22 free parameters as described in §3.6. We initialized the 15 planetary parameters close to the location of the best fit solution from the 3-planet TTV fit, and the 7 RV parameters close to the best fit solution from the 3-planet RV fit. We sampled the posterior distribution with DEMCMC for 8×10^5 steps, which corresponded to > 10 autocorrelation lengths for all parameters after discarding the first 10^5 steps as burn-in. We summarize the prior and posterior distributions for all parameters in Table 3.3.

This new joint fit resolves the previous tension between the orbital periods for the third planet candidate from the separate TTV and RV fits, with a best fit solution that is in good agreement with both the TTV and RV data. This confirms the existence of a third planet in the TOI-1266 system, and from here on we refer to the third non-transiting planet as TOI-1266 d. The joint fit model results for the TTV data are shown in Figure 3.7, while the RV model results are shown in Figure 3.8. We include corner plots for the final planetary mass and eccentricity distributions along with orbital period and t_0 distributions in the Appendix.

The final planetary mass constraints from the joint fit are consistent with those reported in D20, S20, and C24. Our new joint fit decreases the fractional mass uncertainties for TOI-1266 b and c by 1% and 5%, respectively, relative to the RV-only constraints from C24. The joint model also prefers a slightly larger mass for TOI-1266 c and a slightly smaller mass for TOI-1266 d than reported in C24, making all three planets more uniform in mass. This intra-system mass uniformity is consistent with previously reported results for Kepler multi-planet systems ("peas-in-a-pod"; e.g., S. Millholland et al., 2017; Weiss et al., 2018; S. C. Millholland et al., 2022; Otegi et al., 2022; Goyal et al., 2023; Goyal et al., 2024; Rice et al., 2024). The dispersion in planet masses is also consistent with the level of intra-system mass uniformity exhibited by the subset of Kepler multi-planet systems that are in resonance, which typically display even greater mass uniformity (Goldberg et al., 2022).

The joint TTV-RV model fit also results in large improvements in the planetary eccentricity constraints relative to the RV-only fit. Notably, the joint fit indicates that TOI-1266 b and d must have statistically significant nonzero eccentricities. This is due to the proximity of TOI-1266 b and d to the 3:1 resonance and the detection of a short-term chopping signal superimposed on the long-term TTV trend of TOI-1266 b. This chopping signal is strongly dependent on the masses and eccentricities of the planets driving the main TTV super-period (b and d). Unfortunately, we have no TTV observations for TOI-1266 d and the RV observations alone cannot constrain the planetary eccentricities to better than 0.1.

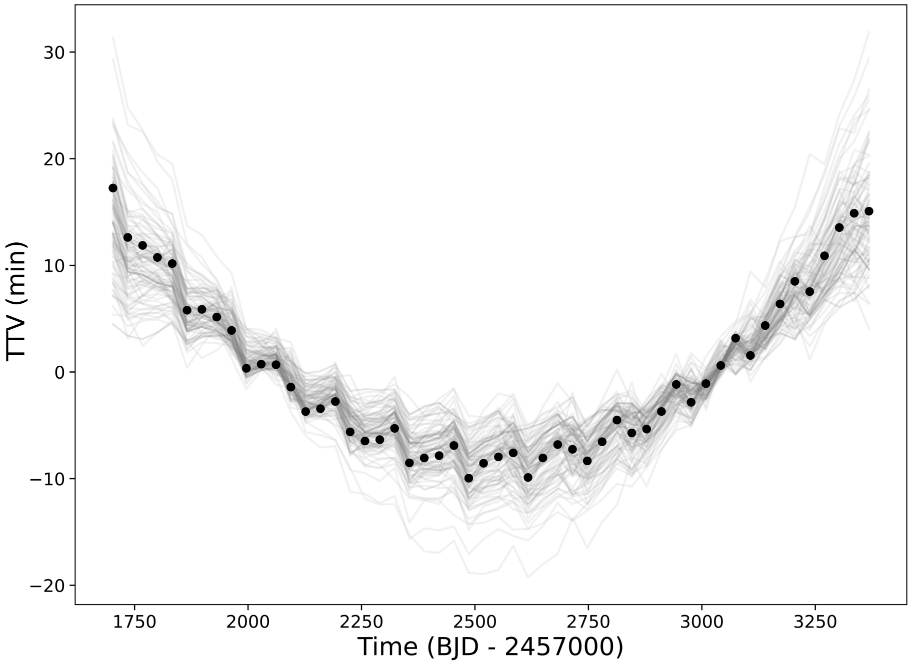

Figure 3.9 Predicted TTVs for TOI-1266 d from our best fit TTV+RV joint model (black points) spanning the same time range as in the previous TTV plots, with 100 random draws from the posterior distribution (gray). The TTV spread of ~ 30 minutes could prohibit the detection of shallow transits in a grazing configuration.

This means that the TTV+RV solution is ambiguous as to the true eccentricity of TOI-1266 d, and there are two families of solutions for TOI-1266 b that depend on the eccentricity of d. If e_d is small (< 0.02), e_b must be larger ($e_b = 0.061^{+0.021}_{-0.017}$), while if e_d is larger (> 0.02), e_b is smaller ($e_b = 0.025^{+0.025}_{-0.015}$). The distribution of e_b therefore has two peaks. The bulk of the posterior volume prefers larger e_b values while e_d is consistent with 0, but there is a second peak where e_d is large and e_b is smaller but still prefers a nonzero eccentricity. Another possible but less likely scenario is where both planets simultaneously have moderate eccentricities $\simeq 0.03$. The joint fit retrieval rules out solutions in which $e_d + e_b < 0.03$, and constrains $e_b + e_d = 0.076^{+0.029}_{-0.019}$. These results are visualized in Figure 3.11. The fact that the inner planet in this compact multi-planet system is eccentric has significant implications for the dynamical history and long-term evolution of this system, which we discuss further in §3.7.

Table 3.3 Priors and posteriors for TOI-1266 model parameters.

Parameter	Prior	Posterior		
		TESS systematics parameters		
Mean flux, f_0 (ppt)	$\mathcal{U}(-\infty, \infty)$	0.000035 ± 0.000026		
Log jitter, $\ln s^2$ (ppt^2)	$\mathcal{U}(-18, 2)$	-14.54 ± 2.04		
σ (ppt)	$\mathcal{U}(10^{-7}, 10^{-2})$	$0.000298^{+0.000019}_{-0.000017}$		
ρ (days)	$\mathcal{U}(10^{-3}, 10^{2})$	$0.644^{+0.078}_{-0.071}$		
		RV systematics parameters		
$\ln \Sigma$ (m/s)	$\mathcal{U}(-3, 3)$	$-0.36^{+0.58}_{-1.61}$		
$P_{\rm rot}$ (days)	$p(P_{\rm rot}\|{\rm H}\alpha)$[1]	$44.33^{+0.97}_{-1.01}$		
$\ln Q_0$	$p(\ln Q_0\|{\rm H}\alpha)$[1]	$0.50^{+0.54}_{-0.51}$		
$\ln dQ$	$p(\ln dQ\|{\rm H}\alpha)$[1]	$-0.65^{+1.68}_{-1.80}$		
$\ln f$	$p(\ln f\|{\rm H}\alpha)$[1]	$-0.18^{+0.25}_{-0.24}$		
Log jitter, $\ln s_{RV}$ (m/s)	$\mathcal{U}(-3, 3)$	$0.57^{+0.14}_{-0.17}$		
Mean velocity, γ_{RV} (m/s)	$\mathcal{U}(-41650, -41630)$	$-41639.96016^{+0.28}_{-0.25}$		
		Measured planetary parameters, transit fit		
		TOI-1266 b	*TOI-1266 c*	*TOI-1266 d*
$a/R_\star$	$p(a/R_\star\|P, M_\star, R_\star)$	$35.97^{+1.21}_{-1.20}$	$51.63^{+1.72}_{-1.71}$	-
$R_p/R_\star$	$\mathcal{U}(0.0, 0.2)$	$0.0545^{+0.0007}_{-0.0007}$	$0.0429^{+0.0010}_{-0.0010}$	-
Impact parameter, b	$\mathcal{U}(0, 1 + R_p/R_\star)$	$0.549^{+0.043}_{-0.047}$	$0.747^{+0.027}_{-0.032}$	-
		Measured planetary parameters, TTV + RV joint fit (adopted)		
		TOI-1266 b	*TOI-1266 c*	*TOI-1266 d*
P (days)	$\mathcal{U}(P - 0.2, P + 0.2)$[1]	$10.89450^{+0.00023}_{-0.00026}$	$18.80270^{+0.00126}_{-0.00116}$	$32.509^{+0.062}_{-0.049}$
t_0 (BJD - 2,457,000)	$\mathcal{U}(t_0 - 2.0, t_0 + 2.0)$[1]	$1691.0068^{+0.0017}_{-0.0017}$	$1689.9588^{+0.0028}_{-0.0026}$	$1729.03^{+1.97}_{-2.25}$
$\sqrt{e}\cos\omega$	$\mathcal{U}(-1, 1)$	$-0.116^{+0.123}_{-0.092}$	$0.116^{+0.087}_{-0.122}$	$0.032^{+0.108}_{-0.134}$
$\sqrt{e}\sin\omega$	$\mathcal{U}(-1, 1)$	$0.038^{+0.123}_{-0.135}$	$0.020^{+0.151}_{-0.150}$	$-0.032^{+0.135}_{-0.143}$
$M_p/M_\star$ x 10^{-5}	$\mathcal{U}(0, 10)$	$3.02^{+0.47}_{-0.48}$	$2.15^{+0.52}_{-0.52}$	$2.50^{+0.71}_{-0.75}$
		Measured planetary parameters, TTV only fit (3-planet case)		
		TOI-1266 b	*TOI-1266 c*	*TOI-1266 d*
P (days)	$\mathcal{U}(P - 0.2, P + 0.2)$[1]	$10.89442^{+0.00021}_{-0.00019}$	$18.80543^{+0.00254}_{-0.00195}$	$32.706^{+0.057}_{-0.049}$
t_0 (BJD - 2,457,000)	$\mathcal{U}(t_0 - 2.0, t_0 + 2.0)$[1]	$1691.0048^{+0.0012}_{-0.0009}$	$1689.9568^{+0.0020}_{-0.0021}$	$1723.09^{+1.71}_{-2.35}$
$\sqrt{e}\cos\omega$	$\mathcal{U}(-1, 1)$	$-0.080^{+0.131}_{-0.098}$	$0.073^{+0.085}_{-0.112}$	$0.114^{+0.111}_{-0.179}$
$\sqrt{e}\sin\omega$	$\mathcal{U}(-1, 1)$	$0.126^{+0.073}_{-0.084}$	$0.015^{+0.106}_{-0.110}$	$-0.111^{+0.132}_{-0.107}$
$M_p/M_\star$ x 10^{-5}	$\mathcal{U}(0, 10)$	$4.03^{+2.67}_{-2.34}$	$2.28^{+0.90}_{-0.81}$	$1.13^{+0.93}_{-0.65}$
		Measured planetary parameters, RV only fit		
		TOI-1266 b	*TOI-1266 c*	*TOI-1266 d*
P (days)	$p(P\|TTV)$	$10.89428^{+0.00032}_{-0.00032}$	$18.80469^{+0.00292}_{-0.00293}$	$32.686^{+0.048}_{-0.046}$
t_0 (BJD - 2,457,000)	$p(t_0\|TTV)$	$1691.0053^{+0.0017}_{-0.0017}$	$1689.9564^{+0.0033}_{-0.0033}$	$1723.41^{+1.16}_{-1.14}$
$\sqrt{e}\cos\omega$	$\mathcal{U}(-1, 1)$	$-0.271^{+0.192}_{-0.126}$	$-0.277^{+0.290}_{-0.212}$	$0.110^{+0.293}_{-0.335}$
$\sqrt{e}\sin\omega$	$\mathcal{U}(-1, 1)$	$0.220^{+0.230}_{-0.306}$	$0.226^{+0.293}_{-0.427}$	$0.169^{+0.284}_{-0.336}$
$M_p/M_\star$ x 10^{-5}	$\mathcal{U}(0, 10)$	$2.95^{+0.48}_{-0.48}$	$2.02^{+0.63}_{-0.64}$	$3.24^{+0.76}_{-0.76}$
		Derived planetary parameters		
Inclination, i (deg)	-	$89.13^{+0.08}_{-0.08}$	$89.17^{+0.04}_{-0.04}$	-
Eccentricity, e	-	$0.039^{+0.035}_{-0.025}$	< 0.071[2]	< 0.087[2]
Planet radius, R_p ($R_\oplus$)	-	2.52 ± 0.08	1.98 ± 0.10	-
Planet mass, M_p ($M_\oplus$)	-	4.46 ± 0.69	3.17 ± 0.76	$3.68^{+1.05}_{-1.11}$
Bulk density, ρ (g/cm^3)	-	1.54 ± 0.28	2.25 ± 0.64	-
Semimajor axis, a (au)	-	$0.0730^{+0.0011}_{-0.0011}$	$0.1050^{+0.0017}_{-0.0017}$	$0.1513^{+0.0024}_{-0.0024}$
Equilibrium temperature, $T_{\rm eq}$[3] (K)	-	415^{+7}_{-7}	346^{+6}_{-6}	288^{+5}_{-5}
TSM[4],	-	120^{+26}_{-20}	69^{+25}_{-16}	-

[1] Marginalized posterior distribution from Cloutier et al., 2024

[2] 95% upper limit

[3] Equilibrium temperature assuming zero albedo and perfect heat redistribution

[4] Transmission Spectroscopy Metric (Kempton et al., 2018).

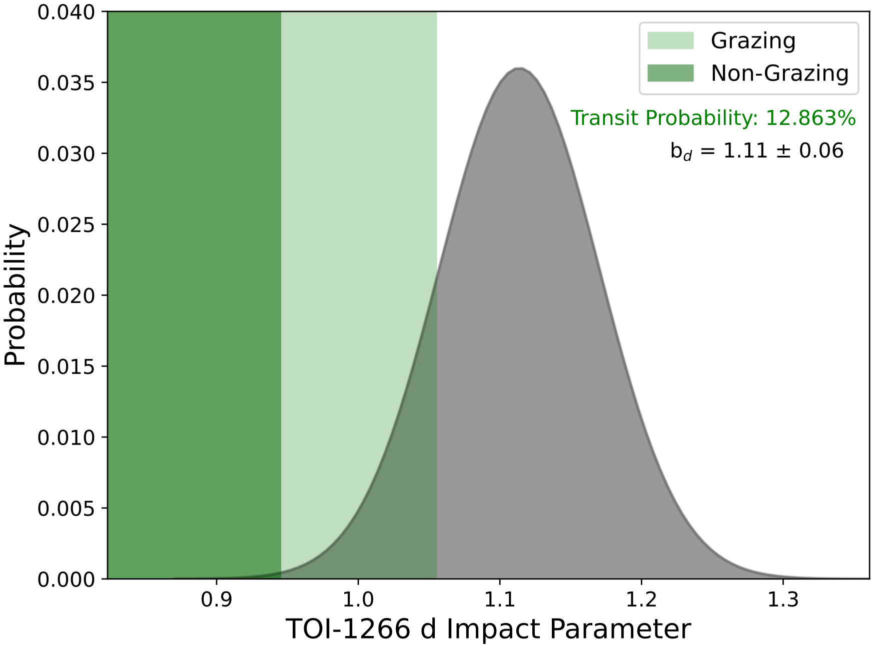

Figure 3.10 Geometric transit probability for TOI-1266 d when projecting out the orbital inclination distribution of TOI-1266 c, for both grazing configurations where $b < 1 + R_p/R_*$ and non-grazing configurations where $b < 1 - R_p/R_*$.

Is TOI-1266 d Transiting?

In §3.5 and §3.6 we confirm the existence of a third non-transiting planet, TOI-1266 d. This planet was originally identified as a candidate signal based on RV observations reported in C24. C24 visually checked for transits of TOI-1266 d using the assumed linear ephemeris from the RV data and also carried out a broader search extending to nearby orbital periods using the Transit Least Squares algorithm (TLS, Hippke et al., 2019), but did not find any evidence for transits.

Standard transit search algorithms such as Box Least Squares (BLS, Kovács et al., 2002) and TLS assume a constant orbital period and can therefore fail to detect transits for planets exhibiting TTVs (García-Melendo et al., 2011), especially when the signal-to-noise of individual transit events is low (e.g., A. Leleu, Chatel, et al., 2021). Our joint fit to the TTV data of TOI-1266 b and c described in §3.6 suggests that TOI-1266 d should indeed exhibit significant TTVs, as shown in Figure 3.9. If TOI-1266 d has a transit depth comparable to or smaller than that of TOI-1266 c, it would be difficult to identify with standard transit search methods.

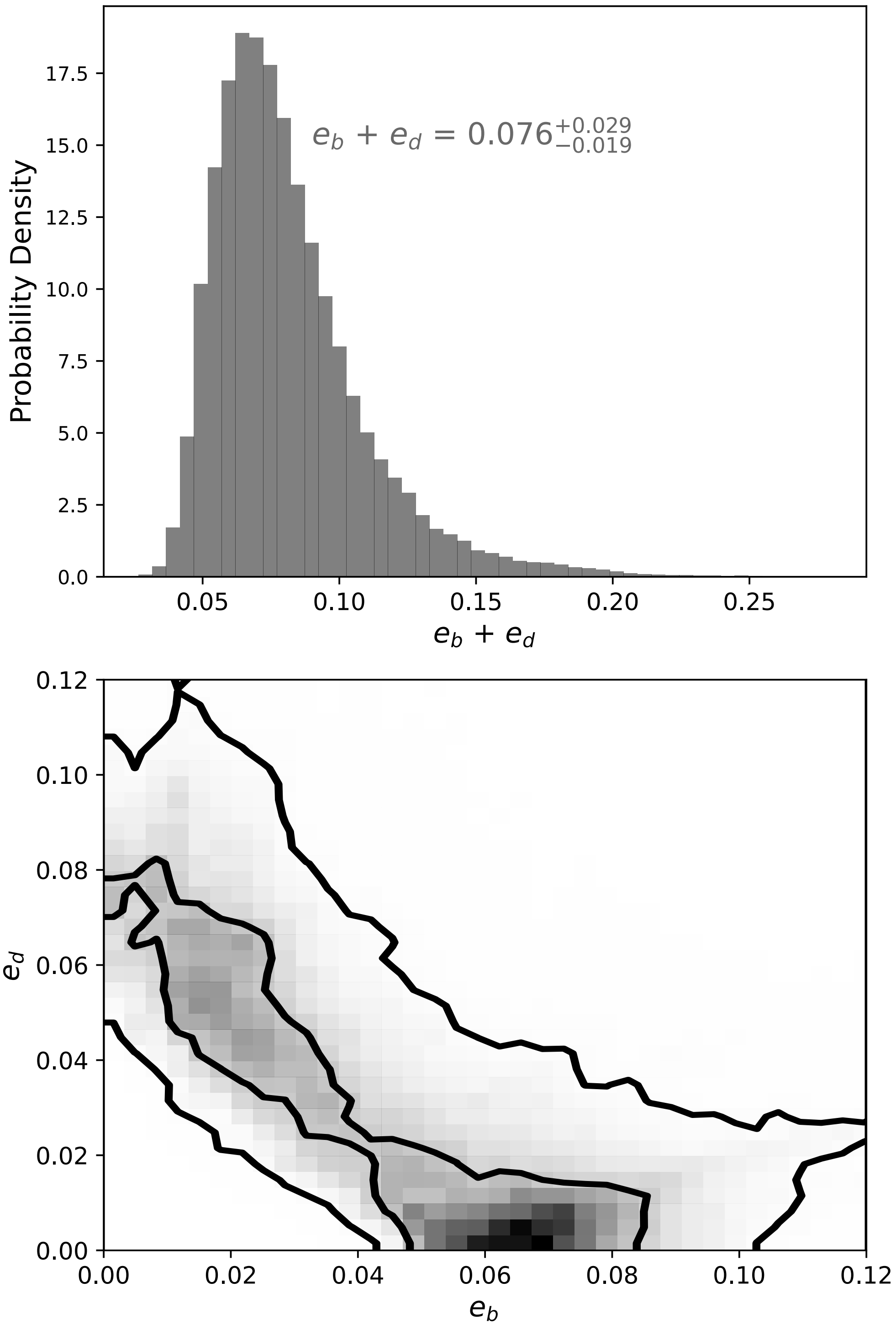

Figure 3.11 Posterior distribution for the eccentricities of TOI-1266 b and d with 1σ and 2σ contour lines (bottom) from TTV+RV joint fit, and the posterior probability distribution for the combined eccentricities of TOI-1266 b and d (top). TOI-1266 b prefers a moderate eccentricity if TOI-1266 d is not eccentric, or a small but nonzero eccentricity if TOI-1266 d is moderately eccentric.

We search for the transit of TOI-1266 d by phase-folding all available TESS data by individual transit midtimes from our joint fit model prediction, ensuring that we account for the effect of TTVs in the phased light curve. We do not find any transit signature, which is not unexpected. Our fits indicate that planets b and c have an extremely low mutual inclination ($\Delta i < 0.1^\circ$). If we assume that planet d is also coplanar with TOI-1266 c, we find that TOI-1266 d has a relatively low geometric transit probability. We plot the geometric transit probability of TOI-1266 d under the coplanar assumption – including grazing transit configurations – in Figure 3.10.

3.7 Dynamical Analysis

System Stability

We investigated the long-term dynamical stability of the TOI-1266 system using the WHFast integrator in the `rebound` *n*-body code (Rein et al., 2015). We initialized *n*-body integrations with planetary masses, semimajor axes, eccentricities, mean anomalies, and longitudes of periastron drawn randomly from the chain of TTV+RV joint fit posterior samples described in §3.6, and converted from the joint fit sampling parameter basis to `rebound` parameterizations and units where appropriate. The orbital inclinations were initialized from a random normal distribution based on the transit fit results described in Table 3.3, while the longitudes of the ascending node were randomly drawn from 0 to 2π. We integrated with a time step of 0.5 days, corresponding to less than 5% of the orbital period of the inner planet, and evolved the system for a total of 92 kyr, or $\sim 10^6$ orbits of the outermost planet, repeating this process for 20 independent simulations.

We found that in all of our simulations, the planetary semimajor axes, eccentricities, and inclinations oscillate around stable equilibria for the duration of the model. The semimajor axes oscillate with an amplitude of $\sim 0.01\%$ of their initial values over the course of the simulation due to planet-planet interactions, but the equilibria do not appear to vary. We conclude that the system is likely stable over the full range of orbital parameters identified by the TTV+RV joint model. The eccentricities in these simulations also oscillate around stable equilibria near their initial values with amplitudes ranging from 0.01 to 0.1. A representative figure from one simulation illustrating the eccentricity evolution is shown in Figure 3.12, and this behavior was common across all simulations.

This confirms that, despite the compact nature of this system, we cannot use stability constraints to obtain tighter constraints on the orbital eccentricities of the three

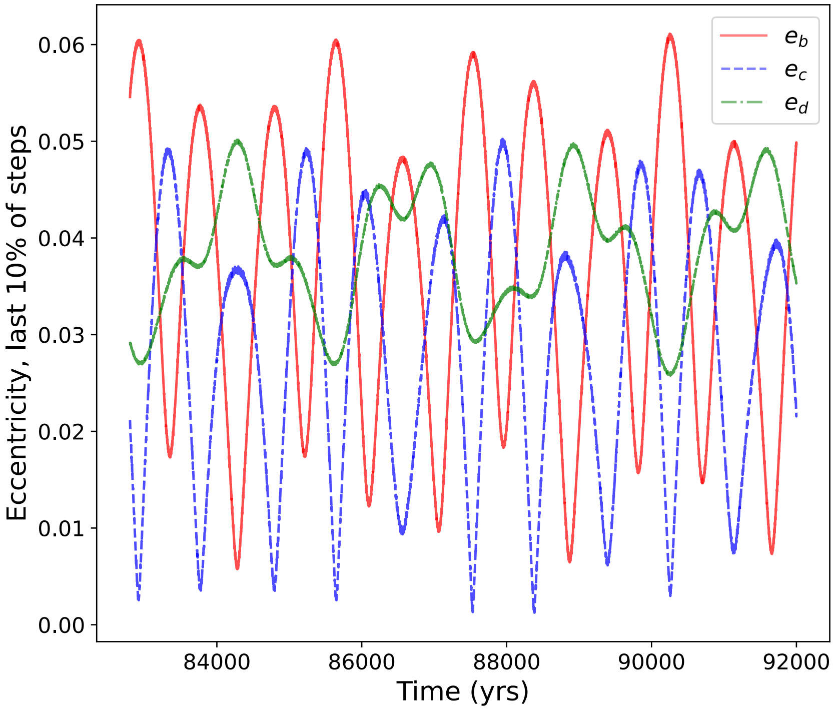

Figure 3.12 Evolution of planetary eccentricities during the last 9.2 kyr (final 10%) of a `rebound` simulation with orbital parameters initialized from the TTV+RV joint fit posterior. All simulations displayed similar behavior: eccentricity oscillation around stable equilibria for the full simulation duration, with oscillation amplitudes ranging from ~ 0.01 to 0.1.

planets. We investigate the more realistic scenario of orbital evolution under the effect of tides in §3.7.

Will TOI-1266 d Become a Transiting Planet?

TOI-1266 b and c are coplanar ($\Delta_i = 0.04°$), and TOI-1266 d is unlikely to be transiting if it also orbits in this plane (§3.6). If we assume TOI-1266 d has a similar radius to TOI-1266 c, then an inclination increase of 0.11° would shift the orbit into a fully transiting, non-grazing configuration. In the *n*-body simulations described in §3.7, we observe the orbital inclination of the outer planet librating around stable equilibria with libration amplitudes that vary between ~0.02° and ~0.2° depending on the initial orbital parameters drawn from the TTV+RV joint fit posterior distribution. In some simulations, the inclination variability timescale is as short as tens of years, while in most simulations it is hundreds of years.

These simulations indicate that TOI-1266d may become observable in transit on decadal timescales. Any future search for transits of planet d will need to account for TTVs (see Fig. 3.10), so we include in Table 3.5 in the Appendix the predicted transit times for all planets from our best fit TTV solution extending 4 years from the present, which is when the uncertainty in our predicted transit times becomes larger than the transit duration. Continued follow-up of TTVs to refine these timing predictions may enable the transit detection of TOI-1266 d, though if TOI-1266 d is already misaligned > 0.2° relative to the orbital plane of TOI-1266 b and c then this scenario is unlikely.

A Search for Orbital Resonances

C24 analyzed the orbital period ratios of the TOI-1266 planets and determined that the b/c and c/d planet pairs do not lie close to any low-order two body MMRs, and that the three planets do not lie close to any three-body resonances — concluding that the planets are likely not in a resonance chain. D20 analyzed TTVs from the TESS PM data and several ground-based transit observations and concluded that the b/c pair was weakly influenced by the stronger first-order 2:1 resonance, although it is nearly 14% away from that resonance with a resonance proximity parameter (Lithwick et al., 2012) of $\Delta_{bc_{2:1}} = 0.137$. This conclusion may have been based on the tentative detection of the chopping TTV in TOI-1266 b, which D20 misattributed at the time to dynamical interactions with planet c. Based on our updated orbital parameter constraints from TTV fitting and detailed dynamical n-body modeling, we reassess whether any resonances exist in the TOI-1266 system.

We first examine possible resonant states for the two adjacent planet pairs. Both TOI-1266 b and c and TOI-1266 c and d are somewhat close to the second-order 5:3 MMR. Our updated mean orbital period constraints place the period ratios at 1.729 for the d/c pair and 1.726 for the c/b pair, respectively. We calculate $\Delta_{bc_{5:3}} = 0.037$ and $\Delta_{cd_{5:3}} = 0.036$, both within 4% of the 5:3 resonance. For a planet pair to be in resonance, there must be a critical resonant angle that librates around a fixed point, rather than circulating from 0 to 2π. We tested resonant angles of the form $\theta = p\lambda - q\lambda' + \varpi$, where λ and λ' are the mean longitudes of the inner and outer planets, ϖ is the longitude of periastron for either planet, and p and q are the integers describing the MMR with $p - q = 1$ for a first-order resonance, $p - q = 2$ for second-order, etc. Given the proximity of the orbital period ratios for the adjacent planet pairs to various MMR commensurabilities, we perform `rebound` simulations to track the evolution of all possible two-body critical angles of the 2:1, 3:2, 5:3, 7:4, 8:5, and 9:5 first through fourth-order resonances for each adjacent planet pair.

We draw initial planetary parameters from the TTV+RV joint fit as described in §3.7, and evolve the system for 100 yr in 50 independent random simulations. We identify circulation in all resonant angles, confirming that neither adjacent planet pair are in a resonance.

Next, we investigate whether the system might be in a three-body resonance by combining multiple two-body resonant angles to determine if there are any three-body critical resonant angles that librate (e.g., Kepler-223, Mills et al., 2016). These three-body resonances take the form $\phi = p\lambda_b - (p + q)\lambda_c + q\lambda_d$ or $\phi = p\lambda_b + (p + q)\lambda_c - q\lambda_d$. In some systems, TTVs have revealed that *only* these three-body angles librate, and the system is in a three-body resonance without any planet pairs in a two-body resonance (Goździewski et al., 2015; Mills et al., 2016; MacDonald et al., 2016). These three-body resonances can be active even when the system is very far from any two-body resonances (e.g., Kepler-221, Goldberg et al., 2021).

We check for libration of all three-body resonant angles with $|p+q| < 15$, integrating the system in `rebound` for 100 years with initial parameters randomly drawn from the joint fit posterior and find circulation in ϕ for all independent simulations. We therefore conclude that the system is not in a three-body resonance.

The only possible resonance configuration left to consider is for the nonadjacent b/d planet pair. Our updated constraint on the period of TOI-1266 d moves it within 1% of the 3:1 resonance with planet b, with $\Delta_{bd_{3:1}} = 0.0053$. We again take 100 random draws from the joint fit posterior distribution and integrate them for an initial 100 years. For a small number of the total draws, we observe a librating ϕ for the 3:1 MMR between planets b and d. This initially suggested that resonant interactions between TOI-1266 b and d might dynamically excite the planetary eccentricities to a level consistent with the TTV observations. To investigate whether the resonant configurations we identify are stable long-term and can maintain the observed nonzero eccentricities against the forces of tidal damping, we evolve these parameter combinations with a librating $\phi_{3:1_{bd}}$ for an additional 100 Myr.

We find that the system is eventually knocked out of resonance and then becomes unstable for all initially resonant simulations. For simulations including tidal effects consistent with the modeling procedure described in §3.7, the inner planet's orbital period shrinks slightly due to tidal circularization. This causes the resonant angle to begin circulating and destabilizes the system, typically scattering the other two

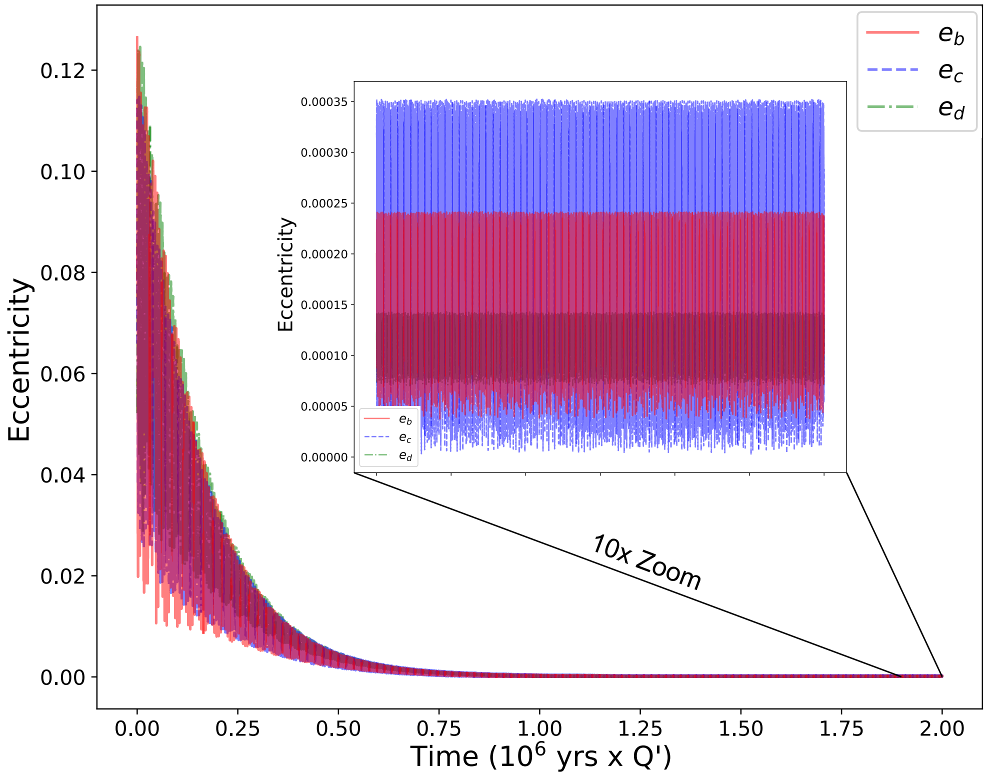

Figure 3.13 Orbital eccentricities of TOI-1266 b (red), c (blue) and d (green) under the effects of tidal forces in a `REBOUNDx` model with initial planet parameters drawn from the TTV+RV joint posterior distribution. Time units are normalized by the uncertain Q/k_2. The inset plot shows the last 10% of simulation steps after the eccentricities have damped to their stable long-term equilibria. For $Q/k_2 > 1200$, the damping timescale is longer than 2 Gyr, consistent with the stellar age.

planets within 100 kyr. Resonant simulations not including tidal effects also went unstable, but on longer timescales ($1 - 10$ Myr), with the middle planet typically undergoing initial rapid orbital variations due to perturbations from the inner or outer planet which then destabilizes the entire system.

We conclude that although there is a small region of our posterior probability space where planets b and d are located in the 3:1 resonance, stability constraints indicate that this configuration is unstable on timescales much shorter than the age of the system ($\leq$ 100 Myr). The TOI-1266 system is therefore in a unique dynamical configuration, with two planets near a second-order near-resonant commensurability and a third planet located in-between them. There are no other known compact multi-planet systems in this kind of configuration, and it is an open question as to how such a system could have originated.

Planetary Eccentricities and Tides

TOI-1266 is a compact multi-planet system with close-in planetary orbits (< 0.15 AU), indicating that tidal forces may play an important role in the dynamical evolution of the system. To investigate the potential for tidal damping of the planetary spins and eccentricities, we perform long-term dynamical simulations of the system incorporating a constant time-lag tidal model (Eggleton et al., 1998) using the `tides-spin` implementation of Lu et al., 2023 in `REBOUNDx 1.6.1` (Tamayo et al., 2020), which includes the effects of tides raised on the star and the orbiting planets and consistently tracks both spin and orbital evolution. In this model framework, the planets and star have physical structure and distortion parameterized by their radii, moment of inertia, potential Love number k_2, spin angular rotation frequency (denoted as S to avoid confusion with the previously described longitude of ascending node, Ω), and the tidal quality factor Q.

Both the planetary k_2 and Q values are highly uncertain parameters, and are therefore sometimes combined as Q/k_2 and referred to as the reduced tidal quality factor Q'. The k_2 value depends sensitively on the internal composition of the planet, rheology, presence of ice/silicate/metal layers, their extent and melting, and other parameters – all of which are unconstrained for the TOI-1266 planets. Tobie et al., 2019 predicts the k_2 values of rocky and ice-rich planets from multi-layer interior structure modeling, and finds values that range from $0.05 - 0.5$ that primarily depend on the relative size of the iron core for rocky planets and the presence of ice-rich outer layers for water-rich planets. Nettelmann et al., 2011 model the interior of the sub-Neptune planet GJ 1214 b, which is similar in radius and mass to TOI-1266 b – assuming a rocky core with a H/He-rich envelope, a pure water envelope, or a mixture of H/He and water envelopes. This study finds k_2 values ranging from $\sim 0.02 - 0.7$, depending on the bulk composition. Kellermann et al., 2018 arrives at similar conclusions from structure modeling of $\sim 2\ R_\oplus$ planets with masses between $1 - 8\ M_\oplus$ approximated with an iron core, silicate mantle, and solar metallicity envelope, or with significant bulk water content. This study finds k_2 values from $0.01 - 0.8$. We adopt the latter range — which is the most generous of the three — for our simulations.

The dissipation rate Q is sensitive to the forcing frequency and internal viscosity, which depends on the thermal evolution of the planet, and is unknown. For Earth-like rocky planets, Q could be as low as 10 (Clausen et al., 2015; Goldreich et al., 1966), while a population-level analysis of compact multi-planet super-Earth and

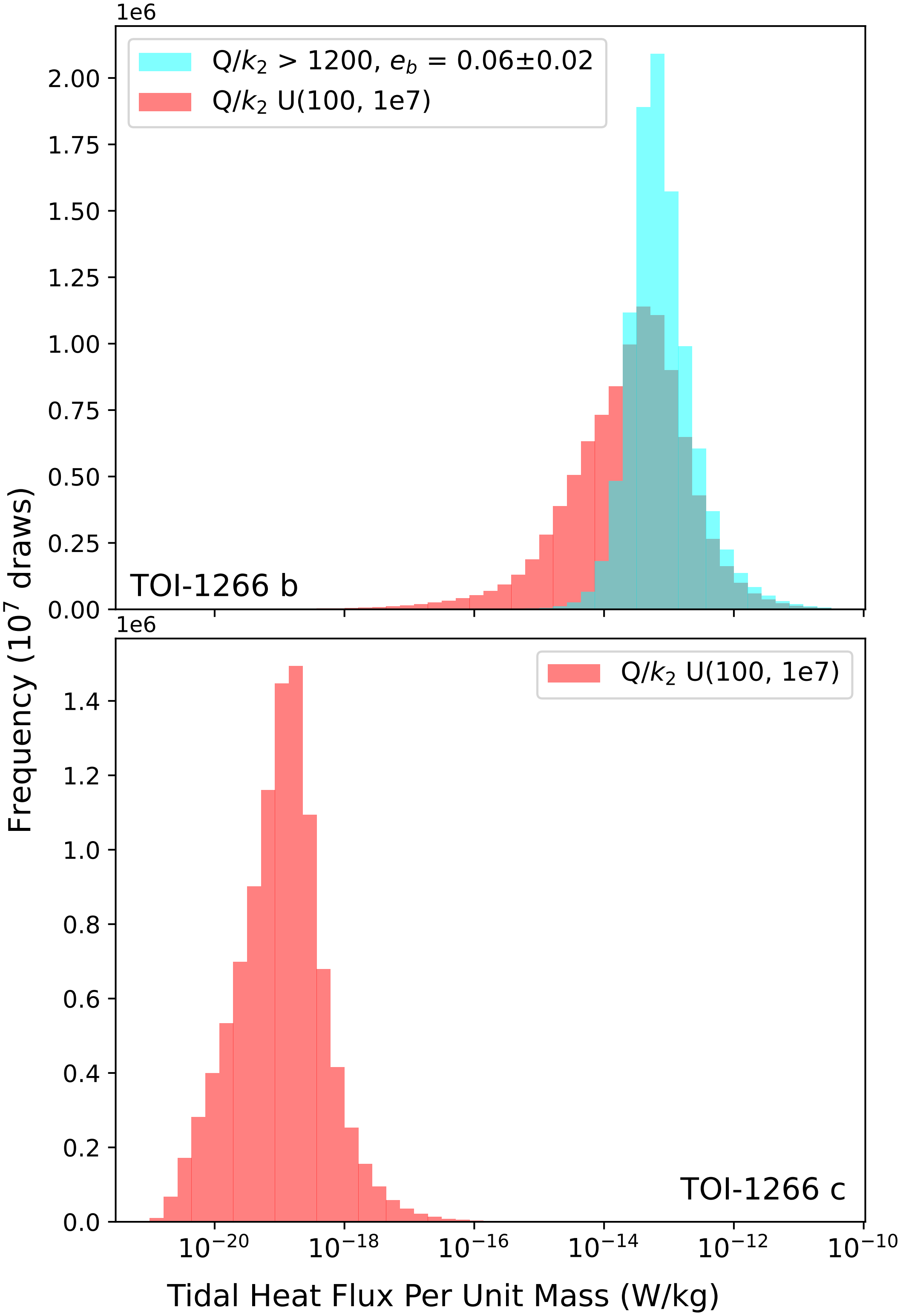

Figure 3.14 The tidal heat flux per unit mass of TOI-1266 b (top) and c (bottom) calculated with a wide range of possible Q (100 - 10000) and k_2 (0.01 - 0.8) values, with e values drawn from the TTV+RV joint posterior distribution (red). Tidal heat fluxes with e_b drawn from the higher eccentricity peak where e_d is small and where Q/k_2 is > 1200 such that the eccentricity damping timescale is > 2 Gyr for TOI-1266 b are shown in blue. For both planets, the lower bound on heat flux is set by the post-damping eccentricity equilibrium e ≃ 0.0001.

sub-Neptune systems suggests that Neptune-like Q values as large as 10^5 may be common (Louden et al., 2023). We adopt a range of $100 - 10000$ for Q in our simulations, since our measured bulk densities for TOI-1266 b and c indicate that they are less dense than Earth but their gas envelopes likely comprise a relatively small fraction of their total masses.

Next, we confirm that TOI-1266 b and c are expected to be tidally locked by calculating the tidal spin locking timescale (Gladman et al., 1996). For all plausible Q and k_2 values, the spin locking timescales for both planets are < 400 Myr – much less than the estimated age of the system. However, in a recent population-level analysis of radius inflation for compact multi-planet sub-Neptune systems, S. C. Millholland et al., 2024 suggested that it may be common for planets that migrate inward to be locked into higher obliquity spin-orbit resonance Cassini states. If TOI-1266 b or c are in a nonsynchronous spin-orbit resonance, the tidal dissipation could be orders of magnitude larger. The analysis we present here therefore represents a lower limit on the tidal heat flux for each planet.

We ran the `REBOUNDx` simulations for $2 \times 10^6 \times (Q/k_2)$ years, so that the damping timescale can easily be mapped onto various possible values of Q and k_2. We initialized the planet orbital parameters and eccentricities by sampling from the joint TTV+RV fit posterior, and randomly selected Q and k_2 values from uniform distributions with ranges of 100 – 10000 and 0.01 – 0.8, respectively. The planetary spins are initialized from a synchronous state. We performed 100 random parameter draws and evolved the system for $2 \times 10^6 \times (Q/k_2)$ years.

We found that all three planetary eccentricities initially oscillated around a constant value, consistent with the results of §3.7, but were then quickly damped until they reached stable equilibria. The changes in planetary semimajor axis in all of the simulations were $< 1\%$, and all of the systems remained stable for the simulation duration. Even after the damping was complete, we found that the planets still maintained slightly nonzero eccentricities at late times, which oscillated around stable values. We show an example of this in Figure 3.13. The final ratios of planetary eccentricities in our simulations depends on the initial configuration, with final e_b equilibrium values typically ranging from $0.0001 - 0.001$. This remains true across all random orbital parameter draws and spans the full range of Q and k_2 values tested.

We can leverage the fact that our TTV+RV joint fit prefers a moderately nonzero eccentricity for TOI-1266 b and the smaller eccentricity values from our tidal damping simulations to constrain the value of Q/k_2. Our dynamical simulations indicate that all of the eccentricity values allowed by our TTV+RV posterior probability distribution are stable long-term, and that there are no orbital resonances that can pump up the planetary eccentricities. However, our long-term dynamical simulations incorporating tidal damping indicate that any primordial eccentricities should be damped to values of e $\simeq$ 0.0001 in less than $2 \times 10^6 \times (Q/k_2)$, while TOI-1266 b has a retrieved orbital eccentricity of $\sim$ 0.06 in a majority of our TTV+RV posterior. Since this system is likely older than $\sim$ 2 Gyr, this implies that Q/k_2 for TOI-1266 b must be greater than 1200, which is the value that sets $\tau_{circ} > 2$ Gyr. An alternate possibility is that TOI-1266 b had its eccentricity excited by a recent dynamical disturbance, for example by a widely separated outer planet that is undetected in the RV observations.

Next, we assess the potential importance of tidal heating caused by the nonzero eccentricity for the overall energy budgets of planets b and c. For TOI-1266 b, we assume a lower bound of 0.0001 on the eccentricity from our simulations of tidal damping and otherwise draw eccentricity values directly from our TTV+RV posterior distribution. For TOI-1266 c, we also assume a lower bound of 0.0001 from our tidal damping simulations. But since the TTV+RV posterior distribution does not indicate any preference for a nonzero eccentricity of TOI-1266 c, we instead impose an upper bound of 0.001 representing the largest values from our tidal damping simulations. We then calculated the range of tidal heat fluxes from Equation 4 of Jackson et al., 2008 for both planets and plot the resulting distribution in Figure 3.14. We find that for Q and k_2 combinations that yield a tidal circularization timescale larger than 2 Gyr and are therefore consistent with the larger eccentricity values preferred for planet b, the upper end of the distribution for tidal heat flux per unit mass is $\sim$ 1% that of Io (TOI-1266 b: $F_{\mathrm{tidal}} \in 5 \times 10^{-15} - 5 \times 10^{-12}$ W/kg, Io: $F_{\mathrm{tidal}} \simeq 10^{-10}$ W/kg, Veeder et al., 2012), while the tidal heat flux in W/m^2 at the surface of TOI-1266 b is nearly equal to the insolation flux (Figure 3.15). This suggests that tidal heating is likely to be important for interpreting the internal and atmospheric composition of TOI-1266 b, with potential implications for long-term atmospheric evolution as well.

Lastly, we compare TOI-1266 b to the broader population of small planets with measured nonzero eccentricities, implying significant tidal heat fluxes. Seligman et al., 2023 analyzed the population of rocky planets with measured eccentricities to identify top candidates for volcanic outgassing by comparing the tidal heat flux per unit mass and the corresponding ratio of tidal heat flux to insolation flux – normalized against the uncertain tidal parameters Q/k_2. In Figure 3.15 we show that TOI-1266 b is also a top candidate for tidally driven outgassing, although the implications of this tidal heating are complicated by the presence of a thick atmospheric envelope. TOI-1266 b may have a molten surface negating traditional volcanism through a solid crust, but the significant tidal heat could still inflate the radius by heating the base of the atmosphere and reduce atmospheric escape rates by increasing the mean molecular weight of the atmosphere via outgassing. We find that TOI-1266 b's tidal heat flux is comparable to its insolation flux ($F_{\text{tidal}}/F_{\text{insolation}} \simeq 0.9$), and is more than four orders of magnitude larger than the tidal heat flux of TOI-1266 c. This provides another promising opportunity for comparative planetology in the TOI-1266 system.

3.8 Discussion

Bulk Density Constraints

Our updated planetary radii (see §3.4) and our updated masses (see §3.6) for TOI-1266 b and c yield slightly smaller radii and larger masses than those reported by C24, and we additionally make small improvements (~1-3%) to the fractional mass and radius uncertainties. Figure 3.16 compares the new mass and radius constraints for TOI-1266 b and c to the previous constraints, and places this system in the context of the broader population of small planets around M dwarfs with well-measured masses and radii.

Our updated planet masses and radii do not change the fundamental interpretations of the planet compositions based on the bulk density constraints from C24. The bulk density of TOI-1266 b is likely too low to be explained solely by rock-water mixtures, given the expected upper limit on water mass fraction (WMF) of ~50% beyond the snow line for solar composition nebulae (Lodders, 2003), although the expected upper limit on WMF for sub-Neptune exoplanets is still debated (e.g., Bitsch et al., 2021; Burn et al., 2024; Rogers et al., 2025). This implies that TOI-1266 b's atmosphere likely contains some hydrogen and helium. TOI-1266 c's smaller radius and larger mass relative to the values reported in C24 now make it easier to match with water-rich scenarios, although it is also consistent with a modest hydrogen-rich envelope (see §3.8). Our updated mass constraint for TOI-1266 c increases the bulk density from 1.6 ± 0.6 g/cm^3 to 2.0 ± 0.6 g/cm^3, reducing the water-to-rock ratio required to explain the observed mass and radius to ~30%. Part of the shift to smaller radii and larger masses for TOI-1266 b and c is also explained

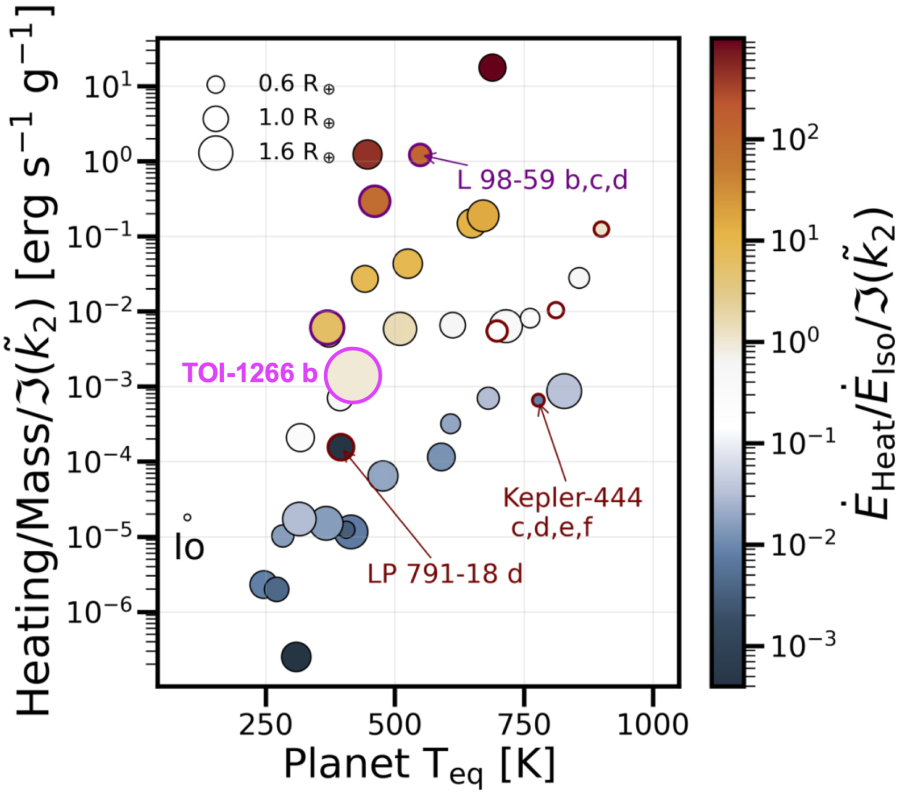

Figure 3.15 Planetary equilibrium temperature versus tidal heat flux per unit mass, adapted from Figure 5 of Seligman et al., 2023, showing the most promising rocky planets for tidal volcanism. Heat fluxes are normalized by the uncertain tidal quality parameters, point sizes are scaled by planet size, and color indicates the ratio of tidal heat flux to insolation flux. TOI-1266 b has an estimated tidal heat flux nearly equal to its insolation flux. If TOI-1266 c has a damped free eccentricity of 0.001, then it falls outside of this plot (Heating/Mass/$\Im(\tilde{k}_2) \simeq 10^{-8}$, $\dot{E}_{Heat}/\dot{E}_{Iso}/\Im(\tilde{k}_2) \simeq 5 \times 10^{-5}$).

by our choice to adopt the stellar parameters from S20, which are based on effective temperature and surface gravity constraints from spectroscopic observations, while C24 adopted stellar parameters from the TIC v8.2 catalog. S20's stellar mass is larger and their stellar radius is smaller than the values reported in C24.

Interior and Atmospheric Compositions

In principle, we can leverage refractory abundance measurements for the host star to break degeneracies in interior structure models derived from planetary mass and radius measurements (Dorn et al., 2017). This method has been applied to small M dwarf planets in a number of previous studies (e.g., Mortier et al., 2020; A. Leleu,

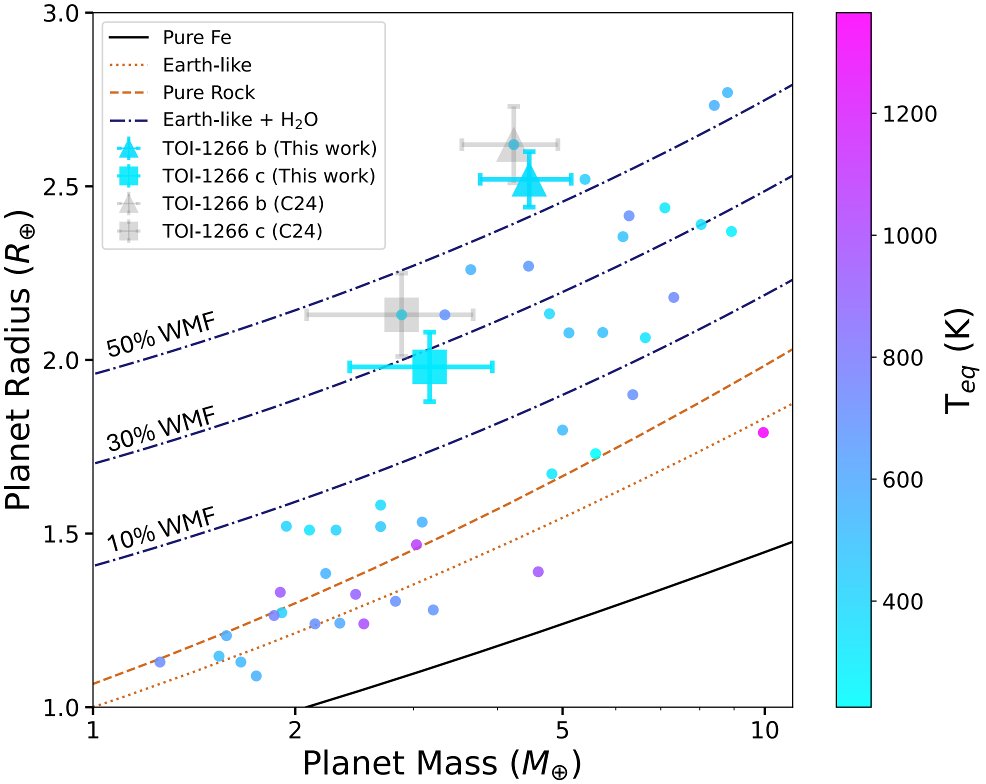

Figure 3.16 Mass-radius diagram for TOI-1266 b (triangle) and c (square), with updated measurements from this work (blue markers) compared to C24 (gray markers). Filled circles represent all small (< 3 $R_\oplus$) planets orbiting M dwarfs ($T_* < 3900$ K) with masses and radii measured to better than 3σ, based on the NASA Exoplanet Archive list of confirmed planets as of Aug 23 2024. The predicted equilibrium temperatures of the planets are indicated by the point color. For comparison, we also plot Earth-like water-rich mass-radius curves from Aguichine et al., 2021 and pure iron, Earth-like, and rocky iso-density curves from Zeng et al., 2016.

Alibert, et al., 2021; Delrez et al., 2021; Demangeon et al., 2021; Bonfanti et al., 2024; Rosário et al., 2024; Cointepas et al., 2024). However, the relation between star and planet composition is not straightforward (e.g., Plotnykov et al., 2020), and our measured stellar [Fe/H], [Mg/H], and [Si/H] values are all close to solar values (see §3.3). This suggests that interior modeling tools that assume Earth-like core and mantle compositions should be sufficient to describe the TOI-1266 system.

We use the ExoMDN code Baumeister et al., 2023 to model the structure of TOI-1266 b and c using a four-layer model with an iron core, Earth-like silicate mantle, water/high pressure ice layer, and solar metallicity H/He atmosphere. ExoMDN uses mixture density networks trained on millions of synthetic planet models computed using the TATOOINE code (Baumeister et al., 2020; MacKenzie et al., 2023). The planets in the training set have masses < 25 $M_\oplus$ and T_{eff} from 100 to 1000 K. Inputs to the model are the planet mass, radius, and equilibrium temperature. This framework has been applied to constrain the range of possible compositions which are degenerate in mass and radius alone for several other super-Earth and sub-Neptune planets (e.g., Murgas et al., 2024; Suárez Mascareño et al., 2024; M. J. Hobson et al., 2024).

We display the parameter distributions from ExoMDN modeling of the four-layer mass fractions for TOI-1266 b and c in Figure 3.19 in the Appendix. We also model the radius fractions for each layer, and find that TOI-1266 b has a radius fraction of $0.29^{+0.15}_{-0.14}$ for its potential H/He layer, while TOI-1266 c has a potential H/He radius fraction of $0.14^{+0.20}_{-0.11}$.

Despite slightly refined planetary mass and radius measurements, the interpretation of the planetary bulk compositions are unchanged relative to C24. Our water and atmospheric mass fractions for both planets are consistent within 1σ. TOI-1266 b is likely a gas-enveloped terrestrial with an envelope mass fraction < 12% (95% upper limit), though we cannot rule out a water-rich interior. TOI-1266 c is more consistent with a water-rich interior without a significant H/He envelope ($m_{env} = 0.0^{+0.03}_{-0.00}\%$), though we cannot rule out a terrestrial composition with a small H/He atmospheric mass fraction. The bulk densities of TOI-1266 b and c are discrepant from each other by 1σ but the compositions for both planets remain degenerate using mass, radius, and equilibrium temperature alone.

Possible Explanations for the Inverted Architecture of TOI-1266

Although TOI-1266 b and c both lie on the larger side of the radius gap, they have different densities and correspondingly distinct constraints on their mantle compositions. Relative to the proposed rocky, water-rich, and gaseous sub-Neptune populations proposed by Luque et al., 2022, TOI-1266 c lies on the border between water worlds and sub-Neptunes, while TOI-1266 b is firmly aligned with the sub-Neptune population. If TOI-1266 c has a significantly higher water mass fraction than TOI-1266 b, it might suggest that planet c formed outside the water ice line while b originated from inside this line. However, this raises the question of why TOI-1266 c did not also accrete significant quantities of hydrogen and helium given its more distant formation location. If both planets instead host hydrogen-rich atmospheres, some mechanism is required to explain why TOI-1266 b was able to accrete and retain a more massive primordial atmosphere than TOI-1266 c. TOI-1266 b has a larger mass than TOI-1266 c, which increases the gravitational potential well and reduces the predicted mass loss rate. However, planet b is also more highly irradiated than planet c, and atmospheric escape modeling in C24 indicates that the predicted mass loss rates for the two planets are not different enough to explain their differing radii if both planets had similar primordial atmospheric compositions. This suggests that TOI-1266 c is more consistent with a water-rich composition.

This picture is additionally complicated by the discovery that TOI-1266 b has a significant tidal heat flux (see §3.7). There are very few compact multi-planet systems with eccentricities as large as our preferred value for TOI-1266 b (e.g., Van Eylen et al., 2019; He et al., 2020). TOI-1266 b's large tidal heat flux means that its atmosphere may be less massive and/or more metal-rich than implied by the models described in §3.8, and might help to reduce the disparity in inferred envelope masses relative to TOI-1266 c.

We can also leverage the unique dynamical configuration of this system to constrain the formation and migration histories of the three planets. The classic picture of close-in sub-Neptune formation assumes that these systems undergo convergent migration that places them in mean-motion resonant chains. These resonant chains then destabilize on $\sim$100 Myr timescales, leaving the planets in orbits that are just wide of commensurability (Batygin et al., 2023). The planet formation simulations of Batygin et al., 2023 produce systems that are on average more mass-uniform than the Kepler sample overall, while post-nebular instabilities and collisions can degrade the mass-uniformity enough to match the Kepler sample for most systems (Goldberg et al., 2022). But the TOI-1266 system is very uniform in mass (consistent with the resonant subset of Kepler multi-planet systems described in Goldberg et al., 2021) and close to resonance, which implies that the current system may be a pristine remnant of planet formation, where the post-nebular relaxation away from resonance happened through some soft instability that did not lead to orbit crossing. This would imply that the differences in atmospheric mass fraction for TOI-1266 b and c are primordial.

Alternatively, Li et al., 2024 recently suggested that some planets can experience major collisions after the destabilization of the original resonance, resulting in a broader range of period ratios. If the three TOI-1266 planets were originally located in a resonant chain (e.g., adjacent pairs in the 3:2 resonance), our simulations predict that the resonance would be destabilized by tidal damping on relatively short timescales (§3.7). If this led to mergers, it could have shifted the orbital period ratios of the b/c and c/d pairs wide of the original resonances (e.g., a chain of 1.5 period ratios) to their current values near 1.7. If TOI-1266 c underwent a giant impact but TOI-1266 b did not, it might also explain the different atmospheric mass fractions of the two planets in the case where the inflated radius of TOI-1266 b relative to c is not due to its larger tidal heat flux.

3.9 Future Observations

TTV Follow-up

There is still much to be gained by additional TTV monitoring of the TOI-1266 system. As shown in Figure 3.7, we have yet to observe a full TTV super-period for TOI-1266 b. This super-period is caused by its proximity to the 3:1 resonance with TOI-1266 d and has a predicted duration of ~2000 days (Lithwick et al., 2012, Equation 5), while the current observational baseline is only 1700 days. This suggests that future TESS and ground-based transit observations over the next decade could significantly improve on current TTV-based mass and eccentricity constraints. To that end, we provide a list of predicted transit times for all three planets from our dynamical fit in Table 3.5 in the Appendix.

For planets with circular orbits, there is a well-known degeneracy between the planet masses and eccentricities when fitting the observed TTV signal (Lithwick et al., 2012). The nonzero orbital eccentricities of planets b and/or d create a short-period chopping signature in the measured TTVs for planet b, allowing us to break this degeneracy in our TTV fits (e.g., Nesvorný et al., 2014b; Deck et al., 2015).

In the future, repeated high-precision timing measurements for TOI-1266 b over shorter timescales could be used to more fully sample this ~2-3 minute chopping signature and further improve the planetary mass and eccentricity constraints. The median TESS timing uncertainty for planet b is larger than the amplitude of the chopping TTV signature, but our most precise WIRC observations have uncertainties of less than two minutes. Transit observations with this level of timing precision could significantly improve the eccentricity and therefore tidal parameter constraints.

TOI-1266 c's location between the near-resonant pair of planets b and d means that its estimated mass and eccentricity are sensitive to the corresponding values of these parameters for TOI-1266 b and d in our current fits. As a result, additional high-precision timing measurements of TOI-1266 c will also improve the mass and eccentricity constraints of all three planets. Improved eccentricity measurements are essential in order to better constrain the tidal heat fluxes of the two transiting planets, enabling a more detailed investigation of the likely planetary interior states, mantle melt fractions, atmospheric outgassing rates, and corresponding atmospheric chemistry.

Improved Interior and Atmospheric Mass Loss Modeling

TOI-1266 has upcoming Cycle 23 XMM-Newton observations. These observations will measure the XUV flux of TOI-1266, providing an improved constraint on the planetary radiation environment. An estimate of the stellar high-energy flux is needed in order to calculate mass loss timescales for solar metallicity atmospheres, potentially yielding improved constraints on the likely envelope compositions of these two planets (e.g., Diamond-Lowe et al., 2022). A high predicted mass loss rate for a solar metallicity envelope around TOI-1266 b would indicate that it likely has a high ($> 100\times$ solar) atmospheric metallicity that acts to suppress photoevaporative mass loss (Zhang et al., 2022). If TOI-1266 c is unable to retain a solar metallicity gas envelope, it could either have a high atmospheric metallicity or a water-dominated envelope as modeled in Harman et al., 2022 and Yoshida et al., 2022.

Atmospheric Characterization

A comparative study of the atmospheric compositions of TOI-1266 b and c would tell us a great deal about possible differences in their formation environment, internal heat fluxes, and atmospheric mass loss histories. As discussed in §3.1, published atmospheric absorption detections for K2-18 b and TOI-270 d (Madhusudhan et al., 2023; Benneke et al., 2024) indicate that colder planets may have less opacity from photochemical hazes in their upper atmospheres, and should therefore be high priority targets for atmospheric characterization via transmission spectroscopy. The low equilibrium temperatures of TOI-1266 b and c therefore make them especially valuable targets for transmission spectroscopy studies with JWST.

TOI-1266 c was previously identified by Hord et al., 2024 as one of the most favorable planets in its size and temperature range for transmission spectroscopy. Our updated masses and radii yield Transmission Spectroscopy Metric (TSM, Kempton et al., 2018) values of 120 and 69 for TOI-1266 b and c, respectively. For planets in the sub-Neptune size category ($1.5 - 2.75\ R_\oplus$), this makes TOI-1266 b a more favorable target than all others with scheduled JWST observations except LP 791-18 c and L 98-59 d, and TOI-1266 c one of the five most favorable targets cooler than 400 K.

If TOI-1266 b has a relatively low atmospheric metallicity (e.g., $1 - 10\times$ solar, measured by the abundance of CH_4), then the trace abundances of CO and CO_2 in the upper atmosphere can be used to constrain the planet's internal heat flux due to tides (e.g., Fortney et al., 2020; Hu et al., 2021). If TOI-1266 b has a more metal-rich envelope (e.g., $> 100\times$ solar), it would have detectable amounts of CO_2 even without tidal heating (e.g., Wogan et al., 2024), but the additional tidal heat flux would produce more CO_2 and deplete NH_3 in the part of the atmosphere probed by transmission spectroscopy. This means that precise abundance measurements for these molecules can be used to constrain the internal heat flux of TOI-1266 b (e.g., Yang et al., 2024).

If transmission spectroscopy reveals that TOI-1266 c hosts a water-rich envelope, it would also be valuable to explore how much water might be sequestered into the planetary core versus the atmosphere. Dorn et al., 2021 presented an interior model for water-rich rocky planets that incorporates the effects of rock melting and the redistribution of water between magma ocean and atmosphere on the planet radius. This study found that accounting for these effects can lead to deviations in planet radius of up to 16%. Our fractional radius uncertainty is already lower than this value, suggesting that it may be possible to use the bulk density and tidal heat flux constraints to assess possible melt fractions in the core and quantify the corresponding distribution of water in TOI-1266 c's interior.

3.10 Summary and Conclusions

In this study, we present updated constraints on the properties of the two temperate sub-Neptune-sized transiting planets in the TOI-1266 system. We analyze new TESS data that extend the TTV baseline to ~4 years, add ten new ground-based transit observations, and incorporate information from archival HARPS-N spectrograph RV measurements in a joint TTV+RV fit. Our joint TTV+RV modeling yields updated mass, radius, and eccentricity measurements that allow us to refine constraints on the planetary compositions and tidal heat fluxes. We summarize our main conclusions below.

First, we use our new transit timing measurements to confirm the existence of a third planet in the system, TOI-1266 d. This companion was previously identified as a planet candidate by Cloutier et al., 2024 using radial velocity observations. Our dynamical fit reveals that this planet is located on an exterior orbit near the 3:1 MMR with TOI-1266 b and has an orbital period of 32.5 days. We use the dynamical model from our joint TTV+RV fit to phase up the TESS photometry around its expected transit times and confirm that it is not currently transiting. However, our dynamical simulations suggest that it may become transiting on timescales of tens to hundreds of years. Our joint TTV+RV fit provides much tighter constraints on the orbital properties of all three planets. We find that although planets b and d are located close to the 3:1 MMR, there are no librating two- or three-body resonant angles in the system. Some combinations of planetary parameters yield a librating two-body resonance between TOI-1266 b and d, but long-term dynamical simulations show that this resonance state is not stable.

Our joint TTV+RV fit also provides improved constraints on the masses and radii of the two inner transiting planets, and on the mass of the outer non-transiting planet. First, we use two additional sectors of TESS data and new ground-based transit observations to resolve the tension in transit depth for TOI-1266 c between the TESS prime and extended missions reported in Cloutier et al., 2024. We conclude that the scatter in observed transit depths is consistent with stochastic variations. We find an updated mass and radius measurement of M_b = 4.46 ± 0.69 $M_\oplus$ and R_b = 2.52 ± 0.08 $R_\oplus$ for TOI-1266 b, and M_c = 3.17 ± 0.76 $M_\oplus$ and R_c = 1.98 ± 0.10 $R_\oplus$ for TOI-1266 c. Separately, we measure a mass of $M_d = 3.68^{+1.05}_{-1.11}$ for TOI-1266 d in joint fits where we assume that all three planets are coplanar. Finally, we confirm that the planet masses and orbital parameters from our joint TTV+RV fit are consistent with results obtained by fitting each data set individually.

Our updated planetary interior and composition modeling confirms that TOI-1266 b requires a hydrogen-rich envelope to explain its observed mass and radius. If we assume that this planet has an Earth-like rocky core and a solar composition envelope, this corresponds to a H/He atmospheric mass fraction of $0.02^{+0.05}_{-0.02}$%. TOI-1266 c has a modestly higher bulk density (ρ_b = 2.24 g/cc, ρ_c = 1.54 g/cc) and can therefore be matched with either a small hydrogen-rich envelope with an atmospheric mass fraction (< 0.06% at 95% confidence), or a water-rich envelope with a mass fraction of $0.50^{+0.36}_{-0.42}$% from interior structure models, though we caution that much of this range is unsupported by formation models which predict maximum water mass fractions for terrestrial planets < 50%. This picture is additionally complicated by our discovery that planet b has a significantly nonzero orbital eccentricity, corresponding to a large tidal heat flux. We simulate the long-term evolution of the system including the effects of tides and find that TOI-1266 b must have relatively weak tidal dissipation ($Q/k_2 > 1200$) in order to maintain this eccentricity over Gyr timescales. In the future, transmission spectroscopy observations of TOI-1266 b with JWST could constrain its internal heat flux, while equivalent observations of TOI 1266 c are needed in order to determine the bulk water content of its envelope. Both planets are among the most favorable temperate sub-Neptune candidates for transmission spectroscopy with JWST, and a detection of atmospheric absorption for either planet would significantly improve our understanding of the TOI-1266 system.

3.11 Appendix

Transit Times and Posterior Probability Distributions

Figures 3.17 and 3.18 show corner plots of the posterior distributions from our joint fit to the TTV and RV data with a 3-planet model. The parameters in our fits were the planet-to-star mass ratio and $\sqrt{e}\cos(\omega)$, $\sqrt{e}\sin(\omega)$, but we have converted these distributions into units of Earth masses and eccentricity for ease of reference in Figure 3.17. Detrended light curves for all new ground-based transit observations presented in this work, and our stacked TESS transit profiles, are available in the TeX source code documents for this paper. Not included in the source code documents for this paper is one free bottle of wine for the first person that notifies me they've read this far into my thesis.

Table 3.4 Observed Transits of TOI-1266 b and c

Planet	Source[a]	Transit Number	Transit Time[b]	Uncertainty
TOI-1266 b	TESS PM	0	1691.004273	0.004655648
TOI-1266 b	TESS PM	1	1701.898951	0.005405627
TOI-1266 b	TESS PM	2	1712.796673	0.004117942
TOI-1266 b	TESS PM	4	1734.586684	0.002735273
TOI-1266 b	D20	14	1843.535750	0.001580000
TOI-1266 b	TESS PM	17	1876.219970	0.001899578
TOI-1266 b	TESS PM	18	1887.115710	0.002404801
TOI-1266 b	D20	20	1908.901470	0.001030000
TOI-1266 b	TESS PM	21	1919.798369	0.001747413
TOI-1266 b	D20	22	1930.692530	0.001270000
TOI-1266 b	D20	23	1941.590140	0.001480000
TOI-1266 b	D20	25	1963.377320	0.002670000
TOI-1266 b	MuSCAT	57	2312.013329	0.000771316
TOI-1266 b	MuSCAT3	58	2322.907835	0.000357439
TOI-1266 b	TESS EM	67	2420.963088	0.001549753
TOI-1266 b	TESS EM	68	2431.856823	0.001426380
TOI-1266 b	TESS EM	69	2442.751478	0.001556668
TOI-1266 b	MuSCAT3	84	2606.172940	0.000626247
TOI-1266 b	TESS EM	85	2617.067416	0.001701500
TOI-1266 b	TESS EM	86	2627.962889	0.001367946
TOI-1266 b	WIRC	87	2638.857341	0.000514139
TOI-1266 b	MuSCAT3	87	2638.859811	0.001039443
TOI-1266 b	TESS EM	88	2649.750889	0.001525124
TOI-1266 b	TESS EM	89	2660.645312	0.001736380
TOI-1266 b	WIRC	96	2736.907201	0.002131367
TOI-1266 b	TESS SEM	152	3347.007129	0.002401229
TOI-1266 b	TESS SEM	154	3368.796296	0.001593378
TOI-1266 b	TESS SEM	155	3379.692673	0.002864712
TOI-1266 b	TESS SEM	156	3390.588036	0.002639571
TOI-1266 c	TESS PM	0	1689.960319	0.042524505
TOI-1266 c	TESS PM	2	1727.560744	0.007774661
TOI-1266 c	D20	10	1877.975750	0.003210000
TOI-1266 c	TESS PM	11	1896.775891	0.009553679
TOI-1266 c	MuSCAT3	35	2348.011768	0.001941440
TOI-1266 c	TESS EM	39	2423.229205	0.005522536
TOI-1266 c	TESS EM	40	2442.021347	0.003062748
TOI-1266 c	MuSCAT	49	2611.240567	0.001092947
TOI-1266 c	TESS EM	49	2611.248289	0.003351727
TOI-1266 c	TESS EM	50	2630.041436	0.003002736
TOI-1266 c	Sinistro	51	2648.843530	0.002544507
TOI-1266 c	WIRC	51	2648.843729	0.001267564
TOI-1266 c	TESS EM	51	2648.845373	0.003014198
TOI-1266 c	WIRC	56	2742.873075	0.015162918
TOI-1266 c	TESS SEM	89	3363.304827	0.003415930
TOI-1266 c	TESS SEM	90	3382.112135	0.002607625

Transit observation sources are D20 (Demory et al., 2020), TESS (PM: Primary Mission, EM: Extended Mission, SEM: Second Extended Mission), WIRC, MuSCAT, MuSCAT3, or Sinistro. Transit times are in units of BJD - 2457000 and uncertainties are in units of days.

Table 3.5 Predicted Transit Times for TOI-1266 b and c

Planet	Transit Number	Midtime[a]	+1σ Uncertainty	-1σ Uncertainty
TOI-1266 b	0	1691.0067	0.0017	0.0017
TOI-1266 b	1	1701.9012	0.0019	0.0024
TOI-1266 b	2	1712.7960	0.0021	0.0030
TOI-1266 b	3	1723.6924	0.0028	0.0037
TOI-1266 b	4	1734.5869	0.0032	0.0042
...	...	...	...	...
TOI-1266 b	288	4828.7047	0.1394	0.2920
TOI-1266 b	289	4839.5993	0.1399	0.2925
TOI-1266 b	290	4850.4937	0.1401	0.2933
TOI-1266 c	0	1689.9588	0.0026	0.0028
TOI-1266 c	1	1708.7610	0.0048	0.0038
TOI-1266 c	2	1727.5597	0.0063	0.0082
TOI-1266 c	3	1746.3620	0.0081	0.0099
TOI-1266 c	4	1765.1629	0.0093	0.0102
...	...	...	...	...
TOI-1266 c	166	4811.0398	0.2963	0.2074
TOI-1266 c	167	4829.8429	0.2988	0.2081
TOI-1266 c	168	4848.6433	0.2995	0.2131

[a] Midtimes are in units of BJD - 2457000. Uncertainties are in units of days. Only a subset of rows are depicted here for conciseness. The entirety of this table is provided in the arXiv source code.

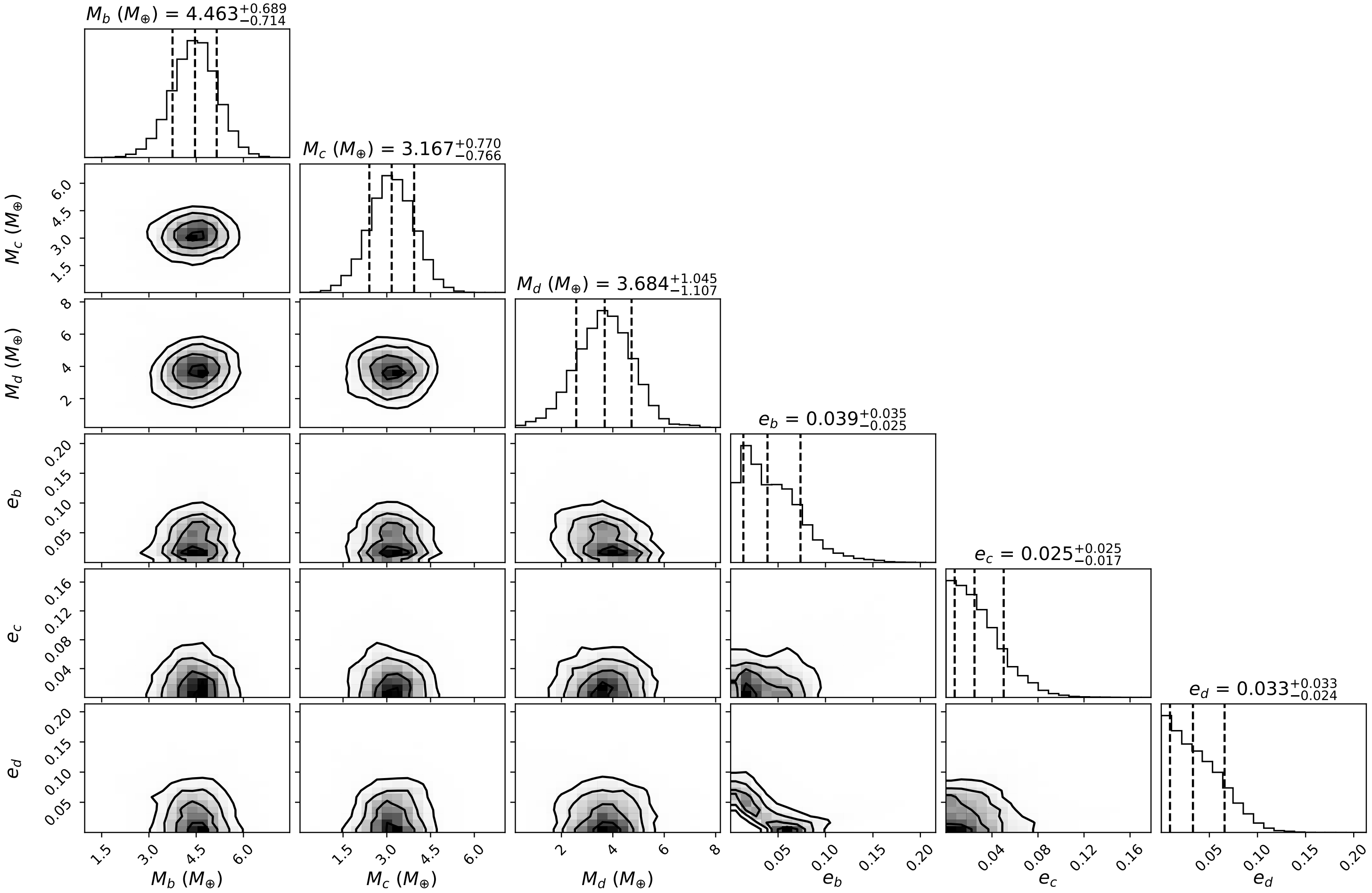

Figure 3.17 Corner plot of posteriors for planetary masses and eccentricities for TOI-1266 b, c, and d from the TTV+RV joint fit, made with the `corner` package (Daniel Foreman-Mackey, 2016)

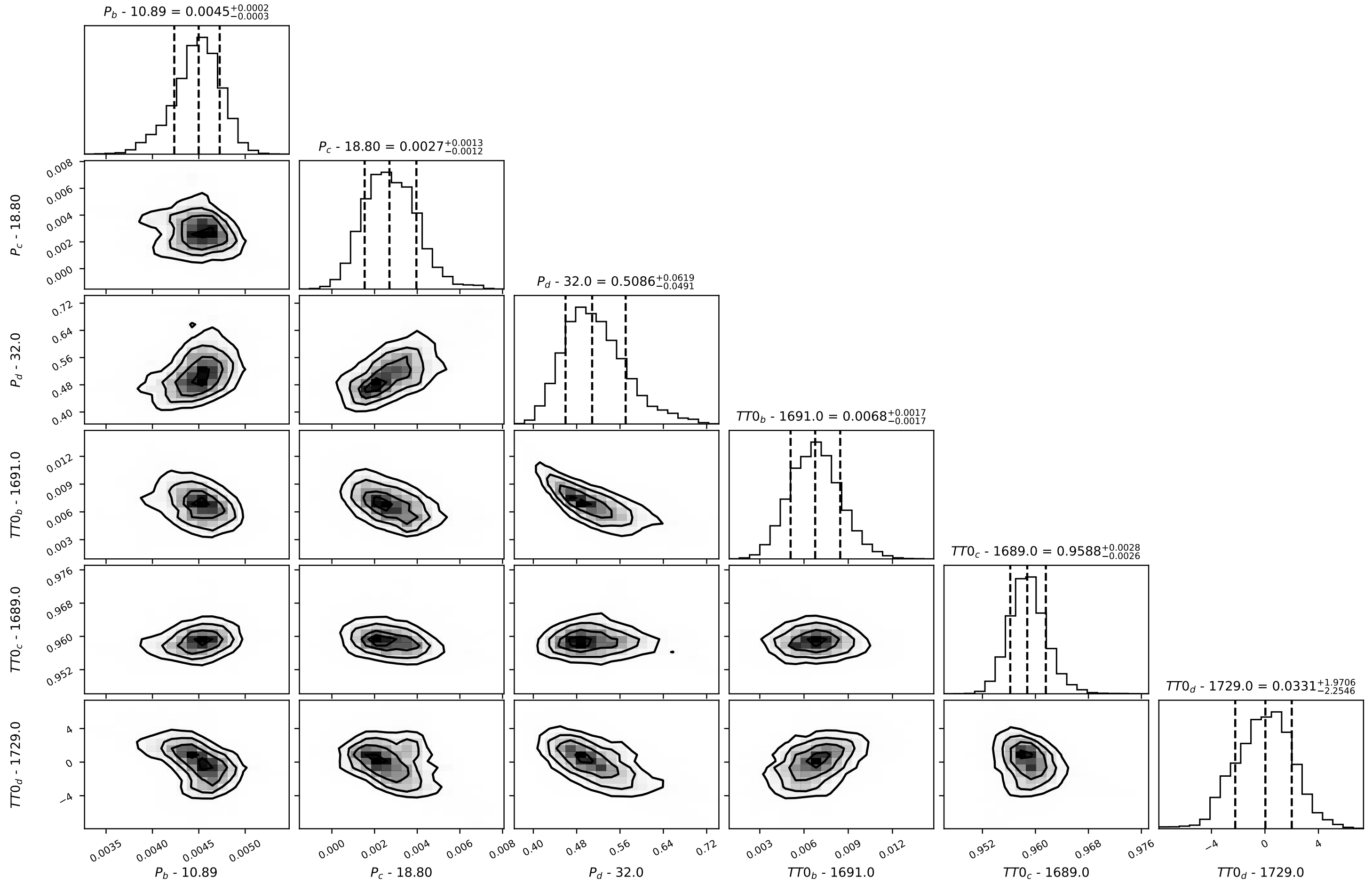

Figure 3.18 Corner plot of posteriors for planetary orbital period and initial transit time for TOI-1266 b, c, and d from the TTV+RV joint fit, made with the `corner` package. Modified periods are reported in units of days, while moditified initial transit times are in units of BJD -2457000.

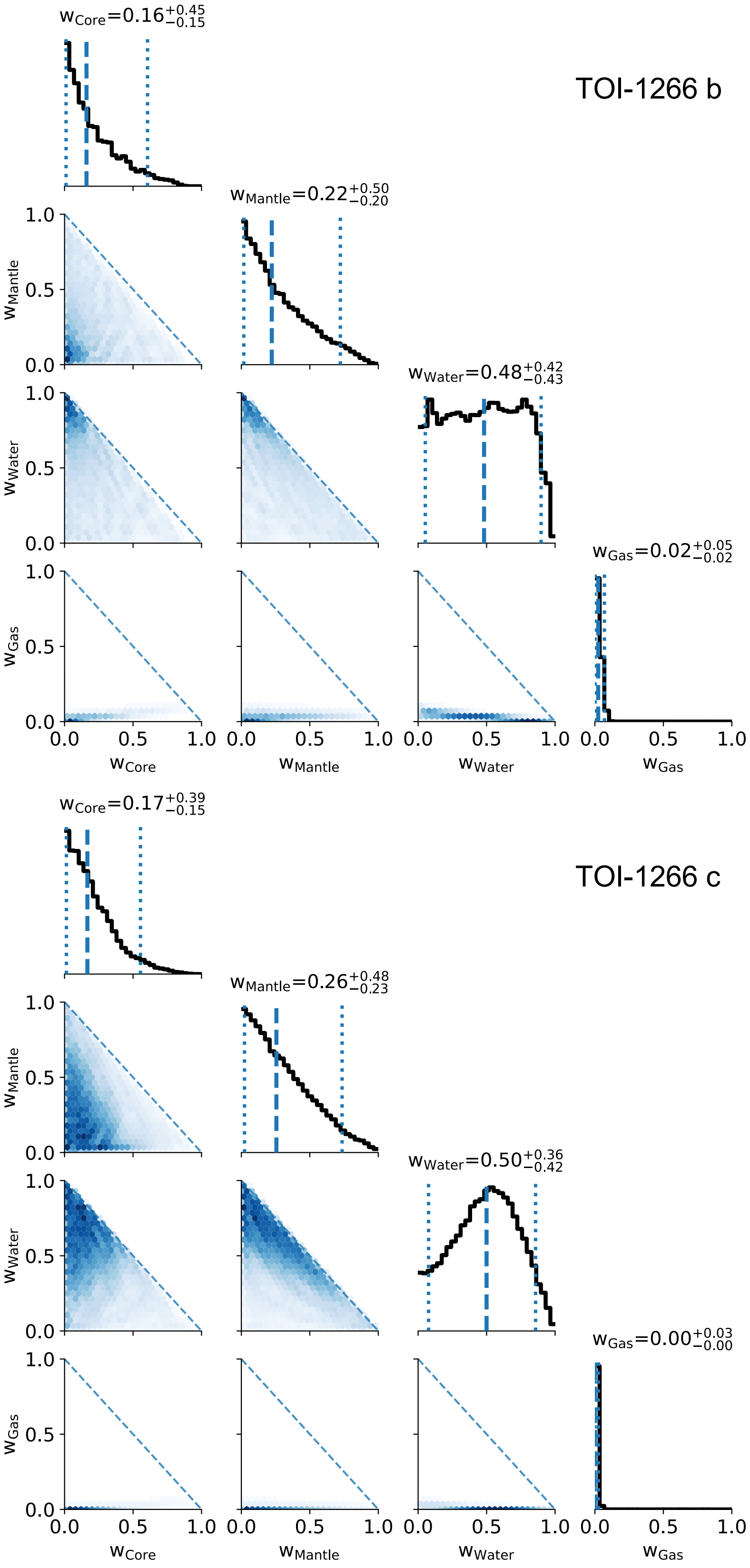

Figure 3.19 Corner plots of the mass fractions from the four-layer ExoMDN interior structure models of TOI-1266 b (top) and TOI-1266 c (bottom).

References

Agol, Eric et al. (Feb. 2021). “Refining the Transit-timing and Photometric Analysis of TRAPPIST-1: Masses, Radii, Densities, Dynamics, and Ephemerides”. In: *PSJ* 2.1, 1, p. 1. DOI: `10.3847/PSJ/abd022`. arXiv: `2010.01074 [astro-ph.EP]`.

Aguichine, Artyom et al. (June 2021). “Mass-Radius Relationships for Irradiated Ocean Planets”. In: *ApJ* 914.2, 84, p. 84. DOI: `10.3847/1538-4357/abfa99`. arXiv: `2105.01102 [astro-ph.EP]`.

Alibert, Y. et al. (Feb. 2017). “Formation and composition of planets around very low mass stars”. In: *A&A* 598, L5, p. L5. DOI: `10.1051/0004-6361/201629671`. arXiv: `1610.03460 [astro-ph.EP]`.

Bailer-Jones, C. A. L. et al. (Aug. 2018). “Estimating Distance from Parallaxes. IV. Distances to 1.33 Billion Stars in Gaia Data Release 2”. In: *AJ* 156.2, 58, p. 58. DOI: `10.3847/1538-3881/aacb21`. arXiv: `1804.10121 [astro-ph.SR]`.

Ballard, Sarah (Mar. 2019). “Predicted Number, Multiplicity, and Orbital Dynamics of TESS M-dwarf Exoplanets”. In: *AJ* 157.3, 113, p. 113. DOI: `10.3847/1538-3881/aaf477`. arXiv: `1801.04949 [astro-ph.EP]`.

Batalha, Natasha E. et al. (Feb. 2017). “Challenges to Constraining Exoplanet Masses via Transmission Spectroscopy”. In: *ApJL* 836.1, L5, p. L5. DOI: `10.3847/2041-8213/aa5c7d`. arXiv: `1701.00012 [astro-ph.EP]`.

Batalha, Natasha E. et al. (Nov. 2019). “The Precision of Mass Measurements Required for Robust Atmospheric Characterization of Transiting Exoplanets”. In: *ApJL* 885.1, L25, p. L25. DOI: `10.3847/2041-8213/ab4909`. arXiv: `1910.00076 [astro-ph.EP]`.

Batygin, Konstantin et al. (Mar. 2023). “Formation of rocky super-earths from a narrow ring of planetesimals”. In: *Nature Astronomy* 7, pp. 330–338. DOI: `10.1038/s41550-022-01850-5`. arXiv: `2301.04680 [astro-ph.EP]`.

Baumeister, Philipp et al. (Jan. 2020). “Machine-learning Inference of the Interior Structure of Low-mass Exoplanets”. In: *ApJ* 889.1, 42, p. 42. DOI: `10.3847/1538-4357/ab5d32`. arXiv: `1911.12745 [astro-ph.EP]`.

Baumeister, Philipp et al. (Aug. 2023). “ExoMDN: Rapid characterization of exoplanet interior structures with mixture density networks”. In: *A&A* 676, A106, A106. DOI: `10.1051/0004-6361/202346216`. arXiv: `2306.09002 [astro-ph.EP]`.

Behmard, Aida et al. (Jan. 2025). “A Data-Driven M Dwarf Model and Detailed Abundances for ~17,000 M Dwarfs in SDSS-V”. In: *arXiv e-prints*, arXiv:2501.14955, arXiv:2501.14955. DOI: `10.48550/arXiv.2501.14955`. arXiv: `2501.14955 [astro-ph.SR]`.

Benneke, Björn et al. (Mar. 2024). “JWST Reveals CH_4, CO_2, and H_2O in a Metal-rich Miscible Atmosphere on a Two-Earth-Radius Exoplanet”. In: *arXiv e-prints*, arXiv:2403.03325, arXiv:2403.03325. doi: `10.48550/arXiv.2403.03325`. arXiv: `2403.03325 [astro-ph.EP]`.

Bitsch, Bertram et al. (Jan. 2020). "Influence of sub- and super-solar metallicities on the composition of solid planetary building blocks". In: *A&A* 633, A10, A10. doi: `10.1051/0004-6361/201936463`. arXiv: `1911.09725 [astro-ph.EP]`.

Bitsch, Bertram et al. (May 2021). "Dry or water world? How the water contents of inner sub-Neptunes constrain giant planet formation and the location of the water ice line". In: *A&A* 649, L5, p. L5. doi: `10.1051/0004-6361/202140793`. arXiv: `2104.11631 [astro-ph.EP]`.

Bonfanti, A. et al. (Feb. 2024). "Characterising TOI-732 b and c: New insights into the M-dwarf radius and density valley". In: *A&A* 682, A66, A66. doi: `10.1051/0004-6361/202348180`. arXiv: `2311.12577 [astro-ph.EP]`.

Braak, C.J.F. ter et al. (2008). "Differential Evolution Markov Chain with snooker updater and fewer chains". In: *Stat Comput* 18, pp. 435–446. doi: `10.1007/s11222-008-9104-9`. url: `https://doi.org/10.1007/s11222-008-9104-9`.

Brande, Jonathan et al. (Jan. 2024). "Clouds and Clarity: Revisiting Atmospheric Feature Trends in Neptune-size Exoplanets". In: *ApJL* 961.1, L23, p. L23. doi: `10.3847/2041-8213/ad1b5c`. arXiv: `2310.07714 [astro-ph.EP]`.

Brown, T. M. et al. (Sept. 2013). "Las Cumbres Observatory Global Telescope Network". In: *PASP* 125.931, p. 1031. doi: `10.1086/673168`. arXiv: `1305.2437 [astro-ph.IM]`.

Burn, Remo et al. (Apr. 2024). "A radius valley between migrated steam worlds and evaporated rocky cores". In: *Nature Astronomy* 8, pp. 463–471. doi: `10.1038/s41550-023-02183-7`. arXiv: `2401.04380 [astro-ph.EP]`.

Cadieux, Charles et al. (Jan. 2024). "New Mass and Radius Constraints on the LHS 1140 Planets: LHS 1140 b Is either a Temperate Mini-Neptune or a Water World". In: *ApJL* 960.1, L3, p. L3. doi: `10.3847/2041-8213/ad1691`. arXiv: `2310.15490 [astro-ph.EP]`.

Castro-González, A. et al. (July 2023). "An unusually low-density super-Earth transiting the bright early-type M-dwarf GJ 1018 (TOI-244)". In: *A&A* 675, A52, A52. doi: `10.1051/0004-6361/202346550`. arXiv: `2305.04922 [astro-ph.EP]`.

Choksi, Nick et al. (June 2023). "Exciting the transit timing variation phases of resonant sub-Neptunes". In: *MNRAS* 522.2, pp. 1914–1929. doi: `10.1093/mnras/stad835`. arXiv: `2211.15701 [astro-ph.EP]`.

Clausen, N. et al. (Dec. 2015). "Dissipation in rocky planets for strong tidal forcing". In: *A&A* 584, A60, A60. doi: `10.1051/0004-6361/201526082`.

Cloutier, Ryan et al. (Jan. 2024). "Masses, revised radii, and a third planet candidate in the 'Inverted' planetary system around TOI-1266". In: *MNRAS* 527.3, pp. 5464–5483. doi: `10.1093/mnras/stad3450`. arXiv: `2310.13496 [astro-ph.EP]`.

Cointepas, M. et al. (May 2024). “TOI-663: A newly discovered multi-planet system with three transiting mini-Neptunes orbiting an early M star”. In: *A&A* 685, A19, A19. DOI: `10.1051/0004-6361/202346899`.

Cutri, R. M. et al. (Feb. 2021). *VizieR Online Data Catalog: AllWISE Data Release (Cutri+ 2013).*

Dai, Fei et al. (Jan. 2023). “TOI-1136 is a Young, Coplanar, Aligned Planetary System in a Pristine Resonant Chain”. In: *The Astronomical Journal* 165.2, p. 33. ISSN: 1538-3881. DOI: `10.3847/1538-3881/aca327`. URL: `http://dx.doi.org/10.3847/1538-3881/aca327`.

Damiano, Mario et al. (June 2024). “LHS 1140 b Is a Potentially Habitable Water World”. In: *ApJL* 968.2, L22, p. L22. DOI: `10.3847/2041-8213/ad5204`. arXiv: `2403.13265 [astro-ph.EP]`.

Deck, Katherine M. et al. (June 2014). “TTVFast: An Efficient and Accurate Code for Transit Timing Inversion Problems”. In: *ApJ* 787.2, 132, p. 132. DOI: `10.1088/0004-637X/787/2/132`. arXiv: `1403.1895 [astro-ph.EP]`.

Deck, Katherine M. et al. (Apr. 2015). “Measurement of Planet Masses with Transit Timing Variations Due to Synodic “Chopping” Effects”. In: *ApJ* 802.2, 116, p. 116. DOI: `10.1088/0004-637X/802/2/116`. arXiv: `1411.0004 [astro-ph.EP]`.

Delrez, Laetitia et al. (June 2021). “Transit detection of the long-period volatile-rich super-Earth ν^2 Lupi d with CHEOPS”. In: *Nature Astronomy* 5, pp. 775–787. DOI: `10.1038/s41550-021-01381-5`. arXiv: `2106.14491 [astro-ph.EP]`.

Demangeon, O. D. S. et al. (Sept. 2021). “Warm terrestrial planet with half the mass of Venus transiting a nearby star”. In: *A&A* 653, A41, A41. DOI: `10.1051/0004-6361/202140728`. arXiv: `2108.03323 [astro-ph.EP]`.

Demory, B. -O. et al. (Oct. 2020). “A super-Earth and a sub-Neptune orbiting the bright, quiet M3 dwarf TOI-1266”. In: *A&A* 642, A49, A49. DOI: `10.1051/0004-6361/202038616`. arXiv: `2009.04317 [astro-ph.EP]`.

Di Maio, C. et al. (Jan. 2023). “Analysis of the planetary mass uncertainties on the accuracy of atmospherical retrieval”. In: *A&A* 669, A150, A150. DOI: `10.1051/0004-6361/202244881`. arXiv: `2211.02897 [astro-ph.EP]`.

Diamond-Lowe, Hannah et al. (Nov. 2022). “The K2-3 System Revisited: Testing Photoevaporation and Core-powered Mass Loss with Three Small Planets Spanning the Radius Valley”. In: *AJ* 164.5, 172, p. 172. DOI: `10.3847/1538-3881/ac7807`. arXiv: `2207.12755 [astro-ph.EP]`.

Dorn, Caroline et al. (Jan. 2017). “A generalized Bayesian inference method for constraining the interiors of super Earths and sub-Neptunes”. In: *A&A* 597, A37, A37. DOI: `10.1051/0004-6361/201628708`. arXiv: `1609.03908 [astro-ph.IM]`.

Dorn, Caroline et al. (Nov. 2021). "Hidden Water in Magma Ocean Exoplanets". In: *ApJL* 922.1, L4, p. L4. DOI: `10.3847/2041-8213/ac33af`. arXiv: `2110.15069 [astro-ph.EP]`.

Eastman, Jason et al. (Jan. 2013). "EXOFAST: A Fast Exoplanetary Fitting Suite in IDL". In: *Publications of the Astronomical Society of the Pacific* 125.923, pp. 83–112. ISSN: 1538-3873. DOI: `10.1086/669497`. URL: `http://dx.doi.org/10.1086/669497`.

Eggleton, Peter P. et al. (May 1998). "The Equilibrium Tide Model for Tidal Friction". In: *ApJ* 499.2, pp. 853–870. DOI: `10.1086/305670`. arXiv: `astro-ph/9801246 [astro-ph]`.

Engle, Scott G. (Jan. 2024). "Living with a Red Dwarf: X-Ray, UV, and Ca II Activity-Age Relationships of M Dwarfs". In: *ApJ* 960.1, 62, p. 62. DOI: `10.3847/1538-4357/ad0840`. arXiv: `2310.04302 [astro-ph.SR]`.

Engle, Scott G. et al. (Sept. 2023). "Living with a Red Dwarf: The Rotation-Age Relationships of M Dwarfs". In: *ApJL* 954.2, L50, p. L50. DOI: `10.3847/2041-8213/acf472`. arXiv: `2307.01136 [astro-ph.SR]`.

Fleming, David P. et al. (Mar. 2020). "On the XUV Luminosity Evolution of TRAPPIST-1". In: *ApJ* 891.2, 155, p. 155. DOI: `10.3847/1538-4357/ab77ad`. arXiv: `1906.05250 [astro-ph.SR]`.

Foreman-Mackey, D. (Feb. 2018). "Scalable Backpropagation for Gaussian Processes using Celerite". In: *Research Notes of the American Astronomical Society* 2.1, p. 31. DOI: `10.3847/2515-5172/aaaf6c`.

Foreman-Mackey, D. et al. (Dec. 2017). "Fast and Scalable Gaussian Process Modeling with Applications to Astronomical Time Series". In: *AJ* 154, p. 220. DOI: `10.3847/1538-3881/aa9332`.

Foreman-Mackey, Daniel (2016). "corner.py: Scatterplot matrices in Python". In: *The Journal of Open Source Software* 24. DOI: `10.21105/joss.00024`. URL: `http://dx.doi.org/10.5281/zenodo.45906`.

Foreman-Mackey, Daniel et al. (Mar. 2013). "emcee: The MCMC Hammer". In: *Publications of the Astronomical Society of the Pacific* 125.925, pp. 306–312. ISSN: 1538-3873. DOI: `10.1086/670067`. URL: `http://dx.doi.org/10.1086/670067`.

Foreman-Mackey, Daniel et al. (Nov. 2019). "emcee v3: A Python ensemble sampling toolkit for affine-invariant MCMC". In: *The Journal of Open Source Software* 4.43, 1864, p. 1864. DOI: `10.21105/joss.01864`. arXiv: `1911.07688 [astro-ph.IM]`.

Foreman-Mackey, Daniel et al. (May 2021). "exoplanet: Gradient-based probabilistic inference for exoplanet data & other astronomical time series". In: *arXiv e-prints*, arXiv:2105.01994, arXiv:2105.01994. arXiv: `2105.01994 [astro-ph.IM]`.

Fortney, Jonathan J. et al. (Dec. 2020). “Beyond Equilibrium Temperature: How the Atmosphere/Interior Connection Affects the Onset of Methane, Ammonia, and Clouds in Warm Transiting Giant Planets”. In: *AJ* 160.6, 288, p. 288. DOI: `10.3847/1538-3881/abc5bd`. arXiv: `2010.00146 [astro-ph.EP]`.

Fukui, A. et al. (Feb. 2011). “Measurements of Transit Timing Variations for WASP-5b”. In: *PASJ* 63, pp. 287–300. DOI: `10.1093/pasj/63.1.287`. arXiv: `1009.5769 [astro-ph.EP]`.

Gaia Collaboration (Apr. 2018). *VizieR Online Data Catalog: Gaia DR2 (Gaia Collaboration, 2018)*. DOI: `10.26093/cds/vizier.1345`.

Gan, Tianjun et al. (Mar. 2022). “TOI-530b: a giant planet transiting an M-dwarf detected by TESS”. In: *MNRAS* 511.1, pp. 83–99. DOI: `10.1093/mnras/stab3708`. arXiv: `2110.04220 [astro-ph.EP]`.

Gao, Peter et al. (July 2023). “The Hazy and Metal-rich Atmosphere of GJ 1214 b Constrained by Near- and Mid-infrared Transmission Spectroscopy”. In: *ApJ* 951.2, 96, p. 96. DOI: `10.3847/1538-4357/acd16f`. arXiv: `2305.05697 [astro-ph.EP]`.

García-Melendo, E. et al. (Oct. 2011). “Potential biases in the detection of planetary systems with large transit timing variations”. In: *MNRAS* 417.1, pp. L16–L20. DOI: `10.1111/j.1745-3933.2011.01111.x`. arXiv: `1107.1666 [astro-ph.EP]`.

Gladman, Brett et al. (July 1996). “Synchronous Locking of Tidally Evolving Satellites”. In: *Icarus* 122.1, pp. 166–192. DOI: `10.1006/icar.1996.0117`.

Goldberg, Max et al. (June 2021). “A Tidal Origin for a Three-body Resonance in Kepler-221”. In: *The Astronomical Journal* 162.1, p. 16. ISSN: 1538-3881. DOI: `10.3847/1538-3881/abfb78`. URL: `http://dx.doi.org/10.3847/1538-3881/abfb78`.

– (Mar. 2022). “Architectures of Compact Super-Earth Systems Shaped by Instabilities”. In: *arXiv e-prints*, arXiv:2203.00801, arXiv:2203.00801. arXiv: `2203.00801 [astro-ph.EP]`.

– (May 2023). “Dynamics and Origins of the Near-resonant Kepler Planets”. In: *ApJ* 948.1, 12, p. 12. DOI: `10.3847/1538-4357/acc9ae`. arXiv: `2211.16725 [astro-ph.EP]`.

Goldreich, Peter et al. (Jan. 1966). “Q in the Solar System”. In: *Icarus* 5.1, pp. 375–389. DOI: `10.1016/0019-1035(66)90051-0`.

Goyal, Armaan V. et al. (Oct. 2023). “Enhanced Size Uniformity for Near-resonant Planets”. In: *ApJ* 955.2, 118, p. 118. DOI: `10.3847/1538-4357/acebe2`. arXiv: `2307.15875 [astro-ph.EP]`.

Goyal, Armaan V. et al. (June 2024). “Peas-in-a-pod across the Radius Valley: Rocky Systems Are Less Uniform in Mass but More Uniform in Size and Spacing”. In: *ApJL* 968.1, L4, p. L4. DOI: `10.3847/2041-8213/ad4f6e`. arXiv: `2405.14091 [astro-ph.EP]`.

Goździewski, K. et al. (Nov. 2015). “The Laplace resonance in the Kepler-60 planetary system”. In: *Monthly Notices of the Royal Astronomical Society: Letters* 455.1, pp. L104–L108. ISSN: 1745-3933. DOI: `10.1093/mnrasl/slv156`. URL: `http://dx.doi.org/10.1093/mnrasl/slv156`.

Greklek-McKeon, Michael et al. (Feb. 2023). “Constraining the Densities of the Three Kepler-289 Planets with Transit Timing Variations”. In: *AJ* 165.2, 48, p. 48. DOI: `10.3847/1538-3881/ac8553`. arXiv: `2208.00022 [astro-ph.EP]`.

Hadden, Sam (Dec. 2019). “An Integrable Model for the Dynamics of Planetary Mean-motion Resonances”. In: *AJ* 158.6, 238, p. 238. DOI: `10.3847/1538-3881/ab5287`. arXiv: `1909.05264 [astro-ph.EP]`.

Hadden, Sam et al. (Sept. 2016). “Numerical and Analytical Modeling of Transit Timing Variations”. In: *ApJ* 828.1, 44, p. 44. DOI: `10.3847/0004-637X/828/1/44`. arXiv: `1510.02476 [astro-ph.EP]`.

Harman, C. E. et al. (Feb. 2022). “A Snowball in Hell: The Potential Steam Atmosphere of TOI-1266c”. In: *PSJ* 3.2, 45, p. 45. DOI: `10.3847/PSJ/ac38ac`. arXiv: `2109.10838 [astro-ph.EP]`.

He, Matthias Y. et al. (Dec. 2020). “Architectures of Exoplanetary Systems. III. Eccentricity and Mutual Inclination Distributions of AMD-stable Planetary Systems”. In: *AJ* 160.6, 276, p. 276. DOI: `10.3847/1538-3881/abba18`. arXiv: `2007.14473 [astro-ph.EP]`.

Henden, Arne A. et al. (Jan. 2015). “APASS - The Latest Data Release”. In: *American Astronomical Society Meeting Abstracts #225*. Vol. 225. American Astronomical Society Meeting Abstracts, 336.16, p. 336.16.

Higson, Edward, Will Handley, Michael Hobson, et al. (Feb. 2019). “NESTCHECK: diagnostic tests for nested sampling calculations”. In: *MNRAS* 483.2, pp. 2044–2056. DOI: `10.1093/mnras/sty3090`. arXiv: `1804.06406 [stat.CO]`.

Higson, Edward, Will Handley, Mike Hobson, et al. (Sept. 2019). “Dynamic nested sampling: an improved algorithm for parameter estimation and evidence calculation”. In: *Statistics and Computing* 29.5, pp. 891–913. DOI: `10.1007/s11222-018-9844-0`. arXiv: `1704.03459 [stat.CO]`.

Hippke, Michael et al. (Feb. 2019). “Optimized transit detection algorithm to search for periodic transits of small planets”. In: *Astronomy & Astrophysics* 623, A39. ISSN: 1432-0746. DOI: `10.1051/0004-6361/201834672`. URL: `http://dx.doi.org/10.1051/0004-6361/201834672`.

Hobson, M. J. et al. (Aug. 2024). “Three super-Earths and a possible water world from TESS and ESPRESSO”. In: *A&A* 688, A216, A216. DOI: `10.1051/0004-6361/202450505`. arXiv: `2406.06278 [astro-ph.EP]`.

Hord, Benjamin J. et al. (May 2024). "Identification of the Top TESS Objects of Interest for Atmospheric Characterization of Transiting Exoplanets with JWST". In: *AJ* 167.5, 233, p. 233. DOI: `10.3847/1538-3881/ad3068`. arXiv: `2308.09617 [astro-ph.EP]`.

Hori, Yasunori et al. (Feb. 2020). "Do the TRAPPIST-1 Planets Have Hydrogen-rich Atmospheres?" In: *ApJ* 889.2, 77, p. 77. DOI: `10.3847/1538-4357/ab6168`. arXiv: `1912.05749 [astro-ph.EP]`.

Hu, Renyu et al. (Nov. 2021). "Unveiling Shrouded Oceans on Temperate sub-Neptunes via Transit Signatures of Solubility Equilibria versus Gas Thermochemistry". In: *ApJL* 921.1, L8, p. L8. DOI: `10.3847/2041-8213/ac1f92`. arXiv: `2108.04745 [astro-ph.EP]`.

Husser, T. -O. et al. (May 2013). "A new extensive library of PHOENIX stellar atmospheres and synthetic spectra". In: *A&A* 553, A6, A6. DOI: `10.1051/0004-6361/201219058`. arXiv: `1303.5632 [astro-ph.SR]`.

Jackson, Brian et al. (Nov. 2008). "Tidal heating of terrestrial extrasolar planets and implications for their habitability". In: *MNRAS* 391.1, pp. 237–245. DOI: `10.1111/j.1365-2966.2008.13868.x`. arXiv: `0808.2770 [astro-ph]`.

Judkovsky, Yair et al. (2023). *The Advantages of Global Photometric Models in Fitting Transit Variations*. arXiv: `2311.06948 [astro-ph.EP]`. URL: `https://arxiv.org/abs/2311.06948`.

Kellermann, C. et al. (July 2018). "Interior structure models and fluid Love numbers of exoplanets in the super-Earth regime". In: *A&A* 615, A39, A39. DOI: `10.1051/0004-6361/201731775`.

Kempton, Eliza M. -R. et al. (Nov. 2018). "A Framework for Prioritizing the TESS Planetary Candidates Most Amenable to Atmospheric Characterization". In: *PASP* 130.993, p. 114401. DOI: `10.1088/1538-3873/aadf6f`. arXiv: `1805.03671 [astro-ph.EP]`.

Kimura, Tadahiro et al. (Nov. 2022). "Predicted diversity in water content of terrestrial exoplanets orbiting M dwarfs". In: *Nature Astronomy* 6, pp. 1296–1307. DOI: `10.1038/s41550-022-01781-1`. arXiv: `2209.14563 [astro-ph.EP]`.

Kochanek, C. S. et al. (Oct. 2017). "The All-Sky Automated Survey for Supernovae (ASAS-SN) Light Curve Server v1.0". In: *PASP* 129.980, p. 104502. DOI: `10.1088/1538-3873/aa80d9`. arXiv: `1706.07060 [astro-ph.SR]`.

Kovács, G. et al. (July 2002). "A box-fitting algorithm in the search for periodic transits". In: *Astronomy &; Astrophysics* 391.1, pp. 369–377. ISSN: 1432-0746. DOI: `10.1051/0004-6361:20020802`. URL: `http://dx.doi.org/10.1051/0004-6361:20020802`.

Kuzuhara, Masayuki et al. (June 2024). “Gliese 12 b: A Temperate Earth-sized Planet at 12 pc Ideal for Atmospheric Transmission Spectroscopy”. In: *ApJL* 967.2, L21, p. L21. DOI: `10.3847/2041-8213/ad3642`. arXiv: `2405.14708 [astro-ph.EP]`.

Leleu, A., Y. Alibert, et al. (May 2021). “Six transiting planets and a chain of Laplace resonances in TOI-178”. In: *A&A* 649, A26, A26. DOI: `10.1051/0004-6361/202039767`. arXiv: `2101.09260 [astro-ph.EP]`.

Leleu, A., G. Chatel, et al. (Nov. 2021). “Alleviating the transit timing variation bias in transit surveys: I. RIVERS: Method and detection of a pair of resonant super-Earths around Kepler-1705”. In: *Astronomy &; Astrophysics* 655, A66. ISSN: 1432-0746. DOI: `10.1051/0004-6361/202141471`. URL: `http://dx.doi.org/10.1051/0004-6361/202141471`.

Leleu, Adrien et al. (July 2024). “Resonant sub-Neptunes are puffier”. In: *A&A* 687, L1, p. L1. DOI: `10.1051/0004-6361/202450587`. arXiv: `2406.18991 [astro-ph.EP]`.

Li, Rixin et al. (2024). *The Resonant Remains of Broken Chains from Major and Minor Mergers*. arXiv: `2408.10206 [astro-ph.EP]`. URL: `https://arxiv.org/abs/2408.10206`.

Linssen, Dion et al. (Aug. 2024). “The open-source sunbather code: Modeling escaping planetary atmospheres and their transit spectra”. In: *A&A* 688, A43, A43. DOI: `10.1051/0004-6361/202450240`. arXiv: `2404.12775 [astro-ph.EP]`.

Lissauer, Jack J. et al. (Nov. 2011). “Architecture and Dynamics of Kepler’s Candidate Multiple Transiting Planet Systems”. In: *ApJS* 197.1, 8, p. 8. DOI: `10.1088/0067-0049/197/1/8`. arXiv: `1102.0543 [astro-ph.EP]`.

Lithwick, Yoram et al. (Dec. 2012). “Extracting Planet Mass and Eccentricity from TTV Data”. In: *ApJ* 761.2, 122, p. 122. DOI: `10.1088/0004-637X/761/2/122`. arXiv: `1207.4192 [astro-ph.EP]`.

Lodders, Katharina (July 2003). “Solar System Abundances and Condensation Temperatures of the Elements”. In: *ApJ* 591.2, pp. 1220–1247. DOI: `10.1086/375492`.

Louden, Emma M. et al. (Dec. 2023). “Tidal Dissipation Regimes among the Short-period Exoplanets”. In: *ApJL* 958.2, L21, p. L21. DOI: `10.3847/2041-8213/ad0843`. arXiv: `2311.03576 [astro-ph.EP]`.

Lu, Tiger et al. (May 2023). “Self-consistent Spin, Tidal, and Dynamical Equations of Motion in the REBOUNDx Framework”. In: *The Astrophysical Journal* 948.1, p. 41. ISSN: 1538-4357. DOI: `10.3847/1538-4357/acc06d`. URL: `http://dx.doi.org/10.3847/1538-4357/acc06d`.

Luque, Rafael et al. (Sept. 2022). “Density, not radius, separates rocky and water-rich small planets orbiting M dwarf stars”. In: *Science* 377.6611, pp. 1211–1214. DOI: `10.1126/science.abl7164`. arXiv: `2209.03871 [astro-ph.EP]`.

MacDonald, Mariah G. et al. (Oct. 2016). “A Dynamical Analysis of the Kepler-80 System of Five Transiting Planets”. In: *AJ* 152.4, 105, p. 105. DOI: `10.3847/0004-6256/152/4/105`. arXiv: `1607.07540 [astro-ph.EP]`.

MacKenzie, Jasmine et al. (Mar. 2023). “Effect of improved atmospheric opacities in modelling sub-Neptunes. A case study for GJ 1214 b”. In: *A&A* 671, A65, A65. DOI: `10.1051/0004-6361/202141784`.

Madhusudhan, Nikku et al. (Oct. 2023). “Carbon-bearing Molecules in a Possible Hycean Atmosphere”. In: *ApJL* 956.1, L13, p. L13. DOI: `10.3847/2041-8213/acf577`. arXiv: `2309.05566 [astro-ph.EP]`.

Maldonado, J. et al. (May 2015). “Stellar parameters of early-M dwarfs from ratios of spectral features at optical wavelengths”. In: *A&A* 577, A132, A132. DOI: `10.1051/0004-6361/201525797`. arXiv: `1503.03010 [astro-ph.SR]`.

Masci, Frank J. et al. (Jan. 2019). “The Zwicky Transient Facility: Data Processing, Products, and Archive”. In: *PASP* 131.995, p. 018003. DOI: `10.1088/1538-3873/aae8ac`. arXiv: `1902.01872 [astro-ph.IM]`.

McCully, Curtis et al. (July 2018). “Real-time processing of the imaging data from the network of Las Cumbres Observatory Telescopes using BANZAI”. In: *Proc. SPIE*. Vol. 10707. Society of Photo-Optical Instrumentation Engineers (SPIE) Conference Series, 107070K, 107070K. DOI: `10.1117/12.2314340`. arXiv: `1811.04163 [astro-ph.IM]`.

Millholland, Sarah et al. (Nov. 2017). “Kepler Multi-planet Systems Exhibit Unexpected Intra-system Uniformity in Mass and Radius”. In: *The Astrophysical Journal Letters* 849.2, p. L33. ISSN: 2041-8213. DOI: `10.3847/2041-8213/aa9714`. URL: `http://dx.doi.org/10.3847/2041-8213/aa9714`.

Millholland, Sarah C. et al. (Aug. 2022). “Edge-of-the-Multis: Evidence for a Transition in the Outer Architectures of Compact Multiplanet Systems”. In: *AJ* 164.2, 72, p. 72. DOI: `10.3847/1538-3881/ac7c67`. arXiv: `2207.10068 [astro-ph.EP]`.

Millholland, Sarah C. et al. (Feb. 2024). “Spin Dynamics of Planets in Resonant Chains”. In: *ApJ* 961.2, 203, p. 203. DOI: `10.3847/1538-4357/ad10a0`. arXiv: `2311.17908 [astro-ph.EP]`.

Mills, Sean M. et al. (May 2016). “A resonant chain of four transiting, sub-Neptune planets”. In: *Nature* 533.7604, pp. 509–512. DOI: `10.1038/nature17445`. arXiv: `1612.07376 [astro-ph.EP]`.

Mortier, A. et al. (Dec. 2020). “K2-111: an old system with two planets in near-resonance”. In: *MNRAS* 499.4, pp. 5004–5021. DOI: `10.1093/mnras/staa3144`. arXiv: `2010.01993 [astro-ph.EP]`.

Murgas, F. et al. (Apr. 2024). “Wolf 327b: A new member of the pack of ultra-short-period super-Earths around M dwarfs”. In: *A&A* 684, A83, A83. DOI: `10.1051/0004-6361/202348813`. arXiv: `2401.12150 [astro-ph.EP]`.

Narita, Norio et al. (Oct. 2015). "MuSCAT: a multicolor simultaneous camera for studying atmospheres of transiting exoplanets". In: *Journal of Astronomical Telescopes, Instruments, and Systems* 1, 045001, p. 045001. DOI: `10.1117/1.JATIS.1.4.045001`. arXiv: `1509.03154 [astro-ph.IM]`.

Narita, Norio et al. (Dec. 2020). "MuSCAT3: a 4-color simultaneous camera for the 2m Faulkes Telescope North". In: *Society of Photo-Optical Instrumentation Engineers (SPIE) Conference Series*. Vol. 11447. Society of Photo-Optical Instrumentation Engineers (SPIE) Conference Series, 114475K, 114475K. DOI: `10.1117/12.2559947`.

Nelson, Benjamin et al. (Jan. 2014). "RUN DMC: An Efficient, Parallel Code for Analyzing Radial Velocity Observations Using N-body Integrations and Differential Evolution Markov Chain Monte Carlo". In: *ApJS* 210.1, 11, p. 11. DOI: `10.1088/0067-0049/210/1/11`. arXiv: `1311.5229 [astro-ph.EP]`.

Nesvorný, David et al. (July 2014a). "The Effect of Conjunctions on the Transit Timing Variations of Exoplanets". In: *ApJ* 790.1, 58, p. 58. DOI: `10.1088/0004-637X/790/1/58`. arXiv: `1405.7433 [astro-ph.EP]`.

– (July 2014b). "The Effect of Conjunctions on the Transit Timing Variations of Exoplanets". In: *ApJ* 790.1, 58, p. 58. DOI: `10.1088/0004-637X/790/1/58`. arXiv: `1405.7433 [astro-ph.EP]`.

Nettelmann, N. et al. (May 2011). "Thermal Evolution and Structure Models of the Transiting Super-Earth GJ 1214b". In: *ApJ* 733.1, 2, p. 2. DOI: `10.1088/0004-637X/733/1/2`. arXiv: `1010.0277 [astro-ph.EP]`.

Ormel, Chris W. et al. (July 2017). "Formation of TRAPPIST-1 and other compact systems". In: *A&A* 604, A1, A1. DOI: `10.1051/0004-6361/201730826`. arXiv: `1703.06924 [astro-ph.EP]`.

Otegi, J. F. et al. (Feb. 2022). "The similarity of multi-planet systems". In: *A&A* 658, A107, A107. DOI: `10.1051/0004-6361/202142110`.

Parc, Léna et al. (Aug. 2024). "From super-Earths to sub-Neptunes: Observational constraints and connections to theoretical models". In: *A&A* 688, A59, A59. DOI: `10.1051/0004-6361/202449911`. arXiv: `2406.04311 [astro-ph.EP]`.

Parviainen, H. et al. (Sept. 2015). "ldtk: Limb Darkening Toolkit". In: *Monthly Notices of the Royal Astronomical Society* 453.4, pp. 3822–3827. ISSN: 1365-2966. DOI: `10.1093/mnras/stv1857`. URL: `http://dx.doi.org/10.1093/mnras/stv1857`.

Pérez-González, Jorge et al. (May 2024). "Detection of an Atmospheric Outflow from the Young Hot Saturn TOI-1268b". In: *AJ* 167.5, 214, p. 214. DOI: `10.3847/1538-3881/ad34b6`. arXiv: `2307.09515 [astro-ph.EP]`.

Piaulet, Caroline et al. (Feb. 2023). "Evidence for the volatile-rich composition of a 1.5-Earth-radius planet". In: *Nature Astronomy* 7, pp. 206–222. DOI: `10.1038/s41550-022-01835-4`. arXiv: `2212.08477 [astro-ph.EP]`.

Piaulet-Ghorayeb, Caroline et al. (Oct. 2024). "JWST/NIRISS Reveals the Water-rich "Steam World" Atmosphere of GJ 9827 d". In: *ApJL* 974.1, L10, p. L10. DOI: `10.3847/2041-8213/ad6f00`. arXiv: `2410.03527 [astro-ph.EP]`.

Pierrehumbert, Raymond T. (Feb. 2023). "The Runaway Greenhouse on Sub-Neptune Waterworlds". In: *ApJ* 944.1, 20, p. 20. DOI: `10.3847/1538-4357/acafdf`. arXiv: `2212.02644 [astro-ph.EP]`.

Plotnykov, Mykhaylo et al. (Nov. 2020). "Chemical fingerprints of formation in rocky super-Earths' data". In: *MNRAS* 499.1, pp. 932–947. DOI: `10.1093/mnras/staa2615`. arXiv: `2010.06480 [astro-ph.EP]`.

Raftery, Adrian E. (1995). "Bayesian Model Selection in Social Research." In: *JSTOR* 25, pp. 111–63. DOI: `10.2307/271063`.

Rein, Hanno et al. (July 2015). "whfast: a fast and unbiased implementation of a symplectic Wisdom–Holman integrator for long-term gravitational simulations". In: *Monthly Notices of the Royal Astronomical Society* 452.1, pp. 376–388. ISSN: 1365-2966. DOI: `10.1093/mnras/stv1257`. URL: `http://dx.doi.org/10.1093/mnras/stv1257`.

Rice, David R. et al. (June 2024). "The Distribution of Planet Radius in Kepler Multiplanet Systems Depends on Gap Complexity". In: *arXiv e-prints*, arXiv:2406.12239, arXiv:2406.12239. DOI: `10.48550/arXiv.2406.12239`. arXiv: `2406.12239 [astro-ph.EP]`.

Ricker, George R. et al. (Oct. 2014). "Transiting Exoplanet Survey Satellite". In: *Journal of Astronomical Telescopes, Instruments, and Systems* 1.1, p. 014003. ISSN: 2329-4124. DOI: `10.1117/1.jatis.1.1.014003`. URL: `http://dx.doi.org/10.1117/1.JATIS.1.1.014003`.

Roettenbacher, Rachael M. et al. (Dec. 2017). "The Stellar Activity of TRAPPIST-1 and Consequences for the Planetary Atmospheres". In: *ApJ* 851.2, 77, p. 77. DOI: `10.3847/1538-4357/aa991e`. arXiv: `1711.02676 [astro-ph.SR]`.

Rogers, James G. et al. (Apr. 2023). "Conclusive Evidence for a Population of Water Worlds around M Dwarfs Remains Elusive". In: *ApJL* 947.1, L19, p. L19. DOI: `10.3847/2041-8213/acc86f`. arXiv: `2301.04321 [astro-ph.EP]`.

Rogers, James G. et al. (Jan. 2025). "Most Super-Earths Have Less Than 3% Water". In: *ApJ* 979.1, 79, p. 79. DOI: `10.3847/1538-4357/ad9f61`. arXiv: `2409.17394 [astro-ph.EP]`.

Rosário, N. M. et al. (June 2024). "Precise characterisation of HD 15337 with CHEOPS: A laboratory for planet formation and evolution". In: *A&A* 686, A282, A282. DOI: `10.1051/0004-6361/202347759`. arXiv: `2403.16621 [astro-ph.EP]`.

Salvatier, John et al. (2016). "Probabilistic programming in Python using PyMC3". In: *PeerJ Computer Science* 2, e55.

Schwarz, Gideon (July 1978). “Estimating the Dimension of a Model”. In: *Annals of Statistics* 6.2, pp. 461–464.

Seligman, Darryl Z. et al. (2023). *Potential Melting of Extrasolar Planets by Tidal Dissipation*. arXiv: `2311.01187 [astro-ph.EP]`. URL: `https://arxiv.org/abs/2311.01187`.

Stassun, Keivan G. et al. (Dec. 2016). “Eclipsing Binaries as Benchmarks for Trigonometric Parallaxes in the Gaia Era”. In: *AJ* 152.6, 180, p. 180. DOI: `10.3847/0004-6256/152/6/180`. arXiv: `1609.02579 [astro-ph.SR]`.

Stassun, Keivan G. et al. (Mar. 2017). “Accurate Empirical Radii and Masses of Planets and Their Host Stars with Gaia Parallaxes”. In: *AJ* 153.3, 136, p. 136. DOI: `10.3847/1538-3881/aa5df3`. arXiv: `1609.04389 [astro-ph.EP]`.

Stassun, Keivan G. et al. (Sept. 2018). “The TESS Input Catalog and Candidate Target List”. In: *AJ* 156.3, 102, p. 102. DOI: `10.3847/1538-3881/aad050`. arXiv: `1706.00495 [astro-ph.EP]`.

Stassun, Keivan G. et al. (Oct. 2019). “The Revised TESS Input Catalog and Candidate Target List”. In: *AJ* 158.4, 138, p. 138. DOI: `10.3847/1538-3881/ab3467`. arXiv: `1905.10694 [astro-ph.SR]`.

Stefansson, Gudmundur et al. (Oct. 2017). “Toward Space-like Photometric Precision from the Ground with Beam-shaping Diffusers”. In: *ApJ* 848.1, 9, p. 9. DOI: `10.3847/1538-4357/aa88aa`. arXiv: `1710.01790 [astro-ph.IM]`.

Stefansson, Gudmundur et al. (Mar. 2020). “A Sub-Neptune-sized Planet Transiting the M2.5 Dwarf G 9-40: Validation with the Habitable-zone Planet Finder”. In: *AJ* 159.3, 100, p. 100. DOI: `10.3847/1538-3881/ab5f15`. arXiv: `1912.00291 [astro-ph.EP]`.

Stefánsson, Guðmundur et al. (Dec. 2020). “A Mini-Neptune and a Radius Valley Planet Orbiting the Nearby M2 Dwarf TOI-1266 in Its Venus Zone: Validation with the Habitable-zone Planet Finder”. In: *AJ* 160.6, 259, p. 259. DOI: `10.3847/1538-3881/abbe19`.

Suárez Mascareño, A. et al. (May 2024). “TESS and ESPRESSO discover a super-Earth and a mini-Neptune orbiting the K-dwarf TOI-238*”. In: *A&A* 685, A56, A56. DOI: `10.1051/0004-6361/202348958`. arXiv: `2402.04113 [astro-ph.EP]`.

Tamayo, Daniel et al. (Jan. 2020). “REBOUNDx: a library for adding conservative and dissipative forces to otherwise symplectic N-body integrations”. In: *MNRAS* 491.2, pp. 2885–2901. DOI: `10.1093/mnras/stz2870`. arXiv: `1908.05634 [astro-ph.EP]`.

Tobie, G. et al. (Oct. 2019). “Tidal response of rocky and ice-rich exoplanets”. In: *A&A* 630, A70, A70. DOI: `10.1051/0004-6361/201935297`.

Van Eylen, Vincent et al. (Feb. 2019). “The Orbital Eccentricity of Small Planet Systems”. In: *AJ* 157.2, 61, p. 61. DOI: `10.3847/1538-3881/aaf22f`. arXiv: `1807.00549 [astro-ph.EP]`.

Veeder, Glenn J. et al. (June 2012). “Io: Volcanic thermal sources and global heat flow”. In: *Icarus* 219.2, pp. 701–722. DOI: `10.1016/j.icarus.2012.04.004`.

Vissapragada, Shreyas et al. (Feb. 2020). “Diffuser-assisted Infrared Transit Photometry for Four Dynamically Interacting Kepler Systems”. In: *The Astronomical Journal* 159.3, p. 108. ISSN: 1538-3881. DOI: `10.3847/1538-3881/ab65c8`. URL: `http://dx.doi.org/10.3847/1538-3881/ab65c8`.

Wallack, Nicole L. et al. (Aug. 2024). “JWST COMPASS: A NIRSpec/G395H Transmission Spectrum of the Sub-Neptune TOI-836c”. In: *AJ* 168.2, 77, p. 77. DOI: `10.3847/1538-3881/ad3917`. arXiv: `2404.01264 [astro-ph.EP]`.

Weiss, Lauren M. et al. (Jan. 2018). “The California-Kepler Survey. V. Peas in a Pod: Planets in a Kepler Multi-planet System Are Similar in Size and Regularly Spaced”. In: *AJ* 155.1, 48, p. 48. DOI: `10.3847/1538-3881/aa9ff6`. arXiv: `1706.06204 [astro-ph.EP]`.

Wilson, John C. et al. (Mar. 2003). “A Wide-Field Infrared Camera for the Palomar 200-inch Telescope”. In: *Instrument Design and Performance for Optical/Infrared Ground-based Telescopes*. Ed. by Masanori Iye et al. Vol. 4841. Society of Photo-Optical Instrumentation Engineers (SPIE) Conference Series, pp. 451–458. DOI: `10.1117/12.460336`.

Wogan, Nicholas F. et al. (Mar. 2024). “JWST Observations of K2-18b Can Be Explained by a Gas-rich Mini-Neptune with No Habitable Surface”. In: *ApJL* 963.1, L7, p. L7. DOI: `10.3847/2041-8213/ad2616`. arXiv: `2401.11082 [astro-ph.EP]`.

Yang, Jeehyun et al. (Aug. 2024). “Chemical Mapping of Temperate Sub-Neptune Atmospheres: Constraining the Deep Interior H_2O/H_2 Ratio from the Atmospheric CO_2/CH_4 Ratio”. In: *ApJL* 971.2, L48, p. L48. DOI: `10.3847/2041-8213/ad6b25`. arXiv: `2406.01955 [astro-ph.EP]`.

Yee, Samuel W. et al. (Feb. 2017). “Precision Stellar Characterization of FGKM Stars using an Empirical Spectral Library”. In: *ApJ* 836.1, 77, p. 77. DOI: `10.3847/1538-4357/836/1/77`. arXiv: `1701.00922 [astro-ph.SR]`.

Yoshida, Tatsuya et al. (Aug. 2022). “Less Effective Hydrodynamic Escape of H_2-H_2O Atmospheres on Terrestrial Planets Orbiting Pre-main-sequence M Dwarfs”. In: *ApJ* 934.2, 137, p. 137. DOI: `10.3847/1538-4357/ac7be7`. arXiv: `2207.06570 [astro-ph.EP]`.

Zeng, Li et al. (Mar. 2016). “Mass-Radius Relation for Rocky Planets Based on PREM”. In: *ApJ* 819.2, 127, p. 127. DOI: `10.3847/0004-637X/819/2/127`. arXiv: `1512.08827 [astro-ph.EP]`.

Zhang, Michael et al. (Feb. 2022). “Escaping Helium from TOI 560.01, a Young Mini-Neptune”. In: *AJ* 163.2, 67, p. 67. DOI: `10.3847/1538-3881/ac3fa7`. arXiv: `2110.13150 [astro-ph.EP]`.

Chapter 4

UPDATED MASS, ECCENTRICITY, AND TIDAL HEATING CONSTRAINTS FOR THE EARTH-SIZED PLANET LP 791-18 D

Greklek-McKeon, Michael, Heather A. Knutson, and W. Garrett Levine, et al. (2025). "Updated Mass, Eccentricity, and Tidal Heating Constraints for the Earth-sized Planet LP 791-18 d". In: *arXiv e-prints* arXiv:2501.18700. DOI: `10.48550/arXiv.2501.18700`.

Abstract

LP 791-18 d is an Earth-sized planet (R_d = 1.03 $R_\oplus$) orbiting a late M dwarf, with an interior super-Earth (R_b = 1.2 $R_\oplus$) and an exterior sub-Neptune (R_c = 2.5 $R_\oplus$). Dynamical interactions between LP 791-18 d and c produce transit timing variations (TTVs) that can constrain the planet masses and eccentricities. These interactions can also force a non-zero eccentricity for LP 791-18 d, which raises its internal temperature through tidal heating and could drive volcanic outgassing. We present three new transit observations of LP 791-18 c with Palomar/WIRC, including the most precise TTV measurements (< 6 second uncertainty) of this planet to date. We fit these times with a TTV model to update the mass, eccentricity, and tidal heating constraints of LP 791-18 d. We reduce the mass uncertainty by more than a factor of two ($M_d = 0.91 \pm 0.19$ $M_\oplus$). We perform an updated fit assuming tidally damped free eccentricities and find $e_d = 0.0011^{+0.0010}_{-0.0008}$ and $e_c = 0.0001 \pm 0.0001$, consistent with circular orbits. We find that the observed TTVs are not sensitive to $e \leq \sim 0.01$. Without a tidally damped eccentricity prior, $e_d = 0.056^{+0.015}_{-0.014}$, though damping is expected if Q'_d is Earth-like. We predict a JWST eclipse timing offset relative to a circular orbit for LP 791-18 d of ($\Delta t = -0.2^{+2.0}_{-2.7}$ and $\Delta t = -117^{+41}_{-47}$ minutes for the damped and undamped eccentricity cases, respectively), which could tightly constrain the eccentricity and tidal quality factor of this Earth-sized exoplanet.

4.1 Introduction

Small planets transiting low-mass stars enable the detailed study of exoplanets with Earth-like sizes and compositions. Of these planets, temperate worlds transiting cooler and smaller late M stars offer the rare opportunity to study the atmospheres of these Earth-sized planets with the James Webb Space Telescope (JWST). Planets orbiting smaller stars have relatively stronger atmospheric transmission features, making even compact, high mean-molecular weight atmospheres accessible to characterization with JWST (e.g., Piaulet-Ghorayeb et al., 2024; Banerjee et al., 2024; Gressier et al., 2024). Yet, despite extensive ongoing searches, there are currently only four known temperate (< 400 K), Earth-sized ($< 1.1\ R_\oplus$) transiting planets outside of the TRAPPIST-1 system (NASA Exoplanet Archive, 2024). This population includes a recently discovered Earth-sized planet transiting the M6 star LP 791-18 (Peterson et al., 2023, hereafter referred to as P23). LP 791-18 d has a radius of $1.03 \pm 0.04\ R_\oplus$, an orbital period of 2.75 days, and an equilibrium temperature of 396 K, with a tidally-locked permanent night-side that could plausibly allow for water condensation (P23). It is part of a three planet system, with a sub-Neptune ($2.5\ R_\oplus$, $P = 4.99$ days) LP 791-18 c on an exterior orbit, and a super-Earth ($1.2\ R_\oplus$, $P = 0.95$ days) LP 791-18 b on an interior orbit (Crossfield et al., 2019).

It is often challenging to measure masses for small planets using the radial velocity technique (e.g., Dai et al., 2024; Wright, 2018; Fischer et al., 2016). Fortunately, dynamical interactions between planets in the LP 791-18 system cause detectable transit timing variations (TTVs) that can be used to constrain the planet masses and orbital eccentricities. P23 carried out an extensive transit follow-up campaign to characterize the TTVs in this system, including a near-continuous 172 hour Spitzer observation that was conducted in 2019 to confirm the existence of LP 791-18 d. These data were supplemented by an additional 19 ground-based transits of planet c and 40 transits of planet d executed on 0.4-1.9m facilities including LCOGT, EDEN, ExTrA, SPECULOOS, TRAPPIST, MEarth, MuSCAT, and MuSCAT2. These observations resulted in the detection of TTV signals with amplitudes of $\sim$2.5 min and $\sim$0.5 min for for planets c and d, respectively. P23 also found that there was a strong “chopping” TTV signal in their data, indicating that the planets in this system have relatively large mass ratios and/or eccentric orbits (Lithwick et al., 2012; Deck et al., 2014). They found that LP 791-18 c has a mass of $7.1 \pm 0.7\ M_\oplus$ and LP 791-18 d has a mass of $0.9^{+0.5}_{-0.4}\ M_\oplus$, and predicted with dynamical simulations that LP 791-18 d maintains a non-zero forced eccentricity of $\sim$0.0015 that is stable long-term over the system age due to dynamical interactions with the nearby orbit of the more massive LP 791-18 c.

LP 791-18 d’s relatively close-in orbit means that this tiny eccentricity of 0.0015 has an outsized impact on the planet’s overall energy budget. Tidal heating in rocky planets impacts interior ice and silicate melting, surface temperature, atmospheric properties, and potential habitability (Jackson et al., 2008; Quick et al., 2020; Seligman et al., 2023). If LP 791-18 d has an Earth-like composition and tidal quality factor, the implied tidal heat flux from an eccentricity of 0.0015 is similar to that of Jupiter's moon Io, the most volcanically active body in the solar system (P23). This has significant implications for the atmosphere of LP 791-18 d, which may be dominated by volcanically produced gases. Recent JWST/NIRSpec/NIRISS transmission spectroscopy of the 1.58 $R_\oplus$ planet L 98-59 d indicated that this planet may host a sulfur-rich atmosphere, potentially due to volcanic outgassing (Gressier et al., 2024; Banerjee et al., 2024). Like LP 791-18 d, L 98-59 d also has a non-zero eccentricity ($0.074^{+0.057}_{-0.046}$) that has been suggested as a potential driver of volcanic outgassing due to tidal heating (Seligman et al., 2023). An upcoming JWST/MIRI program (GO 6457) will search for the presence of an outgassed atmosphere for LP 791-18 d using secondary eclipse observations, but the predicted tidal heat flux and volcanic outgassing rate depends in part on the orbital eccentricity, and the predicted timing of these eclipses depends sensitively on the assumed orbital eccentricity and longitude of periastron.

The precision of the current mass and eccentricity constraints for LP 791-18 d are limited by the relatively small amplitude of the TTVs (~ 40 s) that it induces on the much more massive planet c. Among the ensemble of transit timing measurements presented in P23, the Spitzer observations were the only ones precise enough to detect these timing variations, and as a result they drive the TTV constraints for both planets. In this study, we utilize diffuser-assisted infrared transit photometry with the Wide-field InfaRed Camera (WIRC, Vissapragada et al., 2020) at Palomar Observatory to observe three new transits of LP 791-18 c. With this setup, we achieved a timing precision superior to that of Spitzer. In §4.2, we describe our transit follow-up observations. In §4.3, we describe our TTV modeling and analysis. In §4.4, we discuss our results, and in §4.5 we summarize our key findings.

Table 4.1 Summary of ground-based Palomar/WIRC observations of LP 791-18 c.

UT Date	Start	Finish	Transit %	Baseline %	z_{st}	z_{min}	z_{end}	Transit Midtime (BJD, §4.2)
2023 Dec 9	10:31:42	12:44:43	100%	105%	2.54	1.60	1.60	2460287.987952 ± 0.000070
2024 Jan 8	08:18:33	11:06:46	100%	140%	2.84	1.57	1.57	2460317.927413 ± 0.000050
2024 May 12	03:32:42	06:06:23	97%	120%	1.55	1.55	2.15	2460442.675472 ± 0.000037

Start and Finish columns represent the time of first and last science images in UT time, the transit and baseline fractions are relative to the total transit duration for LP 791-18 c, z_{min} is the minimum airmass of the science sequence while z_{st} and z_{end} are the starting and ending airmasses.

4.2 Transit Follow-up

Palomar/WIRC Observations

We observed three transits of LP 791-18 c in the *J*-band with WIRC on the 200" Hale Telescope at Palomar Observatory, California, USA. The Hale Telescope is a 5.08-m telescope equipped with a 2048 x 2048 Rockwell Hawaii-II NIR detector, providing a field of view of $8'.7 \times 8'.7$ with a plate scale of $0''.25$ per pixel (WIRC, Wilson et al., 2003). Our data were taken with a beam-shaping diffuser that increased our observing efficiency and improved the photometric precision and guiding stability (Stefansson et al., 2017; Vissapragada et al., 2020).

We observed transits of LP 791-18 c on UT 2023-12-09, 2024-01-08, and 2024-05-12. We used 10-second exposure times stacked to 4 total co-added exposures per image, and observed full transits plus at least 1 transit duration of baseline (Figure 4.1). Exposure time is typically varied on the night of observation based on the sky conditions (Moon fraction and proximity, cloud cover, etc.), but we found 40 second total exposure time to be sufficient for all observations. For each night, we obtained calibration images to dark-subtract, flat-field, remove dead and hot pixels, and remove detector structure with a 9-point dithered sky background frame following the methodology of Vissapragada et al., 2020. We extracted photometry for our target star and a set of nearby comparison stars, and we chose up to 10 comparison stars that have minimal variance relative to the time-changing flux of the target star. For the UT 2024-01-08 and 2024-05-12 observations, these were the same 8 comparison stars, while for the UT 2023-12-09 observation we used 2 additional comparison stars for a total of 10. The final number of comparison stars was decided by the significance of their weights in the fitting procedure described in §4.2. We cleaned the target and comparison light curves by applying a moving median filter with a width of 31 data points and removing 5σ outliers. We then tested various target aperture sizes from 5 - 25 pixels and selected the optimal aperture by minimizing the root mean square scatter after the light-curve fitting described in §4.2. Our optimal apertures were 19, 19, and 12 pixels for UT 2023-12-09, 2024-01-08 and 2024-05-12, respectively. For the UT 2023-12-09 observation we experienced poor seeing approaching the 3” width of our diffuser and intermittent partial cloud cover, and for the UT 2024-01-08 observation we experienced poor seeing below 3”. This affected our photometric precision and target PSF width, but we do not exclude any data from these observations because the comparison star fluxes still track very closely with the target star flux resulting in strong transit detections (Figure 4.1). Additional information about our transit observations, including observation times, transit coverage, and airmasses, are provided in Table 4.1.

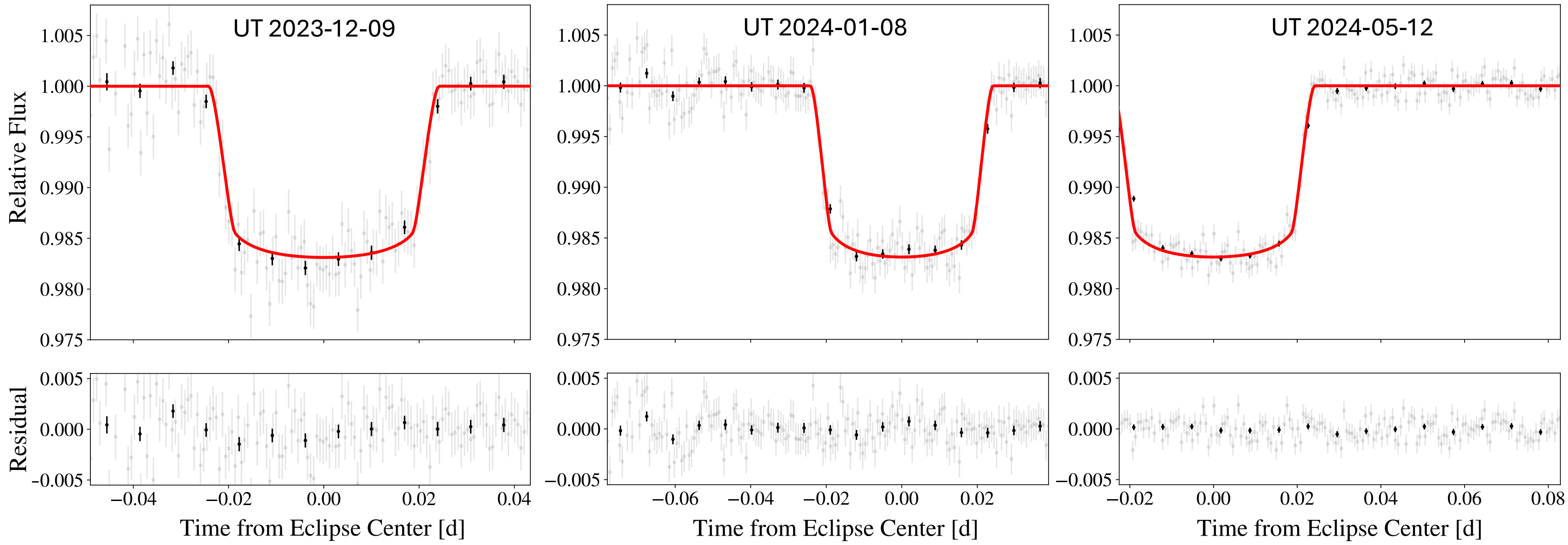

Figure 4.1 Detrended Palomar/WIRC light curves for the three transit observations of LP 791-18 c (upper panels) and residuals after the best-fit transit light curve has been subtracted (lower panels). Unbinned data are shown as grey circles, with 10 minute binned points overplotted as black circles. The best joint-fit transit models are overplotted as red lines, with red shading to indicate the 1σ uncertainties on the transit shape.

Transit Modeling

We fit the WIRC light curves using `exoplanet` with a combined systematics and transit model as described in Greklek-McKeon et al., 2023. Our systematics model for each night included a linear combination of comparison star light curve weights, an error inflation term added in quadrature to the flux errors, and a linear slope. We also tested systematics models with linear combinations of weights for the target centroid offset, PSF width, airmass, and local sky background as a function of time. We compared the Bayesian Information Criterion (BIC, Schwarz, 1978) for all possible combinations of these systematic noise parameters using the same framework as in Pérez-González et al., 2024. We found that the model that produced the lowest BIC value included weights for the target PSF width on UT 2024-01-08, while our UT 2023-12-09 and 2024-05-12 observations preferred no additional detrending parameters in the systematics model. When optimizing the systematics model for each night, we also fit for the transit shape parameters (impact parameter b, planet-star radius ratio R_P/R_*, and semi-major axis ratio a/R_*), and found that they were all consistent within 1σ across all three nights.

We fit the three WIRC transits jointly (Figure 4.1). We used the same model framework as in Greklek-McKeon et al., 2023, with a wide uniform prior of ±2 hours on the transit times, transit shape parameters (impact parameter b, planet-star radius ratio R_P/R_*, semi-major axis ratio a/R_*) shared across nights, with different systematics model parameters and comparison star weights for each night. We adopted stellar parameters from P23 and used `ldtk` (Parviainen et al., 2015) to calculate the J-band quadratic WIRC limb darkening parameters $u_1 = 0.182$ and $u_2 = 0.151$, and held them fixed in our fits. We explored the parameter space with the NUTS sampler in `PyMC3` for 2500 tune and 2000 draw steps with 4 chains, and confirmed that the chains have evolved until the Gelman-Rubin statistic values are < 1.001 for all parameters. Our measured transit times are listed in Table 4.1, and the final transit light curves are shown in Figure 4.1. We achieved transit timing precisions of 6, 4, and 3 seconds for our Palomar/WIRC transits of LP 791-18 c. This represents an improvement over the 9 second transit timing precision of the two Spitzer transits of planet c presented in P23.

4.3 TTV Modeling

Validation of TTV Model and Choice of Eccentricity Parameterization

Before performing an updated TTV model fit using our new transit times, we first fit the original set of transit times listed in Extended Data Tables 1 and 2 of P23, where we independently reproduced their solution. We used the `TTVFast` package to model the observed transit times. `TTVFast` (Deck et al., 2014) is a computationally efficient n-body code that uses a symplectic integrator with a Keplerian interpolator to calculate transit times in multi-planet systems. The modeled transit times are a function of the planetary mass ratios and orbital elements relative to a reference epoch, which we chose to be T_0 = 8546.0 (BJD - 2450000), the same as P23. In our TTV modeling, we also fixed the planetary orbital inclinations (i) to 90°, since the transit fits indicate that planets d and c have a low mutual inclination and are very close to edge-on (i_d = 89.34 ± 0.41, i_c = 89.78 ± 0.13, P23). For a purely edge-on orbital inclination the longitude of the ascending node (Ω) becomes undefined, so we arbitrarily set it to 90° for both planets. The TTV model also includes the planet-to-star mass ratios (M_p/M_*), Keplerian orbital periods (P), mean anomalies reparamaterized with the time of first transit (t_0), and the planetary eccentricities (e) and longitudes of periastron (ω). This results in a total of ten free parameters in our 2-planet TTV model. Prior distributions used for these model parameters are described in Table 4.2. Also as in P23, we did not include planet b in the TTV analysis because the predicted amplitude of its TTVs and its predicted impact on the TTVs of planets c and d are less than one second, independent of the planet masses. Following P23, we initially fit the data with e and ω parameterized as $e\cos(\omega)$ and $e\sin(\omega)$ (Eastman et al., 2013). As originally noted by Ford, 2006, fitting for $e\sin(\omega)$ and $e\sin(\omega)$ results in an effective linear prior on e, which must be corrected by weighting the stepping probability by e_{i-1}/e_i, where the subscript i denotes the current link in the chain. This approach has been used in previous TTV studies (e.g., Agol et al., 2021), and was the approach adopted by P23, so we use it as well.

The orbital periods, mean anomalies, eccentricities, and longitudes of periastron are osculating orbital elements defined at the TTV model start time T_0. Along with this TTV model parameterization, we incorporated the damped-state free eccentricity prior described in P23. This study performed long-term n-body simulations with `REBOUND` (Rein et al., 2015), which indicated that the eccentricities of the planets should be damped to values near zero (~0.001 for d, and ~0.0001 for c) on relatively short timescales (see §4.3 for additional analysis of this). These damped-state eccentricities oscillate around stable long-term equilibria, and represent the forced eccentricities that are preserved due to mutual gravitational interactions between the planets after the free eccentricity has been stripped away by tidal damping. P23 implemented this damped-state prior on the eccentricities by computing the free and forced eccentricity components for planets c and d for each proposed step in the MCMC chain using a two year `REBOUND` simulation, and then imposing Gaussian priors on the values of the free eccentricities centered at zero and with a standard deviation of 0.001 for planet d and 0.0001 for c. We found that we obtained equivalent results using `REBOUND` simulations with a duration of 6 months rather than the two years utilized by P23 and adopted this approach in order to decrease the run time of our fits. This had the added advantage of making sure that our estimate of the forced eccentricity was not biased by the long-term osculations of the free eccentricity term, while still accurately separating the free versus forced eccentricity components by simulating many of the 26-day TTV super-periods of LP 791-18 d and c (P23).

We fit our TTV model to the data from P23 using the affine invariant Markov chain Monte Carlo (MCMC) ensemble sampler `emcee` (Foreman-Mackey et al., 2013), and chose wide uniform priors for all parameters: U(-1, 1) for $ecos(\omega)$ and $esin(\omega)$, U(0, 30$M_{\oplus}$) for the planet-star mass ratios, U(P-100σ, P+100σ) for the planetary orbital periods and U(t_0-100σ, t_0+100σ) for the t_0 parameters using the period and t_0 σ values for each parameter reported in P23, in addition to the damped-state free eccentricity prior. We initialized the MCMC fit with 200 walkers (20 per free parameter) randomly distributed across the full prior volume. We ran the sampler for 7000 steps, which is more than 50 autocorrelation lengths for all parameters after discarding the initial 1500 steps as burn-in. We obtained results consistent within 1σ to those reported in P23 for all fit parameters with this damped-state eccentricity model framework. When we repeated the TTV analysis without the damped-state eccentricity prior, we also obtained planetary mass values consistent with those reported in P23.

Next, we repeated our fit to the TTV data from P23 with an alternative parameterization for e and ω. The correction method used to eliminate the effective positive linear prior in e for the $e$cos(ω) and $e$sin(ω) parameterization described in Ford, 2006 and utilized by P23 preferentially rejects steps with higher eccentricity and results in an approximately but not perfectly uniform prior in e. Due to the singularity at $e = 0$, there is a very slight overcorrection as e approaches zero, as can be seen in Eastman et al., 2013 Figure 1. For this reason, Eastman et al., 2013 recommend using the $\sqrt{e}\cos(\omega)$ and $\sqrt{e}\sin(\omega)$ parameterization, which naturally recovers a uniform prior in e and ω. When we repeated our fit to the P23 data using this parameterization, we found that the small but non-zero eccentricities reported

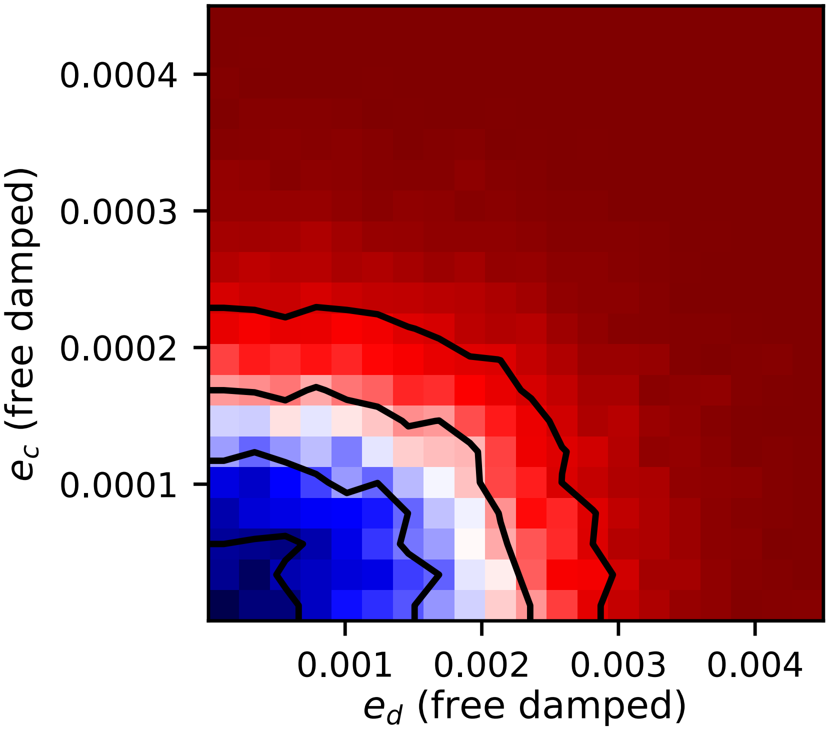

Figure 4.2 The posterior probability density distribution of planetary eccentricities for LP 791-18 d and c with a fit to the TTV data of P23 using a tidally damped-state eccentricity prior and parameterizing e and ω as $\sqrt{e}\cos(\omega)$ and $\sqrt{e}\sin(\omega)$.

by P23 (e_d = 0.0015 ± 0.00014 and e_c = 0.0008 ± 0.0004) for planets d and c vanished and we instead retrieved eccentricity posteriors consistent with zero for both planets (Figure 4.2). When we compared this tidally damped eccentricity fit to one where we forced $e = 0$ for both planets, the difference in best-fit predicted transit times is less than 1 second for both planets, compared to our smallest transit timing precision of 3 seconds. This confirms that the observational data are not sensitive to eccentricities this small (~0.001), and the originally reported values from P23 were an artifact of the chosen e and ω parameterization. In order to avoid this bias, we use the $\sqrt{e}\cos(\omega)$ and $\sqrt{e}\sin(\omega)$ parameterization in all of our TTV model fits going forward.

The Damped Case

We performed an updated TTV fit using the TTV observations from P23 and our three new transit observations of LP 791-18 c, applying the same free eccentricity tidally damped-state prior described in §4.3. We ran the TTV MCMC retrieval with 200 walkers for 25,000 steps, ensuring that all parameters achieved > 50

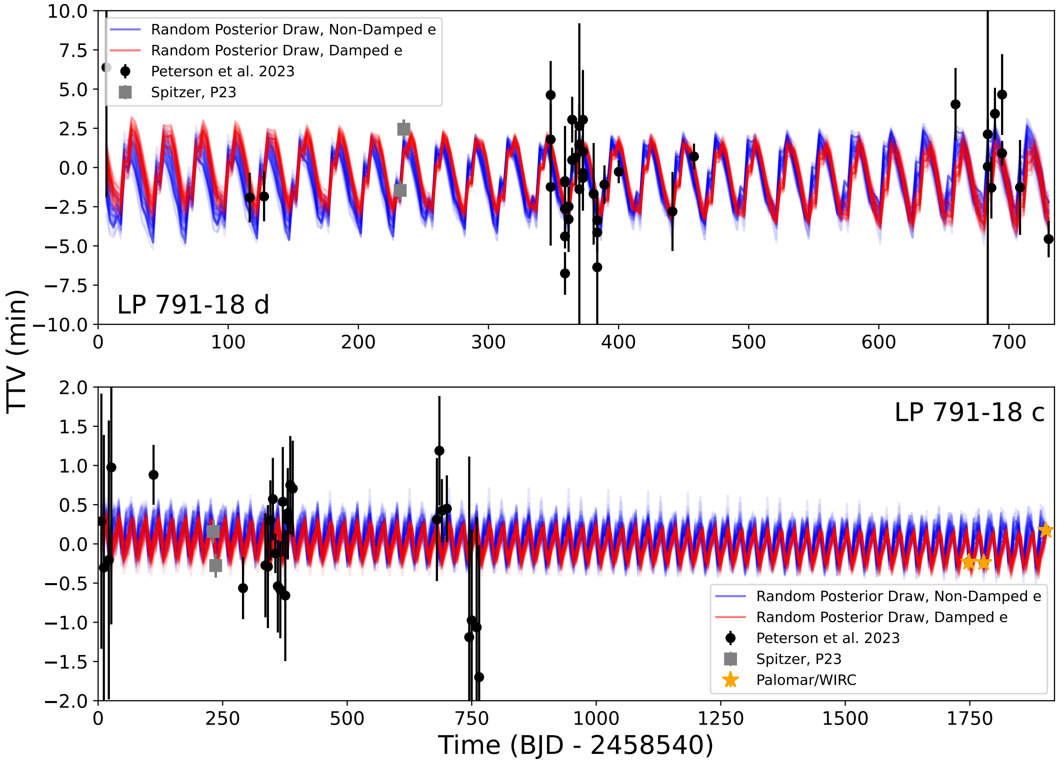

Figure 4.3 TTVs from the ground-based follow-up campaign of P23 (black circles) including the high-precision Spitzer observations (gray squares), and our new Palomar/WIRC follow-up observations (orange stars), with 100 random posterior draws from our damped eccentricity TTV model (red) and free eccentricity TTV model (blue) for LP 791-18 c (top panel) and d (bottom panel). Our Palomar/WIRC timing measurements for LP 791-18 c are the most precise TTV observations of this system so far, a factor of 1.5-3x more precise than Spitzer, and drive the TTV model constraints for LP 791-18 d.

autocorrelation lengths. We show the updated suite of TTV observations in Figure 4.3, with a representative sample of TTV model fits overplotted and a comparison to the non-damped free eccentricity TTV retrieval shown. We found that the TTV-based eccentricities remain consistent with zero when applying the damped-state eccentricity prior (see Figure 4.4). This has significant implications for the tidal heat flux of LP 791-18 d, as discussed in §4.4. Our updated planet masses are consistent with those reported in P23, but with an improvement in the fractional mass uncertainty for LP 791-18 d from ∼45% to ∼20%. We discuss the corresponding implications for the interpretation of this planet's bulk density in §4.4.

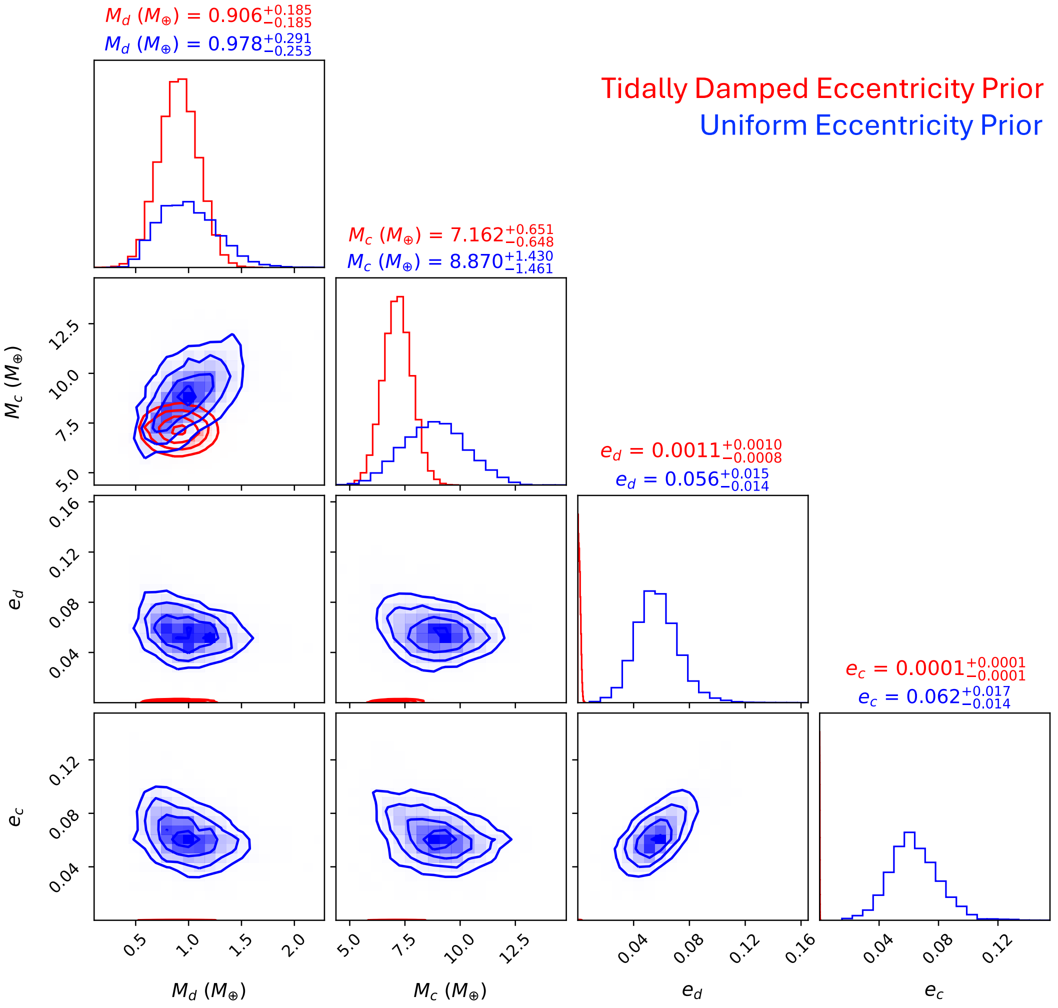

Figure 4.4 Posterior distributions for the masses and eccentricities of LP 791-18 d and c from a fit to the updated set of TTV observations in the case of a tidally damped free eccentricity prior (red), and a uniform eccentricity prior (blue). If we assume that the eccentricities are damped, then the observations are consistent with $e = 0$ and the planetary masses are slightly lower. If the eccentricities are not damped, the planetary masses are slightly higher.

The Non-Damped Case

In order for the tidal circularization timescale Puranam et al., 2018, equation 1 to be comparable to or longer than the age of the system (> 0.5 Gyr, P23), the reduced tidal quality factor Q' (defined as Q/k_2) must be $\geq 10^4$ for LP 791-18 d. This value would be similar to the super-Earth GJ 876 d, whose non-zero eccentricity is maintained by chaotic excitations from nearby planets (Puranam et al., 2018), but much larger (and less dissipative) than the values commonly assumed for terrestrial planets (10-100, Clausen et al., 2015). For LP 791-18 c, $Q_c \geq 7 \times 10^3$ would yield a circularization time comparable to the system age. This is consistent with predictions of the range of Q_p values for sub-Neptune exoplanets from interior modeling and population-level analysis (e.g., Goldreich et al., 1966; Nettelmann et al., 2011; Clausen et al., 2015; Tobie et al., 2019; Louden et al., 2023) and smaller (more dissipative) than measured values for Neptune-sized exoplanets (e.g., GJ 436 b, $Q_p = 2 \times 10^5 - 10^6$, Morley et al., 2017). We caution that if LP 791-18 is considerably older than 1 Gyr, both planets would require higher Q_p values and much less efficient tidal dissipation to retain any free eccentricity. It is therefore likely that LP 791-18 d has a damped free eccentricity based on the predictions of Q_p values for terrestrial planets, but a much larger Q_p also cannot be ruled out.

We explore this possibility by performing an updated TTV fit including our Palomar/WIRC observations for the case with a free eccentricity prior. In this case, we used the same TTV model parameterization as before, with a uniform prior from -1 to 1 on $\sqrt{e}\cos(\omega)$ and $\sqrt{e}\sin(\omega)$, but without the additional damped-state free eccentricity prior. We ran this MCMC retrieval with 200 walkers for 5×10^5 steps, ensuring that our chains extended over more than 50 autocorrelation lengths for each parameter. Without the damped-state prior, which significantly reduces the size of the eccentricity parameter space, this MCMC sampling requires many more steps to fully explore the parameter space as the mass and eccentricity parameters are correlated in the TTV model. The results of this TTV model and the damped-state eccentricity prior TTV retrieval are shown in Figure 4.4.

We find that our undamped fit prefers moderately non-zero eccentricity values for both planets ($e_d = 0.056^{+0.015}_{-0.014}$ and $e_c = 0.062^{+0.017}_{-0.014}$). These higher eccentricities also result in slightly higher masses for both planets, although with larger mass uncertainties and still consistent within 1σ to the fit with a damped eccentricity prior (Figure 4.4).

The current data cannot differentiate between the damped versus undamped models.

We compare the chi-squared values for the maximum likelihood model parameters in the damped versus non-damped eccentricity TTV models, and find that the non-damped χ^2 value is 26% smaller than the damped χ^2 value. This is an insignificant difference in the quality of fit (Wall et al., 2012). We discuss the implications of these potentially higher eccentricity and mass values for the tidal heat fluxes and compositions of the planets in §4.4.

Table 4.2 Priors and posteriors for LP 791-18 model parameters.

Parameter	Prior	Posterior	
Measured planetary parameters, Palomar/WIRC transit fit (§4.2)			
		LP 791-18 c	
$a/R_\star$	$p(a/R_\star \mid P, M_\star, R_\star)$	$37.05^{+0.05}_{-0.07}$	
$R_p/R_\star$	$\mathcal{U}(0.0, 0.2)$	$0.12518^{+0.00027}_{-0.00027}$	
Impact parameter, b	$\mathcal{U}(0, 1 + R_p/R_\star)$	$0.0367^{+0.0323}_{-0.0222}$	
Measured planetary parameters, TTV fit, Non-damped free eccentricity prior (§4.3)			
		LP 791-18 d	*LP 791-18 c*
P (days)	$\mathcal{U}$(P−1.0,P+1.0)[1]	$2.75519^{+0.00044}_{-0.00046}$	$4.98987^{+0.00006}_{-0.00007}$
t_0 (BJD - 2,458,546)	$\mathcal{U}(t_0 - 2.5, t_0 + 2.5)$[2]	$6.37773^{+0.00068}_{-0.00065}$	$6.50935^{+0.00011}_{-0.00011}$
$\sqrt{e}\cos\omega$	$\mathcal{U}(-1, 1)$	$-0.120^{+0.056}_{-0.048}$	$-0.239^{+0.035}_{-0.035}$
$\sqrt{e}\sin\omega$	$\mathcal{U}(-1, 1)$	$0.115^{+0.056}_{-0.086}$	$0.039^{+0.059}_{-0.076}$
$M_p/M_\star$ x 10^{-6}	$\mathcal{U}(0, 90)$	$2.936^{+0.087}_{-0.076}$	$26.63^{+4.29}_{-4.39}$
Measured planetary parameters, TTV fit, Damped-state free eccentricity prior (§4.3)			
		LP 791-18 d	*LP 791-18 c*
P (days)	$\mathcal{U}$(P−1.0,P+1.0)[1]	$2.75485^{+0.00013}_{-0.00013}$	$4.9899100^{+0.0000012}_{-0.0000014}$
t_0 (BJD - 2,458,546)	$\mathcal{U}(t_0 - 2.5, t_0 + 2.5)$[2]	$6.37888^{+0.00037}_{-0.00038}$	$6.509230^{+0.000065}_{-0.000064}$
$\sqrt{e}\cos\omega$	$\mathcal{U}(-1, 1)$	$-0.0033^{+0.0266}_{-0.0262}$	$-0.0001^{+0.0008}_{-0.0008}$
$\sqrt{e}\sin\omega$	$\mathcal{U}(-1, 1)$	$0.0034^{+0.0268}_{-0.0274}$	$-0.00003^{+0.00754}_{-0.00769}$
$M_p/M_\star$ x 10^{-6}	$\mathcal{U}(0, 90)$	$2.719^{+0.056}_{-0.056}$	$21.50^{+1.95}_{-1.95}$
Derived planetary parameters			
		LP 791-18 d	*LP 791-18 c*
Inclination, i (deg)	-	89.34 ± 0.41*	89.94 ± 0.05
Semimajor axis, a (au)	-	0.01992 ± 0.00024*	$0.02961^{+0.00035}_{-0.00036}$
Planet radius, R_p ($R_\oplus$)	-	$1.032^{+0.044}_{-0.043}$*	2.488 ± 0.096
Planet mass, M_p ($M_\oplus$), [Undamped e prior]	-	$0.98^{+0.29}_{-0.25}$	$8.87^{+1.43}_{-1.46}$
Planet mass, M_p ($M_\oplus$), [Damped e prior]	-	0.91 ± 0.19	$7.16^{+0.65}_{-0.65}$
Bulk density, ρ (g/cm^3), [Undamped e prior]	-	4.92 ± 1.63	3.18 ± 0.64
Bulk density, ρ (g/cm^3), [Damped e prior]	-	4.56 ± 1.12	2.56 ± 0.38
Eccentricity, e, [Undamped e prior]	-	$0.056^{+0.015}_{-0.014}$	$0.062^{+0.017}_{-0.014}$
Eccentricity, e, [Damped e prior]	-	$0.0011^{+0.0010}_{-0.0008}$	$0.0001^{+0.0001}_{-0.0001}$

[1] Centered on the reported period values of P23

[2] Centered on the reported t_0 values of P23, adjusted for BJD - 2,458,546

[*] Value from Peterson et al., 2023

4.4 Discussion

Tidal Heating Constraints

In the case where LP 791-18 d's free eccentricity is damped and $e_d = 0.0015 \pm 0.00014$ as reported in P23, then the tidal heat flux at the planet's surface is 10^{-3} times the insolation flux. This is still potentially significant for volcanic activity, however. P23 performs detailed modeling of the planet's internal energy budget in

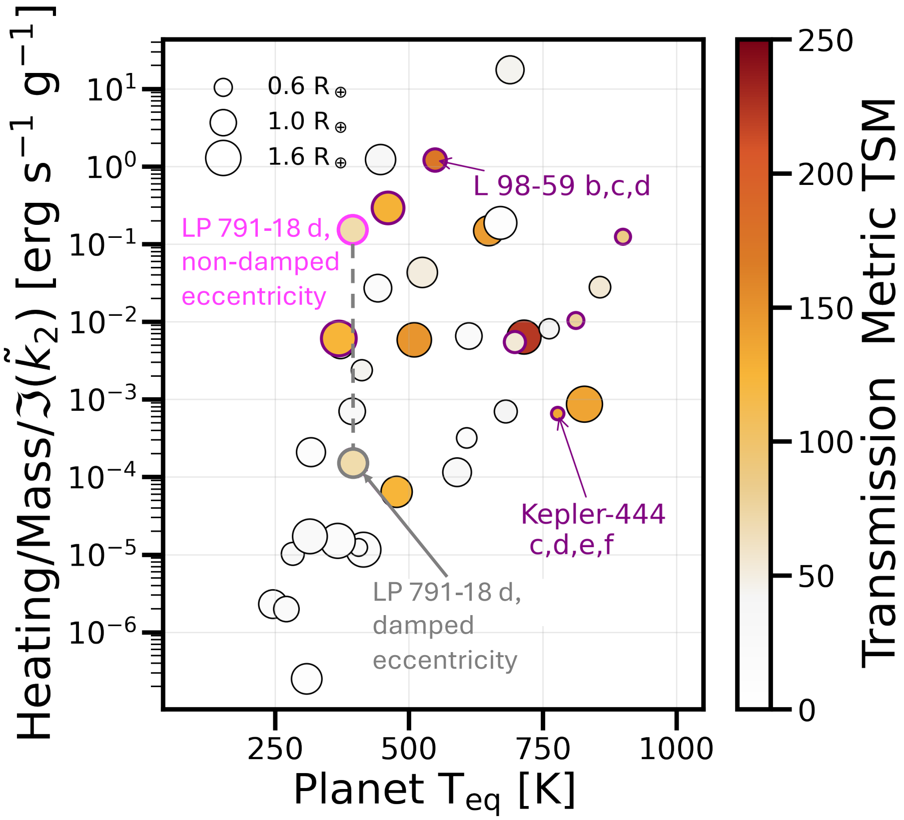

Figure 4.5 Planetary equilibrium temperature versus tidal heat flux per unit mass, adapted from Figure 5 of Seligman et al., 2023, showing the most promising rocky planets for tidal volcanism. Heat fluxes are normalized by the uncertain tidal quality parameters, point sizes are scaled by planet size, and color indicates the favorability for atmospheric characterization through transmission spectroscopy (Kempton et al., 2018). The difference in tidal heat flux per unit mass for LP 791-18 d spans more than three orders of magnitude for the damped versus non-damped eccentricity states.

this case, including the effects of silicate melting in the planet's interior, and finds that a tidal heat flux per unit mass similar to Io is probable if LP 791-18 d has an Earth-like mantle composition and rheology. While it is possible that LP 791-18 d maintains this forced eccentricity due to dynamical interactions with LP 791-18 c, we find that the TTV observations are not sensitive to eccentricities this small.

If we instead consider the larger eccentricity value for LP 791-18 d from our non-damped TTV retrieval (Table 4.2), then the implied tidal heat flux would be much higher than previously reported in P23, with significant implications for the potential outgassing of a secondary atmosphere. In this scenario, the tidal heat flux at the surface of LP 791-18 d increases to a value comparable to the insolation flux, and the tidal heat flux per unit mass jumps by more than three orders of magnitude (see Figure 4.5). Using Equation 1 from Millholland et al., 2020, we calculate a corresponding $T_{\text{int}} \approx 145$ K for $Q_d = 10^4$, compared to a planetary T_{eq} of 395 K. In this scenario LP 791-18 d would be comparable to L 98-59 d in terms of tidal heat flux per unit mass (Demangeon et al., 2021; Seligman et al., 2023).

Impact on Secondary Eclipse Timing

The predicted timing offset of the secondary eclipse relative to the prediction for a planet on a circular orbit is given by $\Delta t = 2Pe\cos\omega/\pi$ (Deming et al., 2005). This means that if the higher eccentricity for LP 791-18 d preferred by our free retrieval is correct, it could result in a significantly larger timing offset than the damped state prediction. This has potentially significant implications for upcoming JWST secondary eclipse observations of this planet in program GO 6457, which have a duration of 4.62 hours per observation, with five total eclipse observations currently scheduled. In Figure 4.6, we compare the distribution of predicted eclipse timing offsets for LP 791-18 d from the tidally damped and free eccentricity TTV retrievals. Notably, with $e_d = 0.056 \pm 0.015$, the most probable eclipse timing offset is nearly two hours earlier than the value for the damped fits, with a 1σ uncertainty window of approximately 45 minutes in either direction. This means that it is possible that the secondary eclipse could occur prior to the start of the JWST observing window. In contrast to this prediction, our tidally damped fit predicts an eclipse timing offset of $-0.2\,^{+2.0}_{-2.7}$ minutes. If this JWST program detects eclipses of planet d with a measured timing offset of more than 10 – 15 minutes, it would provide direct observational confirmation that this system is not in the tidally damped equilibrium state. There are no currently scheduled eclipse observations of LP 791-18 c, but the equivalent eclipse timing offset distributions for the non-damped and damped state eccentricities are -273^{+66}_{-81} minutes and $0.0\,^{+0.3}_{-0.4}$ minutes, respectively.

Bulk Density Constraints

Our new Palomar transit observations of planet c reduce the uncertainty on the planet-to-star radius ratio ($R_p/\ R_*$) by nearly 4× relative to the value reported in P23. Unfortunately, most of the current uncertainty in the planet radius is driven by the stellar radius uncertainty, so our updated planet radius value (shown in Table 4.2) is only minimally shifted relative to P23. Our mass constraint for the tidally damped case is similar to the value reported by P23, although we prefer a slightly higher mass value for the free eccentricity fit as discussed in §4.3. As noted by P23, this

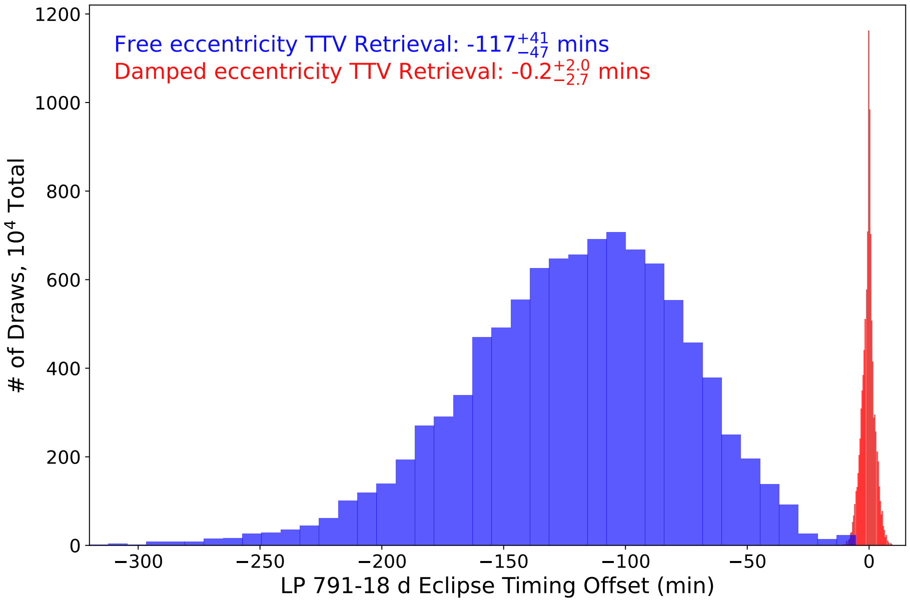

Figure 4.6 Distributions for the eclipse timing offsets of LP 791-18 d, using 10^4 draws from the period, e, and ω distributions of the planets in the damped (red) and non-damped (blue) free eccentricity TTV retrievals.

planet must have a modest hydrogen-rich envelope; this remains true for either of our updated mass values, although the mass fraction of the envelope is slightly lower when we use the higher mass value from the free eccentricity fit (~2%, compared to ~2.5% atmospheric mass fraction for the lower mass from the damped eccentricity retrieval, Lopez et al., 2014 Table 2).

Our updated fits also result in a significantly improved mass constraint for LP 791-18 d. P23 reported a mass of $0.9^{+0.5}_{-0.4}$ $M_\oplus$, while we find a value of 0.91 ± 0.19 $M_\oplus$ for the damped case and $0.98^{+0.29}_{-0.25}$ $M_\oplus$ for the free eccentricity case. This allows us to better constrain the planetary bulk density (Figure 4.7), which we find is consistent with an Earth-like rock-iron composition within 1σ for both the damped and undamped fits. Our best-fit mass for the tidally damped case is slightly lower than the prediction for an Earth-like bulk composition, while the value from our free eccentricity fit is a close match to an Earth-like bulk density.

4.5 Summary and Conclusions

In this study, we present updated constraints on the properties of the temperate Earth-sized planet LP 791-18 d, and its sub-Neptune sized neighbor LP 791-18 c. We collected and analyzed three new transit observations of LP 791-18 c from

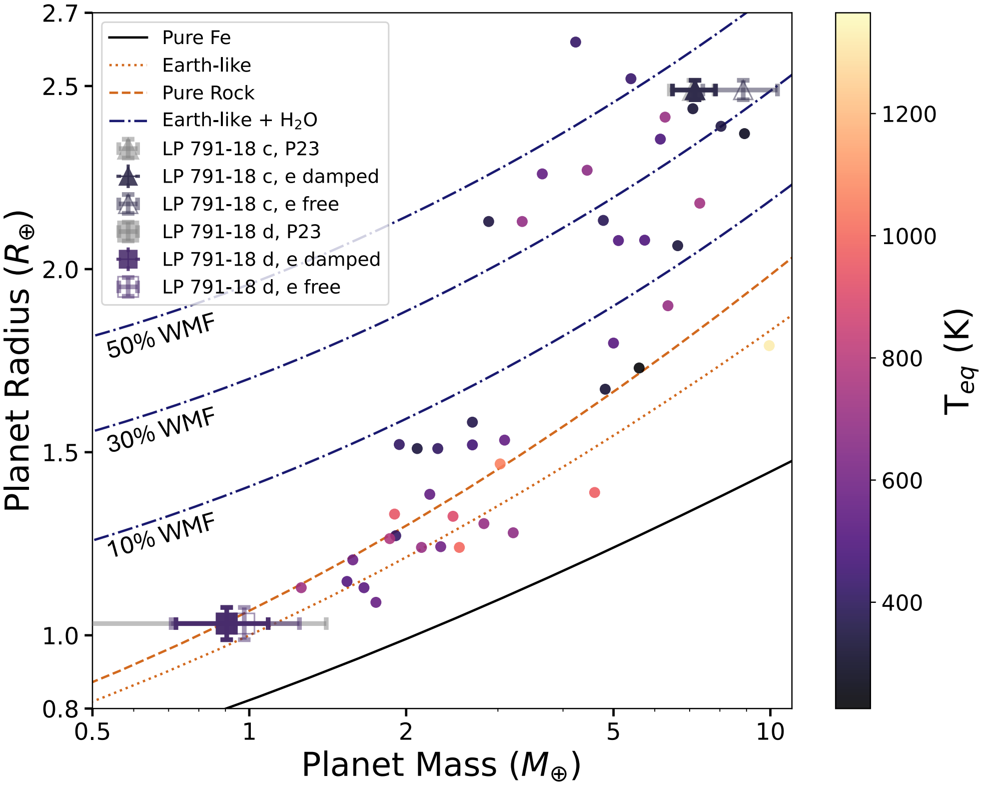

Figure 4.7 Mass-radius diagram for LP 791-18 d (square) and c (triangle), with updated measurements from this work (filled markers from the damped eccentricity TTV results, open markers for the free eccentricity TTV results) compared to the mass constraints from P23 (gray markers). Filled circles represent all small (< 3 $R_\oplus$) planets orbiting M dwarfs ($T_* < 3900$ K) with masses and radii measured to better than 3σ, based on the NASA Exoplanet Archive list of confirmed planets as of Nov 2024. The predicted equilibrium temperatures of the planets are indicated by the point color. For comparison, we also plot Earth-like water-rich mass-radius curves (for 10, 30, and 50% water mass fractions) from Aguichine et al., 2021 and pure iron, Earth-like, and rocky iso-density curves from Zeng et al., 2016.

Palomar Observatory, which extends the TTV baseline by ∼3 years and yields the most precise TTV observations of this system to date (6, 4, and 3 s timing precisions). We use these observations and an updated TTV modeling framework to obtain new constraints on the masses and eccentricities of LP 791-18 c and d, and an updated R_p/R_* constraint for LP 791-18 c, which is limited in improving the planet radius constraint by our knowledge of the stellar radius. An updated stellar characterization is beyond the scope of this work, but improved knowledge of the stellar radius for LP 791-18 would result in significant improvements to the radius constraint for LP 791-18 c. We summarize our main conclusions below.

We find that the TTV retrievals with a damped-state eccentricity prior are sensitive to the chosen parameterization for e and ω. When we fit for $e\cos(\omega)$ and $e\sin(\omega)$ following P23, it results in a small but non-zero eccentricity for both planets due to the effective eccentricity prior bias near zero as described in Eastman et al., 2013 and Ford, 2006. We eliminate this effect by utilizing the $\sqrt{e}\cos(\omega)$ and $\sqrt{e}\sin(\omega)$ parameterization instead, and find that the TTV observations are consistent with zero orbital eccentricity when a damped state prior is applied. When we repeat our fits without this damped eccentricity prior, the observed TTVs yield moderate non-zero eccentricities for LP 791-18 d and c ($e_d = 0.056^{+0.015}_{-0.014}$ and $e_c = 0.062^{+0.017}_{-0.014}$). For these eccentricities to be maintained on timescales relevant for the age of the system (> 1 Gyr), the tidal quality factors must be larger than is typically assumed for Earth-like planets ($Q_d \geq 10^4$) and sup-Neptunes ($Q_c \geq 10^3$), though not outside the range of predicted values from modeling (Tobie et al., 2019) or constraints from population level analysis (Millholland, 2019). It is also possible that any non-zero free eccentricity for LP 791-18 c or d might be caused by a more recent dynamical disturbance such as a stellar flyby.

When using the damped eccentricity prior, we find that the masses of LP 791-18 d and c are consistent with previous constraints reported in P23. However, the addition of our new TTV observations reduces the uncertainty in planet mass for LP 791-18 d by more than a factor of 2. Our updated mass constraint for LP 791-18 d from this fit is lower than an Earth-like value, but still consistent within 1σ. Our free eccentricity TTV retrieval prefers slightly larger masses for both LP 791-18 d and c, making LP 791-18 d potentially more consistent with an Earth-like bulk composition but not fundamentally changing the interpretation of the planetary compositions from bulk density.

Our two fits result in significantly different predictions for LP 791-18 d's tidal heat flux. If the planet's eccentricity is close to zero as suggested by the tidally damped fits, this tidal heat flux would be relatively low, though still potentially significant for the planet's composition and evolution as reported in P23. If the higher eccentricity preferred in the non-damped eccentricity prior fit is correct, the implied tidal heat flux could be orders of magnitude larger. We show that upcoming JWST observations of LP 791-18 d's secondary eclipse can easily differentiate between these two scenarios. As long as the eclipse occurs within the JWST observational window, its timing can be used to obtain a significantly tighter constraint on LP 791-18 d's orbital eccentricity, which will in turn result in improved constraints on the masses of both planets in the TTV fit. If the system is in the tidally damped state, JWST observations will be sensitive to much lower (<0.01) eccentricities than are detectable in the current TTV data. If JWST instead shows that LP 791-18 d has retained some free eccentricity despite ongoing tidal damping, these observations can be used to constrain its tidal quality factor.

4.6 Appendix

Transit Times and Posterior Probability Distributions

Planet	Transit #	Midtime (BJD - 2458540)	$+1\sigma$	-1σ
LP 791-18 d	0	6.3789	0.0004	0.0004
LP 791-18 d	1	9.1314	0.0003	0.0003
LP 791-18 d	2	11.8842	0.0003	0.0003
LP 791-18 d	...	...	...	...
LP 791-18 d	1433	3952.0684	0.0099	0.0117
LP 791-18 d	1434	3954.8219	0.0099	0.0117
LP 791-18 d	1435	3957.5772	0.0101	0.0119
LP 791-18 c	0	6.5092	0.0001	0.0001
LP 791-18 c	1	11.4992	0.0001	0.0001
LP 791-18 c	2	16.4892	0.0001	0.0001
LP 791-18 c	...	...	...	...
LP 791-18 c	789	3943.5488	0.0020	0.0022
LP 791-18 c	790	3948.5389	0.0020	0.0023
LP 791-18 c	791	3953.5286	0.0020	0.0022

Table 4.3 Predicted transit times and uncertainties for LP 791-18 c and d from the TTV fit with a tidally damped eccentricity prior, through January 1, 2030. A subset of rows are depicted here for conciseness. The entirety of this table is provided in the arXiv source code.

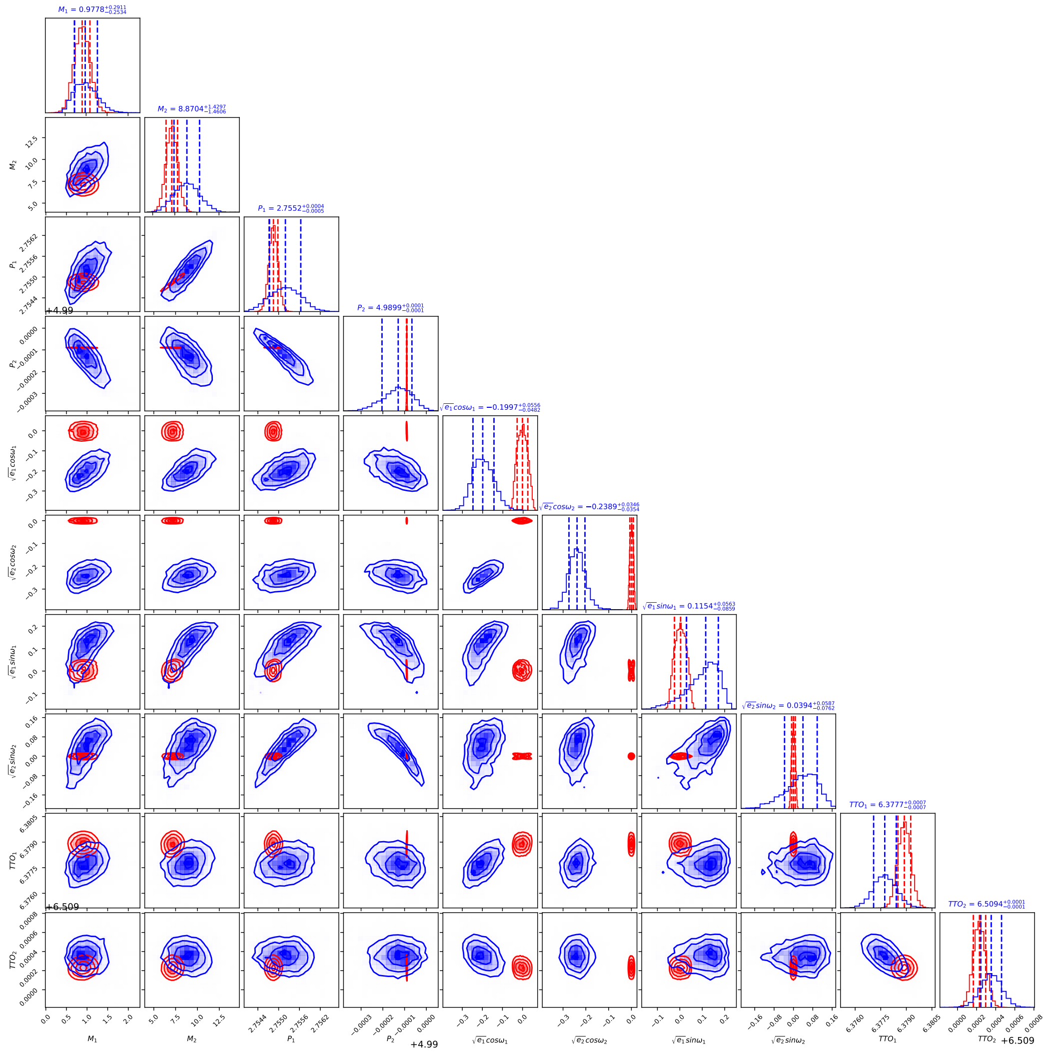

Figure 4.8 Corner plot of posteriors for TTV model parameters for LP 791-18 d and c from the damped eccentricity (red) and undamped (blue) versions of the TTV fit, made with the `corner` package (Foreman-Mackey, 2016). Fit parameters included planet-to-star mass ratios but we have converted these distributions into units of Earth masses for ease of reference. Columns labels are displayed for the undamped fit results.

Planet	Transit #	Midtime (BJD - 2458540)	$+1\sigma$	-1σ
LP 791-18 d	0	6.3778	0.0007	0.0007
LP 791-18 d	1	9.1303	0.0006	0.0006
LP 791-18 d	2	11.8835	0.0005	0.0004
LP 791-18 d	...	...	...	...
LP 791-18 d	1433	3952.0897	0.0678	0.0590
LP 791-18 d	1434	3954.8431	0.0677	0.0589
LP 791-18 d	1435	3957.5981	0.0665	0.0581
LP 791-18 c	0	6.5093	0.0001	0.0001
LP 791-18 c	1	11.4992	0.0002	0.0002
LP 791-18 c	2	16.4892	0.0004	0.0004
LP 791-18 c	...	...	...	...
LP 791-18 c	789	3943.5464	0.1092	0.1125
LP 791-18 c	790	3948.5363	0.1094	0.1126
LP 791-18 c	791	3953.5259	0.1095	0.1128

Table 4.4 The same as Table 4.3, but for the non-tidally damped free eccentricity TTV fit.

References

Agol, Eric et al. (Feb. 2021). "Refining the Transit-timing and Photometric Analysis of TRAPPIST-1: Masses, Radii, Densities, Dynamics, and Ephemerides". In: *PSJ* 2.1, 1, p. 1. DOI: `10.3847/PSJ/abd022`. arXiv: `2010.01074 [astro-ph.EP]`.

Aguichine, Artyom et al. (June 2021). "Mass-Radius Relationships for Irradiated Ocean Planets". In: *ApJ* 914.2, 84, p. 84. DOI: `10.3847/1538-4357/abfa99`. arXiv: `2105.01102 [astro-ph.EP]`.

Banerjee, Agnibha et al. (Nov. 2024). "Atmospheric Retrievals Suggest the Presence of a Secondary Atmosphere and Possible Sulfur Species on L98-59 d from JWST Nirspec G395H Transmission Spectroscopy". In: *ApJL* 975.1, L11, p. L11. DOI: `10.3847/2041-8213/ad73d0`. arXiv: `2408.15707 [astro-ph.EP]`.

Clausen, N. et al. (Dec. 2015). "Dissipation in rocky planets for strong tidal forcing". In: *A&A* 584, A60, A60. DOI: `10.1051/0004-6361/201526082`.

Crossfield, Ian J. M. et al. (Sept. 2019). "A Super-Earth and Sub-Neptune Transiting the Late-type M Dwarf LP 791-18". In: *ApJL* 883.1, L16, p. L16. DOI: `10.3847/2041-8213/ab3d30`. arXiv: `1906.09267 [astro-ph.EP]`.

Dai, Fei et al. (Sept. 2024). "An Earth-sized Planet on the Verge of Tidal Disruption". In: *AJ* 168.3, 101, p. 101. DOI: `10.3847/1538-3881/ad5a7d`. arXiv: `2407.21167 [astro-ph.EP]`.

Deck, Katherine M. et al. (June 2014). "TTVFast: An Efficient and Accurate Code for Transit Timing Inversion Problems". In: *ApJ* 787.2, 132, p. 132. DOI: `10.1088/0004-637X/787/2/132`. arXiv: `1403.1895 [astro-ph.EP]`.

Demangeon, O. D. S. et al. (Sept. 2021). "Warm terrestrial planet with half the mass of Venus transiting a nearby star". In: *A&A* 653, A41, A41. DOI: `10.1051/0004-6361/202140728`. arXiv: `2108.03323 [astro-ph.EP]`.

Deming, Drake et al. (Mar. 2005). "Infrared radiation from an extrasolar planet". In: *Nature* 434.7034, pp. 740–743. DOI: `10.1038/nature03507`. arXiv: `astro-ph/0503554 [astro-ph]`.

Eastman, Jason et al. (Jan. 2013). "EXOFAST: A Fast Exoplanetary Fitting Suite in IDL". In: *Publications of the Astronomical Society of the Pacific* 125.923, pp. 83–112. ISSN: 1538-3873. DOI: `10.1086/669497`. URL: `http://dx.doi.org/10.1086/669497`.

Fischer, Debra A. et al. (June 2016). "State of the Field: Extreme Precision Radial Velocities". In: *PASP* 128.964, p. 066001. DOI: `10.1088/1538-3873/128/964/066001`. arXiv: `1602.07939 [astro-ph.IM]`.

Ford, Eric B. (May 2006). "Improving the Efficiency of Markov Chain Monte Carlo for Analyzing the Orbits of Extrasolar Planets". In: *ApJ* 642.1, pp. 505–522. DOI: `10.1086/500802`. arXiv: `astro-ph/0512634 [astro-ph]`.

Foreman-Mackey, Daniel (2016). "corner.py: Scatterplot matrices in Python". In: *The Journal of Open Source Software* 24. DOI: `10.21105/joss.00024`. URL: `http://dx.doi.org/10.5281/zenodo.45906`.

Foreman-Mackey, Daniel et al. (Mar. 2013). "emcee: The MCMC Hammer". In: *Publications of the Astronomical Society of the Pacific* 125.925, pp. 306–312. ISSN: 1538-3873. DOI: `10.1086/670067`. URL: `http://dx.doi.org/10.1086/670067`.

Goldreich, Peter et al. (Jan. 1966). "Q in the Solar System". In: *Icarus* 5.1, pp. 375–389. DOI: `10.1016/0019-1035(66)90051-0`.

Greklek-McKeon, Michael et al. (Feb. 2023). "Constraining the Densities of the Three Kepler-289 Planets with Transit Timing Variations". In: *AJ* 165.2, 48, p. 48. DOI: `10.3847/1538-3881/ac8553`. arXiv: `2208.00022 [astro-ph.EP]`.

Gressier, Amélie et al. (Nov. 2024). "Hints of a Sulfur-rich Atmosphere around the 1.6 R $_\oplus$ Super-Earth L98-59 d from JWST NIRspec G395H Transmission Spectroscopy". In: *ApJL* 975.1, L10, p. L10. DOI: `10.3847/2041-8213/ad73d1`. arXiv: `2408.15855 [astro-ph.EP]`.

Jackson, Brian et al. (Nov. 2008). "Tidal heating of terrestrial extrasolar planets and implications for their habitability". In: *MNRAS* 391.1, pp. 237–245. DOI: `10.1111/j.1365-2966.2008.13868.x`. arXiv: `0808.2770 [astro-ph]`.

Kempton, Eliza M. -R. et al. (Nov. 2018). "A Framework for Prioritizing the TESS Planetary Candidates Most Amenable to Atmospheric Characterization". In: *PASP* 130.993, p. 114401. DOI: `10.1088/1538-3873/aadf6f`. arXiv: `1805.03671 [astro-ph.EP]`.

Lithwick, Yoram et al. (Dec. 2012). “Extracting Planet Mass and Eccentricity from TTV Data”. In: *ApJ* 761.2, 122, p. 122. DOI: `10.1088/0004-637X/761/2/122`. arXiv: `1207.4192 [astro-ph.EP]`.

Lopez, Eric D. et al. (Sept. 2014). “Understanding the Mass-Radius Relation for Sub-neptunes: Radius as a Proxy for Composition”. In: *ApJ* 792.1, 1, p. 1. DOI: `10.1088/0004-637X/792/1/1`. arXiv: `1311.0329 [astro-ph.EP]`.

Louden, Emma M. et al. (Dec. 2023). “Tidal Dissipation Regimes among the Short-period Exoplanets”. In: *ApJL* 958.2, L21, p. L21. DOI: `10.3847/2041-8213/ad0843`. arXiv: `2311.03576 [astro-ph.EP]`.

Millholland, Sarah (Nov. 2019). “Tidally Induced Radius Inflation of Sub-Neptunes”. In: *ApJ* 886.1, 72, p. 72. DOI: `10.3847/1538-4357/ab4c3f`. arXiv: `1910.06794 [astro-ph.EP]`.

Millholland, Sarah et al. (July 2020). “Tidal Inflation Reconciles Low-density Sub-Saturns with Core Accretion”. In: *ApJ* 897.1, 7, p. 7. DOI: `10.3847/1538-4357/ab959c`. arXiv: `2005.11209 [astro-ph.EP]`.

Morley, Caroline V. et al. (Feb. 2017). “Forward and Inverse Modeling of the Emission and Transmission Spectrum of GJ 436b: Investigating Metal Enrichment, Tidal Heating, and Clouds”. In: *AJ* 153.2, 86, p. 86. DOI: `10.3847/1538-3881/153/2/86`. arXiv: `1610.07632 [astro-ph.EP]`.

NASA Exoplanet Archive (2024). *Planetary Systems Composite Parameters*. Version Version: 2024-11-26. DOI: `10.26133/NEA13`. URL: `https://catcopy.ipac.caltech.edu/dois/doi.php?id=10.26133/NEA13`.

Nettelmann, N. et al. (May 2011). “Thermal Evolution and Structure Models of the Transiting Super-Earth GJ 1214b”. In: *ApJ* 733.1, 2, p. 2. DOI: `10.1088/0004-637X/733/1/2`. arXiv: `1010.0277 [astro-ph.EP]`.

Parviainen, H. et al. (Sept. 2015). “ldtk: Limb Darkening Toolkit”. In: *Monthly Notices of the Royal Astronomical Society* 453.4, pp. 3822–3827. ISSN: 1365-2966. DOI: `10.1093/mnras/stv1857`. URL: `http://dx.doi.org/10.1093/mnras/stv1857`.

Pérez-González, Jorge et al. (May 2024). “Detection of an Atmospheric Outflow from the Young Hot Saturn TOI-1268b”. In: *AJ* 167.5, 214, p. 214. DOI: `10.3847/1538-3881/ad34b6`. arXiv: `2307.09515 [astro-ph.EP]`.

Peterson, Merrin S. et al. (May 2023). “A temperate Earth-sized planet with tidal heating transiting an M6 star”. In: *Nature* 617.7962, pp. 701–705. DOI: `10.1038/s41586-023-05934-8`.

Piaulet-Ghorayeb, Caroline et al. (Oct. 2024). “JWST/NIRISS Reveals the Water-rich “Steam World” Atmosphere of GJ 9827 d”. In: *ApJL* 974.1, L10, p. L10. DOI: `10.3847/2041-8213/ad6f00`. arXiv: `2410.03527 [astro-ph.EP]`.

Puranam, Abhijit et al. (Apr. 2018). “Chaotic Excitation and Tidal Damping in the GJ 876 System”. In: *AJ* 155.4, 157, p. 157. DOI: `10.3847/1538-3881/aab09f`. arXiv: `1802.08385 [astro-ph.EP]`.

Quick, Lynnae C. et al. (Aug. 2020). “Forecasting Rates of Volcanic Activity on Terrestrial Exoplanets and Implications for Cryovolcanic Activity on Extrasolar Ocean Worlds”. In: *PASP* 132.1014, 084402, p. 084402. DOI: `10.1088/1538-3873/ab9504`.

Rein, Hanno et al. (July 2015). “whfast: a fast and unbiased implementation of a symplectic Wisdom–Holman integrator for long-term gravitational simulations”. In: *Monthly Notices of the Royal Astronomical Society* 452.1, pp. 376–388. ISSN: 1365-2966. DOI: `10.1093/mnras/stv1257`. URL: `http://dx.doi.org/10.1093/mnras/stv1257`.

Schwarz, Gideon (July 1978). “Estimating the Dimension of a Model”. In: *Annals of Statistics* 6.2, pp. 461–464.

Seligman, Darryl Z. et al. (2023). *Potential Melting of Extrasolar Planets by Tidal Dissipation*. arXiv: `2311.01187 [astro-ph.EP]`. URL: `https://arxiv.org/abs/2311.01187`.

Stefansson, Gudmundur et al. (Oct. 2017). “Toward Space-like Photometric Precision from the Ground with Beam-shaping Diffusers”. In: *ApJ* 848.1, 9, p. 9. DOI: `10.3847/1538-4357/aa88aa`. arXiv: `1710.01790 [astro-ph.IM]`.

Tobie, G. et al. (Oct. 2019). “Tidal response of rocky and ice-rich exoplanets”. In: *A&A* 630, A70, A70. DOI: `10.1051/0004-6361/201935297`.

Vissapragada, Shreyas et al. (Feb. 2020). “Diffuser-assisted Infrared Transit Photometry for Four Dynamically Interacting Kepler Systems”. In: *The Astronomical Journal* 159.3, p. 108. ISSN: 1538-3881. DOI: `10.3847/1538-3881/ab65c8`. URL: `http://dx.doi.org/10.3847/1538-3881/ab65c8`.

Wall, J. V. et al. (2012). *Practical Statistics for Astronomers*. Cambridge University Press.

Wilson, John C. et al. (Mar. 2003). “A Wide-Field Infrared Camera for the Palomar 200-inch Telescope”. In: *Instrument Design and Performance for Optical/Infrared Ground-based Telescopes*. Ed. by Masanori Iye et al. Vol. 4841. Society of Photo-Optical Instrumentation Engineers (SPIE) Conference Series, pp. 451–458. DOI: `10.1117/12.460336`.

Wright, Jason T. (2018). “Radial Velocities as an Exoplanet Discovery Method”. In: *Handbook of Exoplanets*. Ed. by Hans J. Deeg et al., 4, p. 4. DOI: `10.1007/978-3-319-55333-7_4`.

Zeng, Li et al. (Mar. 2016). “Mass-Radius Relation for Rocky Planets Based on PREM”. In: *ApJ* 819.2, 127, p. 127. DOI: `10.3847/0004-637X/819/2/127`. arXiv: `1512.08827 [astro-ph.EP]`.

Chapter 5

CONFIRMATION OF A THIRD EARTH-SIZED PLANET IN THE TOI-2267 BINARY SYSTEM

Abstract

We report the discovery of a third terrestrial exoplanet in the nearby (22 pc) TOI-2267 system. TOI-2267 is a binary system with stellar components TOI-2267A (M5, 3030 K) and TOI-2267B (M6, 2930 K), with an on-sky separation of $0\farcs384$ (8 au projected separation). TOI-2267 hosts two Earth-sized planets (TOI-2267 b, $0.98 \pm 0.11 R_\oplus$, and TOI-2267 c, $1.12 \pm 0.12 R_\oplus$) with orbital periods of 2.3 and 3.5 days, close to the 3:2 mean motion resonance. This system also contains a third Earth-sized planet candidate with an orbital period of 2.0 days, which has not yet been confirmed. We combine two new transit observations from the 200-inch Hale Telescope at Palomar Observatory with archival TESS data and high-resolution imaging to statistically validate the planetary nature of TOI-2267 d ($0.96 \pm 0.09 R_\oplus$) using the updated TRICERATOPS+ pipeline. Previous work indicates that TOI-2267 b and c likely orbit the primary star. We attempt to determine the host star for TOI-2267 d using transit shape stellar density analysis, but are unable to conclusively assign a host. We conclude that TOI-2267 is either the first known double transiting M dwarf binary system, or hosts three planets in an extremely compact orbital configuration around one star as proposed by Asiru et al. (in prep.).

5.1 Introduction

M dwarfs are the most common type of star in our galaxy. They account for 60–75% of all stars within 10 pc (Henry et al., 2006; Reylé et al., 2021), and ~70% of all stars in the Milky Way (Bochanski et al., 2010). The relatively small masses, radii, and temperatures of M dwarfs make them uniquely favorable targets for the characterization of terrestrial exoplanets (e.g., Triaud, 2021). Terrestrial planets orbiting M dwarfs have larger planet-to-star mass ratios and corresponding radial velocity semi-amplitudes than terrestrial planets around Sun-like stars. Their larger planet-to-star radius ratios also make it easier to detect their thermal emission and search for signs of atmospheric absorption in transit (Wordsworth et al., 2022). The lower temperatures of M dwarfs also mean that the habitable zone is located at smaller orbital separations, where planets are more likely to transit their host star (e.g., Nutzman et al., 2008; Suissa et al., 2020; Gilbert et al., 2023).

Field M dwarfs have a multiplicity rate of 20–30% (e.g., Ward-Duong et al., 2015; Winters et al., 2019; Clark et al., 2024). These stellar companions can alter the formation and evolution of planets in multiple ways. Systems with multiple stars have less massive, shorter-lived, and potentially truncated protoplanetary disks, which can make it harder for planets to accrete gas envelopes (e.g., Harris et al., 2012; Kraus et al., 2016; Sullivan et al., 2023; Sullivan et al., 2024). The presence of a stellar companion can also dynamically perturb a planet's orbit, potentially resulting in migration or ejection (e.g., Kaib et al., 2013). For binary systems with small orbital separations, the increased XUV flux may also result in increased mass loss rates, making it harder for small planets to retain their atmospheres (e.g., Johnstone et al., 2019; Sullivan et al., 2024). All of these effects should be stronger for close (< 50 au) binaries, making these systems especially valuable testbeds for understanding the effects of binarity on planet properties.

A recent survey of M dwarf transiting planet candidates identified by the TESS survey found that $19 \pm 3\%$ have stellar companions, consistent with the rate for field M dwarfs (Matson et al., 2025). They also found that the semi-major axis distribution of these stellar companions was shifted to larger values and the mass ratio distribution peaked at lower values as compared to field M dwarfs (Matson et al., 2025). This suggests that equal mass binaries with small orbital separations may be less likely to host transiting planets, in good agreement with previous results in surveys of Sun-like stars (Ngo et al., 2016; Hirsch et al., 2021). However, to date there has been relatively little work done on the effect of M dwarf binarity on planet properties. Only two confirmed planet-hosting M dwarfs in binary systems have projected separations $\lesssim 50$ au (Kepler-289, Barclay et al., 2015; and K2-288, Feinstein et al., 2019). Two other similar TESS systems have multiple planet candidates awaiting confirmation (TOI-864 and TOI-3494, Matson et al., 2025). These rare systems are therefore extremely valuable for understanding how binarity affects planet formation.

TOI-2267 is a nearby (22 pc) binary star system containing a primary M5, 3030 K component (TOI-2267 A) and secondary M6, 2930 K component (TOI-2267B), initially characterized in Zúñiga-Fernández & Pozuelos et al. (subm., hereafter referred to as ZP25). TOI-2267A and B have an on-sky separation of $0\farcs384$, corresponding to a projected separation of just 8 au. This system contains two Earth-sized planets with orbital periods of 2.3 and 3.5 days, close to the 3:2 mean motion resonance (MMR). ZP25 measured planetary radii of 0.98 ± $0.11 R_\oplus$ and 1.12 ± $0.12 R_\oplus$, respectively, if they orbit the primary star, or 1.18 ± $0.28 R_\oplus$ and 1.35 ± $0.33 R_\oplus$ if they orbit the secondary star. ZP25 were not able to conclusively assign the planets to either star, but they found that the Bayesian evidence favors the primary star as the host. The proximity of the two planets to a MMR also strongly suggests that they orbit the same host star, as such a configuration would be very unlikely to occur if each planet orbited a different star with a period randomly drawn from the observed population-level distribution (Hsu et al., 2020; Hardegree-Ullman et al., 2019; Kaminski et al., 2025; Mignon et al., 2025).

The TESS photometry for TOI-2267 also contains a third transit signal with an orbital period of 2.0 days. However, ZP25 were unable to conclusively validate this candidate due to a lack of ground-based follow-up observations. In this study, we present two new ground-based transits of this candidate observed with Palomar/WIRC and use them to confirm the planetary nature of TOI-2267 d. In Section 5.2, we describe the observations from TESS and Palomar/WIRC. In Section 5.3, we describe our transit analysis and show that the updated false positive probability for this candidate lies below the threshold for statistical validation. In Section 5.4, we explore whether stellar density profiling or dynamical analyses can be used to assign TOI-2267 d to a host star. In Section 5.5, we summarize our key findings and outline future observations that could further improve our understanding of this system.

5.2 Observations

TESS

TOI-2267 was observed in 12 TESS sectors (19, 20, 25, 26, 40, 52, 53, 59, 60, 73, 79, and 86) from December 2019 to December 2024. ZP25 reported the discovery of TOI-2267 b and c at orbital periods of 2.2890887 ± 0.0000016 and 3.4950404 ± 0.0000022 days, respectively, using 2-minute cadence data from the Science Processing Operations Center pipeline (SPOC Jenkins et al., 2016) for the first 10 TESS sectors. A third planet candidate with an orbital period of ~2.0 days was identified by the TESS mission team after the ninth sector of TESS observation (sector 60), and this candidate was independently recovered in the analysis of ZP25. Although this planet candidate was originally labeled as TOI-2267.02, we refer to it as TOI-2267 d throughout this paper in order to avoid confusion.

ZP25 analyzed the TESS target pixel files and SPOC apertures for each sector of

TESS observation and verified that very few faint (Δmag > 5) companion stars were in each aperture, more than 1 TESS pixel away (> 21″) from TOI-2267. ZP25 therefore used the Presearch Data Conditioning Simple Aperture Photometry (PDCSAP) flux data, which are corrected for crowding and systematic effects (Stumpe et al., 2012; Stumpe et al., 2014; Smith et al., 2012), for their subsequent fits. ZP25 performed a global fit including transit light curve models for all three planets, a Gaussian process model for out-of-transit flux variations, and stellar flare models. They incorporated ground-based observations for TOI-2267 b and c in their joint fit, but were unable to obtain any ground-based transit observations for TOI-2267 d. We refer the reader to ZP25 for further details on this transit modeling. We use the detrended and stacked TESS transit profile from ZP25 for TOI-2267 d in a joint fit with our new ground-based observations (see Section 5.3), and to statistically validate TOI-2267 d (see Section 5.3). The phase-folded TESS transit profile for TOI-2267 d was obtained using $P = 2.0344562^{+0.0000037}_{-0.0000046}$, and $t_0 = 2458817.0840^{+0.0017}_{-0.013}$ BJD.

Palomar/WIRC

We observed two transits of TOI-2267 d in the J-band with the Wide-field Infared Camera (WIRC) on the Hale Telescope at Palomar Observatory, California, USA. The Hale Telescope is a 5.08-m telescope equipped with a 2048 x 2048 Rockwell Hawaii-II NIR detector, providing a field of view of 8.′7 × 8.′7 with a plate scale of 0.”25 per pixel (WIRC, Wilson et al., 2003). Our data were taken with a beam-shaping diffuser that increased our observing efficiency and improved the photometric precision and guiding stability (Stefansson et al., 2017; Vissapragada et al., 2020).

We observed transits of TOI-2267 d on UT 2024-11-13 and UT 2025-01-11. We used 4-second exposure times stacked with 9 total co-added exposures per image, and observed full transits plus more than 1 transit duration of baseline both pre-ingress and post-egress on each night (Figure 5.1). For each night, we obtained calibration images to dark-subtract, flat-field, remove dead and hot pixels, and remove detector structure with a dithered sky background frame following the methodology of Vissapragada et al., 2020. We extracted photometry and detrended the light curves with the procedure described in Greklek-McKeon et al., 2023. Conditions were good on both nights, with seeing well below the 3.″0 FWHM of our beam-shaping diffuser. This ensured that PSFs for the target and comparison stars remained stable over the course of our observations.

Table 5.1 Summary of Palomar/WIRC observations of TOI-2267 d.

UT Date	Start	Finish	Transit %	Baseline %	z_{st}	z_{min}	z_{end}
2024 Nov 13	03:53:19	07:44:47	100%	470%	1.749	1.615	1.615
2025 Jan 11	03:43:52	07:27:04	100%	530%	1.617	1.610	1.654

Notes. Start and Finish columns represent the time of first and last science images in UT time, the transit and baseline fractions are relative to the total transit duration for TOI-2267 d, z_{min} is the minimum airmass of the science sequence while z_{st} and z_{end} are the starting and ending airmasses.

We began by extracting photometry for our target star and a set of 10 nearby comparison stars. We cleaned the target and comparison light curves by applying a moving median filter with a width of 31 data points corresponding to a time interval of 34 minutes, and removing 5σ outliers. We then tested circular photometric apertures with radii ranging between 5 - 25 pixels and selected the optimal aperture radius by minimizing the root mean square scatter after the light-curve fitting described in Section 5.3. Our optimal aperture radii were 20 pixels ($5\farcs0$) and 18 pixels ($4\farcs0$) for UT 2024-11-13 and 2025-01-11, respectively. This meant that both binary components of the TOI-2267 system were fully contained within our photometric aperture. We provide additional information about these transit observations, including observation times, transit coverage, airmasses, and measured transit mid-times, in Table 5.1.

5.3 Transit Analysis

Transit Modeling

We used the `exoplanet` package to fit each of the two ground-based WIRC light curves with a combined systematics and transit model as described in Greklek-McKeon et al., 2023. Our systematics model for each night included a linear combination of comparison star light curve weights, an error inflation term added in quadrature to the measured flux errors, and a linear slope. For each night, we chose the 4 comparison stars that have minimal variance relative to the time-changing flux of the target star. These comparison stars were selected because the significance of their weights was more than 1σ from zero in the final posteriors from our systematics optimization procedure described below.

We also tested systematics models with linear combinations of weights for the target centroid offset, PSF width, airmass, and local sky background as a function of time. We compared the Bayesian Information Criterion (BIC, Schwarz, 1978) for all possible combinations of these systematic noise parameters using the same

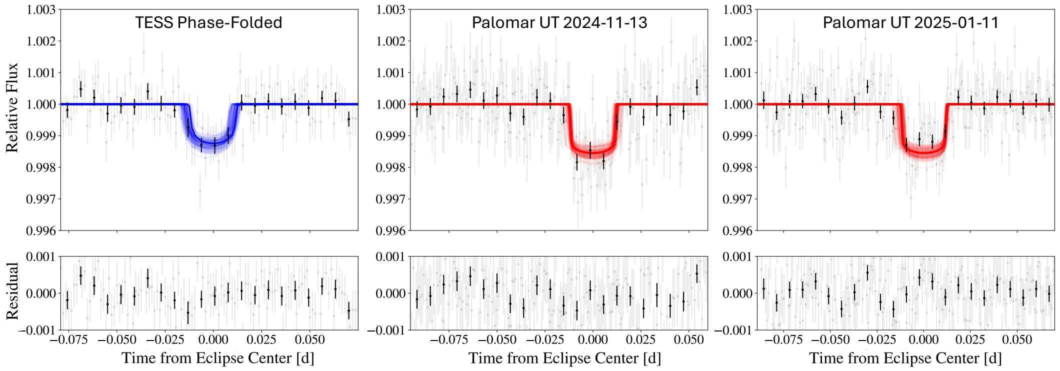

Figure 5.1 Phased-folded and 2-minute binned TESS light curve (left panel) and detrended Palomar/WIRC light curves (middle and right panels) for the two transit observations of TOI-2267 d. Residuals after the best-fit transit light curve model has been subtracted are shown in the lower panels. Unbinned data are shown as grey circles, with 10 minute binned points overplotted as black circles. The best joint-fit transit models are overplotted as blue lines for the TESS data and red lines for the Palomar data, with 100 random draws from the posterior distribution to illustrate the typical model uncertainty. All detrended light curves are available in the arXiv source code.

framework as in Pérez-González et al., 2024. We found that the model that produced the lowest BIC value included weights for the local sky background and target PSF width on UT 2024-11-13, while our UT 2025-01-11 observations preferred no additional detrending parameters in the systematics model.

When optimizing the systematics model for each night of WIRC data, we also fit for the transit shape parameters (impact parameter b, planet-star radius ratio R_p/R_*, and semi-major axis ratio a/R_*), along with the stellar radius. We used wide uniform priors from 0.0 to 1.0 for b and from 0.0 to 0.2 for R_p/R_*, and normal priors on the stellar radius and a/R_* values based on the reported stellar mass, radius, and orbital periods reported in ZP25. We adopted a normal prior on the planetary orbital period P from ZP25, and placed a wide uniform prior on the transit time of ±90 minutes centered on the predicted time using the ephemeris from ZP25. We did not correct the measured R_p/R_* parameter for dilution effects from the other binary component in these initial fits, as the purpose of these fits was only to optimize the systematics model for each night and ensure that the results are consistent regardless of stellar host prior choice.

We performed two fits for each night of data — one assuming the primary star is the host, and one assuming the secondary star is the host. We adopted stellar parameters from ZP25 for each case and used `ldtk` to calculate the J-band quadratic WIRC limb darkening parameters, which we held fixed in our fits. In the primary star case, $u_1 = 0.174$ and $u_2 = 0.136$, and in the secondary star case $u_1 = 0.188$ and $u_2 = 0.168$. We explored the parameter space of our model with the NUTS sampler in `PyMC3` for 2500 tune and 2000 draw steps, and confirmed that the Gelman-Rubin statistic values are < 1.01 for all parameters, indicating good fit convergence.

We confirmed that for both nights of Palomar/WIRC observation, the preferred systematics model is the same regardless of the host star choice, and the R_p/R_* constraint is $> 3\sigma$ from 0 indicating a strong detection of the transit around the target. We also confirmed that the measured R_p/R_*, a/R_*, and b values are consistent with each other within 1σ across the two nights and regardless of the stellar host choice.

We conclude that both transits are strongly detected and that our fitted transit shapes are consistent regardless of host star prior choice. We therefore proceeded to jointly fit both Palomar/WIRC transits assuming a common transit shape. We also confirmed that our fitted b and a/R_* values are consistent with the values from the TESS-only fit reported in ZP25. We therefore incorporated the stacked TESS transit profile into our joint transit fit in order to obtain the most precise constraints on the transit shape parameters. We allowed for separate R_p/R_* values in the TESS and WIRC bandpasses in order to determine whether or not these two parameters are consistent after accounting for the wavelength-dependent dilution from the binary.

We carried out two versions of this joint fit with different assumptions for each. In the first version, we assumed that the primary star is the host, and in the second version we assumed that the secondary star is the host. We used the same model parameters and priors as described in the individual night fits, with b and a/R_* now shared across all three transit light curves. We allowed the individual transit midtimes to vary as free parameters using the `TTVOrbit` module of `exoplanet`, with the stacked TESS transit profile arbitrarily shifted to 1 orbital period before the first Palomar transit. We also fit for the true (undiluted) R_p/R_* value in each bandpass (TESS and J). At each step of the fit, we converted the true R_p/R_* values to predicted transit depths in each bandpass using a radius correction factor X_R incorporating the wavelength-dependent flux dilution from the companion. The radius correction factor was calculated using Equation 7 of Ciardi et al., 2015 for the primary star case, and Equation 6 of Ciardi et al., 2015 for the secondary star case. We assumed a flux ratio $F_{\text{secondary}}/F_{\text{primary}}$ of 0.3045 ± 0.05 in the TESS

Parameter	Unit	Primary host	Secondary host
Model Parameters		TOI-2267 d	
Undiluted $R_p/R_\star$ TESS		0.040 ± 0.003	$0.122^{+0.032}_{-0.030}$
Radius correction factor *TESS*, $X_{\mathrm{R};\,TESS}$		1.142 ± 0.022	$3.577^{+0.865}_{-0.863}$
Undiluted $R_p/R_\star$ WIRC		0.044 ± 0.003	$0.134^{+0.035}_{-0.033}$
Radius correction factor *WIRC*, $X_{\mathrm{R};\,WIRC}$		1.158 ± 0.032	$3.482^{+0.874}_{-0.873}$
a/R_*		$18.778^{+2.657}_{-2.580}$	$22.838^{+2.939}_{-5.790}$
Impact Parameter b		$0.678^{+0.090}_{-0.146}$	$0.442^{+0.300}_{-0.295}$
Mid-transit time, T_0 WIRC Night 1	BJD$_{TDB}$-2457000	$3627.7541^{+0.0008}_{-0.0011}$	$3627.7544^{+0.0006}_{-0.0009}$
Mid-transit time, T_0 WIRC Night 2	BJD$_{TDB}$-2457000	$3686.7538^{+0.0008}_{-0.0010}$	$3686.7539^{+0.0006}_{-0.0007}$
Derived Parameters			
[a]Planet Radius, R_p	$R_\oplus$	0.96 ± 0.09	1.81 ± 0.44
Semimajor axis, a	au	0.0174 ± 0.0003	$0.0145^{+0.0006}_{-0.0007}$
Orbital period, P	days	$2.0344690 \pm 4.41 \times 10^{-5}$	$2.0344639 \pm 3.75 \times 10^{-5}$
Mid-transit time, T_0	BJD$_{TDB}$-2457000	3625.7197 ± 0.0009	3625.7200 ± 0.0008
Inclination, i	°	87.4 ± 0.6	$89.0^{+0.6}_{-0.7}$
[b]Equilibrium Temperature, T_{eq}	K	503 ± 32	422^{+53}_{-56}
Insolation Flux, S	$S_\oplus$	$10.7^{+3.0}_{-2.5}$	$5.3^{+3.2}_{-2.3}$
Transmission spectroscopy metric (TSM)[a]		$18.9^{+8.1}_{-5.8}$	267^{+352}_{-163}
Host density from transit, $\rho_\star$	g cm^{-3}	$32.0^{+14.7}_{-10.8}$	$60.4^{+26.3}_{-35.7}$

Table 5.2 Model and derived parameters for the joint TESS+Palomar transit fitting of TOI-2267 d, for cases where the primary or the secondary star is the host. Adapted from ZP25.

[a] Calculated from the stellar radius values reported in ZP95 ($R_{\text{primary}} = 0.2075 \pm 0.0225$, $R_{\text{secondary}} = 0.130 \pm 0.030$) and taking the error-weighted average across the two bands.

[b] Values calculated assuming an albedo of 0.3 (Earth-like) and an Earth-like bulk density, from Kempton et al., 2018.

bandpass and 0.338 ± 0.075 in the J band, as reported in ZP25. We accounted for the uncertainties on these two flux ratios by making them both free parameters in our fit and placing a Gaussian prior on each that matches the value reported by ZP25.

We explored the parameter space of our joint transit model with the NUTS sampler in `PyMC3` for 10^4 tune and 10^4 draw steps, and confirmed that the Gelman-Rubin statistic values are < 1.01 for all parameters, indicating that the fit has converged. The posterior distributions for our transit model parameters and related derived quantities for both the primary and secondary star fits are summarized in Table 5.2, and corner plots illustrating the posterior distributions for all joint model parameters, including systematics, are included in the appendix.

Planet Validation

We find that for both the primary and the secondary star cases, the dilution-corrected planet-star radius ratio for TOI-2267 d is consistent at the 1σ level between the TESS and *J* bands. This increases our confidence that this candidate is a real planet, as stellar eclipsing binaries often exhibit wavelength-dependent transit depths. In this section, we quantify the effect of this knowledge on the planet's False Positive Probability (FPP) and the Nearby False Positive Probability (NFPP) using the `TRICERATOPS+` statistical validation code. The `TRICERATOPS+` FPP describes the probability that a transit signal does not originate from a planet transiting the target star. The NFPP describes the probability that the observed transit signal originates from a resolved nearby star (i.e., a star farther away than $1''\!.2$ that contributes sufficient flux to the TESS aperture to produce the observed signal) rather than the target star. The FPP encapsulates all possible false positive scenarios, whereas the NFPP considers only a subset of them. Thus, the NFPP will always be less than or equal to the FPP.

The original `TRICERATOPS` code (Giacalone et al., 2021) models the light curves of transiting planets and various astrophysical false positive scenarios, incorporating prior information about the population of stars in the Milky Way to compute the FPP and NFPP for a given planet candidate. This code has been widely used to confirm TESS planet candidates (e.g., Thomas et al., 2025; Scott et al., 2025; Barkaoui et al., 2025; Stalport et al., 2025). In `TRICERATOPS+` (Gomez Barrientos et al. 2025, in review)[1], we updated this code to incorporate information from transit light curves obtained in multiple bandpasses.

`TRICERATOPS+` does not directly utilize any of the information from our transit light curve fits in §5.3. Instead, it generates a series of scenarios for both transiting planet and steller eclipsing binary cases by drawing parameters randomly from a set of prior distributions informed by observations of both populations. For each randomly generated scenario, it calculates a predicted bandpass-specific light curve. It then compares this predicted light curve to the measured light curve in that bandpass and calculates the corresponding log-likelihood value (Equation 16 of Giacalone et al. 2021). The code then sums the individual log-likelihoods for each bandpass to make a single combined log-likelihood for that scenario. The resulting ensemble of log-likelihoods is then used to calculate the FPP and NFPP as described in Giacalone et al., 2021. This package calculates limb darkening coefficients using the `ExoTIC-LD` package (Grant et al., 2022); in order to do so for TOI-2267, we utilize the stellar parameter values reported in Table 2 of ZP25. For scenarios involving eclipsing binaries and/or contamination from unresolved companions, as

---

[1] `https://github.com/JGB276/TRICERATOPS-plus`

is the case for the TOI-2267 system, `TRICERATOPS`+ also incorporates the bandpass-specific flux ratio when computing predicted model light curves for each scenario. We fix the TESS and J band flux ratios to the best-fit values reported in ZP25 for TOI-2267.

We computed the FPP and NFPP for TOI-2267 d using the phased TESS transit light curve, both Palomar light curves, and a high-resolution contrast curve from the ‘Alopeke speckle instrument on the Gemini North 8-m telescope that was published in ZP25. This observation detected the companion star TOI-2267 B at a separation of $0\farcs384$, and found no evidence for any additional companions brighter than 4-5 magnitudes below that of TOI-2267 A out to a distance of $1\farcs2$.

In the `TRICERATOPS` analysis of ZP25, multiple terms are excluded from the NFPP calculation, which correspond to scenarios that have already been ruled out for the TOI-2267 system. These include scenarios where the star does not have an unresolved companion, and scenarios where there is a background star at the current location of TOI-2267, which was ruled out through an analysis of archival images for this high proper motion star. Removing these terms has the effect of decreasing the NFPP value (see equation 5 of Giacalone et al., 2021). ZP25 also added two new terms to the FPP calculation, corresponding to scenarios with a transiting planet around an unresolved bound companion (see equation 4 of Giacalone et al., 2021), which has the effect of decreasing the FPP value. We do not modify the FPP and NFPP calculations, instead adopting the standard approach described in Giacalone et al., 2021. This provides us with a conservative upper limit on the false positive probabilities for TOI-2267 d. Following previous statistical validation studies with `TRICERATOPS` (e.g., Giacalone et al., 2021; Giacalone et al., 2022), we ran the analysis 20 times and report the average value and the 68% confidence interval of the FPP and the NFPP. We obtain a FPP of 2.7×10^{-7}, with a 68% confidence interval range of $(3.7 \times 10^{-8}, 2.0 \times 10^{-6})$. We calculate a NFPP of 0; this reflects the fact that our Palomar observations detected transits with the expected depth around the target star, ruling out events that occur on other nearby spatially resolved stars. As defined in Giacalone et al. 2021, the recommended threshold to validate a planetary candidate is FPP $< 1.5\%$ and NFPP $< 0.1\%$. This means that TOI-2267 d definitively satisfies the requirements for a statistically validated planet.

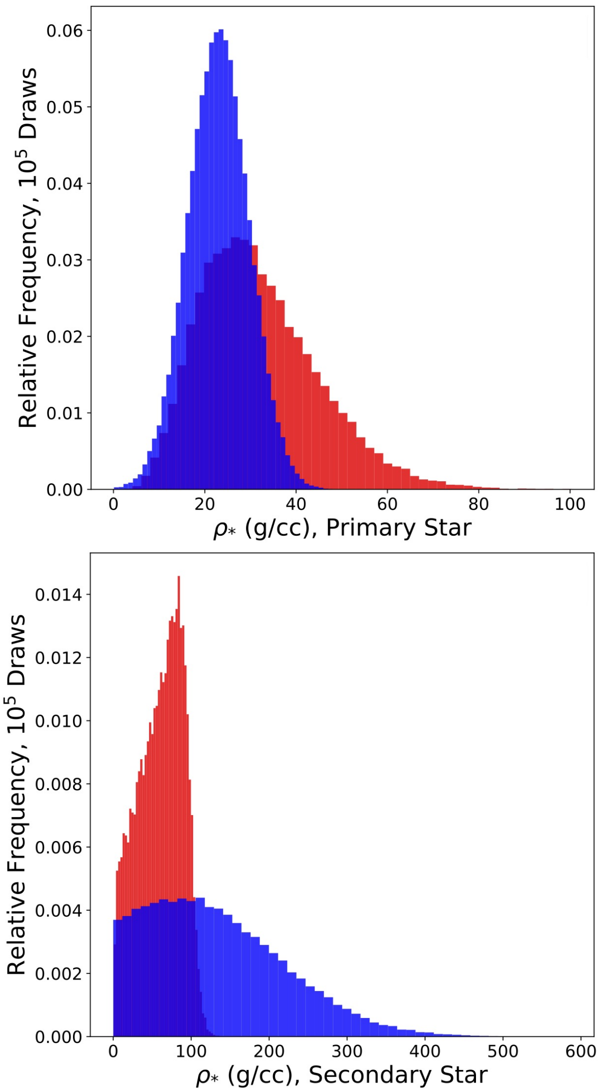

Figure 5.2 Empirical stellar density constraints derived from our transit shape analysis (red) compared to the stellar density measurements from the SED fitting of ZP25 (blue), for the primary (top) and secondary star (bottom) fits. Our empirical constraints on the stellar density are not precise enough to conclusively rule out either star as the host of TOI-2267 d.

5.4 Host Star Identification

Transit Shape Analysis

Having confirmed the planetary nature of TOI-2267 d, we next attempted to determine which binary component it orbits. First, we compared the quality of the joint transit fit from §5.3 for the primary versus secondary star case. Since both cases have the same model framework and number of parameters, we compared the ratio of maximum a posteriori likelihood values identified from each `PyMC3` sampler chain. We measured a likelihood ratio of 1.5 in favor of the primary star over the secondary star case. However, this preference is not statistically significant; a likelihood ratio closer to 10 is typically required in order to provide strong evidence for one model over another (Deeks et al., 2004).

We also attempted to identify the host star using constraints on the stellar density derived from our measurement of the transit shape (e.g., Lester et al., 2022). We combined our retrieved posterior distribution for a/R_* with the orbital period and the measured stellar radius reported by ZP25 to calculate a posterior probability distribution for the mean stellar density. We repeated this process for fits where the planet was assumed to orbit the primary and where it orbited the secondary. We then compared the inferred stellar densities from each transit fit to the independently measured stellar densities from the SED fitting of ZP25. In previous studies using this technique, the star whose measured stellar density from the transit light curve more closely matched expectations from stellar population models was assumed to be the planet host (Lester et al., 2022). Unfortunately, the density of TOI-2267 B is only loosely constrained by SED fitting ($\rho_{*_A} = 23.0^{+5.3}_{-4.0}$, $\rho_{*_B} = 83^{+113}_{-39}$, ZP 25). We found that our empirically constrained stellar densities are consistent with the SED priors in both cases (see Fig. 5.2). We conclude that our combined transit light curves are not precise enough to identify the host star for TOI-2267 d.

Dynamical Modeling[2]

Although we are unable to identify the host star for TOI-2267 d, we can in principle utilize the close orbital spacing of TOI-2267 d and b to explore whether or not the system would be dynamically stable if all three planets orbited the same star. This same approach was recently utilized by Asiru et al. 2025, in prep. The three planets have orbital periods of $2.0344562^{+0.0000037}_{-0.0000046}$, 2.2890887 ± 0.0000016, and 3.4950404 ± 0.0000022 days for the primary star case. ZP25 used the SPOCK

---

[2] This section is not part of the main submitted paper Greklek-McKeon et al. 2025c, but will instead be published as part of the companion paper by Asiru et al.

stability classifier (Tamayo et al., 2020), a machine-learning model trained on numerical integrations of three-planet systems, to predict the stability of the system if all three planets orbit the primary or secondary star. ZP25 found highly unstable architectures from this analysis, hinting that the three-planet configurations orbiting the same star are not possible, and suggesting that if TOI-2267 d is confirmed as a real planet, then the three planets do not orbit the same star. However, Asiru et al. 2025, in prep. proposed that a resonance could stabilize the orbits of d and b, allowing for their long-term survival in the same system. We test this hypothesis with n-body simulations.

We used the WHFast integrator in the `rebound` n-body code (Rein et al., 2015), and initialized 1000 random simulations for a total time of 10^5 years, with a timestep of 0.1 days, $< 5\%$ of the orbital period of the closest planet. We drew planet radii, orbital periods, and semi-major axes randomly from the values reported in ZP25 for TOI-2267 b and c and from Table 1 for TOI-2267 d, and assigned masses to the planets assuming an Earth-like bulk composition. We drew eccentricities from a uniform distribution between 0 to 0.001, as our goal was to evaluate whether or not the system could remain stable in the most optimistic case of low orbital eccentricities. We drew longitudes of periastron from a random uniform distribution from 0 to 2π, and set all orbital inclinations to coplanar at 90 degrees. In 100% of our 1000 random simulations, the system went unstable with at least one planet being ejected or spiraling into the host star within 10^5 years, regardless of whether we ran the simulation with the primary star or the secondary star as the host.

ZP25 noted that TOI-2267 b and c have an orbital period ratio $< 2\%$ from the 3:2 mean-motion resonance. If TTVs can be observed for these planets, it would indicate that they are gravitationally interacting and therefore share a host star. At an orbital period of 2.0345 days (Table 2), the newly confirmed TOI-2267 d is $0.0142 \pm 0.0002\%$ away from the 9:8 mean-motion resonance with TOI-2267 b. We explored whether this orbital resonance might act to stabilize the system by performing additional `rebound` n-body simulations of the system for a case where the inner two planets have a librating resonance angle associated with the 9:8 MMR.

We repeat our random orbital parameter initializations as described above, but in this case we draw masses for planets d and b from a random uniform distribution from 0.1 to 1 $M_\oplus$, and eccentricities from 0.0 to 0.05. We limit the masses to 1 $M_\oplus$ to test the optimistic case where the planets are low-mass and therefore more likely to be stabilized by the resonance. We drew random parameters and simulated the system for 1000 years, calculating the critical 9:8 resonant angle $\phi_{9:8}$ for TOI-2267 d and b in each case. We used equation 1 of (Goldberg et al., 2022) to calculate $\phi_{9:8}$, which depends on the mean longitudes of both planets and the longitude of periastron ϖ for either planet. We repeated this procedure until we identified 10 sets of planetary mass and orbital parameters that result in a $\phi_{9:8}$ that librates around a stable value with an amplitude $< \pi$ over the 1000 years of simulation, for both the primary and secondary star cases. We then took these in-resonance parameter sets and simulated them for an additional 10^6 years. We found that all ten dynamical simulations where TOI-2267 b and d began in the 9:8 resonance are stable over 10^6 years, regardless of whether or not TOI-2267 b and c are in the 3:2 resonance, or whether the planets orbit the primary or secondary star. Our results are in good agreement with previous dynamical modeling by Asiru et al. 2025, in prep., and we concur that it is possible for all three planets in the TOI-2267 system to share a stellar host. If this is indeed the case, this would make TOI-2267 the most compact exoplanet system known, with the highest first-order resonance ever observed. Asiru et al. 2025, in prep., investigates this scenario in more detail.

5.5 Discussion

Could TOI-2267 d Host a Volatile-Rich Envelope?

Small M dwarf planets may be more susceptible to atmospheric mass loss. M dwarfs have higher fractional XUV fluxes, more frequent flares than their sun-like counterparts, and a longer activity lifetime, which could result in enhanced atmospheric mass loss rates (Johnstone, 2020; Harbach et al., 2021; Atri et al., 2021). The observed flaring in TESS photometry and very short rotation periods of the TOI-2267 stars (~ 17 hours for TOI-2267A, and ~15 hours for TOI-2267B, ZP25), suggest both stars may have strong stellar winds and energetic particle emissions. Whether TOI-2267 d orbits the primary or the secondary star, its short orbital period indicates that it is likely subjected to extreme space weather conditions. If TOI-2267 d orbits the primary star it would have a radius of 0.956 ± 0.087 $R_\oplus$ and a predicted equilibrium temperature of 503 ± 32 K. This makes it a close analogue of Trappist-1 b, which was recently shown to have lost most or all of its atmosphere (Greene et al., 2023).

If TOI-2267 d instead orbits the secondary star, it would have a radius of 1.813 ± 0.438 $R_\oplus$ and an equilibrium temperature of 422 ± 55 K. Population-level studies of M dwarf planet masses indicate that planets of this size often host volatile-rich envelopes (e.g., Luque et al., 2022; Rogers et al., 2023). Regardless of which star

TOI-2267 d orbits, with a projected separation of 8 au the companion star is likely close enough to contribute to the planet's local XUV and stellar wind environment, with corresponding implications for its atmospheric mass loss history. We conclude that this system presents an exciting opportunity for future studies on the impact of stellar multiplicity on space weather and atmospheric mass loss for sub-Neptune-sized exoplanets.

Identifying a Host Star for TOI-2267 d

In the future, improved stellar density constraints might make it possible to unambiguously assign TOI-2267 d to a host star. However, there are several alternative approaches that could also provide a definitive identification. The most straightforward solution would be to obtain a transit observation of TOI-2267 d that spatially resolves the two stars; however, ground-based AO imaging has not demonstrated that it can achieve the required photometric precision (e.g., Howell et al., 2019), and this would therefore likely require space-based observations with HST or JWST. ZP25 also pointed out that significantly higher precision measurements of the wavelength-dependent transit shape after correcting for dilution effects could also be used to assign a stellar host.

As a result of their compact orbits, any planet pairs orbiting the same star should exhibit transit timing variations. ZP25 predicted that the TTV amplitudes of TOI-2267 b and c are likely to be small, and are therefore unlikely to be detected using the individual TESS transits times, which have a relatively low SNR. For TOI-2267 d, our individual Palomar/WIRC transit observations achieve a much higher timing precision (1.3 min) than for individual TESS transit observations (median precision of $\sim$12 min). In the future, additional ground-based transit timing measurements of all three planets with a comparable precision could be used to carry out a much more sensitive search for transit timing variations. If TTVs are detected for any of the planets in the TOI-2267 system, the information on planet-to-star mass ratio could also be combined with information on planet-to-star radius ratio and compatibility with each binary component's density to obtain improved constraints on which star the planets orbit.

5.6 Conclusions

We statistically validate a third Earth-sized exoplanet in the TOI-2267 binary system, TOI-2267 d, but cannot unambiguously assign it to a host star. If it orbits TOI-2267A, it is a 1.0 $R_\oplus$ terrestrial planet with a predicted equilibrium temperature of approximately 500 K. Given the relatively high activity levels of both stars and their small projected separation, this would suggest that it has likely lost any primordial atmosphere. If it instead orbits the secondary, it is a 1.8 $R_\oplus$ planet with an equilibrium temperature of approximately 420 K, and therefore might host a volatile-rich envelope. If present, any volatile-rich envelope is likely to experience ongoing atmospheric mass loss driven by the irradiation and winds from both stars.

Regardless of whether TOI-2267 d orbits the primary or secondary star, the presence of three transiting planets in this system provides an exciting opportunity to explore the effect of a close binary companion on the formation and evolution of sub-Neptune-sized planets. If TOI-2267 d orbits a different star than TOI-2267 b and c, this system would be the first double-transiting binary M dwarf system. If all three planets instead orbit one star as proposed by Asiru et al. (in prep.), then TOI-2267 would host an extremely compact and dynamically delicate three-planet system similar to that of TRAPPIST-1 (Luger et al., 2017; Tamayo et al., 2017; Papaloizou et al., 2018). We use dynamical modeling to independently verify the hypothesis first put forward by Asiru et al. 2025, in prep., and confirm that all three planets could orbit the same star if d and b are in an orbital resonance. Any detection of transit timing variations (TTVs) for TOI-2267 b, c, or d would prove that they are gravitationally interacting and therefore share a host star, and could be used to conclusively determine whether TOI-2267 d and b are in resonance. Planet-to-star mass ratios from TTVs could also be combined with planet-to-star radius ratios from the stacked transit profiles to perform updated stellar density analysis and assign a host star (e.g., Lester et al., 2022). There is therefore great value in obtaining additional high-precision ground-based transit observations of all three planets in this exciting new system.

5.7 Appendix

We present the full posterior distribution for all transit model parameters in the primary star joint fit in Figure 5.3, and the posterior distribution for all transit model parameters in the secondary star joint fit in Figure 5.4.

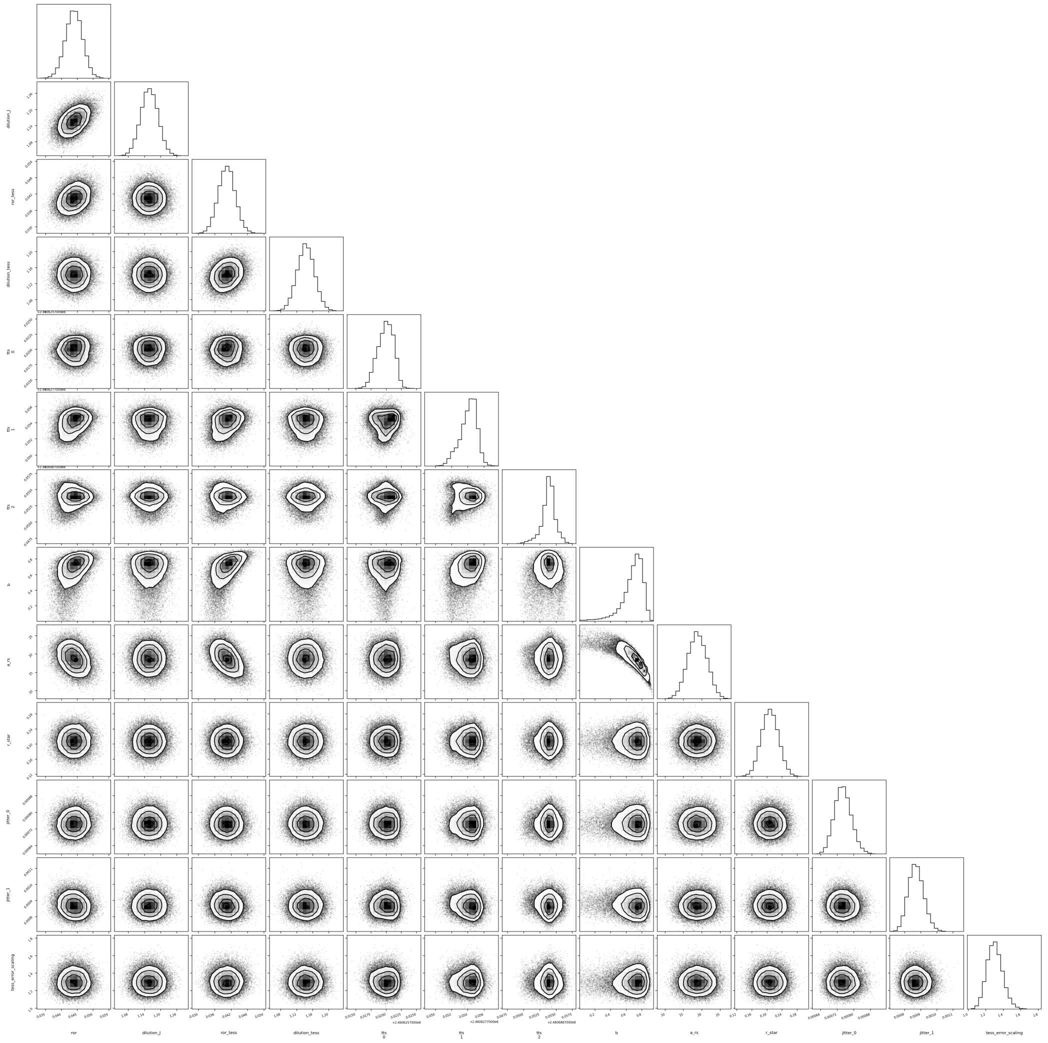

Figure 5.3 Posterior distribution of transit model parameters in our joint transit fit, assuming the primary host star, using both nights of Palomar/WIRC data and the phase-folded TESS photometry for TOI-2267 d.

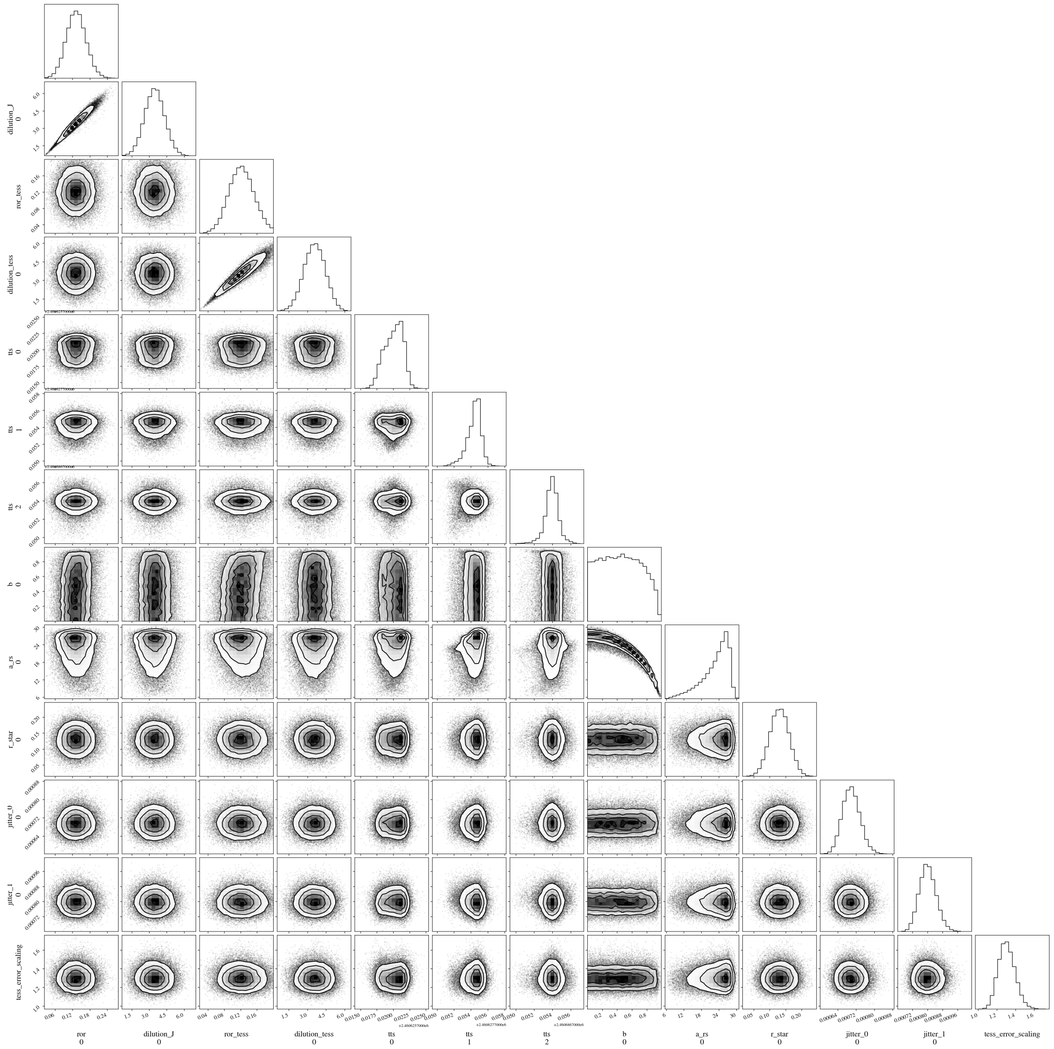

Figure 5.4 Posterior distribution of transit model parameters in our joint transit fit, assuming the secondary host star, using both nights of Palomar/WIRC data and the phase-folded TESS photometry for TOI-2267 d.

References

Atri, Dimitra et al. (Jan. 2021). “Stellar flares versus luminosity: XUV-induced atmospheric escape and planetary habitability”. In: *MNRAS* 500.1, pp. L1–L5. doi: `10.1093/mnrasl/slaa166`. arXiv: `2009.04310 [astro-ph.EP]`.

Barclay, Thomas et al. (Aug. 2015). “The Five Planets in the Kepler-296 Binary System All Orbit the Primary: A Statistical and Analytical Analysis”. In: *ApJ* 809.1, 7, p. 7. doi: `10.1088/0004-637X/809/1/7`. arXiv: `1505.01845 [astro-ph.EP]`.

Barkaoui, K. et al. (Mar. 2025). “TOI-2015 b: A sub-Neptune in strong gravitational interaction with an outer non-transiting planet”. In: *A&A* 695, A281, A281. doi: `10.1051/0004-6361/202452916`. arXiv: `2502.07074 [astro-ph.EP]`.

Bochanski, John J. et al. (June 2010). “The Luminosity and Mass Functions of Low-mass Stars in the Galactic Disk. II. The Field”. In: *AJ* 139.6, pp. 2679–2699. doi: `10.1088/0004-6256/139/6/2679`. arXiv: `1004.4002 [astro-ph.SR]`.

Ciardi, David R. et al. (May 2015). “Understanding the Effects of Stellar Multiplicity on the Derived Planet Radii from Transit Surveys: Implications for Kepler, K2, and TESS”. In: *ApJ* 805.1, 16, p. 16. doi: `10.1088/0004-637X/805/1/16`. arXiv: `1503.03516 [astro-ph.EP]`.

Clark, Catherine A. et al. (Apr. 2024). “The POKEMON Speckle Survey of Nearby M Dwarfs. III. The Stellar Multiplicity Rate of M Dwarfs within 15 pc”. In: *AJ* 167.4, 174, p. 174. doi: `10.3847/1538-3881/ad267d`. arXiv: `2401.14703 [astro-ph.SR]`.

Deeks, Jonathan J et al. (2004). “Diagnostic tests 4: likelihood ratios”. In: *BMJ* 329.7458, pp. 168–169. issn: 0959-8138. doi: `10.1136/bmj.329.7458.168`. eprint: `https://www.bmj.com/content/329/7458/168.full.pdf`. url: `https://www.bmj.com/content/329/7458/168`.

Feinstein, Adina D. et al. (Feb. 2019). “K2-288Bb: A Small Temperate Planet in a Low-mass Binary System Discovered by Citizen Scientists”. In: *AJ* 157.2, 40, p. 40. doi: `10.3847/1538-3881/aafa70`. arXiv: `1902.02789 [astro-ph.EP]`.

Giacalone, Steven et al. (Jan. 2021). “Vetting of 384 TESS Objects of Interest with TRICERATOPS and Statistical Validation of 12 Planet Candidates”. In: *AJ* 161.1, 24, p. 24. doi: `10.3847/1538-3881/abc6af`. arXiv: `2002.00691 [astro-ph.EP]`.

Giacalone, Steven et al. (Feb. 2022). “Validation of 13 Hot and Potentially Terrestrial TESS Planets”. In: *AJ* 163.2, 99, p. 99. doi: `10.3847/1538-3881/ac4334`. arXiv: `2201.12661 [astro-ph.EP]`.

Gilbert, Emily A. et al. (Feb. 2023). “A Second Earth-sized Planet in the Habitable Zone of the M Dwarf, TOI-700”. In: *ApJL* 944.2, L35, p. L35. doi: `10.3847/2041-8213/acb599`. arXiv: `2301.03617 [astro-ph.EP]`.

Goldberg, Max et al. (Dec. 2022). “A criterion for the stability of planets in chains of resonances”. In: *Icarus* 388, 115206, p. 115206. DOI: `10.1016/j.icarus.2022.115206`. arXiv: `2207.13833 [astro-ph.EP]`.

Grant, David et al. (Dec. 2022). *Exo-TiC/ExoTiC-LD: ExoTiC-LD v3.0.0*. Version v3.0.0. DOI: `10.5281/zenodo.7437681`.

Greene, Thomas P. et al. (June 2023). “Thermal emission from the Earth-sized exoplanet TRAPPIST-1 b using JWST”. In: *Nature* 618.7963, pp. 39–42. DOI: `10.1038/s41586-023-05951-7`. arXiv: `2303.14849 [astro-ph.EP]`.

Greklek-McKeon, Michael et al. (Feb. 2023). “Constraining the Densities of the Three Kepler-289 Planets with Transit Timing Variations”. In: *AJ* 165.2, 48, p. 48. DOI: `10.3847/1538-3881/ac8553`. arXiv: `2208.00022 [astro-ph.EP]`.

Harbach, Laura M. et al. (June 2021). “Stellar Winds Drive Strong Variations in Exoplanet Evaporative Outflow Patterns and Transit Absorption Signatures”. In: *ApJ* 913.2, 130, p. 130. DOI: `10.3847/1538-4357/abf63a`. arXiv: `2012.05922 [astro-ph.EP]`.

Hardegree-Ullman, Kevin K. et al. (Aug. 2019). “Kepler Planet Occurrence Rates for Mid-type M Dwarfs as a Function of Spectral Type”. In: *AJ* 158.2, 75, p. 75. DOI: `10.3847/1538-3881/ab21d2`. arXiv: `1905.05900 [astro-ph.EP]`.

Harris, Robert J. et al. (June 2012). “A Resolved Census of Millimeter Emission from Taurus Multiple Star Systems”. In: *ApJ* 751.2, 115, p. 115. DOI: `10.1088/0004-637X/751/2/115`. arXiv: `1203.6353 [astro-ph.SR]`.

Henry, Todd J. et al. (Dec. 2006). “The Solar Neighborhood. XVII. Parallax Results from the CTIOPI 0.9 m Program: 20 New Members of the RECONS 10 Parsec Sample”. In: *AJ* 132.6, pp. 2360–2371. DOI: `10.1086/508233`. arXiv: `astro-ph/0608230 [astro-ph]`.

Hirsch, Lea A. et al. (Mar. 2021). “Understanding the Impacts of Stellar Companions on Planet Formation and Evolution: A Survey of Stellar and Planetary Companions within 25 pc”. In: *AJ* 161.3, 134, p. 134. DOI: `10.3847/1538-3881/abd639`. arXiv: `2012.09190 [astro-ph.EP]`.

Howell, Steve B. et al. (Sept. 2019). “High-resolution Imaging Transit Photometry of Kepler-13AB”. In: *AJ* 158.3, 113, p. 113. DOI: `10.3847/1538-3881/ab2f7b`.

Hsu, Danley C. et al. (Oct. 2020). “Occurrence rates of planets orbiting M Stars: applying ABC to Kepler DR25, Gaia DR2, and 2MASS data”. In: *MNRAS* 498.2, pp. 2249–2262. DOI: `10.1093/mnras/staa2391`. arXiv: `2002.02573 [astro-ph.EP]`.

Jenkins, Jon M. et al. (Aug. 2016). “The TESS science processing operations center”. In: *Software and Cyberinfrastructure for Astronomy IV*. Ed. by Gianluca Chiozzi et al. Vol. 9913. Society of Photo-Optical Instrumentation Engineers (SPIE) Conference Series, 99133E, 99133E. DOI: `10.1117/12.2233418`.

Johnstone, C. P. (Feb. 2020). "Hydrodynamic Escape of Water Vapor Atmospheres near Very Active Stars". In: *ApJ* 890.1, 79, p. 79. DOI: `10.3847/1538-4357/ab6224`. arXiv: `1912.07027 [astro-ph.EP]`.

Johnstone, C. P. et al. (June 2019). "Stellar activity and planetary atmosphere evolution in tight binary star systems". In: *A&A* 626, A22, A22. DOI: `10.1051/0004-6361/201832805`. arXiv: `1904.08295 [astro-ph.SR]`.

Kaib, Nathan A. et al. (Jan. 2013). "Planetary system disruption by Galactic perturbations to wide binary stars". In: *Nature* 493.7432, pp. 381–384. DOI: `10.1038/nature11780`. arXiv: `1301.3145 [astro-ph.EP]`.

Kaminski, A. et al. (Apr. 2025). "The CARMENES search for exoplanets around M dwarfs: Occurrence rates of Earth-like planets around very low-mass stars". In: *A&A* 696, A101, A101. DOI: `10.1051/0004-6361/202453381`. arXiv: `2504.03364 [astro-ph.EP]`.

Kempton, Eliza M. -R. et al. (Nov. 2018). "A Framework for Prioritizing the TESS Planetary Candidates Most Amenable to Atmospheric Characterization". In: *PASP* 130.993, p. 114401. DOI: `10.1088/1538-3873/aadf6f`. arXiv: `1805.03671 [astro-ph.EP]`.

Kraus, Adam L. et al. (July 2016). "The Impact of Stellar Multiplicity on Planetary Systems. I. The Ruinous Influence of Close Binary Companions". In: *AJ* 152.1, 8, p. 8. DOI: `10.3847/0004-6256/152/1/8`. arXiv: `1604.05744 [astro-ph.EP]`.

Lester, Kathryn V. et al. (Aug. 2022). "Determining Which Binary Component Hosts the TESS Transiting Planet". In: *AJ* 164.2, 56, p. 56. DOI: `10.3847/1538-3881/ac75ee`. arXiv: `2206.02825 [astro-ph.SR]`.

Luger, Rodrigo et al. (June 2017). "A seven-planet resonant chain in TRAPPIST-1". In: *Nature Astronomy* 1, 0129, p. 0129. DOI: `10.1038/s41550-017-0129`. arXiv: `1703.04166 [astro-ph.EP]`.

Luque, Rafael et al. (Sept. 2022). "Density, not radius, separates rocky and water-rich small planets orbiting M dwarf stars". In: *Science* 377.6611, pp. 1211–1214. DOI: `10.1126/science.abl7164`. arXiv: `2209.03871 [astro-ph.EP]`.

Matson, Rachel A. et al. (Feb. 2025). "Demographics of M Dwarf Binary Exoplanet Hosts Discovered by TESS". In: *AJ* 169.2, 76, p. 76. DOI: `10.3847/1538-3881/ad9923`. arXiv: `2412.08465 [astro-ph.EP]`.

Mignon, L. et al. (Feb. 2025). "Radial velocity homogeneous analysis of M dwarfs observed with HARPS. II. Detection limits and planetary occurrence statistics". In: *arXiv e-prints*, arXiv:2502.06553, arXiv:2502.06553. DOI: `10.48550/arXiv.2502.06553`. arXiv: `2502.06553 [astro-ph.EP]`.

Ngo, Henry et al. (Aug. 2016). “Friends of Hot Jupiters. IV. Stellar Companions Beyond 50 au Might Facilitate Giant Planet Formation, but Most are Unlikely to Cause Kozai-Lidov Migration”. In: *ApJ* 827.1, 8, p. 8. DOI: `10.3847/0004-637X/827/1/8`. arXiv: `1606.07102 [astro-ph.EP]`.

Nutzman, Philip et al. (Mar. 2008). “Design Considerations for a Ground-Based Transit Search for Habitable Planets Orbiting M Dwarfs”. In: *PASP* 120.865, p. 317. DOI: `10.1086/533420`. arXiv: `0709.2879 [astro-ph]`.

Papaloizou, J. C. B. et al. (June 2018). “The TRAPPIST-1 system: orbital evolution, tidal dissipation, formation and habitability”. In: *MNRAS* 476.4, pp. 5032–5056. DOI: `10.1093/mnras/stx2980`. arXiv: `1711.07932 [astro-ph.EP]`.

Pérez-González, Jorge et al. (May 2024). “Detection of an Atmospheric Outflow from the Young Hot Saturn TOI-1268b”. In: *AJ* 167.5, 214, p. 214. DOI: `10.3847/1538-3881/ad34b6`. arXiv: `2307.09515 [astro-ph.EP]`.

Rein, Hanno et al. (July 2015). “whfast: a fast and unbiased implementation of a symplectic Wisdom–Holman integrator for long-term gravitational simulations”. In: *Monthly Notices of the Royal Astronomical Society* 452.1, pp. 376–388. ISSN: 1365-2966. DOI: `10.1093/mnras/stv1257`. URL: `http://dx.doi.org/10.1093/mnras/stv1257`.

Reylé, C. et al. (June 2021). “The 10 parsec sample in the Gaia era”. In: *A&A* 650, A201, A201. DOI: `10.1051/0004-6361/202140985`. arXiv: `2104.14972 [astro-ph.SR]`.

Rogers, James G. et al. (Apr. 2023). “Conclusive Evidence for a Population of Water Worlds around M Dwarfs Remains Elusive”. In: *ApJL* 947.1, L19, p. L19. DOI: `10.3847/2041-8213/acc86f`. arXiv: `2301.04321 [astro-ph.EP]`.

Schwarz, Gideon (July 1978). “Estimating the Dimension of a Model”. In: *Annals of Statistics* 6.2, pp. 461–464.

Scott, Madison G. et al. (May 2025). “TOI-6478 b: a cold under-dense Neptune transiting a fully convective M dwarf from the thick disc”. In: *MNRAS*. DOI: `10.1093/mnras/staf684`. arXiv: `2504.06848 [astro-ph.EP]`.

Smith, Jeffrey C. et al. (Sept. 2012). “Kepler Presearch Data Conditioning II - A Bayesian Approach to Systematic Error Correction”. In: *PASP* 124.919, p. 1000. DOI: `10.1086/667697`. arXiv: `1203.1383 [astro-ph.IM]`.

Stalport, M. et al. (Apr. 2025). “TESS and HARPS-N unveil two planets transiting TOI-1453: A super-Earth and one of the lowest mass sub-Neptunes”. In: *A&A* 696, A86, A86. DOI: `10.1051/0004-6361/202452969`. arXiv: `2503.07529 [astro-ph.EP]`.

Stefansson, Gudmundur et al. (Oct. 2017). “Toward Space-like Photometric Precision from the Ground with Beam-shaping Diffusers”. In: *ApJ* 848.1, 9, p. 9. DOI: `10.3847/1538-4357/aa88aa`. arXiv: `1710.01790 [astro-ph.IM]`.

Stumpe, Martin C. et al. (Sept. 2012). “Kepler Presearch Data Conditioning I—Architecture and Algorithms for Error Correction in Kepler Light Curves”. In: *PASP* 124.919, p. 985. DOI: `10.1086/667698`. arXiv: `1203.1382 [astro-ph.IM]`.

Stumpe, Martin C. et al. (Jan. 2014). “Multiscale Systematic Error Correction via Wavelet-Based Bandsplitting in Kepler Data”. In: *PASP* 126.935, p. 100. DOI: `10.1086/674989`.

Suissa, Gabrielle et al. (Sept. 2020). “The First Habitable-zone Earth-sized Planet from TESS. III. Climate States and Characterization Prospects for TOI-700 d”. In: *AJ* 160.3, 118, p. 118. DOI: `10.3847/1538-3881/aba4b4`. arXiv: `2001.00955 [astro-ph.EP]`.

Sullivan, Kendall et al. (Apr. 2023). “Revising Properties of Planet-Host Binary Systems. III. There Is No Observed Radius Gap for Kepler Planets in Binary Star Systems”. In: *AJ* 165.4, 177, p. 177. DOI: `10.3847/1538-3881/acbdf9`. arXiv: `2302.08532 [astro-ph.EP]`.

Sullivan, Kendall et al. (Sept. 2024). “Revising Properties of Planet–Host Binary Systems. IV. The Radius Distribution of Small Planets in Binary Star Systems Is Dependent on Stellar Separation”. In: *AJ* 168.3, 129, p. 129. DOI: `10.3847/1538-3881/ad6310`. arXiv: `2406.17648 [astro-ph.EP]`.

Tamayo, Daniel et al. (May 2017). “Convergent Migration Renders TRAPPIST-1 Long-lived”. In: *ApJL* 840.2, L19, p. L19. DOI: `10.3847/2041-8213/aa70ea`. arXiv: `1704.02957 [astro-ph.EP]`.

Tamayo, Daniel et al. (Aug. 2020). “Predicting the long-term stability of compact multiplanet systems”. In: *Proceedings of the National Academy of Science* 117.31, pp. 18194–18205. DOI: `10.1073/pnas.2001258117`. arXiv: `2007.06521 [astro-ph.EP]`.

Thomas, Luis et al. (Feb. 2025). “TOI-5108 b and TOI 5786 b: Two transiting sub-Saturns detected and characterized with TESS, MaHPS, and SOPHIE”. In: *A&A* 694, A143, A143. DOI: `10.1051/0004-6361/202451676`. arXiv: `2501.03803 [astro-ph.EP]`.

Triaud, Amaury H. M. J. (2021). “Small Star Opportunities”. In: *ExoFrontiers*. 2514-3433. IOP Publishing, 6-1 to 6–6. ISBN: 978-0-7503-1472-5. DOI: `10.1088/2514-3433/abfa8fch6`. URL: `https://dx.doi.org/10.1088/2514-3433/abfa8fch6`.

Vissapragada, Shreyas et al. (Feb. 2020). “Diffuser-assisted Infrared Transit Photometry for Four Dynamically Interacting Kepler Systems”. In: *The Astronomical Journal* 159.3, p. 108. ISSN: 1538-3881. DOI: `10.3847/1538-3881/ab65c8`. URL: `http://dx.doi.org/10.3847/1538-3881/ab65c8`.

Ward-Duong, K. et al. (May 2015). “The M-dwarfs in Multiples (MINMS) survey - I. Stellar multiplicity among low-mass stars within 15 pc”. In: *MNRAS* 449.3, pp. 2618–2637. DOI: `10.1093/mnras/stv384`. arXiv: `1503.00724 [astro-ph.SR]`.

Wilson, John C. et al. (Mar. 2003). “A Wide-Field Infrared Camera for the Palomar 200-inch Telescope”. In: *Instrument Design and Performance for Optical/Infrared Ground-based Telescopes*. Ed. by Masanori Iye et al. Vol. 4841. Society of Photo-Optical Instrumentation Engineers (SPIE) Conference Series, pp. 451–458. DOI: `10.1117/12.460336`.

Winters, Jennifer G. et al. (June 2019). “The Solar Neighborhood. XLV. The Stellar Multiplicity Rate of M Dwarfs Within 25 pc”. In: *AJ* 157.6, 216, p. 216. DOI: `10.3847/1538-3881/ab05dc`. arXiv: `1901.06364 [astro-ph.SR]`.

Wordsworth, Robin et al. (Aug. 2022). “Atmospheres of Rocky Exoplanets”. In: *ARA&A* 60, pp. 159–201. DOI: `10.1146/annurev-astro-052920-125632`. arXiv: `2112.04663 [astro-ph.EP]`.

Chapter 6

CONCLUSIONS

6.1 Summary

This thesis has presented new and improved mass, radius, and bulk density measurements for small planets orbiting low-mass stars. These include TTV-based mass and bulk composition constraints for planets in the Kepler-289, TOI-1266, and LP 791-18 systems, and confirmation of a new planet in the unique TOI-2267 binary system. These results shed light on several open topics in exoplanet science, including planet migration from water-rich regions of the outer disk, the occurrence rate of water worlds, the importance of atmospheric mass loss for small planets around M dwarfs, and the effects of tidal heating for near-resonant rocky planets.

In Chapter 2, I measured the densities of two inner sub-Neptune planets and an outer gas giant in the Kepler-289 system, using TTV observations from Palomar Observatory combined with a re-analysis of archival Kepler data. Using the core mass of the gas giant planet, I placed a lower limit on the mass of solids accessible in the inner protoplanetary disk, which constrained the formation location of the outer gas giant planet when compared to the total observed mass of the inner two sub-Neptunes. This was far beyond its present-day location, indicating post-formation orbital migration (Greklek-McKeon et al., 2023). For this project, I obtained extremely precise TTV measurements (~1-min precision), which motivated me to use the near-IR imager at Palomar to apply this method to M dwarf systems. This led to my planning and execution of an international observational campaign to characterize the masses and compositions of many small M dwarf planets, with the goals of revealing the compositional diversity of these planets and to characterize promising targets for atmospheric follow-up.

In Chapter 3 (Greklek-McKeon, Vissapragada, and Knutson, et al., 2025), I characterized the TOI-1266 system. I combined TESS data, ground-based TTVs, and archival RVs to improve the planetary bulk density constraints, confirm a new third planet, and measure a non-zero eccentricity for the inner sub-Neptune planet which may be responsible for inflating its radius through tidal heating. I also found that the middle planet, TOI-1266 c, is a candidate water world, and that both planets are strong candidates for atmospheric characterization with the James Webb Space

Telescope, with large predicted atmospheric features in transmission. The detection of a potentially tidally heated sub-Neptune and a water world that are both accessible to atmospheric characterization motivates further study of this unique system. If TOI-1266 c is confirmed as a water world through the detection of a water-rich atmosphere with transmission spectroscopy, it would be the second ever water world confirmed via direct detection (Piaulet-Ghorayeb et al., 2024a). TOI-1266 is also being observed by an ongoing XMM-Newton space telescope program to characterize the XUV flux of the host star. If this program reveals that TOI-1266 c is highly irradiated and could not retain a primoridal H-rich envelope and therefore its low bulk density can be explained by a water-rich composition, it would be one of only a few bona-fide water worlds confirmed via this indirect technique (Diamond-Lowe et al., 2022; Piaulet et al., 2023).

In Chapter 4, I presented new mass and eccentricity measurements for the potentially volcanically active Earth- sized planet LP 791-18 d (Greklek-McKeon, Knutson, and Levine, et al., 2025). I found that this planet is broadly consistent with an Earth-like composition, but that the TTV data cannot confirm an eccentric orbit if we assume the planet has an Earth-like tidal damping efficiency. If the planet has a much lower tidal efficiency than Earth, it could potentially have a much larger eccentricity and orders of magnitude more tidal heating. This planet still has a predicted non-zero forced eccentricity from dynamical interactions with the other nearby planets in the system, and is being observed in an ongoing JWST program to search for a potentially tidally-driven volcanically outgassed atmosphere via secondary eclipse observations. I made predictions for the secondary eclipse offset time relative to a circular orbit for LP 791-18 d, which will provide some of the first ever constraints on the tidal quality factor and internal heating rate of an Earth-sized exoplanet. These results motivate similar eccentricity analysis for other dynamically interacting terrestrial planets.

In Chapter 5, I presented the results of transit observations used to confirm a new Earth-sized planet (TOI-2267 d) in the TOI-2267 binary M dwarf system, which has a projected stellar separation of just 8 au. This planet has a radius of $\sim 1R_\oplus$ if it orbits the larger primary star, or $\sim 1.8R_\oplus$ if it orbits the smaller secondary star. Both stars are active, with < 18 hour rotation periods and regular flaring observed in TESS data. If TOI-2267 d orbits the secondary, its radius implies the presence of an atmosphere, which means that this planet will be a case study for atmospheric mass loss around active M dwarfs, and in close binary systems. The orbital period of TOI-2267 d is ~2.03 days, while TOI-2267 b is at ~2.29 days, less than 0.02% away from the 9:8 resonance. If TOI-2267 d and b are in this resonance, then it is the most compact exoplanet system detected, with interesting implications for how the planets bypassed all the lower first-order resonances to arrive at their current location, potentially involving dynamical interactions with the secondary star. If these planets are not in the 9:8 resonance, they have no stable orbital configuration, and must orbit separate stars, which would make this system the only M dwarf binary with transiting planets around both stars, with interesting implications for planet formation in truncated protoplanetary disks. In either scenario, TOI-2267 is a unique system that can be used to test the limits of planet formation and migration.

6.2 Lessons Learned and Next Steps in the Search for Water Worlds

New planet masses from this thesis, combined with new mass measurements from other studies in the past several years, have dramatically expanded the population of small planets with well-measured masses and radii (e.g., Brady et al., 2024; Cointepas et al., 2024; Dai et al., 2024; Lacedelli et al., 2024; Murgas et al., 2024; Lacedelli et al., 2025; R. A. Lee et al., 2025). Mass and radius measurements alone are not a unique diagnostic of planet composition, however. Many planetary interior and atmospheric properties remain degenerate, even after incorporating information from measurements of stellar refractory abundances and XUV irradiation (e.g., Diamond-Lowe et al., 2022; Rogers et al., 2023). We can break these degeneracies by directly observing atmospheric compositions with transmission spectroscopy, and recent results from JWST have revealed important new information on sub-Neptune atmospheres. JWST has detected sub-Neptunes with atmospheres dominated by water in a steam envelope (Piaulet-Ghorayeb et al., 2024b); atmospheres dominated by H/He (Madhusudhan et al., 2023; Wogan et al., 2024); and atmospheres in-between — where hydrogen, water, and other molecules are thoroughly mixed (Benneke et al., 2024). We now have confirmation that sub-Neptune atmospheres aren't binary, split between either a primordial solar metallicity envelope or a pure steam envelope, instead they exist on a continuum of composition.

Painting a complete picture of any given sub-Neptune atmosphere using observations that only probe the upper regions of the atmosphere via transmission spectroscopy is not a simple task. Disequilibrium chemistry can significantly impact the observed atmospheric composition, and the strength of vertical mixing plays a major role in affecting both atmospheric clouds and chemistry, despite being poorly constrained for many planets (Mukherjee et al., 2024). Sub-Neptunes with thick envelopes on closer orbits are predicted to have magma oceans underlying their atmospheres, and surface-atmosphere interactions can alter the size and composition of the atmosphere (e.g., Kite et al., 2020; Misener et al., 2023). The more distant, cooler, and potentially water-rich sub-Neptunes may instead host liquid water oceans at their surface (Kimura et al., 2022; Rigby et al., 2024), which can also alter the upper atmospheric composition (J. Yang et al., 2024). To fully understand the compositions of sub-Neptune sized planets, we must now consider them holistically, accounting for interior, surface, and atmospheric properties, and interactions between them. Improved modeling of these interactions will be crucial in revealing the true diversity of small planets. Emerging research is beginning to identify the observational signatures that can be used to investigate atmospheric interaction with surface magma oceans (e.g., Seo et al., 2024; Ito et al., 2025; Werlen et al., 2025) or with liquid water oceans (e.g., Hu et al., 2021; J. Yang et al., 2024).

New models of surface-atmosphere interactions for sub-Neptunes are timely and valuable, but our ability to interpret the observed atmospheric chemistries of sub-Neptunes also depends sensitively on the planetary energy budget — including the irradiation flux from above, and the often-neglected internal heat flux from below. Planets on eccentric orbits have tidal bulges that change in time, which leads to interior friction that raises the internal temperature. Small planets orbiting low-mass stars often have non-zero orbital eccentricities, resulting in tidal heat fluxes large enough to predict volcanic outgassing, and in many cases the tidal heat flux is comparable to the insolation flux (Seligman et al., 2024).

Tidal heating impacts interior ice and silicate melting, surface temperature, atmospheric outgassing, and potential habitability (Jackson et al., 2008). It can also raise the temperature in the deep atmosphere which alters atmospheric composition at the top of the atmosphere through vertical mixing or convection (e.g., Morley et al., 2017; Fortney et al., 2020; J. Yang et al., 2024). Tidal heating also inflates planetary radii (Millholland, 2019), which may bias buk metallicity estimates and potentially increase atmospheric escape (e.g., Thorngren et al., 2023), making it difficult to infer basic properties like the atmospheric mass due to the degeneracy in radius between tidal heat flux and envelope size. Eccentricity also shifts secondary eclipse times, making future observation scheduling difficult without precise constraints. If we cannot account for the influence of tidal heating on the observed properties of small planets, we may grossly misinterpret their structure and compositions.

The original motivation for this thesis was TTV-based mass measurements to determine planetary bulk composition, but it has also produced TTV-based eccentricity that are an essential science case for determining planetary interior and atmospheric properties, especially for the planets being characterized by JWST. This thesis has demonstrated that dynamically excited eccentricities can be stable against tidal circularization and maintained on timescales comparable to the age of the system. Even a tiny ($\lesssim$0.01) orbital eccentricity for a close-in small planet can significantly impact its tidal heat flux and inferred composition (e.g., Peterson et al., 2023), and many of the best rocky planets for atmospheric study are likely to have dynamically excited eccentricities. Out of the top ten highest priority targets identified by the JWST rocky worlds DDT program, four have orbital period ratios within 5% of a mean-motion resonance, and proximity to resonance forces orbital eccentricity (Lithwick et al., 2012). Of the seven cool ($<$ 500 K) sub-Neptunes (2-3 $R_\oplus$) scheduled for JWST observations in cycles 1-3, three are in compact systems near an orbital resonance. Without precise constraints on the eccentricities and tidal heating rates for these planets, we cannot fully understand them.

There are already several rocky planets with tentative atmospheric detections attributed to volcanic outgassing from tidal heating, but without precise eccentricity and tidal heat flux constraints (e.g., Banerjee et al., 2024; Gressier et al., 2024; Bello-Arufe et al., 2025). With tidal heat flux uncertainty ranges that overlap with zero within $1-2\sigma$, it is difficult to be certain of these detections of supposedly outgassed atmospheric species. But more importantly, it is impossible to connect these atmospheric detections to outgassing rates for a given internal heat flux, which could provide a detailed understanding of the planetary interior and interior-atmosphere interactions (e.g., Nicholls et al., 2025). As described in Chapter 4, a combination of TTV observations and dynamical modeling incorporating tidal forces can be used to constrain the steady-state forced eccentricities in near-resonant systems, and place corresponding lower-limit constraints on the tidal heat fluxes of these planets. Comparison of the TTV-based observed eccentricities to those predicted by dynamical modeling can also constrain the tidal efficiency factor Q, which teaches us about the planetary internal structure and temperature (e.g., Welbanks et al., 2024). This analysis is essential in understanding the small planet population, and will hopefully be applied to future studies of near-resonant planets, especially those with claimed atmospheric detections from tidally-driven volcanic outgassing.

Near-resonant systems observed by JWST are highly attractive targets for this analysis. As a byproduct of its normal operations, JWST will produce exquisite new TTV datasets that can be used to probe questions that have never been accessible to study before. There are many near-MMR systems of small planets with scheduled JWST observations, and more will likely be scheduled. Typical JWST timing precisions are < 10 seconds (e.g., Agol et al., 2024), a regime rarely accessed by ground-based observations, or by the Kepler or TESS missions. This precision will usher in a new era of dynamical constraints based on JWST white light curve transits, which can be combined with TESS and ground-based follow-up to yield extremely precise planet masses and eccentricities. For systems known to exhibit TTVs or be near-resonance, even two transits from JWST can significantly improve dynamical constraints (e.g., Wallack et al. 2025, in rev.). JWST transits alone will often not be numerous enough to yield independent TTV solutions, but the extreme timing precision provides an anchor for TESS or ground-based transits that can yield exquisite constraints on planetary masses, orbital parameters, and tidal heating rates. JWST will also likely reveal unexpected TTVs in many systems, which can be used to identify new planets (e.g., Wallack et al. 2025, in rev.). In some cases, these TTVs may be exceedingly small, undetectable with current ground-based observatories.

The methods for TTV modeling and analysis developed in this thesis, especially the posterior sampling technique used to identify extremely narrow peaks in parameter space from a wide prior distribution that does not make limiting assumptions about planet masses or orbital properties, and the dynamical analysis technique used to identify steady-state forced eccentricities and compare with TTV-based eccentricities to constrain tidal efficiency factors, can be applied to many more near resonant systems. In the coming years, this analysis will be applied to many of the small planets whose atmospheres are being characterized with JWST. This will provide us with a deeper understanding of how tidal heating affects the compositions and evolution of rocky planets. Future TTV studies can also push to lower masses and rarer dynamical configurations with JWST data.

The upcoming PLATO (Rauer et al., 2025) and Roman space telescope (Wilson et al., 2023; Tamburo et al., 2023) missions will also discover thousands more transiting planets, some of which will be in dynamically interacting multi-planet systems. TTV analysis can be used to confirm many of the near-resonant planet candidates from Roman that orbit faint stars and are challenging to confirm with standard follow-up observations (Montet et al., 2017), or to measure masses and densities for near-resonant PLATO planets that orbit bright stars and might be amenable to detailed follow-up characterization (Rauer et al., 2025). The future of discovery for small and near-resonant planets is bright. I look forward to the next great observational surprise, and the following re-adjustment that will leave us with a better understanding of these distant rocky worlds.

BIBLIOGRAPHY

Agol, Eric et al. (Oct. 2024). “Updated Forecast for TRAPPIST-1 Times of Transit for All Seven Exoplanets Incorporating JWST Data”. In: *Research Notes of the American Astronomical Society* 8.10, 274, p. 274. DOI: `10.3847/2515-5172/ad8b46`. arXiv: `2409.11620 [astro-ph.EP]`.

Atri, Dimitra et al. (Jan. 2021). “Stellar flares versus luminosity: XUV-induced atmospheric escape and planetary habitability”. In: *MNRAS* 500.1, pp. L1–L5. DOI: `10.1093/mnrasl/slaa166`. arXiv: `2009.04310 [astro-ph.EP]`.

Banerjee, Agnibha et al. (Nov. 2024). “Atmospheric Retrievals Suggest the Presence of a Secondary Atmosphere and Possible Sulfur Species on L98-59 d from JWST Nirspec G395H Transmission Spectroscopy”. In: *ApJL* 975.1, L11, p. L11. DOI: `10.3847/2041-8213/ad73d0`. arXiv: `2408.15707 [astro-ph.EP]`.

Baumeister, Philipp et al. (Jan. 2020). “Machine-learning Inference of the Interior Structure of Low-mass Exoplanets”. In: *ApJ* 889.1, 42, p. 42. DOI: `10.3847/1538-4357/ab5d32`. arXiv: `1911.12745 [astro-ph.EP]`.

Baumeister, Philipp et al. (Aug. 2023). “ExoMDN: Rapid characterization of exoplanet interior structures with mixture density networks”. In: *A&A* 676, A106, A106. DOI: `10.1051/0004-6361/202346216`. arXiv: `2306.09002 [astro-ph.EP]`.

Bello-Arufe, Aaron et al. (Feb. 2025). “Evidence for a Volcanic Atmosphere on the Sub-Earth L 98-59 b”. In: *ApJL* 980.2, L26, p. L26. DOI: `10.3847/2041-8213/adaf22`. arXiv: `2501.18680 [astro-ph.EP]`.

Benneke, Björn et al. (Mar. 2024). “JWST Reveals CH_4, CO_2, and H_2O in a Metal-rich Miscible Atmosphere on a Two-Earth-Radius Exoplanet”. In: *arXiv e-prints*, arXiv:2403.03325, arXiv:2403.03325. DOI: `10.48550/arXiv.2403.03325`. arXiv: `2403.03325 [astro-ph.EP]`.

Berger, Travis A. et al. (Sept. 2020). “The Gaia-Kepler Stellar Properties Catalog. II. Planet Radius Demographics as a Function of Stellar Mass and Age”. In: *AJ* 160.3, 108, p. 108. DOI: `10.3847/1538-3881/aba18a`. arXiv: `2005.14671 [astro-ph.EP]`.

Bitsch, Bertram et al. (May 2021). “Dry or water world? How the water contents of inner sub-Neptunes constrain giant planet formation and the location of the water ice line”. In: *A&A* 649, L5, p. L5. DOI: `10.1051/0004-6361/202140793`. arXiv: `2104.11631 [astro-ph.EP]`.

Bonfils, X. et al. (Jan. 2013). “The HARPS search for southern extra-solar planets. XXXI. The M-dwarf sample”. In: *A&A* 549, A109, A109. DOI: `10.1051/0004-6361/201014704`. arXiv: `1111.5019 [astro-ph.EP]`.

Borucki, W. J. et al. (Feb. 2010). “Kepler Planet-Detection Mission: Introduction and First Results”. In: *Science* 327, p. 977. DOI: `10.1126/science.1185402`.

Brady, Madison et al. (Aug. 2024). “Early Results from the HUMDRUM Survey: A Small, Earth-mass Planet Orbits TOI-1450A”. In: *AJ* 168.2, 67, p. 67. DOI: `10.3847/1538-3881/ad500a`. arXiv: `2405.10400 [astro-ph.EP]`.

Bryant, Edward M. et al. (May 2023). “The occurrence rate of giant planets orbiting low-mass stars with TESS”. In: *MNRAS* 521.3, pp. 3663–3681. DOI: `10.1093/mnras/stad626`. arXiv: `2303.00659 [astro-ph.EP]`.

Chen, Howard et al. (Nov. 2016). “Evolutionary Analysis of Gaseous Sub-Neptune-mass Planets with MESA”. In: *ApJ* 831.2, 180, p. 180. DOI: `10.3847/0004-637X/831/2/180`. arXiv: `1603.06596 [astro-ph.EP]`.

Cointepas, M. et al. (May 2024). “TOI-663: A newly discovered multi-planet system with three transiting mini-Neptunes orbiting an early M star”. In: *A&A* 685, A19, A19. DOI: `10.1051/0004-6361/202346899`.

Dai, Fei et al. (Sept. 2024). “An Earth-sized Planet on the Verge of Tidal Disruption”. In: *AJ* 168.3, 101, p. 101. DOI: `10.3847/1538-3881/ad5a7d`. arXiv: `2407.21167 [astro-ph.EP]`.

Deck, Katherine M. et al. (Apr. 2015). “Measurement of Planet Masses with Transit Timing Variations Due to Synodic “Chopping” Effects”. In: *ApJ* 802.2, 116, p. 116. DOI: `10.1088/0004-637X/802/2/116`. arXiv: `1411.0004 [astro-ph.EP]`.

– (Apr. 2016). “Transit Timing Variations for Planets near Eccentricity-type Mean Motion Resonances”. In: *ApJ* 821.2, 96, p. 96. DOI: `10.3847/0004-637X/821/2/96`. arXiv: `1509.08460 [astro-ph.EP]`.

Diamond-Lowe, Hannah et al. (Nov. 2022). “The K2-3 System Revisited: Testing Photoevaporation and Core-powered Mass Loss with Three Small Planets Spanning the Radius Valley”. In: *AJ* 164.5, 172, p. 172. DOI: `10.3847/1538-3881/ac7807`. arXiv: `2207.12755 [astro-ph.EP]`.

Dressing, Courtney D. et al. (July 2015). “The Occurrence of Potentially Habitable Planets Orbiting M Dwarfs Estimated from the Full Kepler Dataset and an Empirical Measurement of the Detection Sensitivity”. In: *ApJ* 807.1, 45, p. 45. DOI: `10.1088/0004-637X/807/1/45`. arXiv: `1501.01623 [astro-ph.EP]`.

Fabrycky, Daniel C. et al. (Aug. 2014). “Architecture of Kepler’s Multi-transiting Systems. II. New Investigations with Twice as Many Candidates”. In: *ApJ* 790.2, 146, p. 146. DOI: `10.1088/0004-637X/790/2/146`. arXiv: `1202.6328 [astro-ph.EP]`.

Foreman-Mackey, Daniel (2016). “corner.py: Scatterplot matrices in Python”. In: *The Journal of Open Source Software* 24. DOI: `10.21105/joss.00024`. URL: `http://dx.doi.org/10.5281/zenodo.45906`.

Fortney, Jonathan J. et al. (Dec. 2020). “Beyond Equilibrium Temperature: How the Atmosphere/Interior Connection Affects the Onset of Methane, Ammonia, and Clouds in Warm Transiting Giant Planets”. In: *AJ* 160.6, 288, p. 288. DOI: `10.3847/1538-3881/abc5bd`. arXiv: `2010.00146 [astro-ph.EP]`.

Fulton, Benjamin J. et al. (Aug. 2017). “The California-KeplerSurvey. III. A Gap in the Radius Distribution of Small Planets”. In: *The Astronomical Journal* 154.3, p. 109. ISSN: 1538-3881. DOI: `10.3847/1538-3881/aa80eb`. URL: `http://dx.doi.org/10.3847/1538-3881/aa80eb`.

Gaia Collaboration et al. (Nov. 2016). “The Gaia mission”. In: *A&A* 595, A1, A1. DOI: `10.1051/0004-6361/201629272`. arXiv: `1609.04153 [astro-ph.IM]`.

Gan, Tianjun et al. (Jan. 2023). “Occurrence Rate of Hot Jupiters Around Early-type M Dwarfs Based on Transiting Exoplanet Survey Satellite Data”. In: *AJ* 165.1, 17, p. 17. DOI: `10.3847/1538-3881/ac9b12`. arXiv: `2210.08313 [astro-ph.EP]`.

Goldberg, Max et al. (Dec. 2022). “A criterion for the stability of planets in chains of resonances”. In: *Icarus* 388, 115206, p. 115206. DOI: `10.1016/j.icarus.2022.115206`. arXiv: `2207.13833 [astro-ph.EP]`.

Greklek-McKeon, Michael et al. (Feb. 2023). “Constraining the Densities of the Three Kepler-289 Planets with Transit Timing Variations”. In: *AJ* 165.2, 48, p. 48. DOI: `10.3847/1538-3881/ac8553`. arXiv: `2208.00022 [astro-ph.EP]`.

Greklek-McKeon, Michael, Shreyas Vissapragada, and Heather A. Knutson, et al. (2025). “Tidally Heated Sub-Neptunes, Refined Planetary Compositions, and Confirmation of a Third Planet in the TOI-1266 System”. In: *The Astronomical Journal* 169.6, p. 292. DOI: `10.3847/1538-3881/adc0fe`.

Greklek-McKeon, Michael, Heather A. Knutson, and W. Garrett Levine, et al. (2025). “Updated Mass, Eccentricity, and Tidal Heating Constraints for the Earth-sized Planet LP 791-18 d”. In: *arXiv e-prints* arXiv:2501.18700. DOI: `10.48550/arXiv.2501.18700`.

Gressier, Amélie et al. (Nov. 2024). “Hints of a Sulfur-rich Atmosphere around the 1.6 $R_\oplus$ Super-Earth L98-59 d from JWST NIRspec G395H Transmission Spectroscopy”. In: *ApJL* 975.1, L10, p. L10. DOI: `10.3847/2041-8213/ad73d1`. arXiv: `2408.15855 [astro-ph.EP]`.

Gupta, Akash et al. (July 2019). “Sculpting the valley in the radius distribution of small exoplanets as a by-product of planet formation: the core-powered mass-loss mechanism”. In: *MNRAS* 487.1, pp. 24–33. DOI: `10.1093/mnras/stz1230`. arXiv: `1811.03202 [astro-ph.EP]`.

– (Mar. 2020). “Signatures of the core-powered mass-loss mechanism in the exoplanet population: dependence on stellar properties and observational predictions”. In: *MNRAS* 493.1, pp. 792–806. DOI: `10.1093/mnras/staa315`. arXiv: `1907.03732 [astro-ph.EP]`.

Harbach, Laura M. et al. (June 2021). “Stellar Winds Drive Strong Variations in Exoplanet Evaporative Outflow Patterns and Transit Absorption Signatures”. In: *ApJ* 913.2, 130, p. 130. DOI: `10.3847/1538-4357/abf63a`. arXiv: `2012.05922 [astro-ph.EP]`.

Hardegree-Ullman, Kevin K. et al. (Aug. 2019). “Kepler Planet Occurrence Rates for Mid-type M Dwarfs as a Function of Spectral Type”. In: *AJ* 158.2, 75, p. 75. DOI: `10.3847/1538-3881/ab21d2`. arXiv: `1905.05900 [astro-ph.EP]`.

Holczer, Tomer et al. (July 2016). “Transit Timing Observations from Kepler. IX. Catalog of the Full Long-cadence Data Set”. In: *ApJS* 225.1, 9, p. 9. DOI: `10.3847/0067-0049/225/1/9`. arXiv: `1606.01744 [astro-ph.EP]`.

Hsu, Danley C. et al. (Sept. 2019). “Occurrence Rates of Planets Orbiting FGK Stars: Combining Kepler DR25, Gaia DR2, and Bayesian Inference”. In: *AJ* 158.3, 109, p. 109. DOI: `10.3847/1538-3881/ab31ab`. arXiv: `1902.01417 [astro-ph.EP]`.

Hsu, Danley C. et al. (Oct. 2020). “Occurrence rates of planets orbiting M Stars: applying ABC to Kepler DR25, Gaia DR2, and 2MASS data”. In: *MNRAS* 498.2, pp. 2249–2262. DOI: `10.1093/mnras/staa2391`. arXiv: `2002.02573 [astro-ph.EP]`.

Hu, Renyu et al. (Nov. 2021). “Unveiling Shrouded Oceans on Temperate sub-Neptunes via Transit Signatures of Solubility Equilibria versus Gas Thermochemistry”. In: *ApJL* 921.1, L8, p. L8. DOI: `10.3847/2041-8213/ac1f92`. arXiv: `2108.04745 [astro-ph.EP]`.

Huang, Chenliang et al. (July 2022). “MAGRATHEA: an open-source spherical symmetric planet interior structure code”. In: *MNRAS* 513.4, pp. 5256–5269. DOI: `10.1093/mnras/stac1133`. arXiv: `2201.03094 [astro-ph.EP]`.

Ito, Yuichi et al. (May 2025). “Monosilane Worlds: Sub-Neptunes with Atmospheres Shaped by Reduced Magma Oceans”. In: *arXiv e-prints*, arXiv:2505.03200, arXiv:2505.03200. DOI: `10.48550/arXiv.2505.03200`. arXiv: `2505.03200 [astro-ph.EP]`.

Jackson, Brian et al. (Nov. 2008). “Tidal heating of terrestrial extrasolar planets and implications for their habitability”. In: *MNRAS* 391.1, pp. 237–245. DOI: `10.1111/j.1365-2966.2008.13868.x`. arXiv: `0808.2770 [astro-ph]`.

Johnstone, C. P. (Feb. 2020). “Hydrodynamic Escape of Water Vapor Atmospheres near Very Active Stars”. In: *ApJ* 890.1, 79, p. 79. DOI: `10.3847/1538-4357/ab6224`. arXiv: `1912.07027 [astro-ph.EP]`.

Jontof-Hutter, Daniel et al. (Mar. 2016). “Secure Mass Measurements from Transit Timing: 10 Kepler Exoplanets between 3 and 8 $M_\oplus$ with Diverse Densities and Incident Fluxes”. In: *ApJ* 820.1, 39, p. 39. DOI: `10.3847/0004-637X/820/1/39`. arXiv: `1512.02003 [astro-ph.EP]`.

Jontof-Hutter, Daniel et al. (May 2021). "Following Up the Kepler Field: Masses of Targets for Transit Timing and Atmospheric Characterization". In: *AJ* 161.5, 246, p. 246. DOI: `10.3847/1538-3881/abd93f`. arXiv: `2101.01202 [astro-ph.EP]`.

Kempton, Eliza M. -R. et al. (Aug. 2023). "A reflective, metal-rich atmosphere for GJ 1214b from its JWST phase curve". In: *Nature* 620.7972, pp. 67–71. DOI: `10.1038/s41586-023-06159-5`. arXiv: `2305.06240 [astro-ph.EP]`.

Kimura, Tadahiro et al. (Nov. 2022). "Predicted diversity in water content of terrestrial exoplanets orbiting M dwarfs". In: *Nature Astronomy* 6, pp. 1296–1307. DOI: `10.1038/s41550-022-01781-1`. arXiv: `2209.14563 [astro-ph.EP]`.

Kite, Edwin S. et al. (Mar. 2020). "Atmosphere Origins for Exoplanet Sub-Neptunes". In: *ApJ* 891.2, 111, p. 111. DOI: `10.3847/1538-4357/ab6ffb`. arXiv: `2001.09269 [astro-ph.EP]`.

Lacedelli, G. et al. (Sept. 2024). "Characterisation of TOI-406 as showcase of the THIRSTEE program: A 2-planet system straddling the M-dwarf density gap". In: *arXiv e-prints*, arXiv:2409.11083, arXiv:2409.11083. DOI: `10.48550/arXiv.2409.11083`. arXiv: `2409.11083 [astro-ph.EP]`.

Lacedelli, G. et al. (Apr. 2025). "A transiting rocky super-Earth and a non-transiting sub-Neptune orbiting the M dwarf TOI-771". In: *arXiv e-prints*, arXiv:2504.18223, arXiv:2504.18223. DOI: `10.48550/arXiv.2504.18223`. arXiv: `2504.18223 [astro-ph.EP]`.

Latham, David W. et al. (May 1989). "The unseen companion of HD114762: a probable brown dwarf". In: *Nature* 339.6219, pp. 38–40. DOI: `10.1038/339038a0`.

Lee, Eve J. (June 2019). "The Boundary between Gas-rich and Gas-poor Planets". In: *ApJ* 878.1, 36, p. 36. DOI: `10.3847/1538-4357/ab1b40`. arXiv: `1904.10470 [astro-ph.EP]`.

Lee, Eve J. et al. (Feb. 2016). "Breeding Super-Earths and Birthing Super-puffs in Transitional Disks". In: *ApJ* 817.2, 90, p. 90. DOI: `10.3847/0004-637X/817/2/90`. arXiv: `1510.08855 [astro-ph.EP]`.

Lee, Eve J. et al. (Feb. 2021). "Primordial Radius Gap and Potentially Broad Core Mass Distributions of Super-Earths and Sub-Neptunes". In: *ApJ* 908.1, 32, p. 32. DOI: `10.3847/1538-4357/abd6c7`. arXiv: `2008.01105 [astro-ph.EP]`.

Lee, Eve J. et al. (Dec. 2022). "Creating the Radius Gap without Mass Loss". In: *ApJ* 941.2, 186, p. 186. DOI: `10.3847/1538-4357/ac9c66`. arXiv: `2201.09898 [astro-ph.EP]`.

Lee, Rena A. et al. (Apr. 2025). "TOI-6324 b: An Earth-mass Ultra-short-period Planet Transiting a Nearby M Dwarf". In: *ApJL* 983.2, L36, p. L36. DOI: `10.3847/2041-8213/adadd7`. arXiv: `2502.16087 [astro-ph.EP]`.

Lithwick, Yoram et al. (Dec. 2012). "Extracting Planet Mass and Eccentricity from TTV Data". In: *ApJ* 761.2, 122, p. 122. DOI: `10.1088/0004-637X/761/2/122`. arXiv: `1207.4192 [astro-ph.EP]`.

Lopez, Eric D. et al. (Sept. 2014). “Understanding the Mass-Radius Relation for Sub-neptunes: Radius as a Proxy for Composition”. In: *ApJ* 792.1, 1, p. 1. DOI: `10.1088/0004-637X/792/1/1`. arXiv: `1311.0329 [astro-ph.EP]`.

– (Feb. 2016). “Re-inflated Warm Jupiters around Red Giants”. In: *ApJ* 818.1, 4, p. 4. DOI: `10.3847/0004-637X/818/1/4`. arXiv: `1510.00067 [astro-ph.EP]`.

Lu, Tiger et al. (May 2023). “Self-consistent Spin, Tidal, and Dynamical Equations of Motion in the REBOUNDx Framework”. In: *The Astrophysical Journal* 948.1, p. 41. ISSN: 1538-4357. DOI: `10.3847/1538-4357/acc06d`. URL: `http://dx.doi.org/10.3847/1538-4357/acc06d`.

Luque, Rafael et al. (Sept. 2022). “Density, not radius, separates rocky and water-rich small planets orbiting M dwarf stars”. In: *Science* 377.6611, pp. 1211–1214. DOI: `10.1126/science.abl7164`. arXiv: `2209.03871 [astro-ph.EP]`.

Madhusudhan, Nikku et al. (Oct. 2023). “Carbon-bearing Molecules in a Possible Hycean Atmosphere”. In: *ApJL* 956.1, L13, p. L13. DOI: `10.3847/2041-8213/acf577`. arXiv: `2309.05566 [astro-ph.EP]`.

Ment, Kristo et al. (June 2023). “The Occurrence Rate of Terrestrial Planets Orbiting Nearby Mid-to-late M Dwarfs from TESS Sectors 1-42”. In: *AJ* 165.6, 265, p. 265. DOI: `10.3847/1538-3881/acd175`. arXiv: `2302.04242 [astro-ph.EP]`.

Mignon, L. et al. (Feb. 2025). “Radial velocity homogeneous analysis of M dwarfs observed with HARPS. II. Detection limits and planetary occurrence statistics”. In: *arXiv e-prints*, arXiv:2502.06553, arXiv:2502.06553. DOI: `10.48550/arXiv.2502.06553`. arXiv: `2502.06553 [astro-ph.EP]`.

Millholland, Sarah (Nov. 2019). “Tidally Induced Radius Inflation of Sub-Neptunes”. In: *ApJ* 886.1, 72, p. 72. DOI: `10.3847/1538-4357/ab4c3f`. arXiv: `1910.06794 [astro-ph.EP]`.

Misener, William et al. (Sept. 2023). “Atmospheres as windows into sub-Neptune interiors: coupled chemistry and structure of hydrogen-silane-water envelopes”. In: *MNRAS* 524.1, pp. 981–992. DOI: `10.1093/mnras/stad1910`. arXiv: `2303.09653 [astro-ph.EP]`.

Montet, Benjamin T. et al. (Jan. 2014). “The TRENDS High-contrast Imaging Survey. IV. The Occurrence Rate of Giant Planets around M Dwarfs”. In: *ApJ* 781.1, 28, p. 28. DOI: `10.1088/0004-637X/781/1/28`. arXiv: `1307.5849 [astro-ph.EP]`.

Montet, Benjamin T. et al. (Apr. 2017). “Measuring the Galactic Distribution of Transiting Planets with WFIRST”. In: *PASP* 129.974, p. 044401. DOI: `10.1088/1538-3873/aa57fb`. arXiv: `1610.03067 [astro-ph.EP]`.

Morley, Caroline V. et al. (Feb. 2017). “Forward and Inverse Modeling of the Emission and Transmission Spectrum of GJ 436b: Investigating Metal Enrichment, Tidal Heating, and Clouds”. In: *AJ* 153.2, 86, p. 86. DOI: `10.3847/1538-3881/153/2/86`. arXiv: `1610.07632 [astro-ph.EP]`.

Mukherjee, Sagnick et al. (Oct. 2024). “Effects of Planetary Parameters on Disequilibrium Chemistry in Irradiated Planetary Atmospheres: From Gas Giants to Sub-Neptunes”. In: *arXiv e-prints*, arXiv:2410.17169, arXiv:2410.17169. DOI: `10.48550/arXiv.2410.17169`. arXiv: `2410.17169 [astro-ph.EP]`.

Mulders, Gijs D. et al. (Dec. 2015). “An Increase in the Mass of Planetary Systems around Lower-mass Stars”. In: *ApJ* 814.2, 130, p. 130. DOI: `10.1088/0004-637X/814/2/130`. arXiv: `1510.02481 [astro-ph.EP]`.

Murgas, F. et al. (Apr. 2024). “Wolf 327b: A new member of the pack of ultra-short-period super-Earths around M dwarfs”. In: *A&A* 684, A83, A83. DOI: `10.1051/0004-6361/202348813`. arXiv: `2401.12150 [astro-ph.EP]`.

NASA Exoplanet Archive (2025). *Planetary Systems Composite Parameters*. Version Version: 2025-05-13. DOI: `10.26133/NEA13`. URL: `https://catcopy.ipac.caltech.edu/dois/doi.php?id=10.26133/NEA13`.

Nicholls, Harrison et al. (May 2025). “Self-limited tidal heating and prolonged magma oceans in the L 98-59 system”. In: *arXiv e-prints*, arXiv:2505.03604, arXiv:2505.03604. DOI: `10.48550/arXiv.2505.03604`. arXiv: `2505.03604 [astro-ph.EP]`.

Owen, James E. et al. (Oct. 2013). “Kepler Planets: A Tale of Evaporation”. In: *ApJ* 775.2, 105, p. 105. DOI: `10.1088/0004-637X/775/2/105`. arXiv: `1303.3899 [astro-ph.EP]`.

Owen, James E. et al. (Feb. 2020). “Testing exoplanet evaporation with multitransiting systems”. In: *MNRAS* 491.4, pp. 5287–5297. DOI: `10.1093/mnras/stz3435`. arXiv: `1912.01609 [astro-ph.EP]`.

Parc, Léna et al. (Aug. 2024). “From super-Earths to sub-Neptunes: Observational constraints and connections to theoretical models”. In: *A&A* 688, A59, A59. DOI: `10.1051/0004-6361/202449911`. arXiv: `2406.04311 [astro-ph.EP]`.

Pass, Emily K. et al. (July 2023). “Mid-to-late M Dwarfs Lack Jupiter Analogs”. In: *AJ* 166.1, 11, p. 11. DOI: `10.3847/1538-3881/acd349`. arXiv: `2305.19357 [astro-ph.EP]`.

Peterson, Merrin S. et al. (May 2023). “A temperate Earth-sized planet with tidal heating transiting an M6 star”. In: *Nature* 617.7962, pp. 701–705. DOI: `10.1038/s41586-023-05934-8`.

Petigura, Erik A. et al. (Apr. 2022). “The California-Kepler Survey. X. The Radius Gap as a Function of Stellar Mass, Metallicity, and Age”. In: *AJ* 163.4, 179, p. 179. DOI: `10.3847/1538-3881/ac51e3`. arXiv: `2201.10020 [astro-ph.EP]`.

Piaulet, Caroline et al. (Feb. 2023). “Evidence for the volatile-rich composition of a 1.5-Earth-radius planet”. In: *Nature Astronomy* 7, pp. 206–222. DOI: `10.1038/s41550-022-01835-4`. arXiv: `2212.08477 [astro-ph.EP]`.

Piaulet-Ghorayeb, Caroline et al. (Oct. 2024a). “JWST/NIRISS Reveals the Water-rich “Steam World” Atmosphere of GJ 9827 d”. In: *ApJL* 974.1, L10, p. L10. doi: `10.3847/2041-8213/ad6f00`. arXiv: `2410.03527 [astro-ph.EP]`.

– (Oct. 2024b). “JWST/NIRISS Reveals the Water-rich “Steam World” Atmosphere of GJ 9827 d”. In: *ApJL* 974.1, L10, p. L10. doi: `10.3847/2041-8213/ad6f00`. arXiv: `2410.03527 [astro-ph.EP]`.

Rauer, Heike et al. (June 2025). “The PLATO mission”. In: *Experimental Astronomy* 59.3, 26, p. 26. doi: `10.1007/s10686-025-09985-9`. arXiv: `2406.05447 [astro-ph.IM]`.

Ribas, I. et al. (Feb. 2023). “The CARMENES search for exoplanets around M dwarfs. Guaranteed time observations Data Release 1 (2016-2020)”. In: *A&A* 670, A139, A139. doi: `10.1051/0004-6361/202244879`. arXiv: `2302.10528 [astro-ph.EP]`.

Ricker, George R. et al. (Oct. 2014). “Transiting Exoplanet Survey Satellite”. In: *Journal of Astronomical Telescopes, Instruments, and Systems* 1.1, p. 014003. issn: 2329-4124. doi: `10.1117/1.jatis.1.1.014003`. url: `http://dx.doi.org/10.1117/1.JATIS.1.1.014003`.

Rigby, Frances E. et al. (Mar. 2024). “On the ocean conditions of Hycean worlds”. In: *MNRAS* 529.1, pp. 409–424. doi: `10.1093/mnras/stae413`. arXiv: `2402.12330 [astro-ph.EP]`.

Rogers, James G. et al. (Apr. 2023). “Conclusive Evidence for a Population of Water Worlds around M Dwarfs Remains Elusive”. In: *ApJL* 947.1, L19, p. L19. doi: `10.3847/2041-8213/acc86f`. arXiv: `2301.04321 [astro-ph.EP]`.

Seligman, Darryl Z. et al. (Jan. 2024). “Potential Melting of Extrasolar Planets by Tidal Dissipation”. In: *ApJ* 961.1, 22, p. 22. doi: `10.3847/1538-4357/ad0b82`. arXiv: `2311.01187 [astro-ph.EP]`.

Seo, Chanoul et al. (Nov. 2024). “Role of Magma Oceans in Controlling Carbon and Oxygen of Sub-Neptune Atmospheres”. In: *ApJ* 975.1, 14, p. 14. doi: `10.3847/1538-4357/ad7461`. arXiv: `2408.17056 [astro-ph.EP]`.

Tamburo, Patrick et al. (June 2023). “Predicting the Yield of Small Transiting Exoplanets around Mid-M and Ultracool Dwarfs in the Nancy Grace Roman Space Telescope Galactic Bulge Time Domain Survey”. In: *AJ* 165.6, 251, p. 251. doi: `10.3847/1538-3881/acd1de`. arXiv: `2303.09959 [astro-ph.EP]`.

Thorngren, Daniel P. et al. (Mar. 2023). “Removal of Hot Saturns in Mass-Radius Plane by Runaway Mass Loss”. In: *ApJL* 945.2, L36, p. L36. doi: `10.3847/2041-8213/acbd35`. arXiv: `2211.11770 [astro-ph.EP]`.

Van Eylen, V. et al. (Oct. 2021). “Masses and compositions of three small planets orbiting the nearby M dwarf L231-32 (TOI-270) and the M dwarf radius valley”. In: *MNRAS* 507.2, pp. 2154–2173. doi: `10.1093/mnras/stab2143`. arXiv: `2101.01593 [astro-ph.EP]`.

Welbanks, Luis et al. (June 2024). "A high internal heat flux and large core in a warm Neptune exoplanet". In: *Nature* 630.8018, pp. 836–840. DOI: `10.1038/s41586-024-07514-w`. arXiv: `2405.11018 [astro-ph.EP]`.

Werlen, Aaron et al. (Apr. 2025). "Atmospheric C/O Ratios of Sub-Neptunes with Magma Oceans: Homemade rather than Inherited". In: *arXiv e-prints*, arXiv:2504.20450, arXiv:2504.20450. DOI: `10.48550/arXiv.2504.20450`. arXiv: `2504.20450 [astro-ph.EP]`.

Wilson, Robert F. et al. (Nov. 2023). "Transiting Exoplanet Yields for the Roman Galactic Bulge Time Domain Survey Predicted from Pixel-level Simulations". In: *ApJS* 269.1, 5, p. 5. DOI: `10.3847/1538-4365/acf3df`. arXiv: `2305.16204 [astro-ph.EP]`.

Winters, Jennifer G. et al. (Jan. 2015). "The Solar Neighborhood. XXXV. Distances to 1404 m Dwarf Systems Within 25 pc in the Southern Sky". In: *AJ* 149.1, 5, p. 5. DOI: `10.1088/0004-6256/149/1/5`. arXiv: `1407.7837 [astro-ph.SR]`.

Wogan, Nicholas F. et al. (Mar. 2024). "JWST Observations of K2-18b Can Be Explained by a Gas-rich Mini-Neptune with No Habitable Surface". In: *ApJL* 963.1, L7, p. L7. DOI: `10.3847/2041-8213/ad2616`. arXiv: `2401.11082 [astro-ph.EP]`.

Yang, Jeehyun et al. (Aug. 2024). "Chemical Mapping of Temperate Sub-Neptune Atmospheres: Constraining the Deep Interior H_2O/H_2 Ratio from the Atmospheric CO_2/CH_4 Ratio". In: *ApJL* 971.2, L48, p. L48. DOI: `10.3847/2041-8213/ad6b25`. arXiv: `2406.01955 [astro-ph.EP]`.

Yang, Jia-Yi et al. (Apr. 2020). "Occurrence and Architecture of Kepler Planetary Systems as Functions of Stellar Mass and Effective Temperature". In: *AJ* 159.4, 164, p. 164. DOI: `10.3847/1538-3881/ab7373`. arXiv: `2002.02840 [astro-ph.EP]`.

Zhang, Michael et al. (Apr. 2025). "Constraining Atmospheric Composition from the Outflow: Helium Observations Reveal the Fundamental Properties of Two Planets Straddling the Radius Gap". In: *AJ* 169.4, 204, p. 204. DOI: `10.3847/1538-3881/adb490`. arXiv: `2409.08318 [astro-ph.EP]`.